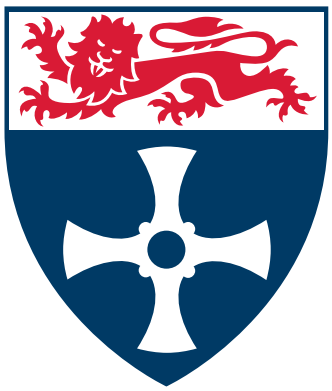

Pluripotent stem cell-derived retinal organoids and retinal pigment epithelium as a model system for screening chemotherapeutic agents in retinoblastoma

Rodrigo Cerna Chavez

A thesis submitted to Newcastle University for the degree of Doctor of Philosophy (PhD)

Student ID: 190571889

Biosciences Institute

Faculty of Medical Sciences

Newcastle University

November 2022

Abstract

Retinoblastoma (Rb) is a rare childhood malignancy of the developing retina affecting 1:15,000 infants worldwide. The biallelic inactivation of the *RB1* gene and the retinoblastoma protein (pRB) loss accounts for up to 98% of Rb cases. Despite the progress in Rb treatments, standard chemotherapeutic agents have been associated with adverse effects on the retina and defects of the retinal pigment epithelium (RPE).

Herein, we developed two disease models through retinal organoid differentiation of a pRB-depleted human embryonic stem cell line (H9 RB1-null hESCs) and an Rb patient-specific induced pluripotent (hiPSC) line displaying an *RB1* biallelic mutation (c.2082delC). Both models were characterised by pRB depletion and a significant increase in the fraction of proliferating cone precursors ($RXR\gamma^{+}Ki67^{+}$). The pRB-depleted retinal organoids displayed similar features to Rb tumours, including undergoing cell growth in an anchorage-independent manner indicative of cell transformation *in vitro*. Applying Rb chemotherapeutics such as melphalan, topotecan and TW-37 significantly reduced the fraction of Rb proliferating cone precursors.

Additionally, we established two hESC-RPE and hiPSC-RPE models to assess the cytotoxicity of the same three drugs. Our results indicated that these agents applied in the clinical range decreased the monolayer barrier's trans-epithelial resistance and affected the cells' phagocytic activity. Moreover, transcriptional analyses demonstrated an altered gene expression in melanin and retinol processing, tight junction and apical-basal polarity pathways. None of the drug treatments within the clinical range caused significant cytotoxicity or changes to the apical-basal polarity, tight junction network or cell cycle. Although standard Rb chemotherapeutics did not induce cytotoxicity in RPE, their application *in vitro* led to compromised phagocytosis and strength of the barrier.

This thesis highlights the applications of retinal organoids and RPE in disease modelling, confirming the suitability of these *in vitro* models for testing novel therapeutics for Rb.

“I must not fear. Fear is the mind-killer. Fear is the little-death that brings total obliteration. I will face my fear. I will permit it to pass over me and through me. And when it has gone past, I will turn the inner eye to see its path. Where the fear has gone there will be nothing. Only I will remain.”

— Frank Herbert, Dune

Acknowledgements

I would like to express my gratitude to my supervisors, Professor Majlinda Lako and Dr Agata Rozanska, for their invaluable guidance and supervision during my PhD studies. This PhD thesis would not have been possible without their advice, support, help and patience. Also, I would like to thank Prof. Majlinda Lako for believing in my abilities and potential and for allowing me to publish research articles in our group and get involved in other projects beyond the scope of my thesis. Additionally, I would like to thank my second supervisor, Dr Agata Rozanska, for her time, insights, and support and for giving essential feedback and the right advice when I needed it the most. I would also like to thank my thesis committee, Prof. David Steel and Prof. Colin Johnson, for their time and expertise.

I would like to express my gratitude to Dr Joseph Colin for all his knowledge, help and expertise with the flow cytometry experiments. Also, I would like to thank Dr Birthe Dorgau for all her knowledge, help and support on retinal organoids and immunohistochemistry. I would like to thank Dr Jack Thornton for his advice on the LDH cytotoxicity experiments, Dr Maria Georgiou and Robert Atkinson for teaching me all the necessary techniques for the RPE experiments, Miss Rozaliya Tsikandelova for her help with flow cytometry data analysis, and our collaborator, MD Manoj Parulekar (Birmingham Women's and Children NHS Foundation Trust) for providing essential samples and reagents for this PhD project. I would like to thank my excellent BSc. student, Miss Giulia Poretti, for her hard work and passion for performing the qPCR experiments on the RPE samples. Finally, I would like to especially thank my sponsor, Consejo Nacional de Ciencia y Tecnologia (CONACYT), as part of the Mexican Government, for funding my PhD studies over the last three years.

I would like to thank my PhD friends, Jack Thornton, Avril Watson, Anastassia Kostenko, and Rozaliya Tsikandelova, for being exceptionally supportive and helpful during the darkest hours. Additionally, I would like to express my gratitude to all my colleagues and friends from the stem cell group for all their support and for creating a friendly and collaborative environment that has

extended beyond the lab. I feel incredibly privileged and grateful for being a member of this group during my PhD.

Last but not least, I am enormously thankful to my mum, dad, family, and friends (especially Catalina Cortes, Stefanie Barnaba and Talita Serpa) for their love and support throughout the years. I am in your debt for all the help, understanding and advice that motivated me to achieve all my personal and professional goals. I would never be here today without all of you.

COVID-19 impact statement

Unfortunately, the start of the COVID-19 pandemic in early March 2020 prevented continuing essential maintenance of cell culture and key experiments for my PhD project. The lab shutdown led to the discarding of essential cell cultures, including retinal organoids, losing consumables and time. Further research approaches could have been taken if access to the labs had not been restricted during the pandemic, including:

1) Additional retinal organoid differentiations:
    a. Apoptosis and cell cycle assays by flow cytometry for retinoblastoma organoids following drug treatments.
    b. Gene expression of retinal markers in drug-treated retinal organoids by quantitative real-time qPCR.
2) Additional retinal pigment epithelium differentiations:
    a. Heterozygous (*RB1*$^{+/-}$) patient-induced pluripotent stem cell-derived retinal pigment epithelium cells for accurately modelling the *in vivo* environment of heritable retinoblastoma of retinal organoids patients.
    b. Gene expression of a broader number of markers in drug-treated retinal pigment epithelium cells by quantitative real-time qPCR.
    c. Transcriptomic profiling of drug-treated retinal pigment epithelium cells by single-cell RNA sequencing.

Data contribution to publications

Data in **3** and **4** from the following subsections contributed to the publication (Rozanska et al., 2022):

- 3.3.1 The steady-state level of pRB is highest at the early stage of differentiation and decreases with time:
    - Figure 3-2. Immunofluorescence analysis for pRB of hESC- and patient hiPSC-derived retinal organoids throughout differentiation stages.
- 3.3.2Expression of pRB in different retinal cell types in H9 control hESC-derived retinal organoids:
    - Figure 3-3. Immunofluorescence analysis of H9 control hESC-derived ROs at days 35 and 90 of differentiation.
    - Figure 3-4. Immunofluorescence analysis of H9 control hESC-ROs at day 150 of differentiation.
- 3.3.3 pRB inactivation results in a significant increase in proliferating cone precursor, horizontal, retinal ganglion cells, and a decrease in amacrine cells during retinal organoid maturation:
    - Figure 3-5. Immunohistochemical analysis of hESC-derived retinal organoids at day 35 of differentiation.
    - Figure 3-6. Immunohistochemical analysis of hESC-derived retinal organoids at day 90 of differentiation.
    - Figure 3-7. Immunohistochemical analysis of hESC-derived retinal organoids at day 150 of differentiation.
- 3.3.4 The mitotic and tumorigenic activity is limited to the homozygous RB1+$^{/+}$ but not heterozygous RB1+$^{/-}$ hiPSC-RO phenotype:
    - Figure 3-10. Immunohistochemical analysis of patient hiPSC-derived retinal organoids at day 35 of differentiation.Figure 3-10. Immunohistochemical analysis of patient hiPSC-derived retinal organoids at day 35 of differentiation.
    - Figure 3-11. Immunohistochemical analysis of patient hiPSC-derived retinal organoids at day 90 of differentiation.

- Figure 3-12. Immunohistochemical analysis of patient hiPSC-derived retinal organoids at day 150 of differentiation.

- 4.3.2 Rb chemotherapeutic agents cause a significant decrease of proliferating cone precursor cells in pRB-depleted retinal organoids:
  - Figure 4-4. Proliferating cone precursor assessment of chemotherapeutic agents for Rb treatment in 150-day-old H9 control and H9 RB1-null hESC-derived retinal organoids.
  - Figure 4-6. Proliferating cone precursor assessment of chemotherapeutic agents for Rb treatment in 150-day-old patient hiPSC-derived retinal organoids.

- Rozanska, A., **Cerna-Chavez, R**., Queen, R., Collin, J., Zerti, D., Dorgau, B., Beh, C. S., Davey, T., Coxhead, J., Hussain, R., Al-Aama, J., Steel, D. H., Benvenisty, N., Armstrong, L., Parulekar, M. & Lako, M. 2022. pRB-Depleted Pluripotent Stem Cell Retinal Organoids Recapitulate Cell State Transitions of Retinoblastoma Development and Suggest an Important Role for pRB in Retinal Cell Differentiation. Stem Cells Translational Medicine, 29;11(4):415-433. doi: 10.1093/stcltm/szac008.

Data in **5** from the following subsections contributed to the publication under review (Cerna-Chavez et al.):

- ✓ 5.3.1 Drug testing in hESC- and hiPSC-derived RPE cells
  - Figure 5-1. Characterisation and drug screening of H9 hESC- and hiPSC-derived RPE cells.
  - Figure 5-2. Immunofluorescence analysis for the apical-basal polarity of H9 hESC- and hiPSC-derived RPE cells.
  - Figure 5-3. Immunofluorescence analysis for the tight junctions of H9 hESC- and hiPSC-derived RPE cells.
  - Figure 5-4. Transepithelial electrical resistance analysis of H9 hESC- and hiPSC-derived RPE cells.

- Figure 5-6. Cell-cycle phase distribution analysis of clinically used chemotherapeutic agents for Rb treatment in H9 hESC- and hiPSC-derived RPE cells.
- Figure 5-8. Assessment of clinically used chemotherapeutic agents for Rb treatment in H9 hESC-derived RPE cells.
- Figure 5-9. Assessment of clinically used chemotherapeutic agents for Rb treatment in hiPSC-derived RPE cells.

✓ 5.3.2 Gene expression regulation in drug-treated hESC- and hiPSC-derived RPE cells:

- Figure 5-10. Quantitative real-time PCR validation of selected genes of clinically used chemotherapeutic agents for Rb treatment in H9 hESC-derived RPE cells.
- Figure 5-11. Quantitative real-time PCR validation of selected genes of clinically used chemotherapeutic agents for Rb treatment hiPSC-derived RPE cells.

✓ 5.3.3 Phagocytic activity is affected in drug-treated hESC- and hiPSC-derived RPE cells:

- Figure 5-13. Phagocytic activity assessment of clinically used chemotherapeutic agents for Rb treatment in H9 hESC- and hiPSC-derived RPE cells.

✓ **Cerna-Chavez, R.** and Rozanska, A. L. and Poretti, G. L. and Benvenisty, N. and Parulekar, M. and Lako, M. Retinal Pigment Epithelium Exhibits Gene Expression and Phagocytic Activity Alterations When Exposed to Retinoblastoma Chemotherapeutics. Available at SSRN: https://ssrn.com/abstract=4244886 or http://dx.doi.org/10.2139/ssrn.4244886

Table of Contents

List of Figures

List of Tables

List of Abbreviations

2D	Two-dimensional
3D	Three-dimensional
AC	Amacrine Cell
AMD	Age-related Macular Degeneration
AP2α	Activating Enhancer-Binding Protein 2-Alpha
ATAC-Seq	Assay for Transposase-Accessible Chromatin with sequencing
ATP	Adenosine Triphosphate
BC	Bipolar Cell
Bcl-2	B-cell leukaemia anti-apoptotic proteins
bFGF	Basic Fibroblast Growth Factor
BMP-4	Bone Morphogenetic Protein 4
BrM	Bruch's Membrane
BRN3	Brain-specific homeobox/POU domain protein 3
BSA	Bovine Serum Albumin
Casp-3	Cleaved Caspase-3
CC BY-NC	Creative Commons Attribution Non-Commercial Licence
CDK	Cyclin-dependent kinases
Chx10	Ceh-10 Homeodomain Containing Homolog
ColIV	Collagen IV
CRALBP	Cellular Retinaldehyde-Binding Protein
CRX	Cone Rod Homeobox
DAPI	4′,6-diamidino-2-phenylindole
DMEM/F12	Dulbecco's Modified Eagle Medium: Nutrient Mixture F-12
E2F1	E2F Transcription Factor 1
EAAT5	Excitatory amino acid transporter
EB	Embryoid Body
ECM	Extracellular Matrix
EV	Extracellular Vesicle
EZR	Ezrin
FBS	Foetal Bovine Serum
FDA	Food and Drug Administration
FGF2	Fibroblast Growth Factor 2
FGFR	Fibroblast Growth Factor Receptor
Fig	Figure
FITC	Fluorescein Isothiocyanate
Fwk	Foetal Week
GABA	γ-aminobutyric acid
Gad1	Glutamate Decarboxylase 1
GlutaMAX	L-alanyl-L-glutamine
GlyT1	Sodium- And Chloride-Dependent Glycine Transporter 1

GSK3	Glycogen Synthase Kinase 3
G_t	G protein Transducin
H&E	Haematoxylin and Eosin
HC	Horizontal cell
HDAC	Histone Deacetylase
hESC	Human Embryonic Stem Cell
hiPSC	Human induced Pluripotent Stem Cell
HMGA2	High Mobility Group AT-Hook 2
HPV	Human papillomavirus
hTSC	Human Trophoblast Stem Cell
IGF-1	Insulin-like Growth Factor 1
IMDM	Iscove's Modified Dulbecco's Media
INL	Inner Nuclear Layer
IPL	Inner Plexiform Layer
KOSR	KnockOut™ Serum Replacement-Multi-Species
Lhx1	Lhx1 homeobox protein
LIF	Leukaemia Inhibitory Factor
Matrigel	Basement-membrane matrix components
MEK	Extracellular signal-regulated Kinase
mESC	Mouse Embryonic Stem Cell
miRNA	MicroRNA
MMP	Matrix Metalloproteinases
mTSC	Murine Trophoblast Stem Cell
NR	Neural Retina
NRL	Neural Retina Leucine Zipper
O-PDX	Orthotopic patient-derived xenograft
OPL	Outer Plexiform Layer
Opsin R/G	Opsin Red/Green
P	Passage
Pax6	Paired Box 6
PBS	Phosphate-Buffered Saline
PCW	Post-conception Week
Pen/-Strep	Penicillin-Streptomycin
PI	Propidium Iodide
PKC-α	Protein Kinase C α
POSs	Photoreceptor Outer Segments
PR	Photoreceptor
pRB	Retinoblastoma Protein
pRBC	C-terminal domain of pRB
PROX1	Prospero Homeobox 1
PRPFs	Pre-mRNA Processing Factors
PSC	Pluripotent Stem Cell

Rb	Retinoblastoma
RCF	Relative Centrifugal Force
RCVRN	Recoverin
RGC	Retinal Ganglion Cell
RHO	Rhodopsin
RO	Retinal Organoid
ROCKi	Rho-associated Coiled-coil protein Kinase inhibitor
RP	Retinitis Pigmentosa
RPC	Retinal Progenitor Cell
RPE	Retinal Pigment Epithelium
RT	Room Temperature
RXRγ	Retinoid X Receptor Gamma
scRNA-seq	Single-cell RNA-sequencing
SFEBq	Serum-free Floating and growth-factor-reduced
Shh	Sonic hedgehog homolog
Six6	SIX Homeobox 6
SKP2	S-Phase Kinase Associated Protein 2
SNCG	Synuclein Gamma
snRNA-seq	Single-Nuclei RNA sequencing
SOX9	SRY-Box Transcription Factor 9
STGD1	Stargardt Disease
SYK	Spleen Tyrosine Kinase
TCR	T-Cell Receptor
TEER	Transepithelial Electrical Resistance
TEM	Transmission Electron Microscopy
TGF-beta	Transforming Growth Factor beta
TKO MEFs	Triple Knock-Out Mouse Embryonic Fibroblasts
TSP-1	Thrombospondin-1
VEGF-A	Vascular Endothelial Growth Factor-A
VSX2	Visual System Homeobox 2
ZO-1	Tight Junction Protein 1

Chapter 1

1 Introduction

1.1 The human retina

The retina is the light-sensitive component of the eye composed of three layers of neurons, two layers of synapses and Müller glial cells that stretch across the thickness of the retina (Blond and Léveillard, 2019). There are five central neural cell populations in the neural retina: rod and cone photoreceptors (PRs), horizontal cells (HCs), bipolar cells (BCs), amacrine cells (ACs) and retinal ganglion cells (RGCs) (Stenfelt et al., 2017). The mammalian retina collects visual information and processes it as images through an internal circuitry involving other neuronal cell populations (Busskamp et al., 2010) (**Figure 1-1**).

Phototransduction starts when light enters the eye, reaches the retina and photons are absorbed by the outer segments –light-sensitive organelles that are modified cilia– of PRs, where an isomerisation of the chromophore conjugated with the visual pigment occurs (Sung and Chuang, 2010). The signal transduction cascade is initiated by the photoexcited visual pigment that amplifies the signal by activating the heterotrimeric G protein transducin (G_t), leading to the closure of cGMP-gated cation channels on the plasma membranes and hyperpolarisation of cells (Yau and Hardie, 2009). As a result of the change in the membrane potential, synapses release fewer glutamate neurotransmitters. The information is relayed to the bipolar cells to provide excitation to the ganglion cells, which integrate the signal from bipolar and amacrine cells and forward it as electrical responses via the optic nerve (Sung and Chuang, 2010) (**Figure 1-1**). In addition to this vertical and excitatory pathway, the amacrine cells in the inner retina can provide inhibition of both the bipolar and the retinal ganglion cells (Guo et al., 2014).

The optic cup derived from the rostral diencephalon –a division of the forebrain– is composed of inner and outer layers. During retinal development, these inner walls differentiate into the neural retina (NR), while the outer layers differentiate into retinal pigment epithelium (RPE) (Kuwahara et al., 2019). The macula is located in the centre of the human retina, subdivided into concentric areas with a progressive lower density of photoreceptors and poorer visual resolution: the foveola, fovea, parafovea, and perifovea (Labhishetty et al., 2019),

from central to outer location, respectively. The peripheral retina is positioned beyond the macula and consists of most of the retinal surface. The fovea is a particular area of the mammalian retina that is a critical spatial layout of the neuronal network (Malek et al., 2006, Jager et al., 2008). It is a specific region characterised by a high concentration of cone photoreceptors for high-acuity vision (Busskamp et al., 2010).

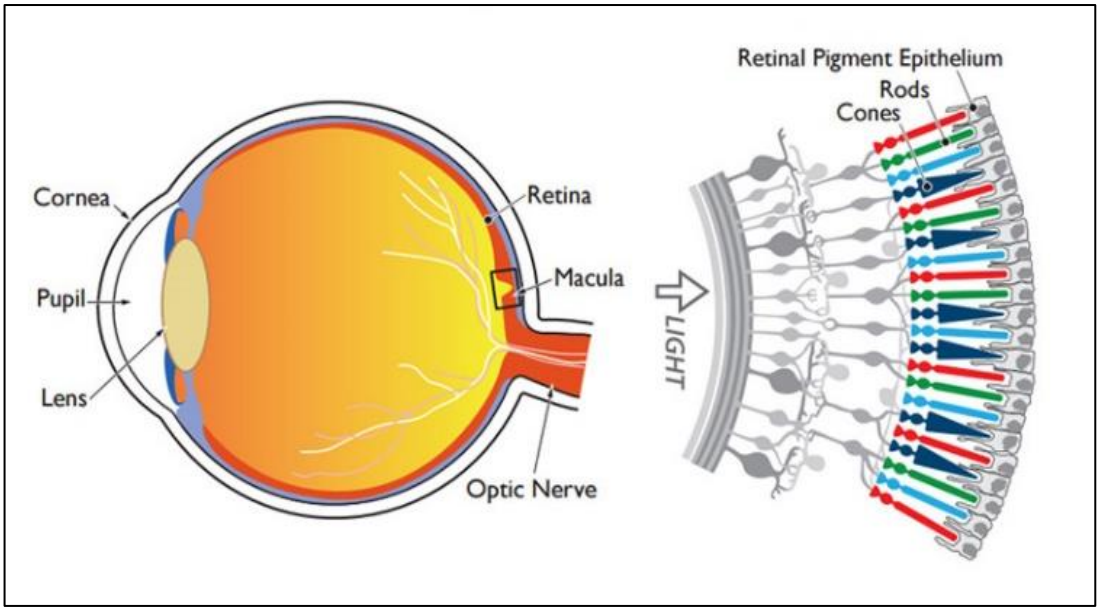

Figure 1-1. Schematic representation of the human eye, the retina, and the location of the RPE.
The light enters the eye, reaches the retina, and then is processed as a chemical signal starting in the photoreceptors. PRs convert light energy into membrane potential; BCs act as interneurons depolarising and hyperpolarising according to illumination. Finally, RGCs integrate the signal by firing action potential and acting as output neurons that send it to the central nervous system to be interpreted as images. The three layers of neurons and the two layers of synapses are included in the zoomed-in region of the retina. Rod (red, green, and light blue) and cone (navy blue) PRs are supported by another layer of cells, the retinal pigmented epithelium (grey, integrated with cones and rods). Copyright © 2023 by International Society For Stem Cell Research (https://www.closerlookatstemcells.org/stem-cells-medicine/macular-degeneration/). In the public domain.

The mammalian retinal circuitry is constructed from approximately 100 specific neuronal cell types (Demb and Singer, 2015, Vlasits et al., 2019). These cell types can be defined based on criteria from gene expression patterns, morphology, anatomical connectivity, and functional response properties (Vlasits et al., 2019). However, identifying a cell type or several types based on one criterion can be misleading. Thus, the priority of the requirements for defining cell

types must be considered as more classification schemes based on refined criteria arise. To this end, recent single-cell RNA-sequencing (scRNA-seq) studies have provided insights into retinal development and the emergence of the different retinal cell lineages in the mammalian retina (Ying et al., 2021), revealing 129 molecularly distinct retinal neurons and glia in the mouse retina (Ying et al., 2021), 64 foveal and 71 peripheral cell types in the monkey retina (Peng et al., 2019) and 58 foveal and 57 peripheral cell types in the human retina (Yan et al., 2020). The retinal cells are derived from retinal progenitor cells (RPCs) in an orderly manner, encompassing the emergence of RGCs, followed by interneurons, photoreceptors, bipolar and Müller glial cells.

Although human and non-human primates differ from mice in visual acuity and colour vision, the visual system's structure is mainly maintained across species (Bakken et al., 2021). However, as the mouse retina does not have a fovea, there are underlying differences in the distribution and number of retinal cells between primates and mice (Ying et al., 2021). These species-specific differences include the expression of transcription factors that regulate cone photoreceptor (PR) and horizontal cell (HC) specification and gene regulation networks in the macula (Lu et al., 2020). Additionally, two different subtypes of HCs were observed in the human retina in agreement with a previous study on macaques (Peng et al., 2019), showing the conserved features between the human and non-human primate retina.

1.1.1 Structure and function of retinal cells

1.1.1.1. Photoreceptors: cone and rod cells

Photoreceptors (PRs), cones and rods are the first layer of cell types that develop a visual stimulus as a chemical signal to retinal bipolar cells at the start of the neuronal network to be ultimately revealed as images in the brain (Busskamp et al., 2010, Euler et al., 2014). Rod photoreceptors are active during night vision and can encode single photons' absorption, making them far more sensitive than cones. On the other hand, cone photoreceptors are functional during daylight vision. However, there are intermediate lightning conditions where rods and cones are active (Demb and Singer, 2015).

When light focuses on the retina, rods and cones convert the light energy into changes in membrane potential (Demb and Singer, 2015). These photoreceptors make synapses in the region named the outer plexiform layer (OPL) with bipolar cells, which transmit the information to the next layer called the inner plexiform layer (IPL) (Fain and Sampath, 2018) (**Figure 1-2**). PRs make synapses as well with horizontal cells, which interconnect bipolar cells and photoreceptors with their lateral processes (Fain and Sampath, 2018).

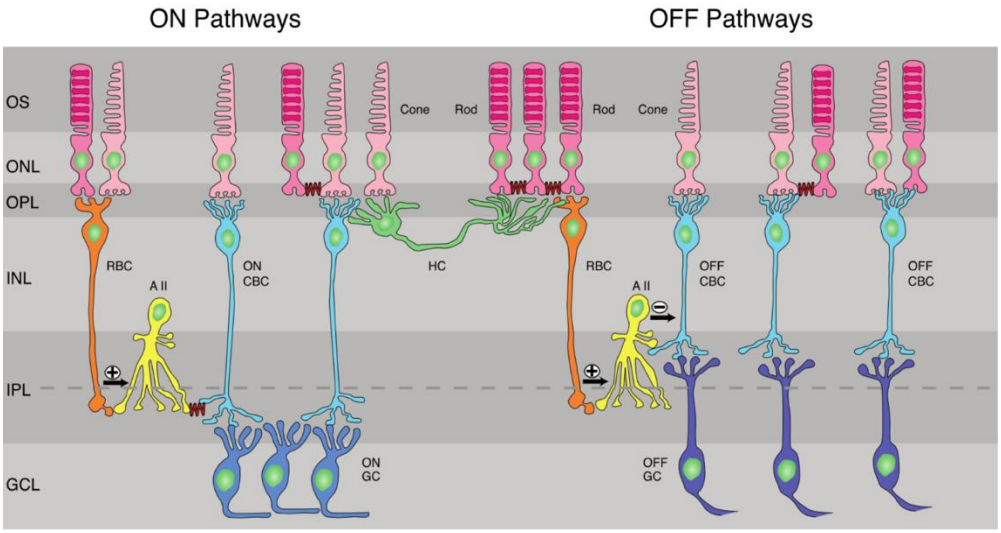

Figure 1-2. Rod and cone interactions in the mammalian retina.
(Left) ON pathways where bipolar cells (RBCs) receive the signal from cones and rods and make excitatory glutamatergic synapses onto amacrine cells (A-II). (Centre) Horizontal cells (HC) receive cone and rod signals through gap junctions. (Right) OFF pathways, where ganglion cells (GC) make inhibitory glycinergic synapses onto OFF cone bipolar cells (CBC). Reproduced from (Fain and Sampath, 2018). Creative Commons Attribution Non-Commercial Licence (CC BY-NC).

1.1.1.2. Bipolar and ganglion cells

The retina of vertebrates has two kinds of bipolar cells that act as interneurons (Fain and Sampath, 2018): **1) ON-type**, which depolarises to light in the centre, and hyperpolarising to surrounding illumination; and **2) OFF-type**, which hyperpolarises to central illumination and depolarises to the surround. The particular morphology of two protrusions, one going 'up' and another going 'down', indicates their function by linking the outer and the inner retina (Euler et al., 2014). Notably, in the mammalian retina, there are ten types of bipolar cells;

nonetheless, they typically consist of slightly more ON than OFF types, plus a single type of rod bipolar cell (**Figure 1-2**).

Retinal ganglion cells are the output neurons of the retina that specify the nature of the signal sent by the aggregate of integration of the whole retina to the central nervous system to be interpreted as images (Euler et al., 2014, Fain and Sampath, 2018). Although some RGCs receive only signals from cones, most RGCs receive input from rod and cone cells, spanning a broad and dynamic range of light intensities (Fain and Sampath, 2018).

1.1.1.3. Horizontal and amacrine cells

Horizontal cells are a primary neuronal class that receives glutamatergic inputs from rod and cone photoreceptors in the mammalian retina (Ströh et al., 2018) (**Figure 1-3**). Additionally, they return lateral feedback signals to photoreceptors to change their glutamate release in a light-dependent manner. The feedforward signal of horizontal cells is then transduced to bipolar cells. However, the mode of signal transmission and the contribution of horizontal cells to the visual processing in the temporal, spatial and contrasting tuning are still to be elucidated (Ströh et al., 2018). Recent publications show that horizontal cells are responsible for increasing the dynamic range of RGCs for contrast and temporal changes contributing together with ACs to the centre and surrounding the organisation of their receptive fields (Ströh et al., 2018).

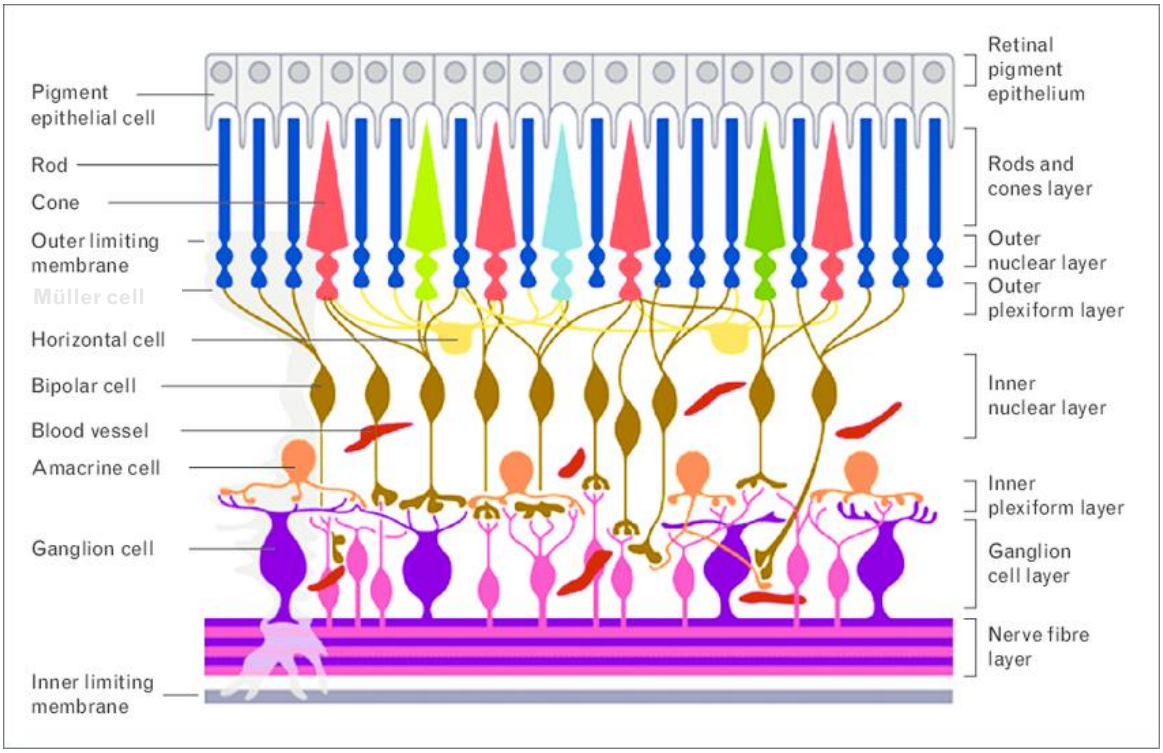

Figure 1-3. Schematic showing the cellular organisation of the retina, including the layers and different cell types.
The RPE apical membrane layer (grey) faces the outer photoreceptor segments. The first layer of neurons includes rods (dark blue) and cones (red, green, and light blue). The next layer is (inner nuclear layer) INL, composed of bipolar cells (brown) that receive the signal from photoreceptors and make excitatory glutamatergic synapses onto amacrine cells (orange), which are in the IPL as one of the two synapse layers of the retina. HCs (yellow) are synapses that receive both PRs' signals through gap junctions. The last layer of neurons, the RGC (violet and pink) layer, is the output section of the retina that sends the signal to the central nervous system to be processed as images. Müller glial cells (light grey) stretch across the retina from the inner limiting membrane to the outer limiting membrane. Reproduced from (Lorber et al., 2016). CC BY-NC.

Amacrine cells are relevant interneurons of the IPL of the retina that interact at the second synaptic level of the vertically direct pathways of the photoreceptor-bipolar-ganglion cell chain (Kolb, 1997) (**Figure 1-3**). They have diverse functions due to their unique patterns of size, numbers and stratification (Masland, 2012). There are more than 40 different types of amacrine cells, so they are divided into wide-, medium- and narrow-field cells for convenience. Amacrine cells' diversity might also be related to RGC diversity. This division by size is appropriate, considering that the dendritic field spread determines the cell's function in visual processing (Masland, 2012).

Gap junctions work as sign-conserving synapses that allow ACs to couple to RGCs or other ACs, depending on their wide or narrow field. ACs have an excitatory function by releasing γ-aminobutyric acid or an inhibitory function by GABA or glycine release (Masland, 2012). However, the function of medium-field ACs is conceptually difficult to elucidate as they are too large for creating local subunits within the dendritic field but too narrow for carrying out the contextual functions mediated by the wide-field cells. The highly specialised geometry of amacrine cells suggests a particular role –yet unknown– as they actively communicate among the retinal layers (Masland, 2012).

1.1.1.4. Müller glial cells

Müller cells are the predominant type of retinal glia present in all retinal layers (Gallina et al., 2014) (**Figure 1-3**). They display a radial morphology where their cell bodies and nuclei are located in the retina's inner nuclear layer (INL), extending their processes to the outer and inner retinal limiting membranes and lateral interaction with neighbouring neurons (Wan and Goldman, 2016).

These glial cells significantly contribute to retinal function by providing ion homeostasis and structural, synaptic, and metabolic support (Gallina et al., 2014, Jadhav et al., 2009). With appropriate stimulation, these cells can also give rise to rod progenitors and de-differentiate to become proliferating neurogenic progenitors when the retina is injured (Gallina et al., 2014). Their regenerative potential for neurons in the avian and mammalian retina is limited. Although they may potentially become stem or progenitor cells at a molecular level, they should not be referred to or defined as stem cells in the normal retina (Gallina et al., 2014, Jadhav et al., 2009).

The neurogenic potential of Müller glial was first described in the chick retina and then identified in the murine retina. Nonetheless, the evidence for Müller cells from primate retina to become progenitor-like cells is limited to *in vitro* (Gallina et al., 2014, Jadhav et al., 2009). Another activity of Müller cells carried out in addition to the retinal pigment epithelium, is to facilitate the recycling of photopigments via cellular retinal binding protein (CRALBP) mediated uptake and conversion of all-*trans*-retinal to 11-*cis*-retinol (Jadhav et al., 2009).

1.1.1.5. Developmental time-courses and lineages of retinal cells

The formation of the seven different types of retinal cells is known as retinogenesis (O'Hara-Wright and Gonzalez-Cordero, 2020). RPCs, as multipotent cells, undergo division in a competence differentiation model to define and differentiate retinal cell types sequentially. Different retinal cell types arise in the early phase of differentiation, including RGCs, cone PRs, HCs and ACs, overlapping with the late phase of the genesis of rod PRs, BCs, and Müller glial cells (O'Hara-Wright and Gonzalez-Cordero, 2020, Cepko et al., 1996) (Error! R eference source not found.).

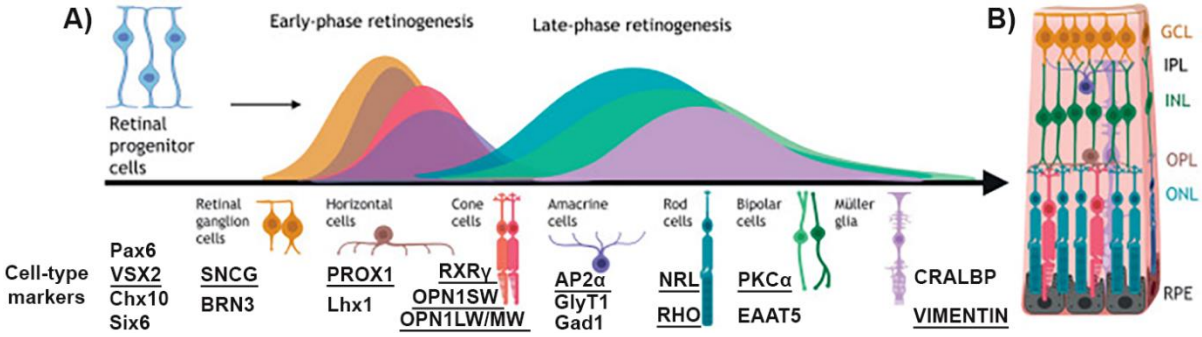

Figure 1-4. Schematic showing the developmental time-courses and lineages of different retinal cell types.
A. The differentiation time-course of the seven main retinal cell types starts with RPCs, followed sequentially in an early retinogenesis wave by RGCs, HCs, cone PRs and ACs. The next generation wave is an overlapping late-phase of rod PRs, BCs, and Müller glial cells. Cell-type specific markers are shown below each group of retinal cells. Underlined markers were used in Chapters 3 and 4 for immunofluorescence staining of sections. **B.** Retinal cell types populate the multi-layered retina from the basal-most GCL, IPL, INL, OPL and apical-most ONL adjacent to the RPE. Adapted from (O'Hara-Wright and Gonzalez-Cordero, 2020). CC BY-NC.

RGCs are the first retinal neuronal cells that arise and act as outputs connecting to the brain through the optic nerve (Cepko et al., 1996). The development and innervation of the axonal projections of the RGCs with the optic nerve are regulated by complex signalling pathways (Drescher et al., 1995). Laminin is a key molecular cue alongside the expression of *HUC* and *HUD* markers for RGC development (Dorgau et al., 2018, O'Hara-Wright and Gonzalez-Cordero, 2020). In fact, laminin subtypes (α, β and γ chain) show

temporal-spatial expression patterns during retinogenesis (Byström et al., 2006, Libby et al., 2000, O'Hara-Wright and Gonzalez-Cordero, 2020).

RPCs give rise to interneuron HC populations at an early stage of development. All HCs express homeodomain transcription factors PROX1 and Pax6, while only axon-bearing HCs express Lhx1 and axon-less subtypes express Isl1 (Edqvist et al., 2009, Edqvist et al., 2008, Boije et al., 2016). ACs exhibit the highest degree of diversity in terms of morphology and function in the retina, classified majorly based on the expressed neurotransmitter type (Balasubramanian and Gan, 2014). Amacrine interneuron cells are specified early along with RGCs, cone PRs and HCs. During early retinogenesis, factors such as *Pax6, Sox2, and Bclaf1* influence the competence of RPCs towards an AC fate. *Neurod4*, *Neurod1* and *Ptf1a* expression are also essential for AC genesis. Several transcription factors have a role in AC subtype specification. For example, *Barhl2* is an important regulator of the glycinergic subtype development (Mo et al., 2004), while *Isl1* regulates cholinergic AC development (Elshatory et al., 2007). TFAP2A (AP2α marker) and TFAP2B are key transcription factors that belong to the TFAP2 family and are expressed in the AC of the developing retina (Li et al., 2010).

RPC fate choices towards rod and cone PR subtypes require a complex cascade of gene regulatory networks (Kim et al., 2019, Xie et al., 2020). *CRX* is the most popular reporter gene for the characterisation of PR precursor and PR formation in retinogenesis (Collin et al., 2016, Collin et al., 2019). Cone precursors are detectable by the expression of retinoid X receptor gamma (*RXRγ*) at a mid-stage phase of retinal development. The cone PR developmental dynamics are characterised by the expression of S-opsin-positive cones (*OPN1SW*), followed by the onset of L/M-opsin (*OPN1LW/MW*) expressing cones analogously to the foetal retina. Expression of the neural retina leucine zipper (*NRL*) and rhodopsin (*RHO*) in rods determines the fate decision between rod and cone PR cells (Eldred et al., 2018).

BCs arise in the late-phase of retinogenesis, where VSX1 and GRM6 markers can be detected (Kim et al., 2019). Additional markers such as PKCα and EAAT5 are molecular cues indicative of the presence of BCs. Müller glial

cells display their unique morphology spanning the neural retina and express specific markers, including cellular retinaldehyde binding protein (*CRALBP*) and vimentin (Capowski et al., 2019, Mellough et al., 2019a, Collin et al., 2019).

A research study from our group (Mellough et al., 2019a) analysed alternatively spliced transcripts in the human retina, which resulted in the identification of three key developmental windows during embryonic and foetal retinal development:

1) **4.6-7.2 post-conception week (PCW):** characterised by retinal progenitor proliferation, RPE and lens emergence, and upregulation of signalling pathway genes (TGF/BMP, WNT) related to eye and retinal development.
2) **7.7-10 PCW:** the emergence of RGCs, and the beginning of transcriptional programmes for HC, AC, and cone PR development.
3) **12-18 PCW:** sequential emergence of cone and rod PRs, ACs, BCs, and Müller glial cells.

Transcriptome analyses of the human foetal retina from another study (Hoshino et al., 2017) reported similar results describing three major epochs of gene expression:

1) The early stage includes the first 59 days of retinal development characterised by the dominance of RPCs, and later by the emergence of RGCs.

2) Comprising from day 59 to 80, this stage is characterised by the switch from proliferation to differentiation. By day 70, there is a major shift from RGCs to inner retinal neurons, including HCs and ACs.

3) The last epoch begins from day 80 onwards. The gene expression starting at day 90-100 was characterised by cone and rod PRs, BCs, some types of ACs, Müller glial cells, and synapse formation.

1.1.2 Retinal Pigment Epithelium

The retinal pigment epithelium is a pigmented polygonal cell monolayer arranged at the outermost layer of the retina (**Figure 1-5**), part of the blood-retina barrier that plays a pivotal role in vision (Strauss, 2005, Yang et al., 2021c). The central nervous system neuroepithelium gives rise to the bilateral outpocketings at the diencephalon from the optic anlage. Then, the invagination of the optic vesicles generates a two-layered structure, with the inner layer forming the neural retina and the outer layer comprising the RPE (Salero et al., 2012). In humans, the RPE differentiates at an early stage (around day 32 to 50), becomes postmitotic and quiescent, and remains non-proliferative throughout life. On the contrary, the neural retinal progenitor cells further proliferate beyond the human foetal week (FW) 23 to give rise to late-born retinal cell types (BCs, certain kinds of ACs, rod PRs, and Müller glial cells) to form the multi-layered retina (Salero et al., 2012, Quinn and Wijnholds, 2019).

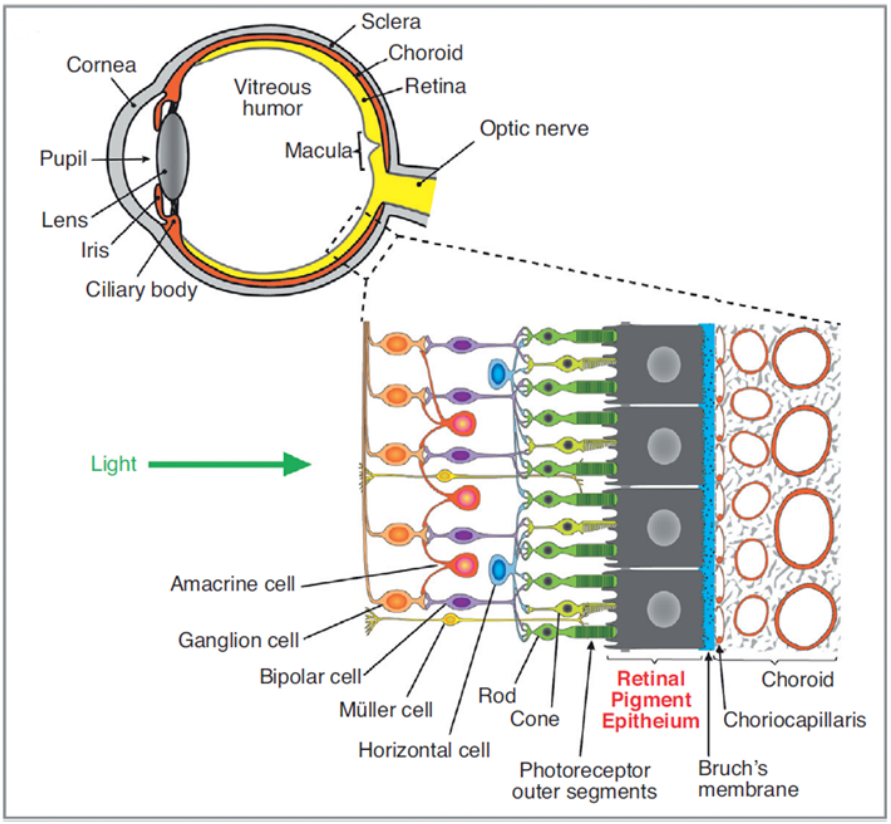

Figure 1-5. Retinal cell organisation and relation to the RPE.
Localisation of RPE in the eye as part of the blood-retina barrier. Photoreceptor outer segments (POSs) face the apical membrane of the RPE. Reproduced from (Caceres and Rodriguez-Boulan, 2020).

The vastly pigmented monolayer is comprised of highly polarised hexagonal cells that rarely divide and is located between the retina and the choroid (Milyushina et al., 2011). RPE cells have a dark brown appearance due to their melanin content, which protects the retina from ultraviolet light along with lipofuscin. As a typical cell barrier, the RPE monolayer guards the inside and the outside of the retina, strictly controlling the entry and exit of substances. They form tight junctions through ZO-1, claudin, and occludin. The monolayer acts as the outer blood barrier between the choroidal pore capillaries and the retinal PR layer (Yang et al., 2021c). The RPE cell junctions and polarity are vital to maintaining the blood-retinal barrier homeostasis, as the integrity is compromised when cell polarity and cell junctions are disrupted. The unique apical and basal structures of the RPE cells affect the phagocytic activity and material exchange when the stability of the RPE polarity and cell junctions are at risk (Yang et al., 2021c).

In the adult human eye, RPE cells are highly differentiated and weakly proliferating, but when damaged upon triggering pathological events, they can transdifferentiate into macrophage- and fibroblast-like cells (Milyushina et al., 2011). Typically, the RPE monolayer is closely opposed to the photoreceptors, playing a significant role in the maintenance of these retinal cells (Tamiya et al., 2010). The photoreceptor outer segments face the RPE's apical membrane, where long apical microvilli surround the long-sensitive POSs, enabling a complex and synergic structure interaction. The RPE is separated from the endothelium of the choriocapillaris by a complex pentalaminar tissue of 2-4 μm Bruch's membrane (BrM) (**Figure 1-6**). BrM oversees removing metabolic waste from the outer retina, which is faced by the basolateral membrane of the RPE (Strauss, 2005, Lynn et al., 2017).

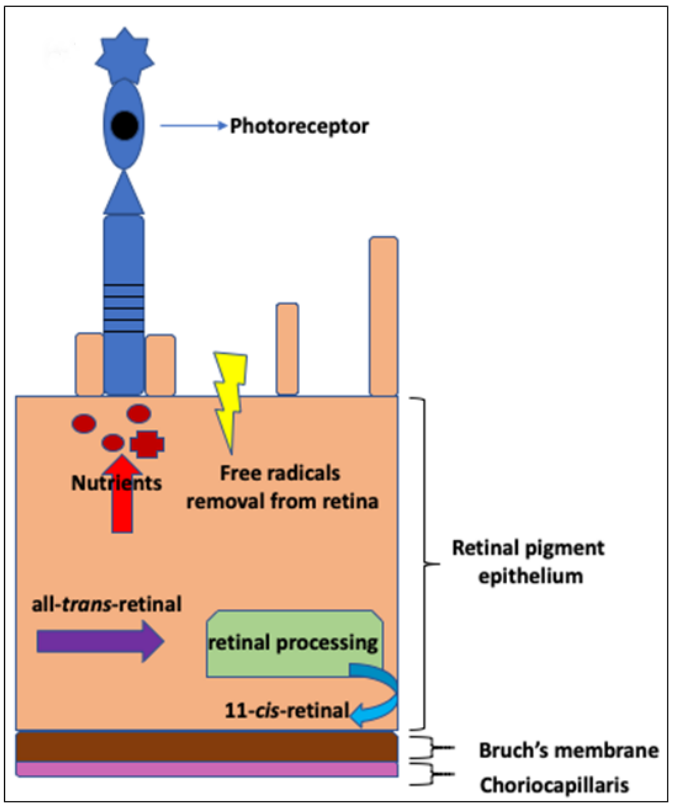

Figure 1-6. RPE metabolism and interactions with photoreceptors. Metabolism in the RPE, showing its interactions with PRs and the localisation of BrM and choriocapillaris. Nutrients are transported from the blood to the PRs. All-*trans*-retinal is reisomerised into 11-*cis*-retinal. Adapted from (Caceres and Rodriguez-Boulan, 2020).

Essentially, the RPE is responsible for transporting nutrients, ions, water, and metabolic end products from the subretinal space to the choroidal blood (Sharma et al., 2021). Similarly, nutrients such as glucose, retinol, and fatty acids are taken from the blood and delivered to the photoreceptors (Strauss, 2005). When PRs absorb photons as part of the retinal visual cycle, they cannot reisomerise all-*trans*-retinal back into 11-*cis*-retinal (**Figure 1-6**). Therefore, the retinal is transported to the RPE to be reisomerised and transported back to PRs to maintain their excitability and stabilise ion composition in the subretinal space (Strauss, 2005).

Furthermore, the RPE cells recycle essential substances such as retinal and photoreceptor outer disks to maintain visual cells (Strauss, 2005). Phagocytosis, a vital function of the RPE, allows engulfing and elimination of exfoliated POSs. It is divided into three stages: binding, endocytosis, and elimination. After binding to the shed POSs of the visual cell, the inner microvilli

cell membranes of the RPE cells are endocytosed into the cell and then carried by the cytoskeleton and extracellular vehicles (EVs) to the lysosomes for degradation (Yang et al., 2021c). Additionally, the RPE secretes a variety of growth, differentiation, and immunosuppressive factors to maintain the structural integrity of photoreceptors and choriocapillaris endothelium (Strauss, 2005).

Other functions include removing the excessive accumulation of free radicals from the photo-oxidative retinal environment and absorbing stray light through pigment granules (Lynn et al., 2017, Yang et al., 2021c) (**Figure 1-6**). Failure of these functions might result in retinal degeneration, loss of visual function, and blindness. RPE's functional impairment can lead to retinopathy, including Age-related Macular Degeneration (AMD), retinitis pigmentosa (RP), and Stargardt disease (STGD1) as the most prevalent retinal diseases (Lynn et al., 2017).

1.2 The hallmarks of cancer and oncogenesis

Cancer is a disease characterised by dynamic alterations in the genome. Mutations in oncogenes with a dominant gain of function and tumour suppressor genes with recessive loss of function determine the origin of the malignancies (Hanahan and Weinberg, 2000). Human cancers are developed due to a multistep process where cells acquire functional capabilities that initiate tumour pathogenesis (Hanahan, 2022). Tumours are more than insular masses of proliferating cells. They are complex tissues comprising multiple distinct cells contributing to different interactions (Hanahan and Weinberg, 2011).

Research over the last decades has revealed common patterns at a molecular, biochemical and cellular level that are shared by most -if not all- types of human cancer. Tumourigenesis in humans starts with genetic alterations that lead to the progressive transformation of normal cells into malignant ones with deregulated molecular machinery. Regulation of cell processes such as proliferation, differentiation, and death is compromised in a malignant environment. Cancer cells exhibit multiple defects in cell proliferation and homeostasis regulatory circuits. To this end, there are ten basic biological alterations in cell physiology plus four proposed hallmarks and enabling

characteristics that enable malignant growth (Hanahan and Weinberg, 2000, Hanahan and Weinberg, 2011, Hanahan, 2022):

1) **Sustaining proliferative signalling:** The cornerstone of traits of cancer cells is the capability to support chronic proliferation. Normal cells ensure homeostasis of cell number and maintenance of tissue architecture and function by having strict control of the production and release of growth-promoting signals of entry and progression of the cell cycle. However, cancer cells deregulate these signals, typically expressed by growth factors that bind cell-surface receptors, which usually contain intracellular tyrosine kinase domains. These signals also influence other cell properties, such as cell survival and energy metabolism. Neoplastic cells can develop the capability of proliferative signalling in different ways: producing growth factor ligands themselves or sending signals to stimulate normal cells within the supporting tumour-associated stroma, supplying the cancer cells with diverse growth factors. Additionally, components of the signalling pathways operating downstream of the receptors may contribute to growth factor independence. Somatic mutations in certain tumours can activate additional downstream pathways. Disruptions to negative-feedback mechanisms that attenuate various types of signalling can enhance proliferative signalling. These disruptions may contribute to developing adaptative resistance toward drugs targeting mitotic signalling.

2) **Evading growth suppressors:** Neoplastic cells also circumvent robust programmes that negatively regulate cell proliferation, many of them depending on tumour suppressor genes. Some of these tumour suppressors act by limiting cell growth and proliferation. Examples include TP53 and retinoblastoma proteins, which operate as central control nodes of key complementary cellular regulatory circuits that dictate the decision of either proliferate or activate senescence and apoptotic programmes. Retinoblastoma protein (pRB) transduces inhibitory growth signals that originate outside the cell, while TP53 receives inputs from stress and abnormality sensors within intracellular operating systems. If alarm

signals indicate irreparable damage, TP53 can trigger apoptosis. Cell-to-cell contact allows inhibition of further cell proliferation to ensure normal tissue homeostasis, which can be evaded by cancer cells during tumourigenesis. One mechanism to achieve this inhibition is the loss of the product of the *NF2* gene, which is a tumour suppressor that generates contact inhibition. A second mechanism involves LKB1 epithelial polarity protein, which keeps the epithelial integrity and the normal tissue structure. LKB1, as a tumour suppressor, overrules the mitogenic effects of Myc oncogene, but when lost, the epithelial integrity is compromised, and epithelial cells become susceptible to Myc-induced transformation (Partanen et al., 2009, Hezel and Bardeesy, 2008, Shaw, 2009). Alternatively, cancer cells can evade the antiproliferative effects of TGF-β and redirect away its signalling to activate the epithelial-to-mesenchymal transition, conferring high-grade malignancy to neoplastic cells (Ikushima and Miyazono, 2010, Bierie and Moses, 2006).

3) **Enabling replicative immortality:** Cancer cells need unlimited replicative potential to generate tumours. Normal cells can replicate only a limited number of successive growth-and-division cycles. The two main limitations to proliferation are senescence, which is an irreversible entrance into a viable but nonproliferative state, and crisis, which involves cell death. Some cells can circumvent these events and emerge from a population in crisis and manifest unlimited replicative potential, which has been termed in cell culture as immortalisation. Evidence suggests that telomeres protecting the ends of chromosomes are involved in the unlimited proliferative potential (Blasco, 2005, Shay and Wright, 2000). Telomeres are multiple tandem hexanucleotide repeats that protect the ends of chromosomal DNA from end-to-end fusions and are progressively shortened in nonimmortalised cells in culture. In fact, the length of the telomeric DNA determines the number of successive cell generations before telomeres are eroded and trigger the entrance into crisis. Human cancer cells and most immortalised cells express telomerase, a specialised DNA polymerase that adds telomere repeats segments to the

ends of telomeric DNA. Progressive telomere erosion is countered by the extension of telomeric DNA, which is correlated with the resistance to the induction of both proliferative barriers, senescence and crisis/apoptosis. These two barriers to proliferation have been thought to be crucial anticancer defences as they impede the outgrowth of neoplastic cells. Immortalised and tumour cells have achieved the ability to upregulate the expression of telomerase or alternative recombination-based telomere maintenance mechanism to avoid triggering senescence or apoptosis.

4) **Tumour-promoting inflammation:** Inflammatory conditions are enhanced in tumours by cells from the innate and adaptative arms of the immune system (Dvorak, 1986). Studies have shown that every neoplastic lesion contains immune cells at a different range of densities that paradoxically enhance tumourigenesis and progression instead of exhibiting antitumoural conditions. Hence, immune cells show tumour-promoting effects by supplying bioactive molecules to the tumour microenvironment that include: growth factors sustaining proliferative signalling, survival factors limiting cell death, proangiogenic factors, extracellular matrix-modifying enzymes that facilitate angiogenesis, invasion and metastasis, and inductive signals that activate endothelial-to-mesenchymal transition (DeNardo et al., 2010, Grivennikov et al., 2010, Qian and Pollard, 2010, Karnoub and Weinberg, 2007). Also, pro-inflammatory cells can release mutagenic reactive oxygen species for cancer cells, accelerating their evolution toward a higher malignancy state (Grivennikov et al., 2010).

5) **Activating invasion and metastasis:** Carcinomas emerging from epithelial tissues progressed to higher pathological grades of malignancy, showing local invasion and distant metastasis. Cancel cells associated with these features show alterations in shape and attachment to other cells and the extracellular matrix (ECM). The most characterised alteration is the loss of E-cadherin, a critical molecule for cell-to-cell adhesion that maintains the cells' quiescence. Upregulation of E-cadherin expression is

an antagonist of invasion and metastasis, while downregulation potentiates these phenotypes (Berx and van Roy, 2009, Cavallaro and Christofori, 2004). Genes expressing other cell-to-cell and cell-to-ECM adhesion molecules, especially those favouring cytostasis, have been reported to be altered during tumourigenesis. Interestingly, adhesion molecules associated with cell migrations (for example, N-cadherin), occurring during embryogenesis and inflammation, are upregulated (Cavallaro and Christofori, 2004). The term invasion-metastasis cascade is a multistep succession of cell-biologic changes (Talmadge and Fidler, 2010, Fidler, 2003): **1)** local invasion; **2)** intravasation of cancer cells into nearby blood and lymphatic vessels; **3)** transit of cancer cells through the lymphatic and haematogenous systems; **4)** escape of cancer cells of the lumina of such vessels into the parenchyma of distant tissues; **5)** formation of small nodules of cancer cells; and **6)** the growth of micrometastatic lesions into macroscopic tumours. The epithelial-to-mesenchymal transition programme has been involved as transformed epithelial cells acquire the ability to invade, resist apoptosis, and proliferate (Klymkowsky and Savagner, 2009, Polyak and Weinberg, 2009, Thiery et al., 2009, Yilmaz and Christofori, 2009, Barrallo-Gimeno and Nieto, 2005). Transcriptional factors such as Slug, Snail, Twist, and Zeb1/2 influence the epithelial-to-mesenchymal transition during embryogenesis. During tumourigenesis, these transcriptional regulators are expressed in different combinations as part of invasion and metastasis (Micalizzi et al., 2010, Taube et al., 2010, Schmalhofer et al., 2009, Yang and Weinberg, 2008). Several cell-biologic traits involved in invasion and metastasis include the loss of adherens junctions and associated conversion from a polygonal/epithelial to a spindly/fibroblastic morphology, expression of matrix-degrading enzymes, increased motility, and heightened resistance to apoptosis. Some of these transcription factors can repress E-cadherin gene expression in neoplastic epithelial cells (Peinado et al., 2004). Transcription factors inducing epithelial-to-mesenchymal transition are involved in most of the steps of the invasion-metastasis cascade as they programme malignant traits in tumours.

There are two principal phases in metastasis: **1)** the physical dissemination of neoplastic cells from the primary tumour to distant tissues; and **2)** the adaptation of these cells to foreign tissue microenvironments, resulting in successful colonisation. Different types of cancer cells must develop their specific adaptation as part of the colonisation programme in the microenvironment of the foreign tissue (GUPTA et al., 2005).

6) **Inducing or accessing vasculature:** Both normal and cancer cells require nutrients and oxygen and the ability to export metabolic end products and carbon dioxide. Angiogenesis fulfils these requirements by inducing neovasculature in tumours. During embryonic development, new endothelial cells assemble into tubes (vasculogenesis), followed by the sprouting of new vessels from existing ones, known as angiogenesis. After this process, the normal vasculature becomes largely quiescent. In adults, angiogenesis is transiently turned on for physiologic processes such as wound healing and female reproductive cycling. Nonetheless, angiogenesis is switched on during tumourigenesis, forcing normally quiescent vasculature to sprout new vessels that help sustain tumour development and neoplastic outgrowth (Hanahan and Folkman, 1996). Some factors either induce or oppose angiogenesis, such as signalling proteins that bind to stimulatory or inhibitory cell-surface receptors expressed by vascular endothelial cells. Examples of these angiogenesis factors include vascular endothelial growth factor-A (VEGF-A) inducer and thrombospondin-1 (TSP-1) inhibitor. VEGF-A induces the generation of new blood vessel growth during embryonic and postnatal development, as well as for endothelial homeostatic survival and physiological and pathological situations in adults. Additionally, Fibroblast Growth Factor (FGF) family members act as proangiogenic signals when chronically upregulated by supporting tumour angiogenesis (Baeriswyl and Christofori, 2009). When angiogenesis is chronically activated within tumours, the new blood vessels are aberrant and characterised by capillary sprouting, complex and exacerbated vessel branching, distorted

and enlarged vessels, erratic blood flow, leakness and abnormal levels of endothelial cell proliferation and apoptosis (Nagy et al., 2010, Baluk et al., 2005). Angiogenesis is induced early during the multistage development of invasive cancer, contributing to the microenvironment and premalignant phase of neoplastic progression. Some studies have shown that innate immune system cells such as macrophages, neutrophils, mast cells, and myeloid progenitors infitrate premalignant lesions and tumours and assemble at the margin of the lesions (Qian and Pollard, 2010, Zumsteg and Christofori, 2009, Murdoch et al., 2008, De Palma et al., 2007). As a result, the angiogenic switch is activated from a quiescent state to ongoing angiogenesis associated with tumour growth and facilitating local invasion.

7) **Genome instability and mutation:** Certain genotype mutations confer the advantage of subclones of cells that allow their outgrowth and dominance in a specific tissue environment. Tumour progression is a multistep process of clonal expansions that can be triggered by the acquisition of a mutant genotype. Epigenetic changes can also acquire manifestation of a cancer phenotype. Cancer cells often increase the rates of mutations kept very low in normal cells for genome maintenance. One strategy to achieve a higher mutability rate is to increase sensitivity to mutagenic agents by breaking down one or several components of the genomic maintenance machinery. Additionally, compromising the surveillance systems that typically monitor genomic integrity and repair is another strategy to prevent genetically damaged cells from senescence or apoptosis (Jackson and Bartek, 2009, Kastan, 2008, Sigal and Rotter, 2000). Also, the loss of telomeric DNA is another causative factor of karyotypic and genomic instability, as some chromosomal fragments are amplified and deleted (Artandi and DePinho, 2010). Amplifications and deletions of particular sites of the genome likely harbour genes that favour tumourigenesis when altered (Korkola and Gray, 2010). Additional telomere-independent functions have been attributed to telomerase, including enhancement of cell proliferation and/or resistance to apoptosis

(Kang et al., 2004), involvement in DNA-damage repair (Masutomi et al., 2005), and RNA-dependent RNA polymerase function (Maida et al., 2009).

8) **Resisting cell death:** Programmed cell death by apoptosis has been the natural barrier to cancer development. Apoptosis is a complex multistep process integrating upstream regulators and downstream effector components (Adams and Cory, 2007). Regulators, on one side, receive and process extracellular death-inducing signals, and on the other, a variety of intracellular signals. Each terminates in activating a latent protease (caspases 8 and 9, respectively), initiating a cascade of proteolysis where cells are disassembled and ultimately consumed by phagocytic cells. The trigger for apoptosis that transmits the signal between regulators and effectors is controlled by pro- and anti-apoptotic members of the Bcl-2 family of regulatory proteins, broadly described in subsection **1.6.4 TW-37**. When notable DNA damage is detected, TP53 triggers apoptosis by upregulating the expression of the Noxa and Puma BH3-only proteins, which stimulates the pro-apoptotic members of the Bcl-2 family. Tumours develop multiple strategies to limit apoptosis, the most common being the loss of the TP53 tumour suppressor. Another alternative for tumours is increasing the expression of anti-apoptotic regulators (Bcl-2, Bcl-x_L) or survival signals (Igf1/2), downregulating pro-apoptotic factors (Bax, Bim, Puma), or short-circuiting the extrinsic ligand-induced death pathway.

   TW-37

9) **Deregulating cellular metabolism:** Normal cells process glucose to pyruvate via glycolysis in the cytosol and then to carbon dioxide in the mitochondria under aerobic conditions. On the other hand, glycolysis is favoured under anaerobic conditions as little pyruvate is dispatched to the oxygen-consuming mitochondria. Nonetheless, neoplastic cells can reprogram their glucose metabolism and energy production by limiting their energy metabolism primarily to glycolysis. These cells upregulate GLUT1, a glucose transporter that allows glucose import into the cytosol

(Jones and Thompson, 2009, DeBerardinis et al., 2008, Hsu and Sabatini, 2008). Cancer cells must compensate for the 18-fold lower efficiency of adenosine triphosphate (ATP) production afforded by glycolysis relative to mitochondrial oxidative phosphorylation. Activation of oncogenes like *RAS* and *MYC* and mutant tumour suppressor such as *TP53* has been associated with glycolytic fueling (Jones and Thompson, 2009, DeBerardinis et al., 2008) in tumour cells, where cell proliferation, cytostatic control avoidance, and apoptosis attenuation capabilities are acquired. These conditions can be exacerbated in a specific hypoxic tumour microenvironment, where glucose transporters and enzymes of the glycolytic pathway are upregulated (Semenza, 2010, DeBerardinis et al., 2008) (Jones and Thompson, 2009). When glycolysis is increased, and glycolytic intermediates are diverted into various biosynthetic pathways, nucleosides and amino acids are generated, facilitating the biosynthesis of macromolecules and organelles for assembling new cells (Potter, 1958, Vander Heiden et al., 2009). Two subpopulations of neoplastic cells differing in their energy-generating pathways have been found in some tumours. One subpopulation is glucose-dependent cells that secrete lactate, while the cells from the other subpopulation import and utilize lactate produced by neighbours as the primary source of energy (Kennedy and Dewhirst, 2009, Feron, 2009, Semenza, 2010) (Kennedy and Dewhirst, 2009, Feron, 2009, Semenza, 2008). Alterations to the energy metabolism are a core characteristic of cancer cells alongside other well-established core hallmarks.

10) **Avoiding immune destruction:** Normally, cells and tissues are constantly under immune surveillance to detect and eliminate most developing cancer cells. Therefore the immune system acts as a barrier to tumour formation and progression. However, solid tumours have avoided recognising the immune system or limited the extent of the immunological killing. Highly immunogenic cancer cells evade immune destruction by disabling immune system components designed to eradicate them.

New hallmarks and enabling characteristics (Hanahan, 2022):

1) **Unlocking phenotypic plasticity:** Cellular differentiation is terminated when cells assume their homeostatic functions in tissues after their development, determination and organisation. As this result is, in most cases, antiproliferative, it constitutes a barrier for the necessary proliferation in neoplasia. Unlocking the phenotypic plasticity of cells is a crucial component of cancer pathogenesis. Plasticity can be achieved in several manifestations:
    a. **Dedifferentiation:** Normal cells that follow their differentiation pathway reverse their course back to a progenitor-like state.
    b. **Blocked differentiation:** Cancer cells arising from a progenitor cell, whose fate leads to end-stage differentiation, short-circuit the process, maintaining the neoplastic cells in a partially differentiated progenitor-like state.
    c. **Transdifferentiation:** Committed cells to a determined differentiation pathway switch to a different developmental programme, acquiring specific traits not predetermined by their normal cells-of-origin.

2) **Non-mutational epigenetic reprogramming:** Instrumental gene-regulatory circuits and networks in tumours can be controlled by corrupted and co-opted mechanisms independent of genome instability and gene mutations. Aberrant physical properties of the tumour microenvironment may cause broad changes in the epigenome, which is beneficial to some hallmark capabilities resulting in the outgrowth of cancer cells with proliferative expansion potential. Because of insufficient vascularisation, hypoxia in tumours is a common feature that enables changes in the methylome, particularly hypermethylation. As the bioavailability of critical blood-borne nutrients is limited in a hypoxic environment, nutrient deprivation can enhance the malignant phenotype in some cancer cells. The invasive growth capability of cancer cells is another characteristic of the epigenetically regulated microenvironment. For example, the reversible induction of invasiveness in neoplastic cells at the margins of solid

tumours, where a developmental regulatory programme of epithelial-to-mesenchymal transition occurs (Bakir et al., 2020, Gupta et al., 2019, Lambert and Weinberg, 2021). Also, intratumoural heterogeneity is critical in generating the fittest cells for proliferation and invasion, which can be epigenetically regulated. One example is the repression of the linker histone H1.0 in cancer cells, allowing them to exhibit stem cell-like features and enhancing a tumour-initiating capability. Lastly, it is hypothesised that accessory (stromal) cells in solid tumours do not suffer genetic instability but are epigenetically reprogrammed to support tumour development functionally.

3) **Polymorphic microbiomes:** The microbiota is the collection of microorganisms that symbiotically associate with the barrier tissues of the body exposed to the external environment. Some of these tissues include the epidermis, the internal mucosa, the lung, the breast, and the urogenital system. This symbiotic association has an impact on health and disease. For example, there is evidence that polymorphic variability in the microbiomes between individuals within a population can impact cancer phenotypes (Dzutsev et al., 2017, Helmink et al., 2019). The gut microbiome and its importance for the function of the colon are currently of research interest. The role of the gut microbiome in degrading and importing nutrients into the body is critical in maintaining metabolic homeostasis, as distortions to microbiome populations can lead to physiologic diseases. The susceptibility, development and pathogenesis of colon cancer are highly influenced by the gut microbiome, as there are cancer-protective and tumour-promoting microbiomes that can modulate the incidence and development of the tumours (Sears and Garrett, 2014).

4) **Senescent cells:** Cellular senescence is an irreversible form of proliferative arrest. It is likely an evolutionary trait for maintaining tissue homeostasis and a complimentary mechanism to apoptosis. The senescence programme allows inactivation and removes diseased, dysfunctional or unnecessary cells. It changes the cell morphology and

metabolism and activates a senescence-associated secretory phenotype that releases bioactive proteins, including chemokines, cytokines and proteases, depending on the tissue origin type. Different conditions can induce cells into senescence, including microenvironmental stresses such as nutrient deprivation and DNA damage, organelle damage and cellular infrastructure, and imbalances in signalling networks (Birch and Gil, 2020, Gorgoulis et al., 2019). Although senescence protects cells by limiting malignant progression, evidence suggests it can stimulate tumour development and malignant progression (Kowald et al., 2020, Wang et al., 2020). Senescent cancer cells on cancer phenotypes can switch from reversible and transitory senescent states of a nonproliferative condition to cell proliferation and the manifestation of oncogenic capabilities, commonly observed in therapy resistance cases (De Blander et al., 2021).

1.3 Retinoblastoma

1.3.1 Aetiology

Retinoblastoma (Rb) is a retinal malignancy affecting children younger than five years with a prevalence of around 1:15,000 infants worldwide that can cause death within 1-2 years if left untreated (Stenfelt et al., 2017, Valverde et al., 2005, Saengwimol et al., 2018). The retinal tumour is initiated by the biallelic inactivation of the *RB1* tumour suppressor gene, which accounts for up to 98% of Rb cases (Kaewkhaw and Rojanaporn, 2020). On average, 40% of patients have bilateral (germline) disease, while the remaining 60% of patients present unilateral (of which 15% are germline and the rest somatic) disease (Liu et al., 2019, Collin et al., 2021).

Rosettes are round clusters of cells that are found in tumours and serve as diagnostic features in pathology. They typically consist of a central cellular lumen surrounded by a spoked circle of cells resembling gothic cathedrals' rose casements (Das et al., 2014). The identification of rosettes aids in the tumour-diagnosing process in pathology, as there are clusters of different kinds of rosettes and different names (Das et al., 2014, Eagle Jr, 2009, Eagle et al., 1989). Flexner-Wintersteiner rosettes, named after pathologist Simon Flexner and ophthalmologist Hugo Wintersteiner, are a diagnostic feature of Rb. Similarly,

Homer Wright rosettes (named after James Homer Wright, the first director of the Massachusetts General Hospital in Boston) are frequently observed in Rb, medulloblastoma, neuroblastoma, and primitive neuroectodermal tumours (Anthony, 1990, Eagle Jr, 2009). The difference between Flexner-Wintersteiner and Homer Wright rosettes is that the latter lacks a central lumen, and their constituent cells surround a central tangle of neural filaments (**Figure 1-7**) (Das et al., 2014, Anthony, 1990, Nork et al., 1995).

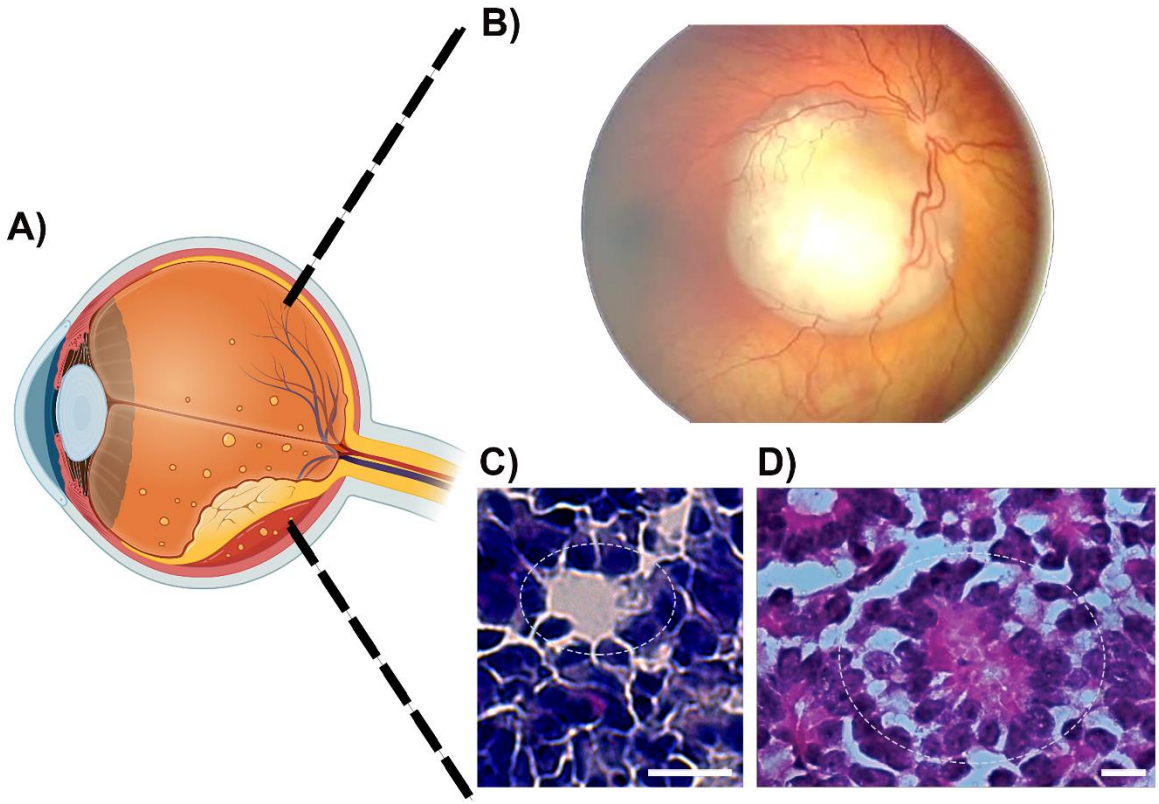

Figure 1-7. Schematic showing an affected human eye with Rb.
(**A**) A retinoblastoma-affected human eye with an Rb tumour and seeding. (**B**) Ocular fundoscopy image of Rb; adapted from (Aerts et al., 2006) CC BY-NC. (**C**) Haematoxylin and eosin (H&E)-stained section of a retinal tumour showing a Flexner-Wintersteiner rosette (marked with a dashed ellipse) with a clear lumen at the centre. (**D**) H&E-stained section of a retinal tumour showing a Homer Wright rosette (marked with a dashed ellipse) with no clear lumen at the centre. Reproduced from (Das et al., 2014) CC BY-NC. Scale bars; 50 μm.

Near-complete cure rates of Rb are possible, with patients retaining normal vision in at least one eye when the condition is diagnosed early and treated with standard protocols of systemic chemotherapy and focal consolidative therapy (Sachdeva and O'Brien, 2012). Confinement of the malignant mass to

the eye in the early stages and correct diagnosis in developed countries result in high cure rates of up to 95% (Parulekar, 2010). However, in developing countries, spread beyond the eye is associated with poor prognosis, lowering the cure rates below 5-10% (Parulekar, 2010). Tumour dissemination might be throughout the retina, optic nerve, brain parenchyma, and systemically (Sachdeva and O'Brien, 2012). Despite the progress in treatments, Rb survivors are left with impaired vision having an adverse effect on correct motion processing, depth perception, and judging distances. Enucleation is an important treatment to reduce mortality in patients with advanced Rb; it leads to total loss of vision and severe impairment of the quality of life (Wong et al., 2022). Patients under Rb treatment can suffer hearing loss, cataracts, cosmetic deformities, and impaired neurocognitive development (Belson et al., 2019, Ing et al., 2012).

Currently, the strategies for Rb treatment aim to salvage not only the patient's life but also the ocular globe and the visual function (Saengwimol et al., 2018). Advanced Rb includes associated vitreous and subretinal tumours (known as "vitreous" and "subretinal seeds") in addition to the individual retinal tumour (Saengwimol et al., 2018). The standard Rb chemotherapeutic treatment protocols include two or three-drug treatments with alkylating, DNA-damaging agents and/or cytoskeletal inhibitors, which have been associated with significant toxicity (Sachdeva and O'Brien, 2012).

1.3.2 Retinoblastoma protein

Rb is initiated in response to biallelic *RB1* inactivation and the loss of the retinoblastoma protein (pRB), which is a 928 amino acid protein and functional tumour suppressor (Xu et al., 2014, Dimaras et al., 2015). pRB plays a significant role in regulating cell proliferation, differentiation, senescence, apoptosis, and genome maintenance by direct and indirect gene suppression and protein expression (Sachdeva and O'Brien, 2012). *RB1* gene is located on chromosome 13q14.2; it has 27 exons and spans 180 kb (Stenfelt et al., 2017). The most recurrent causes of *RB1* inactivation are deletions and nonsense mutations, accounting for approximately 40% of *RB1* gene mutations in sixteen hot points (Valverde et al., 2005). Nonetheless, in a research study (Tomar et al., 2017), 61

point mutations were identified among the Rb patients. The different mutation types included: nonsense (55.7% of all cases), frameshift (24.6%), splicing (9.8%), missense (8.2%), and promoter alterations (1.64%) (**Figure 1-8**).

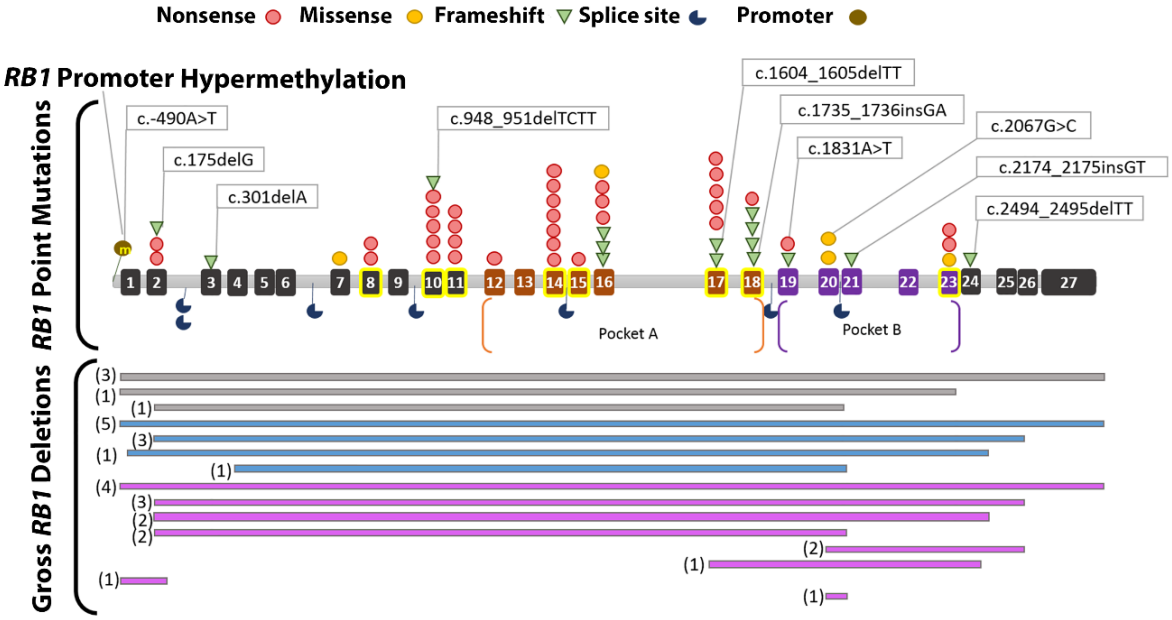

Figure 1-8. Sequence mutation hotspots across *RB1* gene.
Schematic representation of identified mutations spanning the entire *RB1* gene. The pocket domains are highlighted in orange (Pocket A) and purple (Pocket B), while exons are numbered sequentially. Exons known to be mutational hotspots are highlighted with yellow boxes. The spectrum of different mutation types among point mutations includes nonsense (red circle), missense (yellow circle), frameshift (green triangle), splicing (blue moon), and promoter alterations (brown circle). Gross *RB1* deletions are shown in blue for paternal and pink for maternal loss of allele, while grey is unknown inheritance. The respective gross deletion frequencies are shown in brackets. Reproduced from (Tomar et al., 2017). CC BY-NC.

RB1 mutations are transmitted in an autosomal-dominant fashion, meaning that almost all children with one mutated germline copy of the gene will develop the disease (Sachdeva and O'Brien, 2012). The first (heterozygous) hit is a somatic mutation in the *RB1* gene, then predisposing for a second hit and to Rb tumour development with biallelic mutations (Knudson, 1971, Draper et al., 1992, Kamihara et al., 2017). Analysis of sporadic and heritable Rb led to the development of Knudson's Two-Hit Hypothesis, which states a predisposition in *the RB1* gene to the growth of tumours with biallelic mutations (Mendoza and Grossniklaus, 2015) (**Figure 1-9**). As pRB loss initiates cancer in the retina, the

function of *RB1* can be lost with progression in almost all cancer types (Dimaras et al., 2015). *RB1* mutations also increase the risk of second malignancies of the bladder, lung, bone, soft tissue, skin, and brain throughout life, especially if the children are treated with radiation (Dimaras et al., 2012).

In heritable Rb, the first hit is in the germ cell and is carried in every cell in the body, making them susceptible to Rb and other secondary malignancies (Rao and Honavar, 2017). Usually, the mutation of the second allele occurs within the developing retina when the initial mutation is present in the family or when it may have arisen *de novo* in the parental gametes (Sachdeva and O'Brien, 2012). In non-heritable Rb, both hits occur in the retinal cell, limiting the mutation to only one retinal cell (Rao and Honavar, 2017). Non-heritable Rb accounts for 60-70% of all Rbs, while the rest 30-40%, are heritable. As most Rb cases are non-heritable, both mutations occur locally within the affected retina, leading to unilateral Rb. All bilateral cases have been shown to result from heritable germline mutations (Sachdeva and O'Brien, 2012, Naik et al., 2016, Dimaras and Corson, 2019), whilst only 10-15% of unilateral Rb patients carry a germline mutation (Rao and Honavar, 2017).

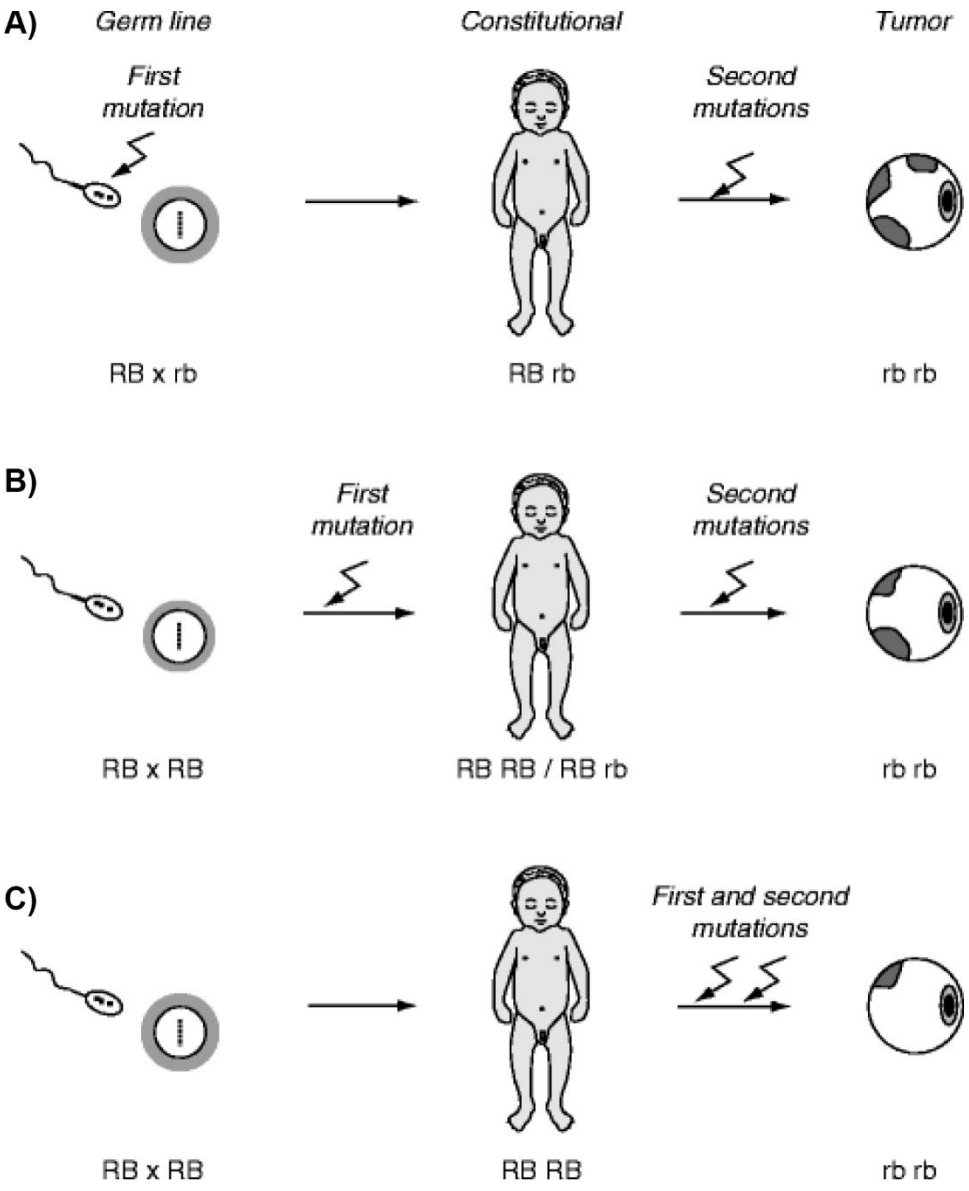

Figure 1-9. The inherited and non-heritable forms of Rb.
Mutation of the *RB1* gene is transmitted in an autosomal-dominant fashion. Timing of the first *RB1* gene mutation as described by Knudson's Two-Hit Hypothesis with a predisposition of a second mutation for the growth of a tumour with homozygous mutations. **A.** The first mutation appears in the germ line, while the second mutation develops after birth. **B.** The first mutation occurs after fertilisation, and the second happens after birth. **C.** Both mutations take place any time after birth. In all three cases, the child develops Rb. Reproduced from (Lohmann, 2011). Copyright © 2011 by Springer-Verlag Berlin Heidelberg.

1.3.3 pRB and other pocket family proteins

pRB plays a vital role in the cell cycle by repressing the E2F1 transcription factor and SKP2 (S-phase Kinase Associated Protein 2) during the G1/S transition and binding to chromatin remodelling proteins (Reis et al., 2012, Mendoza and Grossniklaus, 2015, Kaewkhaw and Rojanaporn, 2020). E2F transcription factors regulate gene expression through G1- and S-phase, DNA metabolism, and cell proliferation (Sachdeva and O'Brien, 2012). Phosphorylation of pRB by proline-directed, serine/threonine cyclin-dependent kinases (Cdks) inhibits its association with E2F, thus allowing cell cycle progression (Sachdeva and O'Brien, 2012, Zarkowska et al., 1997) (**Figure 1-10**). Underphosphorylated active forms of pRB dominate during G1-phase, while hyperphosphorylated inactive forms are dominant in G2/M-phases (Buchkovich et al., 1989).

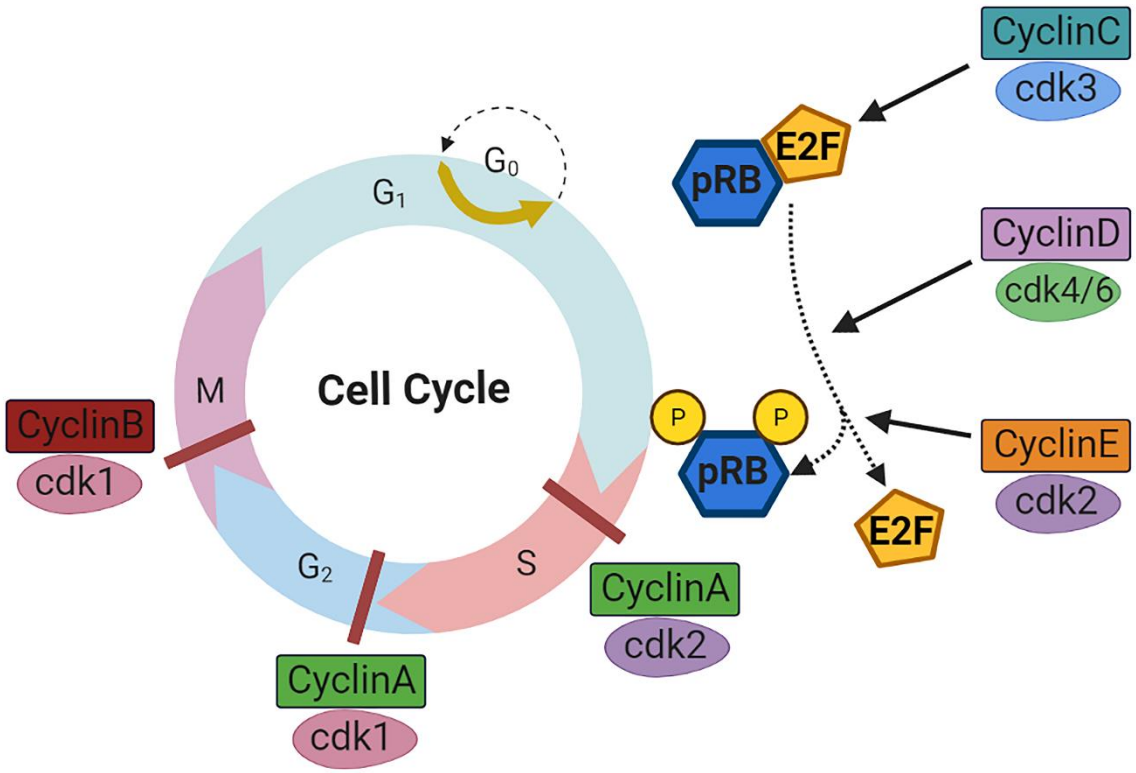

Figure 1-10. The role of pRB in the cell cycle.
pRB associates with E2F factors and blocks their transactivation domain in G0- and early G1-phase. Then, in the late G1-phase, phosphorylated pRB releases E2F, allowing gene expression that encodes vital products for S-phase progression. Adapted from (Giacinti and Giordano, 2006) using Biorender. Copyright © 2006 by Nature Publishing Group.

Hypermethylation of pRB and promoter region can also affect transcription and continue tumour progression because of epigenetic changes (Dyson, 2016, Reis et al., 2012). It is interesting to outline that Rb lacks mutations in p53 -a tumour suppressor protein-, a common feature of tumours (Boije et al., 2016). When the *TP53* tumour suppressor gene is mutated, tumourigenesis is initiated, and p53 mutant proteins gain additional oncogenic functions (Rivlin et al., 2011). *TP53* is the most commonly mutated gene in human cancer, as it is found in over half of human cancers (Zhu et al., 2020). Some malignancies initiated after the p53 mutation include hepatocellular carcinoma, prostate, colorectal, lung, oesophageal, and bladder cancer (Rivlin et al., 2011, Olivier et al., 2010).

The p107 (also known as RBL1) and p130 (RBL2) proteins are structurally and functionally similar to pRB, as they have "pocket" domains and binding sites for interacting proteins (Sachdeva and O'Brien, 2012). These pRB family members regulate the cell cycle at the G1/S transition by modulation of the E2F transcription factors (Stengel et al., 2009, Haigis et al., 2006). p107 and p130 phosphorylation by G1 cyclins and Cdks allow E2Fs dissociation. The inhibition of the cell cycle progression starts when E2F target gene expression is silenced. p107 and p130 preferentially bind to E2F4 and E2F5 repressors, essential for regulating different E2F-responsive genes. Conversely, pRB binds to E2F3b repressor and E2F activators such as E2F1, E2F2, and E2F3a (Cobrinik, 2005) (**Figure 1-11**).

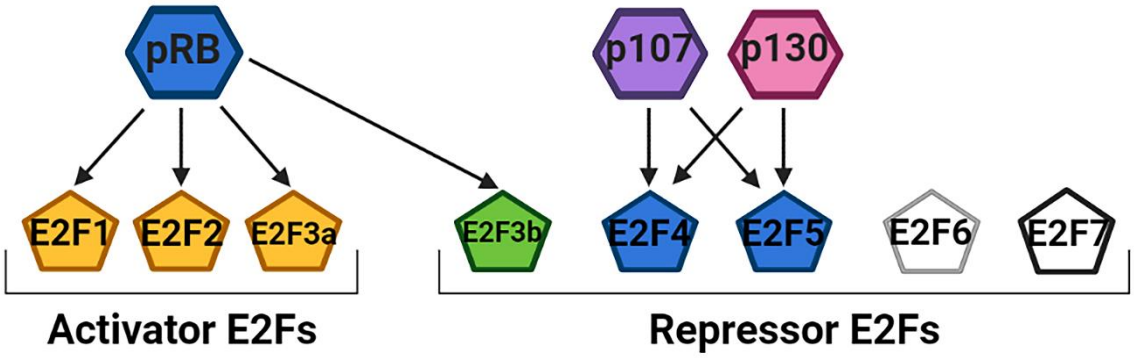

Figure 1-11. Interactions of pocket family proteins and E2F transcription factors.
pRB preferentially binds to the activator E2Fs: E2F1, E2F2, and E2F3a; and E2F3b repressor. p107 and p130 favourably bind to the repressor E2Fs: E2F4 and E2F5. E2F6 and E2F7 form transcriptional repressor complexes but do not bind pocket family proteins. Adapted from (Cobrinik, 2005). Created in Biorender.

The key portion to the biological effects of the pocket family proteins is a ~45K 'pocket' region, which consists of the A and the B boxes. This region is where most pRB-binding proteins make their primary contact and the main target of genetic alterations during tumourigenesis (Lee et al., 1998, Hu et al., 1990, Kaelin et al., 1990). Structurally-wise, the A and the B boxes contain the cyclin fold, a five-helix structural motif present in cyclins and the basal transcription factor TFIIB (Lee et al., 1998, Jeffrey et al., 1995). The pocket region contains 10 helices of the two cyclin folds, 8 other helices, a β-hairpin, and an extended tail. The A-B interface is part of the overall pocket structure with a hydrophobic core that is continuous with that of the B box. Interactions between the A and the B boxes are mediated by a compact hydrophobic core of about 20 side chains and networks of backbone and side-chain hydrogen bonds (Lee et al., 1998). The B box binds to linear LxCxE sequence motif in viral oncoproteins, such as E7 from human papillomavirus (HPV), via its cleft (Zhou et al., 2022).

Surface residues of pRB are conserved in the p107 and p130 family members across species. One of them is the LxCxE binding site on the B box, which is crucial to the cellular function of pRB. The second residue is the A-B interface that participates in the binding to E2F and to other proteins that mediate transcriptional repression by pRB (**Figure 1-12**). The two end regions of the E2F peptide make extensive contact with pRB. The targeting of these conserved interface residues by tumourigenic missense mutations leading to transcriptional repression (Xiao et al., 2003) takes place in the hydrophobic core (Alanine 562) and hydrogen-bond networks (Arginine 661 and Serine 567) (Lee et al., 1998). The C-terminal domain of pRB is crucial for mediating growth arrest and recruitment of specific cyclin/cdk complexes as it also contains several residues whose phosphorylation leads to the deactivation of the pRB tumour suppressor function (Xiao et al., 2003).

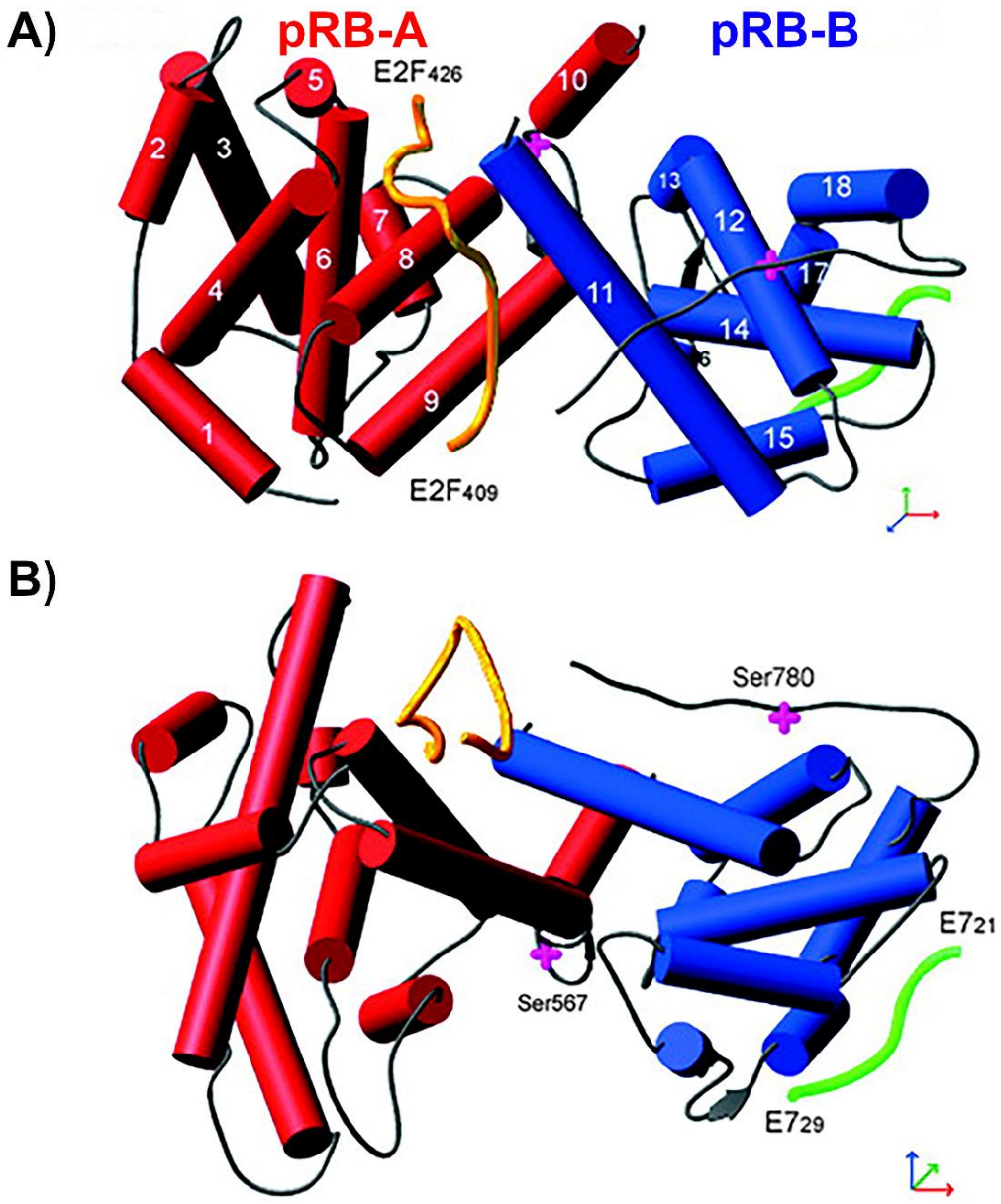

Figure 1-12. Crystal structure of the interaction of pRB pocket domain and E2F/E7 transcription factors.
Schematic ribbon representation showing two orthogonal views of the mechanistic interaction between A and B boxes of the pRB pocket domain and E2F/E7 transcription factors. The helices of the A domain are shown in red cylinders, while those of the B domain are shown as blue cylinders. The α10 helix corresponds to the A-B interface. The main-chain trace of (**A**) $E2F_{(409-426)}$ and (**B**) the human papillomavirus (HPV) $E7_{(21-29)}$ protein are shown as yellow and green worms, respectively. Certain oncogenic viruses, like HPV, responsible for cervical cancer, produce specific proteins for pRB phosphorylation. Adapted from (Xiao et al., 2003).

In addition to the wide-range effects of E2F-mediated regulation of the cell cycle transitions, pocket proteins modulate these transitions through E2F-independent mechanisms. p107 and p130 bind and inhibit cyclin E/cdk2 and cyclin A/cdk2 kinases, which are crucial for S-phase entry regulation (Cobrinik, 2005).

Phosphorylation of pRB at multiple residue sites induces site-specific and diverse global conformational changes to modulate pRB functional outputs, which affects its interaction with E2F LxCxE motif-containing proteins (Zhou et al., 2022). One of these pRB residue sites is serine 608, an authentic phosphorylation site by cyclin A/cdk2 and cyclin D1/cdk4 kinases that occurs prior to entry into the S-phase as part of the cell cycle regulation of the tumour suppressor (Zarkowska et al., 1997). Consequently, E2F1 binding is inhibited, dependent on the presence of the pRB N-terminal domain (Rubin et al., 2005, Knudsen and Wang, 1997).

In the early G1-phase, phosphorylation of the C-terminal domain of pRB (pRBC) at serine 788/serine 795 by cdk4-CyclinD induces dissociation of $pRBC_{786\text{-}800}$, reducing the overall affinity of the C-terminal domain of pRB and the E2F-DP heterodimer complex (Rubin et al., 2005), and disrupts the interaction of the pocket domain of pRB and E2F (Zhou et al., 2022). Phosphorylation at serine 608, 788, and 795 residues shows the molecular relevance of these sites in the overall regulation of the cell cycle and tumour suppressor function of pRB.

Furthermore, p107 and p130 have a role to play in cell differentiation. A study (Cobrinik et al., 1996) reported that *p107* and *p130* homozygous mutant mice had differentiation defects in cartilages and bones and failed to develop terminally differentiated keratinocytes. These results demonstrate the ability of p130 and p107 to regulate chondrocyte proliferation during limb development (Cobrinik et al., 1996).

Although all three proteins negatively control cell cycle progression, only pRB meets the criteria to be a bona fide tumour suppressor as it is commonly expressed in both proliferating and nonproliferating cells (Tedesco et al., 2002, Cobrinik, 2005). Despite being structurally related, these pocket family proteins are differentially regulated during the cell cycle. p107 is predominantly in

proliferating cells, while p130 is more commonly expressed in arrested cells (Cobrinik, 2005). Thus, their biological activity and expression for cell proliferation and differentiation tasks depend on cell type and development stage (Tedesco et al., 2002).

Pocket family proteins and their interactions with Rb may have different mechanisms among mammals. For example, in heterozygous *RB1*$^{+/-}$ mice, a pRB loss is partially compensated by upregulation of p107 expression, which has not been observed in humans yet (Sachdeva and O'Brien, 2012, Haigis et al., 2006). However, heterozygous mice do not develop Rb, whilst homozygous die before the 16th embryonic day due to an abnormal haematopoietic system, confirming that pRB is essential for normal development (Lee et al., 1992).

Together these findings indicate different underlying mechanisms in Rb between humans and mice. The complete pathophysiological role of *RB1* still needs to be elucidated once a reliable human disease model is delineated (Zheng et al., 2020).

1.3.4 Cell of origin of retinoblastoma

In the murine model, *Rb1* knock-out does not lead to tumour formation, which suggests that p107 or p130 may compensate for the lack of Rb1. As a result, pRb;p107- or pRb;p130-deficient mice develop tumours in the retina (MacPherson and Dyer, 2007). However, in humans, pRB deficiency primarily drives tumourigenesis since no p107 or p130 compensation has been reported, suggesting differences between human and murine Rb.

Defining the cell type of origin for Rb is relevant to understand tumour development and designing effective therapeutic treatments. Mouse bulk RNA-seq studies suggested that mouse Rb tumours (MacPherson and Dyer, 2007) have features of ACs, HCs (Qi and Cobrinik, 2017), PRs, and RPCs (Zhang et al., 2004, Donovan et al., 2006). (Singh et al., 2018) reported in their *in vitro* study using murine retina cultures that only pRb-depleted immature (Arr3^{-}) cone precursors entered the cell cycle and failed to progress from the S- to the M-phase. In contrast, pRB-depleted maturing (ARR3^{+}) but not immature (ARR3^{-}) human cone precursors entered the cell cycle, proliferated and were able to form

Rb-like lesions, including Flexner-Wintersteiner rosettes. These results pointed to pRB-depleted maturing ARR3^{+} cone precursors as the cell of origin in human Rb.

The first seminal studies were performed by Cobrinik's group (Xu et al., 2009, Xu et al., 2014), who used RNA interference to model pRB depletion by *RB1* knockdown in isolated human foetal retinal populations revealing that cone precursor populations were remarkably enriched compared to other cell types. The authors also reported that two events collaborated for pRB loss: **1)** high expression of MYCN and MDM2 oncoproteins; **2)** cone lineage factors (thyroid hormone receptor TRβ2 and RXRγ), and SKP2-mediated p27 downregulation (Xu et al., 2014). SKP2 plays a significant role in binding the pRB pathway with cone-specific signal circuitry as it is a crucial survival signal in pRB-deficient tumours (Kaewkhaw and Rojanaporn, 2020). These cone precursors are induced to form differentiated Rb tumours and probably obtain non-cone features. This suggests the human cone precursor population might be the cell type of origin since its circuitry is primarily needed for Rb proliferation, where tumour cells take advantage of the cancer-predisposing cone circuitry (Xu et al., 2014).

Tumours originating from pRB-depleted cone precursors exhibited differentiated histology but lacked gross DNA aberrations (Xu et al., 2014), resembling early Rb elements (Dimaras et al., 2008). These results suggest a model where pRB-deficient cone precursors form differentiated Rbs, followed by dedifferentiation and possible acquisition of non-cone features (Xu et al., 2014). In our recent work (Rozanska et al., 2022), scRNA-seq analyses reported starting cone precursors acquiring HC markers upon entry into the cell cycle, as we observed an increase of proliferating HCs (PROX1^{+}Ki67^{+}) in two different pRB-depleted retinal organoid models. Our scRNA-seq data supports the idea of cone precursors acquiring non-cone features. These findings for cone precursors in Rb development have been corroborated by recent scRNA-seq studies (Liu et al., 2020, Kanber et al., 2022, Li et al., 2022, Yang et al., 2021b, Wu et al., 2022).

Neoplastic cells, possibly originating from pRB-depleted cone precursors, orchestrate tumourigenesis by exploiting the cone precursor circuitry. The human cone-specific signalling circuitry is cancer-predisposing as it is susceptible to the oncogenic effects of *RB1* mutations (Xu et al., 2009). The cone precursor circuitry

directs the expression of the oncogene MDM2 in cones and Rb cells. Bioinformatic analyses of the *MDM2* P2 promoter matched the RXRγ homodimer binding site, a cone-specific transcription factor (Danko et al., 2007, Xu et al., 2009). Additionally, ARF-induced apoptosis is impaired because of MDM2 amplification, particularly during cone cell maturation. MDM2 abrogates E2F- and ARF-mediated responses by inhibiting p53 and is crucial for Rb cell proliferation and survival. The cone-specific thyroid hormone receptor β2 isoform (TRβ2) alongside RXRγ contributes to Rb cell proliferation and survival. N-Myc, a proliferation-related protein, is also highly expressed in cone precursors during Rb tumourigenesis. MDM2 and MYCN amplification in cone precursor and Rb cells suggests the role of these proteins in tumourigenesis and propagation (Xu et al., 2009).

A recent study from our group (Collin et al., 2021) performed the first scRNA-seq and the assay for transposase-accessible chromatin with sequencing (ATAC-Seq) analyses of primary tumour tissues. This study aimed to profile the transcriptional and chromatin accessibility heterogeneity of proliferating cone precursors in human Rbs, revealing the prevalent presence of proliferating cone precursors at different cell cycle stages in the tumours and identifying the G2/M cone precursors as the cell of origin for human Rb.

Similarly, a single-cell transcriptome profiling study by (Yang et al., 2021b) sequenced 14,739 cells from two human Rb samples revealing the heterogeneity and the fundamental mechanisms of tumour progression. The results showed two major cell types with different transcriptomic profiles in Rb: cone precursors and Rb cells. However, in opposition to results from scRNA-seq studies in the murine model, the cell trajectory analysis identified cone precursors as the cell of origin required for the differentiation and malignancy of human Rb. Moreover, in this publication (Yang et al., 2021b), the group described the predominant expression of the UBE2C gene in differentiated tumour cells, which is reported as a potential novel ‘switch gene’ marker during the early critical stages of human Rb development. Additionally, the authors suggested that retinoma-like cells could be an intermediate cell stage between cone precursors and tumour cells.

Lastly, a recent single-cell transcriptomic and whole-exome sequencing study by (Wu et al., 2022) used Rb samples from seven patients to profile more than 70,000 cells. The results revealed two major cell types: cone precursor-like and proliferating cone precursor cells. They also identified the large clonal heterogeneity of the Rb samples, where proliferating cone precursor cells displayed larger copy number changes. The conversion of cone precursor-like cells to proliferating cone precursor cells resulted in the loss of function in PRs and increased cell proliferating ability. Together these studies point to proliferating cone precursors as the cell of origin for human Rb.

The hallmarks of cancer (Hanahan, 2022), described in a previous subsection of this thesis (**1.2 The hallmarks of cancer**), are observed in Rb oncogenesis, including the following:

- **Evading growth suppressors and resisting cell death:** loss of pRB protein as a tumour suppressor.
- **Activating invasion and metastasis and senescent cells:** generation of retinal tumours and recurrent seeds for an active invasion, while metastasis is triggered if Rb is untreated and cancer cells disseminate throughout the retina, the optic nerve, and systemically (Sachdeva and O'Brien, 2012).
- **Genome instability and mutation, and non-mutational epigenetic reprogramming:** alterations in the absence of pRB including upregulation of some oncogenes, *RB1* promoter hypermethylation, chromothripsis, chromosome abnormalities among others, which are broadly described in subsection **1.3.5 Retinoblastoma in the absence of RB1 gene mutations.**
- **Sustaining proliferative signalling and enabling replicative immortality:** cell cycle alterations leading to proliferation deregulation and tumour progression when pRB is lost.
- **Deregulating cellular metabolism:** amplification of oncogenes like *MYC* (Benavente and Dyer, 2015, McEvoy et al., 2011), which has been associated with glycolytic fuelling (Jones and Thompson, 2009, DeBerardinis et al., 2008).

- **Unlocking phenotypic plasticity:** cone precursors following a dedifferentiation fate, potentially acquiring HC markers, and blocking differentiation of other retinal cells (Rozanska et al., 2022) are examples of phenotypic plasticity observed in Rb.

1.3.5 Retinoblastoma in the absence of RB1 gene mutations

Additional genetic and epigenetic changes might initiate Rb even when *RB1* is intact. A recent estimation (Benavente and Dyer, 2015) reports that 2.7% of Rb tumours have no *RB1* inactivation but are characterised by *MYCN* oncogene amplification. Particularly, 1.5% of Rbs with *MYCN* amplification express the wild-type *RB1* (McEvoy et al., 2014). *MYCN* is essential in regulating cell growth, proliferation, apoptosis, and activation of the *E2F1, E2F2,* and *E2F3* genes as *RB1* does (Rushlow et al., 2013, Benavente and Dyer, 2015). These unilateral $RB1^{+/+}$ Rbs with *MYCN* amplification are characterised by distinct histological features, including only a few genomic copy-number changes and the very early age of diagnosis (Rushlow et al., 2013). Most importantly, they do not show genomic aberrations other than *MYCN* amplification, which indicates that epigenetics is the driver of tumour progression in Rb and that E2F transcriptional targets might be the mediators in the process (Benavente and Dyer, 2015). Rb tumours originating from *MYCN* amplification (Singh et al., 2022) arise at an earlier stage than pRB-depleted tumours (median age 4.5 months vs 24 months, respectively), respond less well to chemotherapy, and are more metastatic.

MYCN Rbs are characterised by pRB phosphorylation and lack Flexner-Wintersteiner rosettes (Ewens et al., 2017). pRB phosphorylation as an alternate mechanism of *RB1* inactivation is necessary for initiating tumourigenesis in Rb, especially when driven by *MYCN* amplification. The alterations in the structure of pRB by phosphorylation at multiple serine (S) residues, particularly S608/S612, cause conformational changes that inhibit the association to E2F, allowing cell cycle progression needed for DNA replication. Additionally, pRB phosphorylation at S795 inhibits binding to the marked box domain of E2F1. The observation of pRB phosphorylation at serine 608 (S608) and/or serine 795 (S795) residue (Ewens et al., 2017) is a specific mechanistic link of *MYCN*-amplified Rbs in the

absence of *RB1* mutations. These two residues are key to determining the interaction with the E2F family of transcription factors (Ewens et al., 2017) crucial for cell cycle progression. In fact, (Liu et al., 2015) showed that after a pRB loss in Rbs by *RB1* inactivation, there is Myc-dependent E2F3 accumulation and exacerbated cell proliferation and factors such as MYCN and E2Fs are modified to support unregulated cell proliferation (Osorio, 2015).

A recent study (Singh et al., 2022) showed that overexpressed N-Myc protein in explanted cultured retinae induces cell cycle entry in cells expressing markers of several retinal types. Nonetheless, induced continuous proliferation and tumourigenesis were uniquely observed in cone precursors. Furthermore, N-Myc–overexpressing retinal cells were also found to be occasionally co-expressing the cone precursor marker (RXRγ) with the rod-specific (Nrl), amacrine-specific (AP2α), the progenitor and Müller cell-specific (SOX9), or the RGC-specific BRN3 and GAP43 markers. These results indicate that these cone precursor cells overexpressing N-Myc lose cell lineage constraints and opportunistically use an undifferentiated retinal or neurogenic progenitor feature to drive Rb tumourigenesis (Singh et al., 2022).

Moreover, several gene candidates different to *RB1* promote tumour progression defined by minimally overlapping regions of each common gain or loss. These include *MDM4, KIF14, DEK, E2F3, ID4, SOX4, CHD11*, and *RBL2* (Kaewkhaw and Rojanaporn, 2020). *MDM2,* or its homolog *MDMX,* genes are amplified in about 75% of human Rb, suppressing p53-mediated cell death (Laurie et al., 2009). MDMX binds to pRB and promotes its degradation, thus exerting oncogenic activity. Specifically, the MDMX C-terminal ring domain binds to the pRB C-pocket and enhances MDM2–pRB interaction. *In vivo* silencing of *MDMX* using short hairpin RNA in a study (Zhang et al., 2015) revealed pRB accumulation induction, cell cycle arrest and senescence-like phenotypes, which are reverted by simultaneous pRB knockdown. Additionally, *MDM4* is responsible for the inhibition of cell cycle arrest and apoptosis since it binds to and inhibits the activity of the transcriptional domain of the p53 tumour suppressor protein (Benavente and Dyer, 2015). It has been shown that the q31-q32 region of chromosome 1 is a typical region for gains (Benavente and Dyer, 2015).

pRB has also been implicated in regulating epigenetic processes, including microRNA (miRNA) regulation, DNA methylation, and histone modification (Benavente and Dyer, 2015). The loss of pRB causes ATP-dependent chromatin reorganisation and remodelling required for tumourigenesis, where oncogenes switch to active chromatin while usually transcribed tumour suppressors become repressed. These recent discoveries of epigenetic changes as a major cancer driver in the absence of other genetic lesions have led to the identification and design of novel therapeutic targets against Rb (Benavente and Dyer, 2015). A recent research study of epigenetically modified hub genes associated with Rb (Karmakar et al., 2022) identified three genes (*E2F3, ESR1* and *UNC5D*) significantly deregulated by modified DNA methylation, mRNA and miRNA expression in Rb tumours. *ESR1* codes for oestrogen receptor alpha (ERα), which is a nuclear receptor agonist for oestrogen hormone involved in breast cancer treatment, was found to be downregulated. *E2F3* encodes the E2F3 transcription factor that drives cell cycle progression, while *UNC5D* is a potent tumour suppressor. Both were found to be upregulated. These three genes have the potential to act as Rb therapeutic targets and biomarkers.

miRNAs regulate gene expression by transcriptional and posttranscriptional regulation leading to gene silencing via translational repression or target degradation (Chen and Rajewsky, 2007). As miRNA deregulation is associated with Rb, several miRNAs are potential candidates for oncogenic and tumour suppressor networks, including (Benavente and Dyer, 2015): **1)** members of the let-7 family involved in repressing members of the Ras family, HMGA2 (High Mobility Group AT-Hook 2), and c-Myc oncogenes (Johnson et al., 2005, Mayr et al., 2007, Sampson et al., 2007); **2)** miR-34a tumour suppressor, which is transcriptionally activated by p53 and of interest for therapeutic development (Yang et al., 2019); and **3)** the overexpressed oncogenic miR-17∼92 cluster (OncomiR-1) in Rb, which promotes proliferation, inhibits differentiation, increases angiogenesis and sustains cell survival (Dal Bo et al., 2015). All these miRNAs are potential new therapeutic targets that aim to decrease the oncogenic activity, increase tumour suppressive functions, and promote cell differentiation in patients.

Regarding DNA methylation, hypermethylation of the *RB1* promoter was correlated to decreased gene expression when methylation of a CpG island (CpG 106) overlaps the *RB1* promoter and exon 1 (Benavente and Dyer, 2015). Other nine tumour suppressor genes involved in Rb have been examined for their promoter methylation status: *p16INK4A, MGMT, GSTP1, RASSF1A, APC, DAPK, RAR$_{\beta}$, CDH11,* and *CDH13.* For example, *MGMT* hypermethylation has been associated with advanced-stage Rb, while functional relationships of some of these genes remain to be elucidated (Benavente and Dyer, 2015).

On this basis, groups of epigenetic drugs have been approved for cancer treatment, mainly histone deacetylase (HDAC) inhibitors. For example, Trichostatin A is an HDAC inhibitor that reduces Rb cell survival by triggering morphological changes and apoptosis of Rb cells (Karasawa and Okisaka, 2004). Vorinostat is another drug that regulates *c-Myc* expression, increases p53 expression and apoptosis, and activates the caspase signalling pathway. Entinostat increases caspase-3/7 activity, induces G1 arrest and reduces Rb cell survival (Dalgard et al., 2009, Chai et al., 2022). DNMT inhibitors are another group of epigenetic drugs that target DNMT enzymes to achieve DNA hypomethylation as a therapeutic strategy to reactivate aberrantly silenced tumour suppressor genes (Guzman et al., 2020). Decitabine induces a methylation decrease in the corresponding promoter regions and increases the expression of tumour suppressor genes [(*TP53, HINT2*, *MGMT* and *CDKN2B* (*p15*)] (Jones and Baylin, 2002, Daskalakis et al., 2010, Christman, 2002), thus enhancing the apoptosis of Rb cells (Chai et al., 2022). Potential new therapeutic targets include the histone methyltransferase inhibitors, GSK126 and SAH-E2H2. Their mechanism of action is impairing intracellular ATP production in Rb cells in a dose-dependent manner (Khan et al., 2015). These drugs inhibit *E2H2*, which supports cell proliferation and is highly expressed in Rb cells (Chai et al., 2022).

Recently, it has been documented that chromothripsis contributes to *RB1* inactivation in humans by shattering a chromosome and its mechanism of uncoupled DNA replication in micronuclei as part of a random reassembly (Dyer, 2016). These genomic rearrangements might go from tens to hundreds in a

single event in localised and confined genomic regions in one or more chromosomes (Benavente and Dyer, 2015).

Recurrent chromosomal abnormalities include the unique isochromosome 6p reported in 45% of Rbs, the gain of regions of chromosome 1q (44%), monosomy of chromosome 16 (18%), the gain of 1p (13%), and less common loss of sex chromosome, and alterations in chromosomes 17 and 19 (Benavente and Dyer, 2015). Mainly, gains of 6p are the most common changes in Rb, with the band p22 characterised as the minimal region of gains. Gene expression of this region pointed to *DEK* and *E2F3* as the potential targets of 6p gains in Rb (Grasemann et al., 2005, Orlic et al., 2006, Benavente and Dyer, 2015). *E2F3* is a transcription factor regulated by pRB and overexpressed in cancer, as discussed previously in section **1.3.3 pRB and other pocket family proteins**. *DEK* is involved in chromatin reconstruction and gene transcription, which plays a significant role in apoptosis and various human malignancies (Benavente and Dyer, 2015, Hu et al., 2007). The second most common changes in Rb are 1q gains, where the minimal common region gained spans 1q31-q32 with validated *KIF14* and *MDM4* genes in this region. *KIF14* plays a role in cell division and intracellular transport, but also it is overexpressed in human Rb (Benavente and Dyer, 2015, Dimaras et al., 2008, Madhavan et al., 2007). Loss of whole chromosome 16 or 16q was identified in 32% of Rb cases, where *CDH11* was reported as the candidate tumour suppressor in this region (Corson and Gallie, 2007). *CDH11* encodes cadherin-11, an integral membrane protein that mediates calcium-dependent cell-cell adhesion (Benavente and Dyer, 2015). When CD11 protein is lost in Rb, it may lead to tumour progression and optic nerve invasion (Laurie et al., 2009).

A research study (van Harn et al., 2010) using triple knock-out mouse embryonic fibroblasts (TKO MEFs) lacking *RB1, p107,* and *p130* tested cell cycle control by mitogen deprivation and addition. Results showed accumulated DNA damage, chromatid breaks, chromatid cohesion defects, and aneuploidy. Some chromosomal aberrations include the gain of chromosome 15 and the partial loss of chromosome 12. A lack of G1/S-phase control resulted in genomic instability in the descendent cell populations (van Harn et al., 2010).

Another example of epigenetic alteration is the deregulation of the spleen tyrosine kinase (*SYK)* proto-oncogene after *RB1* inactivation, which is expressed at high levels and prevents apoptosis through MCL1. This could explain the quick progress of Rb after *RB1* inactivation (Dyer, 2016). Targeting *SYK* by using small-molecule inhibitors induces Rb tumour cell death *in vivo* and *in vitro* by the degradation of MCL1 (Zhang et al., 2012).

1.3.6 Retinoma

Retinomas are benign retinal tumours that do not proliferate and can coexist with Rb (Kaewkhaw and Rojanaporn, 2020, Dimaras et al., 2008). They can be found in 2% of individuals who carry at least one mutation in the *RB1* allele. It is hypothesised that retinoma is a precursor of Rb with both mutated copies of *RB1* but lacking other events that could drive progression to Rb as retinoma cells express senescence proteins, $p16^{INK4A}$ and p130, incapable of proliferating, thus blocking malignant transformation. Cone circuitry might be affected by cumulative genetic and epigenetic changes that lead to premalignant cells becoming highly proliferative Rb cells (Kaewkhaw and Rojanaporn, 2020, Dimaras et al., 2008). Clinical evidence shows that diagnosed retinoma has progressed to Rb as the clonal change includes major alterations in proliferative markers and increased genomic instability involving tumour suppressor genes and specific oncogenes (Dimaras et al., 2008).

1.3.7 Disease models of retinoblastoma

1.3.7.1 Animal model

The retina has an uneven density distribution of cones between mammalian species, particularly in the periphery (Hendrickson, 2005). The main difference between mammalian retinas is that primates, including humans, have a fovea where 99% of the cones reside. However, the mouse eye lacks the fovea and has fewer photoreceptors covering a specific area of the visual scene. These features make the entire mouse retina like the peripheral retina of primates, which appropriates its use for low-acuity studies but not high-contrast and high-acuity studies (Huberman and Niell, 2011). Therefore, these anatomical

differences in the eye limit a murine retinal model compared to a human retinal model.

As discussed previously, there are underlying differences in the disease mechanisms of Rb in mammals, particularly between humans and mice. In humans, heterozygous *RB1* mutations predispose to Rb tumour development with homozygous mutations (Knudson, 1971). pRb-depleted mouse cone cells do not develop tumourigenesis, even when *MDM2* and *MYCN* are ectopically expressed. Thus, different susceptibilities to tumourigenesis exist between humans and mice. Given this, candidate drugs may show therapeutic effects in preclinical murine models, which might not be effective in humans as the epigenetic landscape between human and mouse tumours differs.

The complete pathophysiological role of *RB1* still needs to be elucidated once a reliable human disease model is established (Zheng et al., 2020). To this end, an *RB1* knockdown disease model would help understand the nature of Rb. Using human foetal retinal cells *in vitro*, (Xu et al., 2011) showed that when *RB1* is knocked down by RNA interference, proliferation ($Ki67^+$) is explicitly induced in L/M $opsin^+$ and Crx^+ cone precursors. Additionally, apoptosis is induced in Müller glia and RPCs. Thus, cone precursors proliferate and form tumours that resemble human Rb at histological, structural, retinal marker and molecular cytogenetic levels (Xu et al., 2014).

1.3.7.2 Orthotopic Patient-Derived Xenografts

Xenografts are exogenous living cells, tissues or organs from individuals of species that are transplanted into another species (Cascalho and Platt, 2008). These can be created through orthotopic or subcutaneous implantations of patient-derived tumour cells into immunodeficient animals (Kaewkhaw and Rojanaporn, 2020). Mainly, xenotransplantation refers to the transplantation of xenografts. Regarding the origin of xenografts, it is a priority to obtain them from genetically similar species to minimise the immunological barrier and risk of rejection, thus improving the viability and functionality of the transplantation (Cascalho and Platt, 2008).

Xenografts from solid tumours can be used to establish new preclinical models of Rb. Understanding Rb has led to the development of the first

orthotopic patient-derived xenografts (O-PDXs), which are obtained by collecting cells after surgery and orthotopically implanting them in immunocompromised mice by injection into the vitreous of the eye. These xenografted tumours are then passaged from mouse to mouse as they retain a patient's tumour's molecular, cellular, and genetic features (Dyer, 2016). These Rb O-PDX tumours grow as a disorganised mass with intercellular regions of neuronal plexus reflecting their retinal origins and retaining the genomic features of the patient tumours (Stewart et al., 2017, Dyer, 2016). Contrary to the established knowledge in the field, Rb O-PDXs have remarkably stable genomes, as studies have shown (Dyer, 2016), indicating a lack of genomic abnormalities.

O-PDX models provide translational relevance for new therapies to treat Rb tumours (Dyer, 2016). A xenograft could deliver genetic material in complex metabolic pathways to highly express heterologous genes (Cascalho and Platt, 2008). Today, xenografts have been developed as advanced systems that compete with differentiation into functional tissues and organs of stem cells.

Nonetheless, xenografts are not exempt from biological barriers that include (Cascalho and Platt, 2008, Stewart et al., 2017): **1)** the need for an invasive patient surgery to obtain a source of tumour cells; **2)** the graft injury to the recipient caused by its immune system; **3)** physiological incompatibility between the recipient and the transplant; **4)** the engraftment efficacy of the tumour; **5)** any possibility that the exogenous transplant might transfer an infectious organism to the recipient (e.g. herpes B and retroviruses).

O-PDXs are usually consistent in genome and karyotype stability. Still, Rb O-PDXs have been reported to be genomically unstable as they undergo molecular, cellular, and histological characterisation concurrently with the patient tumour (Zhang et al., 2012, Stewart et al., 2017). It is important that O-PDXs are developed in patients with recurrent disease to retain the patient tumour's molecular and cellular features and the epigenetic landscape of their developmental origins (Stewart et al., 2017). Nonetheless, this genomic instability is not a hallmark of Rb, and it is insufficient to thoroughly explain the progression of tumour growth in Rb (Zhang et al., 2012). Therefore, Rb O-PDXs might not be suitable for chemotherapeutic drug testing in Rb disease modelling.

1.4 Stem cells

Stem cells are responsible for building and maintaining the body as they are the foundation of mammalian life (Clevers, 2019). Depending on their capacity to differentiate into different tissues, embryonic stem cells are the prototypical stem cells due to their ability to give rise to progenitors of the three embryonic germ layers: ectoderm, endoderm and mesoderm (Sylvester and Longaker, 2004). The primary characteristic that a cell must show to be considered a "stem cell" is the capacity for symmetrical and asymmetrical cell division. There are two types of symmetrical division: a proliferation division resulting in two stem cells and a differentiation division generating two differentiated cells. Conversely, the asymmetric division produces an exact multipotent replica cell and an additional progeny cell capable of a more specialised function (Sylvester and Longaker, 2004, Shahriyari and Komarova, 2013). There are two basic types of stem cells (Clevers, 2019):

I. **Adult stem cells**: This group comprises multipotent and unipotent stem cells that replace the tissue damaged or lost due to wear and tear, trauma, or disease. As these cells are highly specialised, they can only produce the tissue in which they reside, accordingly to the idea that every organ in the body contains its dedicated stem cells (Clevers, 2019). Therefore, these cells have a 'multipotency' (multiple cell types) or 'unipotency' (only one cell type, their own) feature, depending on their ability to develop specific tissue. Examples of multipotent stem cells include bone marrow, haematopoietic, mesenchymal, and neural stem cells. Unipotent cell examples include muscle stem cells and epithelial progenitor cells (A and B, 2011).
II. **Pluripotent stem cells**: The main characteristic of these cells is harbouring the potential to build every tissue type in the body that can be grown *in vitro* indefinitely. Due to their origin, two kinds of cells are discerned: embryonic stem cells and induced pluripotent stem cells, further described in the following section.

1.4.1 Embryonic Stem Cells

Human embryonic stem cells (hESCs) are pluripotent cells derived from the inner cell mass of the developing blastocyst (Boyer et al., 2005). They have the potential to build and develop every tissue in the body and can be grown *in vitro* indefinitely in an undifferentiated state (Clevers, 2019). They are briefly present in the embryo a few days after fertilisation. They can give rise to all of the fully developed organism's somatic and germ-line cells (Sylvester and Longaker, 2004).

1.4.2 Naïve Embryonic Stem Cells

Naïve embryonic stem cells allow increased developmental potential as they can robustly differentiate all three germ lineages (Ware et al., 2014) and give rise to the trophectoderm lineage (Cinkornpumin et al., 2020). The naïve stem cells represent the early stage of the preimplantation inner cell mass, which specifies both the hypoblast and the pluripotent epiblast that gives rise to all embryonic tissues (ectoderm, mesoderm, and endoderm) of the organism (Cinkornpumin et al., 2020). On the contrary, the mouse epiblast stem cells and hESCs represent the "primed" state of embryonic stem cells (Ware et al., 2014). Changes in the epiblast, including epithelialisation, increased DNA methylation, and expression of new genes and cell surface receptors, prime the epiblast to differentiate rapidly. Thus, the epiblast is transitioning from the naïve pluripotent state to the primed pluripotent state (Cinkornpumin et al., 2020). Maintenance of naïve cells is particularly challenging due to their nature of getting differentiation stimuli. However, their culture is possible if they are maintained in medium with leukaemia inhibitory factor (LIF), extracellular signal-regulated kinase (MEK) and glycogen synthase kinase 3 (GSK3) inhibitors (2i) (Sim et al., 2017). Also, hypomethylation is an epigenetic hallmark of a naïve state that is valuable for an epigenetic reprogramming model (von Meyenn et al., 2016). Moreover, *in vitro* studies have reported different approaches for maintaining the naïve ground state of T cells by overexpression of let-7 miRNAs (Pobezinskaya et al., 2019) or by inhibiting T cell receptor (TCR) signalling by adenosine through adenosine A_{2A} receptor (Cekic et al., 2013).

Mouse embryonic stem cells (mESCs) can also be maintained in culture using MEK/GSK3 inhibitors and LIF in the medium (Ware et al., 2014). mESCs can be isolated from the blastocyst inner cell mass and be differentiated into all embryonic lineages due to their exhibited pluripotency (Nichols and Smith, 2009). Murine trophoblast stem cells (mTSCs) can be obtained from blastocysts or early post-implantation embryos to form all placental lineages (Tanaka et al., 1998). The human counterparts of these stem cells have been challenging to achieve as their behaviour does not always match that of the murine part. Although hESCs can be obtained from pre-implantation blastocysts, they still have an epithelial morphology and a transcriptome typical of primed post-implantation epiblasts (Cinkornpumin et al., 2020).

It has been challenging to capture the *in vitro* naïve stage in human cells. Induced pluripotent stem cells (iPSCs) can be maintained in the naïve state if the pluripotency-inducing transgenes are not silenced, as has been reported (Ware et al., 2014). Furthermore, hESC lines in the later primed state can be conditioned to the naïve stage by exposure to histone deacetylase inhibitors before naïve culture (Ware et al., 2014). A study by (Cinkornpumin et al., 2020) has reported that naïve hESCs can differentiate into the trophoblast lineage and form human trophoblast stem cells (hTSCs). The results show that naïve hESCs can be transdifferentiated to an extraembryonic lineage to model human trophoblast specification and placental methylome establishment (Cinkornpumin et al., 2020).

1.4.3 Induced Pluripotent Stem Cells

Induced pluripotent stem cells were initially somatic adult cells that were conditioned to return to an undifferentiated stage to replicate the properties of ESCs (Clevers, 2019). De-differentiation involves reversion to an immature state (Gallina et al., 2014). Reprogramming of murine somatic cells to iPSCs –and similar genetic manipulation for human iPSCs– occurs after ectopic expression of four transcription factors: *Oct4, Klf4, Sox2* and *c-Myc* (Zhou et al., 2009) (

Figure 1-13). iPSCs are closely similar to ESCs, easier to create, much less controversial in the case of human cells, and adequate for clinical applications and research, particularly for generating retinal disease models. iPSCs have normal karyotypes, express cell surface markers and normal telomerase activity and show a transcriptional program akin to human ESCs (Yu et al., 2007).

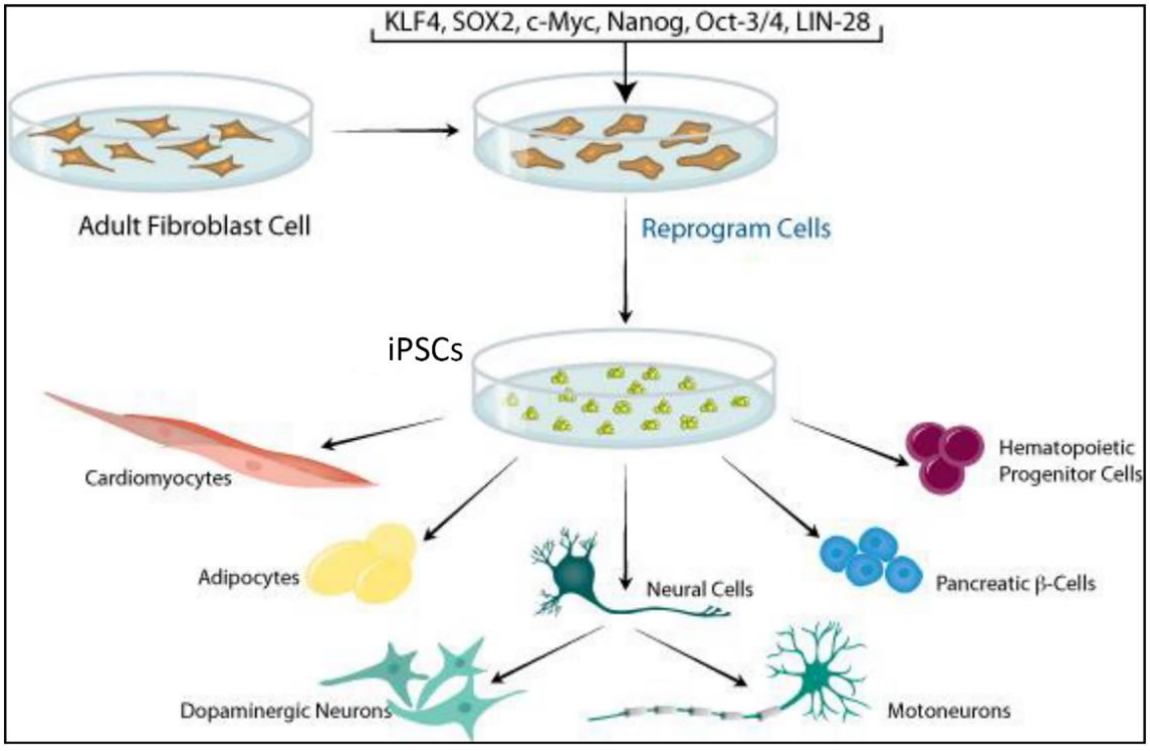

Figure 1-13. Diagram of differentiation of iPSCs.
Adult somatic cells are reprogrammed into induced pluripotent stem cells that can be differentiated into multiple cell types. Reprogramming of adult fibroblast cells is possible in the presence of factors that include Klf4, Sox2, c-Myc, Nanog, Oct-4, and Lin-28. Reproduced from (Amabile and Meissner, 2009).

1.4.4 Retinal organoids

hESCs and hiPSCs can be differentiated into different types of tissues (neuronal, retinal, intestinal, epithelial, kidney, lung, and blood vessel, among other examples) (Kim et al., 2020) that can potentially give rise to three-dimensional tissue organoids reflecting a developmental environment closely related to the *in vivo* environment (Llonch et al., 2018). Initially, the term organoid (Smith E Fau - Cochrane and Cochrane, 1946) referred to a teratoma and its histological features. Today (Lancaster and Huch, 2019), an organoid is an artificial self-organising tissue resembling an organ. It must satisfy the criteria defining an organ:

1) **A 3D structure:** recapitulate the developmental programme to result in the proper identity of the modelled organ.
2) **Multiple cell types:** involve more than one key cell type, as in the organ.
3) **Function:** exhibit the specialised function of the organ.
4) **Self-organise:** develop and mature according to intrinsic spatial organising principles, as in the organ.

Pluripotent stem cells (PSCs) can be guided towards a specific organ fate by mimicking early human embryonic development. PSCs and/or adult-tissue cells can give rise to the three primary germ layers to form (Lancaster and Huch, 2019):

a) **Ectoderm organoids:** PSC-derived 3D aggregates that can form cerebral, brain-region specific, retinal, and inner ear organoids, while adult-tissue-derived biopsies can generate mammary and salivary gland organoids.
b) **Mesoderm organoids:** PSC-derived 3D aggregates can be derived into kidney organoids, while adult-tissue biopsies can be derived into bone, fallopian tube, and endometrial organoids.
c) **Endoderm organoids:** PSC-derived 3D aggregates can form gut, thyroid, stomach, liver bud, and lung organoids. Adult-tissue

biopsies can also be derived from the pancreas, gut, stomach, liver, and lung organoids.

Nonetheless, one fundamental difference between *in vivo* tissues and organoids is the lack of vasculature and immune cells (Augustyniak et al., 2019). Other limitations include organoid growth restriction to low-adhesion plates, variability in structure, difficulties achieving maturity in some cases, and absence of surrounding tissue for tissue cross-communication (Augustyniak et al., 2019, Yin et al., 2016). Although organoids are not precisely like adult organs, they are the best tool for *in vivo* research into disease mechanisms, drug discovery and toxicology studies.

Retinal organoids (ROs) are three-dimensional cellular structures comprising all the key retinal cell types organised in a laminated structure akin to the human retina. These complex organoids recapitulate retinal development, morphology and maturation (Fernando et al., 2022). Work from our group (Hallam et al., 2018, Mellough et al., 2019b, Chichagova et al., 2019, Dorgau et al., 2022) and others (Cora et al., 2019, Zhong et al., 2014, Capowski et al., 2019, Fernando et al., 2022, Saha et al., 2022, Samimi et al., 2022, Wahlin et al., 2017) have shown that pluripotent stem cell-derived retinal organoids contain light-sensitive photoreceptors at the apical layer. These retinal organoids are effective *in vitro* models (Kim et al., 2020) and can be generated from ESCs and iPSCs, cancer- and patient-derived cells, including unaffected controls and cells affected by diseases (**Figure 1-14**). Due to the evolutionary divergence, human biology and disease mechanisms have multiple features that cannot be accurately modelled in animals. Single-cell data from (Cowan et al., 2020) revealed that human retinal organoids are morphologically and transcriptomically closer to peripheral than to foveal retina (Afanasyeva et al., 2021). Although results from another group (Sridhar et al., 2020) also showed that retinal organoids are closer to human foetal than the adult retina in terms of cell composition, they still reproduced the adult's retina five-layered structure and aspects of the cell type and function. However, they are the most optimal platform to date to mimic the retina's unique features.

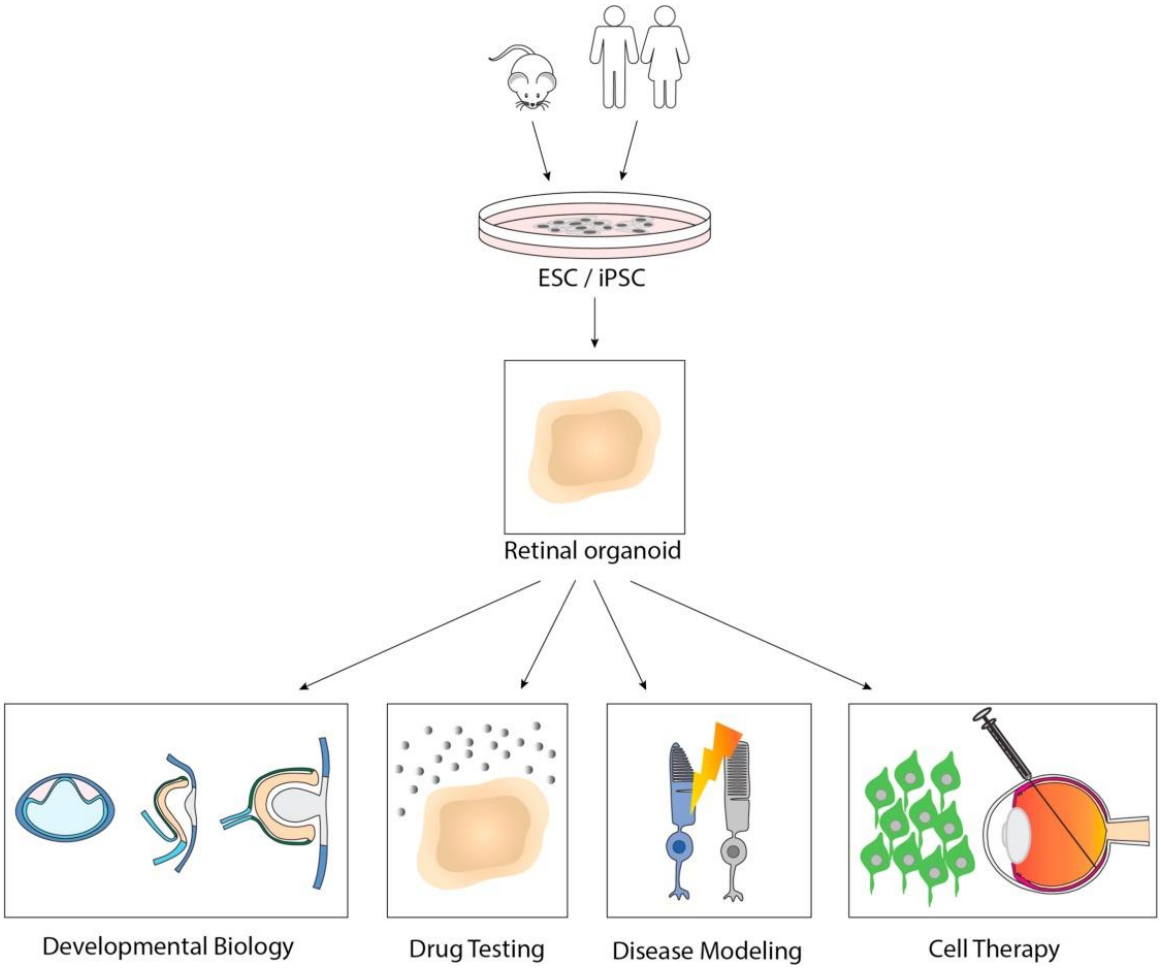

Figure 1-14. Potential applications for retinal organoids.
ESCs and iPSCs from mammals can be differentiated into retinal organoids for different applications, including developmental biology analysis, drug testing/screening, retinogenesis, *in vitro* disease modelling and establishing a cell therapy for retinal diseases. Reproduced from (Llonch et al., 2018). CC BY-NC.

Cell-fate specification and neuronal differentiation mechanisms have been better understood through RNA-seq technologies for transcription network analyses (Finkbeiner et al., 2022). The genome-wide approaches have provided insights into retinal development and the trajectories that lead to cell fates. Although retinal organoids are currently a prominent model for studying retinal development, long-term cultures from the human foetal retina have been traditionally of interest for understanding retinal lamination. There are differences between human retinal organoid and long-term foetal retina (also known as retinosphere) cultures. To this end, **Table 1-1** summarises the advantages and disadvantages of both models.

Table 1-1. Comparison between the human retinal organoid and foetal retina cultures.

Model	Advantages	Disadvantages
hiPSC-derived retinal organoids	• Similar cellular composition at equivalent ages as foetal retina. • All major retinal cell types are present. • Increased proportion of retinal cell progenitors (Sridhar et al., 2020). • ROs are an expandable source suitable for high-throughput drug screening and testing (Kaewkhaw and Rojanaporn, 2020).	• Differences in gene expression in some cell types, such as amacrine, horizontal and bipolar cells. This limitation is related to the lack of endothelial cells and microglia. • A reduced proportion of RGCs and other retinal cell types (Llonch et al., 2018). • Lower levels of Notch signalling and a reduced rate of AC and HC genesis (Finkbeiner et al., 2022). • Inner retinal lamination is disrupted and less characterised at more advanced stages than the foetal retina, but not due to culture conditions. • Variability is due to the specific cell line used to differentiate. • Tissue reaches the stage where vasculature perfusion is critical for normal development, particularly for the inner plexiform layer (IPL) development (Sridhar et al., 2020).
Long-term retinal cultures from the human foetal retina (retinospheres or organoid-like cultures)	• Better inner retinal lamination than retinal organoids, maintaining neuron proportion for amacrine, horizontal and bipolar cells. • Extensive development of the IPL and outer plexiform layer (OPL) (Sridhar et al., 2020).	• They are derived from the human foetal retina, limiting the source availability to obtain retinospheres. • A large development gradient accounts for differences in developmental time between the central and peripheral retina (Sridhar et al., 2020).

The early stages of *in vitro* retina modelling started with two-dimensional (2D) differentiation. The retinal progenitors derived from stem cells in 2D conditions have been reported in some studies (Zhong et al., 2014, Zheng et al., 2020) to be reliable and efficient but only generated certain retinal cell types, such as RGCs and PRs, as they are commonly found within mixed cell populations that lack tissue architectural characteristics. These 2D cell culture systems lacked the appropriate cell-cell contact environment typically observed *in vivo* (Zheng et al., 2020). Additional studies achieved retinal neuron differentiation from hESCs (Lamba et al., 2006) and PRs from mouse foetal retinas and mice, monkey and human ESCs (Osakada et al., 2008). Furthermore,

other groups (Eiraku et al., 2011, Nakano et al., 2012, van Harn et al., 2010) generated retinal aggregates and 3D optic cups from hESCs and hiPSCs.

The advancement of organoids as a 3D *in vitro* model to study the development of complex tissues and disease pathomechanisms started in 2013 with Yoshiki Sasai's pioneering work. His study (Sasai, 2013) of mimicking embryonic development in 3D by inducing organogenesis from stem cells in culture was a milestone for the retinal organoid field. Organogenesis was induced by aggregating mouse or human ESCs in suspension with minimal medium for efficient retinal differentiation. Then, the ESC-derived epithelia evaginate to form optic-vesicle-like structures that undergo invagination to build optic cups without any external forces or cues. As seen in the embryo, the optic cups have two walls: outer pigment epithelium and inner neural retina. In long-term culture, these retinal organoids are laminated, containing all six components (PRs, BCs, ACs, HCs, RGCs and Müller glial cells) of the retinal structure. These cells are correctly located in the layers corresponding to their position in the postnatal retina (Sasai, 2013).

Further studies (Nakano et al., 2012, Zhong et al., 2014) based on Sasai's work allowed the development of three-dimensional human ESC and iPSC-derived retinal progenitor cultures with all major retinal cell types and Müller glial cells arranged in their respective layers. The new differentiation protocols enabled the generation of 3D retinal cups with all major retinal cell types in proper layers obtained from hiPSCs (Zhong et al., 2014). Other groups (Kuwahara et al., 2015, Lakowski et al., 2018, Kuwahara et al., 2019, Brooks et al., 2019, Akhtar et al., 2019, Regent et al., 2020, West et al., 2022), including ours (Hallam et al., 2018, Chichagova et al., 2019, Mellough et al., 2019b, Chichagova et al., 2020), developed 3D PSC-derived retinal organoids by modulating different pathways (WNT, FGF, TGFβ, and BMP using chemical compounds like BMP-4, IGF-1, retinoic acid, levodopa, triiodothyronine, γ-secretase inhibitor DAPT, docosahexaenoic acid and fibroblast growth factor 1).

The development of novel and improved protocols from other groups (Zhong et al., 2014, Capowski et al., 2019, Cora et al., 2019, Fernando et al., 2022, Saha et al., 2022, Samimi et al., 2022) and ours (Hallam et al., 2018,

Mellough et al., 2019b, Chichagova et al., 2019, Dorgau et al., 2022) for organoid differentiation enabled the generation of organoids containing light-sensitive photoreceptors. Different methods for retinal tissue and organoid differentiation are summarised in **Table 1-2.**

Nonetheless, there are current disadvantages and limitations in the retinal organoid model when using different pluripotent stem cell lines, including the following (Llonch et al., 2018): **1)** high heterogeneity of cell composition and areas that were properly patterned in retinal nuclear layers; **2)** extended culturing times; **3)** incomplete maturation of PRs with outer-segment-like structures but not fully mature outer segments (Lowe et al., 2016), making it challenging to mimic the ageing-related phenotype; **4)** lack of vascularisation and absence of inflammatory cell types (Aasen and Vergara, 2019); **5)** lack of juxtaposition of a polarised RPE (Aasen and Vergara, 2019); **6)** variability between iPSC lines and differentiation efficiency (Aasen and Vergara, 2019); **7)** formation of correct number and location of interneuron synapses between retinal cells in long-term cultures even though synaptic proteins have been observed (Dorgau et al., 2019, Llonch et al., 2018).

Despite the current drawbacks and limitations, ROs are the closest model of recapitulation of *in vivo* organogenesis with retinal development in self-organising pluripotent stem cell (PSC) cultures. As a robust modelling platform, ROs are useful for assessing neuroretina-specific gene regulation, pathological processes, and therapeutic manipulation (Afanasyeva et al., 2021).

Table 1-2. Retinal tissue differentiation methods from ESCs and iPSCs.

Method	Year	Description	Reference
Retinal neurons derivation from hESCs in 2D culture and co-cultured in 3D with foetal retinas	2006	Retinal neurons were obtained by differentiation of the H1 hESC line with a success rate of 80%. They had a gene expression profile similar to progenitors derived from human foetal retinas. They primarily differentiate into RGCs and ACs. Then, the progenitors were co-cultured with retinas derived from a mouse model of retinal degeneration. They integrated with degenerated mouse retina, then increased PR-specific makers' expression (Lamba et al., 2006).	(Lamba et al., 2006)
Rod and cone PR generation in 2D from ESCs	2008	Cone and rod PRs were generated from mice, monkeys and hESCs in the absence of retinal tissues. With mouse ES, the precursors were treated with a Notch signal inhibitor. Fibroblast growth factors, Shh, taurine and retinoic acid, produced more rhodopsin^{+} rod PR and default cone PR generation. With monkey and hESCs, they were cultured in feeder- and serum-free suspension cultures with Wnt and Nodal inhibitors. This condition produced RPE cells, while treatment with retinoic acid and taurine generated PR differentiation (Osakada et al., 2008).	(Osakada et al., 2008)
2D/3D retinal development from hESCs and hiPSCs	2009	hESCs were differentiated as free-floating aggregates and prompted to adhere to laminin-coated culture dishes. A neural rosette was formed, and after 16 days of differentiation, these colonies were removed to grow as neurospheres. Prolonged maintenance of these neurospheres allowed maturation toward a PR phenotype. RPE cells were obtained as well. hiPSCs were differentiated with the same protocol into aggregates, neural rosettes and then neurospheres, which over time showed positive PR markers (Meyer et al., 2009).	(Meyer et al., 2009)
Optic-cup morphogenesis in 3D culture	2011	Formation of the optic cup structure from 3D mESC aggregates in serum-free floating and growth-factor-reduced (SFEBq) culture medium with basement-membrane matrix components (Matrigel). Spontaneous formation of the cup in the absence of a lens or surface ectodermal tissues mimicking *in vivo* development (Eiraku et al., 2011).	(Eiraku et al., 2011)
Optic cup and stratified neural retina formation from hESCs	2012	Optic cup structure and neural retina were formed from human ESCs in SFEBq culture. The 3D aggregates were cultured with knockout serum replacement additive (KOSR), then with 10% foetal bovine serum (FBS) as an effective enhancer of retinal differentiation. These structures were much larger and thicker than the mouse ESC-derived ones. The stratified neural retina contained cone and rod PRs, whereas cone differentiation is rare in mESC culture (Nakano et al., 2012).	(Nakano et al., 2012)
3D retinal tissue with functional PRs from hiPSCs	2014	Three-dimensional retinal cups with all major retinal cell types in proper layers were obtained from hiPSCs. For this 3D-2D-3D method, they first cultured the hiPSC in	(Zhong et al., 2014)

		suspension with mTeSR1 medium and 10 μM Blebbistatin to induce aggregate formation. Then, the medium was switched to a neural-induction medium (NIM). On day 7, the aggregates were seeded onto Matrigel-coated dishes with NIM at an approximate density of 20 aggregates per cm^2 and then switched to DMEM/F12 (3:1) NIM. After four weeks of differentiation, the horseshoe-shaped neural retina domains were cut and cultured in suspension until they developed the 3D structure. PRs achieved the advanced maturation stage and the beginning of outer-segment disc formation and photosensitivity. The aggregates were cultured in a chemically defined neural differentiation medium and attached to Matrigel-coated dishes (Zhong et al., 2014).	
Ciliary margin-like to form retinal tissue from 3D hESC culture	2015	Neural retina tissue differentiation was achieved using timed BMP-4 (bone morphogenetic protein 4) treatment in hESC SFEBq culture without Matrigel. Then, inhibiting GSK3 and FGFR (fibroblast growth factor receptor) induced the transition from NR to RPE. Conversely, removing this inhibition facilitated the reversion of RPE to NR aggregates with RPE at the margin of central-peripherally polarised NR. This boundary NR-RPE tissue self-organises a niche for ciliary-margin-like stem cells (Kuwahara et al., 2015).	(Kuwahara et al., 2015)
Human PR precursors from PSC-derived retinal organoids	2018	PR cell precursors were obtained from hiPSC-derived retinal organoids. These organoids were differentiated in a medium containing DMEM/F12, N2 supplement, MEM nonessential amino acids, GlutaMAX and heparin (Lakowski et al., 2018).	(Lakowski et al., 2018)
3D retina formation by modulation of TGF-beta and Shh signalling from hiPSCs	2019	An established culture protocol efficiently differentiates feeder-free iPSCs to self-organise 3D retina formation by modulating TGF-beta and Sonic hedgehog (Shh) signalling pathways. Inhibition of TGF-beta signalling pathways permits the promotion of neural differentiation, while Shh signalling promotes ventralisation and posteriorisation in neural patterning and the formation of retinal tissue (Kuwahara et al., 2019).	(Kuwahara et al., 2019)
Light-responsive retinal organoids from hiPSCs	2018	Five hiPSC lines were differentiated into 3D retinal organoids with significant variability in their differentiation efficiency. The differentiation protocol included seeding 3000-12,000 cells into each well in a 96-well lipidure-coated U-bottom plate in 100 μl of mTeSR1 with 10 μM Rho-associated coiled-coil protein kinase inhibitor (ROCKi). After 2 days, the medium was switched to a differentiation medium and changed every 2 days. On day 6, BMP-4 was added, and media changes were done every 2 days until day 18. Then, “pooled” retinal organoids were transferred to ultra-low attachment 6-well plates, and the medium was changed to a maintenance medium. Differentiated ROs exhibited outer nuclear layer PRs, connecting cilium and outer-like segments. After five months of differentiation, ROs generated light responses comparable to the earliest light responses recorded from the mouse	(Hallam et al., 2018)

		retina, which is close to the eye opening. The multiwell plate format enhanced the scale generation of ROs for toxicology and drug screening assays (Hallam et al., 2018).	
Retinal organoid differentiation from hESCs/hiPSCs via IGF-1 signalling	2019	Retinal organoids were generated from human pluripotent stem cells (hPSCs) in 96-well U-bottom plates. The differentiation approach is based on adding insulin-like growth factor 1 (IGF-1) with retinoic acid and triiodothyronine for retinal development. After 22 weeks in culture, the ROs formed a thick layer of neuroepithelium containing PRs, BCs, HCs, ACs, RGCs, and Müller cells.	(Chichagova et al., 2019)
Retinal organoids derived from hESCs/hiPSCs	2019	hESCs and hiPSCs are differentiated into retinal organoids by an initial phase of embryoid body (EB) formation that allows the self-formation of optic cup structures. A mechanical approach for EB formation with early ROCKi markedly prevents dissociation-induced apoptosis, enhancing survival and showing that it is the most efficient approach for producing retinal organoids compared to other derivation methods (Mellough et al., 2019b, Kuwahara et al., 2019, Gao et al., 2019). The organoids have been confirmed to contain the necessary structures for phototransduction as electrophysiological properties like cGMP sensitivity have been demonstrated in photoreceptors compared to the eye-opening period) (Mellough et al., 2019b).	(Mellough et al., 2019b)
Docosahexaenoic acid and fibroblast growth factor 1 improve mouse retinal organoid differentiation	2019	Mouse iPSCs were differentiated into retinal organoids using the modified HIPRO protocol (DiStefano et al., 2018) in 96-well U-bottom plates. Addition of docosahexaenoic acid and fibroblast growth factor 1 to mouse organoid cultures specifically promoted the maturation of cone and rod PRs. scRNA-seq analyses allowed the construction of regulatory networks that revealed that adding these two reagents improved PR differentiation and maturation (Brooks et al., 2019).	(Brooks et al., 2019)
Contact co-culture of hiPSC-derived retinal organoids with mouse RPE improves photoreceptor differentiation	2019	Retinal organoids were generated from hiPSCs following the differentiation protocol described by (Zhong et al., 2014). Mouse primary RPE cells were contact co-cultured with hiPSC-ROs with RO medium at different time points. Contact with RPE allowed accelerated PR differentiation in ROs. ROs older than 20 weeks were cut into 4 or 5 pieces of about 500 µm size prior to co-culture as the whole ROs started to die in 2D co-culture due to diffusion-limited delivery of exogenous factors (nutrients and oxygen) to the internal cells.	(Akhtar et al., 2019)
2D to 3D human retinal organoid differentiation	2020	hESCs and hiPSCs were differentiated into retinal organoids following the protocol described by (Kaewkhaw et al., 2015). hPSCs were firstly conditioned to form optic vesicles in 6-well plates. Adherent cells from 60-mm Petri dishes were scraped into small clumps (<5 mm^2). The resulting clumps were transferred to Petri dishes in free-floating culture with retinal inducing medium supplemented with IGF-1 and later with	(Regent et al., 2020)

		retinoic acid. Emerging optic vesicles in a free-floating condition allowed the formation of retinal organoids between day 20 and day 30.	
Light-sensitive human retinal organoids from hiPSCs	2020	Multi-layered and light-responsive 3D retinal organoids were obtained from patient hiPSCs. They displayed three nuclear and two synaptic layers, and PRs responded to light and transmitted visual information synaptically. Single-cell transcriptomes were obtained from dissociated ROs to build a comparative cell-type atlas of human ROs and healthy human retinas, allowing the identification of cellular targets for studying disease mechanisms (Cowan et al., 2020).	(Cowan et al., 2020)
Photoreceptor outer segment development in hiPSC-derived retinal organoids	2022	Retinal organoids derived from mESCs and X-linked retinitis pigmentosa type 3 patient hiPSCs were generated using an improved protocol that includes bovine serum albumin (BSA)-bound fatty acids and antioxidants. These antioxidants included vitamin E, vitamin E acetate, superoxide dismutase, catalase and glutathione antioxidants, and docosahexaenoic acid for fatty acids as part of the antioxidant-rich medium and retinal maturation medium. Outer segment-like structure formation for rod and cone PRs, including organised stacked discs, was improved for better retinal disease modelling (West et al., 2022).	(West et al., 2022)

1.4.4.1 The developmental rate in retinal organoids vs the human retina

The developmental rate of a RO *in vitro* differs from that of the human retina *in vivo*. Therefore, a thorough characterisation of the development of all retinal cell lineages in ROs would require the analysis of at least three time points corresponding to early, mid-, and late-stage retinogenesis. An early phase of day 35 of differentiation in ROs corresponds to the developmental time point of an FW10 retina (Kim et al., 2019). Development of human ROs during 30-70 days of culture *in vitro* is equivalent to embryonal development at 8-14 weeks (Li et al., 2021). Cell-type specific markers, including CRX, VSX2 and SNCG, are detectable at this early stage of development in both ROs and foetal retina. The expression of these markers exhibits the consolidation of post-mitotic PR precursors, RPCs and RGCs, respectively (Gonzalez-Cordero et al., 2017, Mellough et al., 2015, Singh et al., 2015, O'Hara-Wright and Gonzalez-Cordero, 2020).

A recommended second time point for characterising ROs would be at day 90 of differentiation as it corresponds to a mid-stage retinogenesis of PCW14 onwards, as estimated in a scRNA-seq study (Cowan et al., 2020) where bulk transcriptomes of human ROs and retina were crossed-correlated. At this phase, ROs exhibit expression of NRL, PROX1, AP2α, RXRγ, VSX2, SNCG, PKCα, VIMENTIN, and PR markers RCVRN and ARR3. These markers are expressed in a laminar manner, indicating that retinal differentiation in the ROs mimics embryonic retinogenesis (Kim et al., 2019).

The late-phase retinogenesis stage of the day 150 of organoid differentiation corresponds to a time point around PCW17-19, as observed in the same scRNA-seq study (Cowan et al., 2020). At this stage, several markers of mature PRs, including NRL, RHO, OPN1SW, OPN1LW/MW, RCVRN, and ARR3, are expressed alongside PROX1, AP2α, RXRγ, VSX2, SNCG, PKCα, and VIMENTIN markers observed at earlier stages.

However, transcriptome analyses have shown a progressive maturation of retinal cells in ROs, reaching a stable state between weeks 30 and 38. These transcriptomic changes during RO maturation are reported to be similar to the developing human retina *in vivo* (Cowan et al., 2020). Similarly, in their bulk RNA-

sequencing profiling study (Kim et al., 2019), Kim and colleagues found that 6.5 and 9-month-old ROs were increasingly similar to human adult retinas. Also, as the retinal development is recapitulated more precisely at this mature stage by the ROs, outer segment-like structures are reported to form and grow to 39 µm terminal length (Wahlin et al., 2017).

1.4.5 RPE differentiation

The differentiation potential of hESCs and hiPSCs is not limited to retinal cell types, as other human eye cells, such as RPE cells, can be generated. As some inherited retinal diseases affect the retina and the RPE, studying their common pathological mechanisms is vital. The clinical translation of hESC and hiPSC technologies for disease modelling of the RPE promises to accelerate novel treatments and delivery methods. To this end, the early stages of pluripotent stem cell (PSC)-derived RPE cells for use in clinical trials relied on spontaneous differentiation (Klimanskaya et al., 2004, Lund et al., 2006, Buchholz et al., 2009). Then, further research was conducted by performing directed RPE differentiation from hESCs and hiPSCs, including factors such as Wnt inhibitors (Dkk-1 and bFGF) and Nodal signalling inhibitors (Lefty-A) (Lund et al., 2006, Osakada et al., 2008). Directing PSC towards a range of retinal fates is possible by inhibiting WNT and Nodal signalling pathways. New protocols added Activin A (Hirami et al., 2009, Ferrer et al., 2014), nicotinamide, TGFB1, fibroblast growth factor 2 (FGF2), triiodothyronine, hydrocortisone, taurine, B27 supplement (Hazim et al., 2017), Purmorphamine (Hallam et al., 2017), SB431542, noggin, and CHIR990021 (Buskin et al., 2018, Regent et al., 2019), among other formulations (Limnios et al., 2021). A summary of different methods of RPE differentiation from hESCs and hiPSCs is described in **Table 1-3**.

Table 1-3. RPE differentiation methods from ESCs and iPSCs

Method	Year	Description	Reference
Spontaneous RPE differentiation from hESCs	2004	hESCs were spontaneously differentiated into polygonal-shaped cells surrounded by neuronal cells after 2-3 weeks. Then, pigmented cells started to arise after 6-8 weeks. Over 6-9 months, all cells became pigmented. RPE-specific protein expression profile correlates with previously described ones in primary RPE cultures	(Klimanskaya et al., 2004)
Spontaneous hESC-RPE differentiation	2006	Reproducible RPE monolayer batches were spontaneously generated from hESCs. The medium was supplemented with bFGF and human LIF. Pigmentation was observed after 6-8 weeks of differentiation. Cells show a molecular profile more closely resembling native foetal RPE.	(Lund et al., 2006)
Directed RPE differentiation from monkey and human ESCs	2008	Monkey and human ESCs were differentiated into RPE monolayers in a feeder-free system. Dkk-1 (Wnt antagonist) and Lefty-A (nodal antagonist) were added to promote the differentiation of retinal progenitors from mESCs. By day 40 of differentiation, pigmented cells with polygonal morphology could be observed, and by day 90, they expressed the RPE65 marker of maturation. Pigmentation and maturation continued up to day 200.	(Osakada et al., 2008)
Spontaneous RPE differentiation from hiPSCs	2009	RPE monolayers were obtained by spontaneous differentiation from hiPSC and reprogrammed using the Thomson factors (Oct4, Sox2, Nanog, and Lin28). Pigmentation was observed 20-35 days after removing the basic fibroblast growth factor (bFGF). Cultures were large enough for mechanical dissection and replating after 60-90 days. The hiPSC-RPE cells were quantitatively and functionally similar to foetal RPE and hESC-RPE cells.	(Buchholz et al., 2009)
RPE differentiation from mouse and human iPSCs	2009	Reprogrammed mouse and human iPSCs with Yamanaka factors (Oct3/4, Sox2, Klf4, c-Myc) were differentiated into RPE monolayers. Recombinant Dkk-1 and recombinant Lefty A were added to the medium during the suspension culture. Activin A was later added on day 5. RPE mature cells were obtained after 80-120 days.	(Hirami et al., 2009)
hiPSC-RPE differentiation	2014	RPE differentiation from hiPSCs was induced by supplementing the medium with Noggin and SB431542 for 3 days. Then, by day 5, nicotinamide and activin A were added to the differentiation medium. Pigmented cells with cobblestone morphology started to arise at an early stage (days 25-35). RPE colonies were picked and transferred to 24-well plates with an RPE medium enriched with taurine, hydrocortisone, and triiodothyronine.	(Ferrer et al., 2014)
RPE differentiation from integration-free hiPSCs	2017	Human dermal fibroblasts were reprogrammed with nonintegrative RNA to iPSC and then differentiated into RPE cells. The differentiation medium sequentially included nicotinamide, activin A, TGFB1, and fibroblast growth factor 2. The pigmented regions in the EBs were separated by scalpel dissection and plated in an RPE medium. Further supplementation to the medium included triiodothyronine, hydrocortisone, taurine, and B27. Cells were mature after 2-3 months in culture. The hiPSC-RPE cells exhibited key features of native RPE.	(Hazim et al., 2017)

hiPSC-RPE differentiation from AMD patients	2017	RPE cells were differentiated from AMD-patient hiPSC lines following a feeder-free protocol. Once hiPSC were confluent, mTeSR1 medium was switched to RPE differentiation medium (Advanced RPMI, B27 supplement), and Purmorphamine was added from day 16 until day 21. Media changes were performed twice weekly during the next 3-4 months until cell maturation.	(Hallam et al., 2017)
hiPSC-RPE differentiation from RP patients	2019	RPE monolayers were differentiated from RP-patient hiPSC lines following a sequential combination of SB431542 (days 0-5), noggin (days 5-9), Activin A (days 10-15), and CHIR990021 (days 16-21). RPE cells were mature after 21 weeks.	(Buskin et al., 2018)
Large-scale production of hPSC-RPE cells	2019	Directed differentiation of RPE monolayers from hPSCs was achieved following a protocol combining nicotinamide, activin A and CHIR99021 sequentially. RPE cells mature after 8-12 weeks. High cell purity and functionality are maintained for large batch production.	(Regent et al., 2019)
Small molecule screening for optimised hESC-derived RPE differentiation	2021	Small molecules were added in a feeder-free system to efficiently produce hESC-derived RPE cells in 14 days, followed by cell function maturation. Their high-efficiency model aims to mimic key RPE developmental pathways. First, SB43218, LDN193189, CKI-7 and nicotinamide were used for RPE differentiation induction by inhibiting TGFβ and WNT signalling. Then, the medium was supplemented with IDE-1/2 for Activin activation and CHIR99021 for the WNT signalling pathways.	(Limnios et al., 2021)

1.5 Retinal disease modelling

The development of the human retina is a complex process that involves generating multiple cell types of neurons from RPCs in a spatiotemporal-specific fashion (Mao et al., 2019). Both hESCs and hiPSCs are fundamental tools due to their utility for generating ROs that allow the modelling of retinal diseases such as AMD (Yang et al., 2014), STGD1 (Khan et al., 2020), Rb (Liu et al., 2020), RP (Buskin et al., 2018), and glaucoma (Teotia et al., 2017) for developing therapeutic strategies. 3D cultures of organoids are critical strategies for organogenesis and optic cup formation research (**Figure 1-15**), which is not possible otherwise due to the lack of very early human retinal samples.

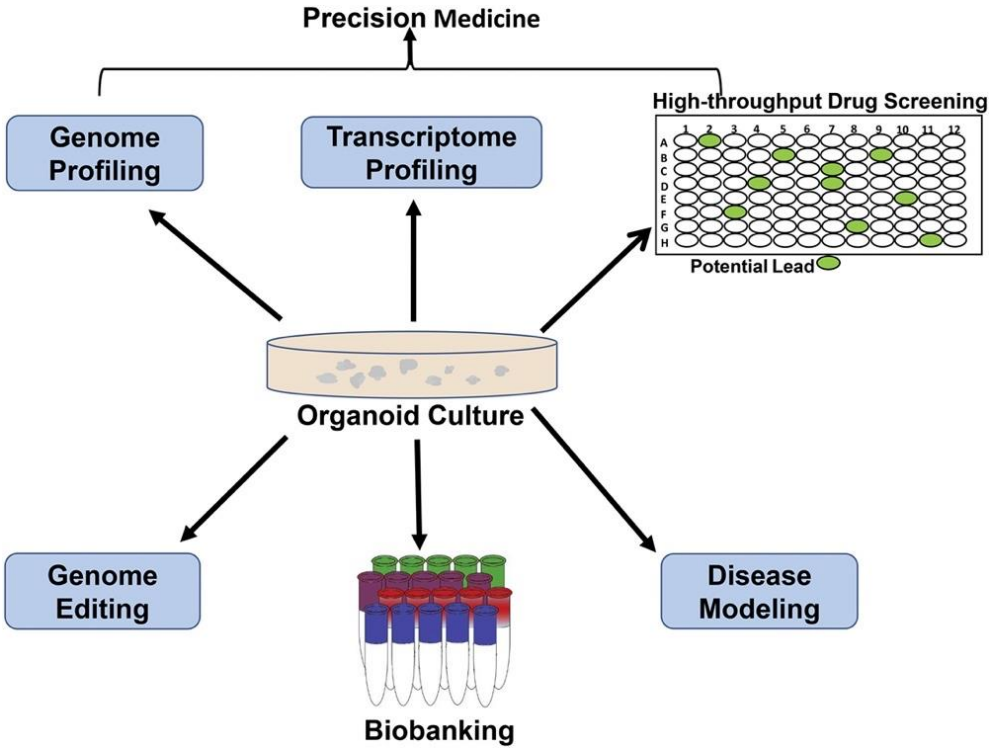

Figure 1-15. Drug screening and other applications of organoid cultures.
Schematic showing the generation of organoid cultures that could be used for multiple applications, including precision medicine, genome editing, biobanking, and disease modelling. In precision medicine, organoids could be helpful for genome and transcriptome profiling and high-throughput drug screening in 96-well plates. Drug screening assesses large compound libraries for activity against biological targets. Reproduced from (Praharaj et al., 2018). CC BY-NC.

Glaucoma is one of the retinal degenerative diseases that can be modelled *in vitro* by differentiating hiPSCs directly into retinal neurons. The disease is characterised by progressive RGC degeneration that leads to irreversible vision loss. To this end, as RGCs are intrinsically vulnerable to glaucoma, in a research study (Teotia et al., 2017) using an *in vitro* model, the authors efficiently generated functional RGCs from patient hiPSCs carrying glaucoma by the *SIX6* risk allele. Their results showed a significant decrease in RGC genesis and repressed developmental expression of RGC regulatory genes. These RGCs were characterised by simple and short neurites, reduced expression of guidance molecules, immature electrophysiological signature, and expression of glaucoma-associated genes *CDKN2A* and *CDKN2B*. This disease modelling study revealed the relevance of SIX6 in RGC differentiation and its risk allele that may lead to cellular and molecular abnormalities that make RGCs vulnerable to glaucoma.

Autosomal dominant RP is linked to 31 genes representing 20-25% of overall cases (Hamel, 2006). Pre-mRNA Processing Factors (PRPFs) are among those disease genes implicated in autosomal dominant RP. These PRPF genes include PRPF3, PRPF4, PRPF6, PRPF8, PRPF31, SNRNP200 and RP9, which are involved in the formation and maturation of the spliceosome (Růžičková and Staněk, 2017). Since the retina is one of the highest metabolically active tissues in the body, the burden posed on the local splicing machinery is significant (Yang et al., 2021a). Hence, the retina is at higher risk of mis-splicing events causing differential gene expression and protein dysfunction. To this end, PRPF-disease models have been developed to explore the pathogenesis of autosomal dominant RP caused by the *PRPF31* (RP11) gene. Work from our group (Buskin et al., 2018) generated RP11 hiPSC-ROs from patients with severe RP. The PRs of the ROs displayed an affected morphology with a 150% increase of apoptotic nuclei compared to controls and the presence of stress vacuoles typical of adaptive survival. Moreover, there was a reduced RGC spiking rate in response to the neurotransmitter GABA on multi-electrode arrays. Interestingly, there were splicing defects where the most affected genes were related to pre-mRNA and alternative mRNA splicing (Buskin et al., 2018). This study from our group was the first of its kind to model RP11 with patient hiPSC-derived retinal cells, which provided novel molecular and developmental insights confirming that RPE cells are the primary cells affected.

Disease modelling for Stargardt Disease (STGD1) has been achieved in a recent study (Khan et al., 2020), where patient-specific hiPSCs were differentiated into ROs holding the pathogenic variants that reside within the introns of the *ABCA4* gene, where the biallelic mutations cause the disease. The affected gene encodes the ATP-binding cassette, subfamily A, member 4 transporter protein. In this model, the authors rescued the splicing defects by administrating antisense oligonucleotides designed to block the pseudo-exon insertion. In a second study (Su et al., 2021), STGD1 ROs were generated from hiPSCs from four patients affected by STGD1. One patient was homozygous for the p.Gly1961Glu variant, two were compound heterozygous, and the last one had two deleterious *ABCA4* alleles. Results for this RO disease model allowed the characterisation of the pathophysiological features of *ABCA4* mutations in patients, showing short and nascent outer segments along the outer edge of PRs, which was not observed in control ROs. The development of this STGD1 RO model allowed to characterise the physiological consequences of *ABCA4* mutations in individual patients, particularly the shorter outer segments.

Disease modelling for Rb has benefited from 3D RO cultures as work from our group (Rozanska et al., 2022) and others have been recently published. The first study by (Zheng et al., 2020) showed that pRB loss promoted cell cycle entry in RB1-null hESC-derived ROs. Additionally, the authors reported fewer viable PRs and decreased fractions of BCs and RGCs. Tumourigenesis was not observed *in vitro* or *in vivo* in immunocompromised mice. Interestingly, in a subsequent study (Liu et al., 2020), tumourigenesis was reported *in vitro* in RB1-null hESC-derived ROs similar to characteristic *in vivo* Rb features, namely transcriptome and genome-wide methylation and upregulation of the SYK pathway. Maturing cone precursor ($ARR3^{+}$) cells were described as the cell of origin of Rb.

Interestingly, (Norrie et al., 2021) showed *in vitro* tumourigenesis by deriving ROs from patient $RB1^{-/-}$ hiPSCs and maturing them to 45 days of differentiation. Then, once the ROs were dissociated, they were injected intravitreally into immunocompromised mice, which developed retinal tumours. *MYCN* and *MDM4* were reported to be amplified as well. Moreover, the authors proposed an RPC or rod cell of origin identity for human Rb, which is in opposition to scRNA-seq studies from our group (Collin et al., 2021, Rozanska et al., 2022) and others (Liu et al.,

2020, Kanber et al., 2022, Li et al., 2022, Yang et al., 2021b, Wu et al., 2022) suggesting an Rb cell of origin stemming from a maturing cone precursor.

In our recent publication (Rozanska et al., 2022), we developed an Rb disease model using pRB-depleted ROs derived from hESCs and patient hiPSCs. We established a disease model that outlines Rb's genetic and tumourigenic components and can be used as a robust Rb chemotherapeutic drug screening platform. Our results showed a significant increase in the fraction of proliferating cone precursors ($RXR\gamma^{+}Ki67^{+}$) in the homozygous mutant ROs for *RB1*, in addition to starting cone precursors expressing RGC and HC markers. Further examples of studies modelling Rb using retinal organoids are discussed in the following chapters of this document.

RPE cells derived from PSCs are a promising therapy for treating some retinal degenerative diseases such as AMD, RP and STGD1. Some disease modelling studies using RPE cells derived from patient hiPSCs are discussed below.

In an AMD study (Yang et al., 2014), the disease was modelled with AMD-RPE cultures derived from early-stage AMD patient hiPSCs. To mimic RPE cell senescence, the authors allowed the accumulation of a pyridinium bisretinoid, A2E fluorophore, which is one of the lipofuscin fluorophores that accumulate with age in the RPE. As A2E generates oxidative stress by the light-mediated formation of singlet oxygen and superoxide, it contributes to RPE ageing processes. The antioxidant defence ability was tested by the activity of the mitochondrial SOD2, which is responsible for oxidative stress protection. Since SOD2 was identified as one of the downstream targets of the pathology, its decreased activity due to ARMS2/HTRA1 risk alleles was correlated to diminished antioxidant capacity in the AMD-RPE. These results revealed a potential therapeutic strategy by enhancing SOD2 activity in the development of AMD pathogenesis, where the RPE is more susceptible to oxidative damage. In a different study (Juuti-Uusitalo et al., 2015), mature hESC-RPE cells were obtained and exposed to inflammatory cytokines (IFN-γ or TNF-α) for 24 hours or oxidative stress (hydrogen peroxide, H_2O_2) for 1 hour. The results showed that cytokines induced matrix metalloproteinases (MMPs) MMP-1 and MMP-2 gene and protein expression, while H_2O_2 induced MMP-3 and MMP-9

gene expression but no protein secretion. Mature hESC-RPE cells resemble their native counterpart in the human eye regarding MMP secretion.

Our group (Buskin et al., 2018) also developed RP11-RPE derived from severe RP patient hiPSCs. This model showed the most significant disease phenotype, revealing that these cells are the most affected by *PRPF31*-mediated disease. Likewise, splicing defects were reported in RP11-RPE as they exhibited the most significant differential exon usage with many transcripts retaining introns and using alternative 3' splice sites. In fact, in another study (Georgiou et al., 2022) from our group, the impacts of *PRPF31* mutations in RP11-ROs and RP11-RPE cells were assessed by quantitative proteomics analyses. The results showed alterations in RNA splicing, autophagy, lysosome, unfolded protein response and visual cycle-related pathways. In addition, the RP11-RPE cells were characterised by large amounts of cytoplasmic aggregates containing the mutant PRPF31 and ubiquitin-conjugated proteins, including key visual cycle and other RP-linked tri-snRNP proteins. Finally, the impaired waste disposal mechanisms enhanced aggregate accumulation, which could be a therapeutic target through autophagy pathway activation using drugs such as rapamycin to reduce cytoplasmic aggregates.

Finally, in a study by (Hu et al., 2020), recessive Stargardt patient hiPSCs were differentiated into RPE, focusing on the role of the complement system in disease pathogenesis. The results showed a disruption of the cellular membrane, elevated C3/C3b/iC3b component and MAC deposition, and age-dependent cell loss in STGD1 hiPSC-RPE cells. The conclusion points to a common inflammatory aetiology of AMD and STGD1 pathologies.

1.6 Chemotherapeutic agents used for the treatment of retinoblastoma

The chemotherapy treatments available to date are (Yanık et al., 2015): **1) systemic**, which comprises drug injection (melphalan, topotecan, vincristine, etoposide, and carboplatin) into a vein or oral intake to avoid complications related to development of secondary cancers and limited to treat seeds that exhibit massive infiltration, showing a small response to chemotherapy due to difficulty in penetration of delivered drugs; **2) intravitreal**, which involves direct injection [usually melphalan and/or topotecan every 7-21 days depending on response and toxicity (Schaiquevich et al., 2022)] into the vitreous humour to increase availability of drugs in-site and

exhibits striking control of vitreous seeds, achieving the highest concentration of the delivered drug in the confined intraocular space; **3) intraarterial**, which encompasses an injection (usually melphalan, but also combined topotecan and carboplatin) into the ophthalmic artery with the advantage that this approach can impede the development of new tumours in patients with genetic Rb; **4) periocular**, which is an injection, commonly carboplatin, that allows a higher local concentration of the drugs, as the route of delivery has varied as either subconjunctival or subtenon's space location, circumventing the blood-retinal barrier.

Vitreous seeding is a significant problem in Rb treatment since the vitreous is an avascular tissue, which means that the transition of chemotherapy drugs via intraarterial administration is limited (Winter et al., 2019). If vitreous seeding is recurrent, it may lead to enucleation of the affected eye (Süsskind et al., 2016). There has been a shift in Rb treatment over the last decade from systemic chemotherapy infusion to intravitreal injection due to the low bioavailability of drugs in retinal tissue and adverse toxic effects (Winter et al., 2019). The response of vitreous seeds to intravitreal injections has an efficacy of 85 to 100% (Schaiquevich et al., 2022).

Chemotherapy drugs extensively used alone or in combination based on the favourable ocular disposition to treat Rb with a variable degree of success include melphalan, topotecan, carboplatin and Bcl-2 inhibitors such as TW-37 (Saengwimol et al., 2018).

1.6.1 Carboplatin

Carboplatin is the most widely investigated Rb management drug, and it is reported to be less toxic than melphalan and topotecan. Its systemic treatment is associated with haematopoietic toxicity, nephrotoxicity and ototoxicity, while local treatment has been associated with ocular complications, including reduced motility and optic atrophy with ischemic necrosis (Sachdeva and O'Brien, 2012, Schaiquevich et al., 2022). It is administered via intraarterial and intravitreal injection with concentrations between 500-1666 μg/mL and 60-120 μg/mL, respectively (Süsskind et al., 2016).

1.6.2 Melphalan

Melphalan was first described in 1953 as the synthesis product of substituting L-phenylalanine for the methyl group on nitrogen mustard (Bayraktar et al., 2013). It is an alkylating agent that attaches to an alkyl group to guanine bases, forming DNA inter-strand crosslinks, leading to apoptosis as part of the mechanism of action and cytotoxicity (Vasquez, 2010, Mougenot et al., 2006). Due to its broad antitumour activity, melphalan has been used to treat a range of malignancies, including breast and ovarian cancer, lymphomas, neuroblastomas, acute leukaemias, and multiple myeloma (Sarosy et al., 1988, Bayraktar et al., 2013). It is the most common chemotherapy drug administered in intraarterial and intravitreal injections for recurrent vitreous seeds following treatment of Rb. It represents complex management that often might lead to enucleation (Shields et al., 2014). Moreover, some degree of visual acuity is retained or regained, allowing significant tumour reduction with salvage of the eye. Furthermore, solid tumours show excellent responses to systemic and intraarterial methods (Shields et al., 2014).

Melphalan is administered in concentrations between 3 to 7.5 mg/30 mL with a standard dosage of 5 mg/30 mL in intraarterial, whilst a concentration between 166-200 µg/mL (usually 20-30 µg/0.1 mL to minimise complications) for intravitreal injection performed every 7-10 days (Süsskind et al., 2016).

Unfortunately, it is associated with adverse effects such as chorioretinopathy, electroretinographic abnormalities, RPE alterations, and retinal vasculitis, among other complications in darkly pigmented iris (physical association to melanin), including pupillary synechiae, iris atrophy and cataracts (Paez-Escamilla et al., 2017, Xue et al., 2019). Moreover, reported retinal toxicity of intravitreal melphalan exhibits a 5 µV decrement of retinal function measured by electroretinogram for every 30 µg of the drug (Schaiquevich et al., 2022). Due to the melanin-binding capacity of this drug, it is uptaken and retained in the RPE, resulting in retinal toxicity.

1.6.3 Topotecan

Topotecan is an anticancer agent that targets the topoisomerase I enzyme involved in DNA replication, and that was developed as a semisynthetic version of camptothecin (Dennis et al., 1997). It entered clinical trials in 1989, and by 1996 it

was approved for use by the Food and Drug Administration (FDA) in patients with ovarian cancer previously treated (Takimoto and Arbuck, 1997). Its antitumour activity was reported in small-cell lung cancer, hematologic malignancies, paediatric neuroblastoma and rhabdomyosarcoma (Takimoto and Arbuck, 1997). Additionally, pharmacologic studies of topotecan combined with carboplatin, cisplatin, doxorubicin, and etoposide have been performed in adult and paediatric patients with solid tumours with primary antineoplastic responses observed but with exhibited toxicologic effects (Rowinsky and Kaufmann, 1997).

As a potent antineoplastic agent, it induces a p53 response in Rb cells (Laurie et al., 2006). Clinically, it is used to treat Rb in systemic and intravitreal chemotherapies and causes less cytotoxic effects, but it may also be less effective than melphalan for persistent vitreous seeds (Winter et al., 2019, Paez-Escamilla et al., 2017, Rao et al., 2018b). A concentration between 0.15 to 1.5 mg/30 mL is used for intraarterial, and 133 to 333 µg/mL for intravitreal use is given every three weeks (Süsskind et al., 2016). Typically, it is administered in combination with melphalan or carboplatin for better clinical efficacy, particularly for recurrent seeds that have been reported to achieve complete regression (Winter et al., 2019, Saengwimol et al., 2018). Nonetheless, the main drawback is its haematotoxicity associated with systemic delivery. In periocular injection, there is only minimal conjunctival congestion and eyelid chemosis (Rao et al., 2018b).

1.6.4 TW-37

TW-37 is a novel small molecule inhibitor of the Bcl-2 and Bcl-2 family (B-cell leukaemia anti-apoptotic proteins) that induces apoptosis in cells and effectively inhibits tumour growth, particularly in melanoma-derived tumours and a reduction in microvessel density in angiogenesis (Zeitlin et al., 2008). The Bcl-2 family proteins are crucial in balancing cell apoptosis regulation and proliferation (Lei et al., 2017). These proteins can be divided into two major categories: the anti-apoptosis proteins, Bcl-2, Bcl-xL, Bcl-w, and Mcl-1; and the pro-apoptotic proteins, Bim, Puma, Bid, Bad, Bax, Bak and others. The anti-apoptosis Bcl-2 proteins have four BH regions (BH1-BH4), while the pro-apoptosis Bcl-2 proteins only contain a BH3 region (Lei et al., 2017).

Since Stanley J. Korsmeyer first described the role of the Bcl-2 family of proteins regarding cell commitment to death through the mitochondrial apoptotic pathway a few decades ago, the Korsmeyer rheostat model has become widely accepted (Azmi et al., 2011). This model defined the balance between pro and anti-apoptotic Bcl-2 family proteins controlling the decision-making process and modulating cell sensitivity to death at the mitochondrion (Azmi et al., 2011). (Chao et al., 1995, Chao and Korsmeyer, 1998) reported that overexpression of Bcl-2, Mcl-1, BclXL and other members of the family of proteins contributes to the progression of cancer. Resistance to apoptosis is conferred by standard anticancer therapies, setting the urgent medical need to find and develop new therapies that inhibit the function of anti-apoptotic members (Azmi et al., 2011). Preclinical studies indicate that TW-37 reduces the tumour size in xenograft models and cell proliferation of pancreatic and B-cell lymphomas (Mohammad et al., 2007).

The expression of high levels of Bcl-2, Mcl-1, or Bcl-xL in tumours often makes them resistant to chemotherapeutic agents and radiotherapy as they are essential for tumour growth (Lei et al., 2017, Zeitlin et al., 2008). Therefore, the relevance of TW-37 as an inhibitor of the Bcl-2 and Bcl-2 family highlights its efficacy against chemotherapy-resistant tumours. Furthermore, TW-37 binds directly to the BH3 domain of the Bcl-2 protein family to shut down the heterodimerisation of pro-apoptotic proteins with Bcl-2 (Lei et al., 2017), then preventing cell apoptosis mechanisms. The most useful features shared by these Bcl-2 inhibitors are their low overall toxicity compared to conventional chemotherapeutic drugs and their synergising ability with other therapeutic agents to inhibit tumour cell survival (Zeitlin et al., 2008).

1.7 Drug discovery in retinoblastoma

Novel drugs and repurposed agents are needed to develop new drug treatments that are more effective and specific for Rb management. The availability of preclinical models is limited to mimicking the retinal response and clinical observations of chemotherapeutic treatments. Identifying deregulated pathways in specific tumours is crucial for designing targeted agents and repurposing drugs as an expedited and cheaper Rb drug discovery strategy. A comprehensive pharmacological characterisation is needed to select the most suitable candidates

for Rb treatment according to their selective tumour cytotoxicity (Schaiquevich et al., 2022). However, the antitumour activity of potential candidates should not be the main factor to prioritise. Several factors, including drug penetration across the ocular and brain barriers, the toxicity profile, and the availability of proper formulations, should also be considered for clinical utility (Cancela et al., 2021). To this end, large libraries of compounds should be tested using high-throughput screens of several cell lines for accounting for the diverse drug response observed in patients (Schaiquevich et al., 2022). Establishing and validating a 3D *in vitro* retinal model for Rb is an essential step in novel drug discovery, allowing for assessing drug response and cytotoxicity before translation to humans.

1.8 Aims of the study

This project is aimed to:

- ✓ Generate and characterise a disease model for Rb using PSC-derived retinal organoids. To this end, H9 and H9 RB1-null hESC- and patient hiPSC-derived ROs (isogenic control, heterozygous and homozygous *RB1* mutants) were established. The characterisation was assessed using immunofluorescence, flow cytometry and soft agar assays (**3 Generation and characterisation of hESC- and patient hiPSC-derived retinal organoids**).
- ✓ Validate the Rb retinal organoid models for drug testing studies. Three clinically used chemotherapeutic drugs (melphalan, topotecan and TW-37) were tested on both PSC-derived Rb-deficient models. Drug responses of the organoids were analysed for cytotoxicity, immunohistochemistry, apoptosis, and cell cycle assays (**4 Drug screening of hESC- and patient hiPSC-derived retinal organoids**).
- ✓ Investigate the impact of the three chemotherapeutic agents (melphalan, topotecan and TW-37) on hESC- and patient hiPSC-derived RPE cells. The characterisation was assessed by immunohistochemistry, apical-basal polarity and tight junction markers, and flow cytometric assays. Drug response analyses were determined by cytotoxicity, cell cycle and apoptosis assays, phagocytic capacity and transepithelial electrical resistance (**5 Generation, characterisation, and drug screening of hESC- and hiPSC-derived RPE**).

Chapter 2

2 Materials and methods

2.1 Cell culture

2.1.1 Cell lines

Two H9 hESC lines were used in this study, H9 control and H9 RB1-null. Collaboration with Prof. Nissim Benvenisty (Avior et al., 2017) allowed us to obtain the H9 RB1-null line in which both copies of *RB1* were inactivated by CRISPR/Cas9 gene editing. Three patient-specific hiPSC lines, including heterozygous (*RB1*$^{+/-}$), homozygous (*RB1*$^{-/-}$), and isogenic control (*RB1*$^{+/+}$), were derived in our lab using CRISPR/Cas9 gene editing as described in (Rozanska et al., 2022).

The total number of heterozygous (*RB1*$^{+/-}$) hiPSC-derived clones with c.2082delC that have been investigated for the project was 15. 3 clones (c3, c10 and c14) were selected for retinal organoid differentiation due to their low steady-state level of pRB confirmed by Western blots (data not shown; experiments performed by Dr Agata Rozanska). The structure of the retinal organoids generated from two of the hiPSC clones (c3 and c14) fell apart in the long term (day 150), which led to keep the optimal clone (c10). One isogenic (*RB1*$^{+/+}$) control [wild-type (WT) clone] and one homozygous (*RB1*$^{-/-}$) mutant (c61) clones were used for retinal organoid differentiation. All clones investigated for this project showed a stable karyotype and no genetic abnormalities, as documented in our publication (Rozanska et al., 2022).

2.1.2 Cell culture maintenance

The hESC and hiPSC lines were cultured with mTeSR™ Plus (100-0276 Stem Cell Technologies) on growth factor reduced Matrigel-coated 6-well plates (354230 Corning® Matrigel® Growth Factor Reduced Basement Membrane Matrix; Corning, NY). Cells were washed with DPBS 1X (14190136 Gibco®/Life Technologies/Life Technologies) and dissociated with Versene™ EDTA (15040066 Gibco®/Life Technologies/Life Technologies) and passaged at a 1:6 ratio twice per week.

2.1.3 Cell culture storage

All hESC and hiPSC lines were cryopreserved in Fisherbrand™ cryovials (11787939 ThermoFisher) in 10% DMSO in Foetal Bovine Serum (FBS) with 10 µM Rho-kinase inhibitor (ROCKi; Y-27632 dihydrochloride) in liquid nitrogen.

2.1.4 Mycoplasma detection

All human stem cell lines used for this project were tested for mycoplasma by the core staff of the Biosciences Institute at the Centre for Life as part of the mycoplasma detection service run by the Faculty of Medical Sciences of Newcastle University. The samples were tested using the MycoAlert® Mycoplasma Detection Kit (LT07-118 Lonza) based on the manufacturer's instructions. The assay performs two luminescence readings; the first (reading A) after adding 100 µl MycoAlert™ Reagent and the second (reading B) after adding 100 µl MycoAlert™ Substrate per sample. The ratio of reading B to reading A determines whether a cultured cell is contaminated by mycoplasma. A value of less than 0.9 is considered uninfected, while values greater than 1 are infected with mycoplasma. A MycoAlert™ Positive Control (LT07-518 Lonza) and MycoAlert™ Buffer (LT27-218 Lonza) were used as positive and negative controls, respectively, for every experiment. The luminescence was measured in a Varioskan™ LUX multimode microplate reader (Thermo Fisher Scientific). The tests were done twice per cell line before setting up a new differentiation, and the results for all five stem cell lines were negative. Afterwards, all samples were tested every 8 to 10 weeks.

2.2 Retinal organoids differentiation

Retinal organoids were generated using the protocol developed by (Hallam et al., 2018) by dissociating cells at ~80% confluence with Accutase (00-4555-56 Thermo Fisher Scientific, Waltham, MA) and seeding 7,000 cells into each well of a 96-well lipidure-coated U-bottom plate (AMS.LCP-A-U96 Amsbio, Boston, MA) in 100 µl of mTeSR™ Plus with 10 µM ROCK inhibitor (Y27632, Tocris, Bristol, UK). In total, 14 x 96-well plates were seeded per cell line.

After two days, mTeSR™ Plus + 10 µM ROCK inhibitor was changed to differentiation medium, which comprised: 41% IMDM (12440046 Iscove's Modified Dulbecco's Medium by Gibco®/Life Technologies/Life Technologies), 41% HAM's

F12 (1765054 Gibco®/Life Technologies/Life Technologies), 15% KOSR (A3181502 KnockOut™ Serum Replacement-Multi-Species, Gibco®/Life Technologies/Life Technologies), 1% GlutaMAX™ (35050038 Gibco®/Life Technologies/Life Technologies), 1% Chemically Defined Lipid Concentrate (11905031 Gibco®/Life Technologies/Life Technologies), 1% Pen/-Strep (15140122 Gibco®/Life Technologies/Life Technologies) and 10 µl 1-Thioglycerol (225 µM, M6145 Sigma-Aldrich-Aldrich).

The medium was half-replaced every two days up to day 6 when it was once supplemented with recombinant human BMP-4 (1.5 nM; PHC9534 Bone morphogenetic protein 4, Life Technologies) as described in (Hallam et al., 2018) and (Kuwahara et al., 2015), followed by half-replacements every three days. At day 18, maintenance medium was introduced [DMEM/F12 (11320033 Gibco®/Life Technologies/Life Technologies), 10% FBS (16141079 Gibco®/Life Technologies/Life Technologies), 1% GlutaMAX™, 1% N2 (17502001 Gibco®/Life Technologies/Life Technologies), 1% Pen/Strep, 0.1 mM Taurine (T8691 Sigma-Aldrich), 40 ng/ml T3 (T6397-100MG Sigma-Aldrich-Aldrich), 0.25 µg/ml Fungizone (15290026 Gibco®/Life Technologies/Life Technologies), and 0.5 µM Retinoic Acid (R2625 Sigma-Aldrich); the latter was added fresh up to day 120 of differentiation]. Media changes were performed three times per week.

2.3 RPE cell differentiation

Retinal pigment epithelium cells were generated according to an established differentiation protocol described in our group (Buskin et al., 2018). hESCs at ~80% confluence were washed with DPBS (14200166 Gibco) to switch mTeSR™ Plus medium to RPE differentiation medium [76.9% DMEM/F12 + GlutaMAX™, 20% KOSR, 50 µM β-mercaptoethanol (M3148 Sigma-Aldrich), 1% MEM NEAA (11140068 Gibco®/Life Technologies), 10 mM Nicotinamide (N0636 Sigma-Aldrich)] from day 0 to day 7. The second RPE medium [78.8% DMEM/F12 + GlutaMAX™, 20% KOSR, 50 µM β-mercaptoethanol, 1% MEM NEAA, 100 ng/ml Activin A (120-14E-250UG Preprotech)] was introduced from day 7 to day 14. Then, from day 14 to day 42, media was switched to a third medium formulation [78.8% DMEM/F12 + GlutaMAX™, 20% KOSR, 50 µM β-mercaptoethanol, 1% MEM NEAA, 3 µM CHIR99021 (SML1046 Sigma-Aldrich)]. The medium was changed every second

day by aspirating ¾ of the total volume. Finally, from day 42 formulation was changed to mature stage RPE medium [94% DMEM/F12 + GlutaMAX™, 4% KOSR, 50 µM β-mercaptoethanol, 1% MEM NEAA, 1% Pen/Strep]. The medium was changed twice weekly by aspirating ¾ of the total volume. Patient-specific hiPSC-derived RPE cells were obtained from hiPSC-derived retinal organoids that developed RPE spheroids. The organoids were cut into small pieces and seeded into Matrigel-coated 24-well plates (5 pieces per well). The medium was switched to B-27™ RPE medium [86% Advanced RPMI 1640 Medium (12633012 Gibco®/Life Technologies), 10% KOSR, 2% B-27™ Supplement (50X) (17504001 Gibco®/Life Technologies), 1% GlutaMAX™, 1% Pen/Strep]. The medium was changed twice per week by aspirating ¾ of the total volume. After two months, hiPSC-derived RPE cells were transferred into 96-well plates, and transwell inserts in 24-well plates (as described in the next section) with B-27™ RPE medium.

2.4 Transwell inserts seeding

RPE cells were washed with DPBS, dissociated with TrypLE™ Select Enzyme (10X) (A1217701 Gibco®/Life Technologies), and incubated for 20 minutes at 37ºC. Fresh mature stage RPE medium was added, and cells were passed through a 40 µm cell strainer (11587522 Fisher Scientific) centrifuged for 5 minutes at 300 Relative Centrifugal Force (RCF), the supernatant was aspirated, and the cell pellets were resuspended in fresh RPE media. Cell suspension concentration was adjusted, and 150,000 cells were seeded into each Matrigel-coated transwell insert in 24-well plates. Cells were left undisturbed for four days, and media changes were done twice per week.

2.5 Drug screening of retinal organoids and RPE cells

To assess the cytotoxic effect of chemotherapeutic drugs on hESC-, patient-specific hiPSC-derived retinal organoids, and RPE cells, three agents commonly used in intravitreal chemotherapy were added in different concentrations to the culture medium for 72 hours under 5% CO_2 in a 37°C humidified incubator. The three agents include melphalan (16665 Cayman Chemical; final concentration of 8 µM, 16 µM, 32 µM, 320 µM), topotecan (14129 Cayman Chemical, final concentration of 5 µM, 10 µM, 15 µM, 150 µM) and TW-37 (20999 Cayman Chemical; final concentration 0.1 µM, 0.5 µM, 1 µM, 10 µM). Vehicle control

consisted of 0.1% DMSO (C6164 Sigma-Aldrich). After the incubation period, retinal organoids, the RPE cells, and the supernatants were collected for further processing, including cytotoxicity, cryosectioning, immunostaining assays, and flow cytometry for apoptosis, cell cycle and phagocytosis assays.

2.6 Cryosectioning and immunostaining of organoids

Organoids were collected on days 35, 90, and 150, washed with PBS, and then fixed in 2% paraformaldehyde in PBS (sc-281692 Santa Cruz Biotechnology) solution for 15 minutes**.** They were washed for 10 minutes with PBS three times before being placed in a 30% sucrose in PBS (S0389 Sigma-Aldrich) overnight. Organoids were placed into cryogenic embedding moulds (18985-1 Tebu-Bio UK) and immersed in optimum cutting temperature compound (6478.1 OCT Embedding Matrix, CellPath Carl ROTH®). 10 µm slices were sectioned on a Leica cryostat (CM1850) and mounted onto slides (10149870 Fisher Scientific).

Cut sections were washed with PBS for 10 minutes three times. Then, slides were blocked in 0.3% Triton-X-100 (93443 Sigma-Aldrich) and 10% normal goat serum (S-26 Sigma-Aldrich) in PBS for 1 hour. This solution was replaced with an antibody diluent (0.3% Triton-X-100, 1% normal goat serum in PBS) with appropriate antibody dilution (**Table 2-1**) at 4ºC overnight. Sections were washed in PBS for 10 minutes each and incubated with secondary antibodies (**Table 2-2**) for 1 hour at room temperature. Sections were rewashed as stated previously with two additional washes in PBS for 3 minutes each and mounted in Vectashield® (H-1000-10 Vector Labs, Burlingame, CA) with Hoechst (1:1000 dilution, 33342 Thermo Scientific). Five images per antibody combination for each cell line were captured using Zeiss Axio ImagerZ2 equipped with an Apotome2 (Zeiss, Germany).

Table 2-1. Primary antibody list.

Antibody	Species	Company	Cat. No	Concentration
Ap2α	Mouse	Santa Cruz Biotechnology	SC-12726	1 in 200
ARR3	Rabbit	Novus Biologicals	NBP2-41249	1 in 100
CASP3	Rabbit	Cell Signaling	9661S	1 in 400
Collagen IV	Rabbit	Abcam	AB6586	1 in 200
CRX	Mouse	Abnova	H00001406-M02	1 in 200
Ezrin	Mouse	Sigma-Aldrich-Aldrich	E8897-100UL	1 in 100
Ki67	Mouse	BD Pharmingen	550609	1 in 50
Ki67	Rabbit	Abcam	AB15580	1 in 200

NRL (F2)	Mouse	Santa Cruz Biotechnology	SC-374277	1 in 100
OPN 1LW/MW	Rabbit	Millipore	AB5405	1 in 200
OPN1SW	Rabbit	Millipore	AB5407	1 in 200
PKC-α	Rabbit	Sigma-Aldrich-Aldrich	SAB4502354	1 in 50
PROX1	Rabbit	Millipore	AB5475	1 in 1500
RB1	Mouse	BD Pharmingen	554136	1 in 400
Recoverin	Rabbit	Millipore	AB5585	1 in 1000
RHO	Rabbit	Abcam	AB59260	1 in 100
RHO (Clone ID4)	Mouse	Millipore	MAB5356	1 in 200
RXRγ	Rabbit	Santa Cruz Biotechnology	SC-555	1 in 500
RXRγ	Mouse	Santa Cruz Biotechnology	sc-365252	1 in 50
SNCG	Mouse	Abnova	H00006623-M01A	1 in 500
SNCG	Rabbit	Abcam	AB55424	1 in 200
Vimentin	Rabbit	Abcam	AB92547	1 in 400
VSX2	Rabbit	Sigma-Aldrich Atlas	HPA003436	1 in 50
ZO1	Goat	St. John's Laboratory Ltd	STJ140055	1 in 50

Table 2-2. Secondary antibody list.

Host	Against	Conjugate	Isotype	Company	Catalogue number
Goat	Mouse	Alexa Fluor 488	IgG	Jackson Immuno Research	115-545-146-JIR
Goat	Mouse	Cy3	IgG	Jackson Immuno Research	115-165-003-JIR
Goat	Rabbit	Alexa Fluor 488	IgG	Jackson Immuno Research	111-545-003-JIR
Goat	Rabbit	Cy3	IgG	Jackson Immuno Research	111-165-003-JIR
Rabbit	Goat	Alexa Fluor 488	IgG	Life Technologies	A11078
Rabbit	Goat	Cy3	IgG	Jackson Immuno Research	305-165-003
Donkey	Rabbit	Alexa Fluor 546	IgG	Invitrogen	A10040
Donkey	Goat	Alexa Fluor 488	IgG	Invitrogen	A32814
Donkey	Mouse	Alexa Fluor 488	IgG	Invitrogen	A21202

2.7 Immunostaining of RPE cells

The transwell inserts of vehicle- and drug-treated RPE cells were briefly washed with PBS and fixed in 4% paraformaldehyde for 30 minutes. After the removal of the fixative, three subsequent washes with PBS were performed. The transwell membrane with RPE cells was removed from the insert and sliced into small v-shaped slices. Additional steps were completed when performing ZO-1 and

Collagen IV immunostaining. The first one is an incubation of the RPE sections at -20°C for 4 minutes in methanol. The second one is removing melanin pigment in cells with a melanin bleach pre-treatment kit (24883 Polysciences) by incubating the sections in melanin bleach pre-treatment solution A for 5 minutes, three subsequent washes with PBS, and incubation with melanin bleach pre-treatment solution B for 1 minute and three washes with PBS. Then, sections were blocked and permeabilised for 1 hour in 0.3% Triton-X-100 and 10% Donkey Serum (7332100-LAM-500ml Stratech) in PBS. The blocking solution was removed, and the primary antibody was applied at concentrations shown in **Table 2-1** in 0.1% Triton-X-100 and 1% Donkey Serum in PBS. Sections were washed three times with PBS after overnight incubation at 4°C and incubated with secondary antibodies (**Table 2-2**) in PBS for 1 hour at room temperature (RT). Sections were rewashed three times and incubated with 1:1000 Hoechst in PBS for 20 minutes. Sections were washed again and mounted in Vectashield®. Fluorescent images of the RPE sections were taken using Zeiss Axio ImagerZ2 equipped with an Apotome2 (Zeiss, Germany). Secondary antibody controls were performed similarly, with the primary antibody step omitted. Qualitative analysis of immunostained sections was carried out using ZEN (Blue edition; ZEISS) in at least three immunostained sections of RPE cells of each biological replicate.

2.8 Quantification analysis

All quantitative analyses of immunostained sections were carried out using ZEN® (blue edition; ZEISS) and MATLAB® (MathWorks®) software to measure marker-positive areas from the list (**Table 2-1**) as described by (Dorgau et al., 2019). All positive cells were counted using the same thresholding in five randomly selected fields (318.2 µm×318.2 µm each) in immunostained slices per cell line-derived organoid. Five to ten images were obtained from six different sections per sample. Then, the percentage of marker-positive cells was calculated by obtaining the ratio of positive cells with the total Hoechst$^+$ cells in the area. Co-localisation with the Ki67 proliferation marker, the rate of marker-positive cells, was calculated out of the whole Ki67$^+$ cells using MATLAB® software.

2.9 Lactate dehydrogenase (LDH) cytotoxicity assay

To assess the cytotoxicity of the three chemotherapeutic agents (melphalan, topotecan, and TW-37), 90- & 150-day-old hESC-, patient hiPSC-derived ROs and RPE cells in 96-well plates were incubated for 72 hours under 5% of CO_2 in a 37°C humidified incubator as described before. To perform this assay, samples were prepared as follows:

- **Spontaneous LDH Activity**: 20 µl of sterile, ultrapure water was added to one set of triplicate wells of cells.
- **Maximum LDH Activity**: 20 µl of Triton-X-100 was added to one set of triplicate wells of cells. Each well was mixed by gentle tapping. The obtained value is the total (100%) corresponding to a completely disrupted cell sample for the cytotoxicity calculation.
- **Chemical-treated LDH Activity**: 1 row (12 wells) of cells was used per drug treatment (8 µM, 16 µM, 32 µM, and 320 µM melphalan; 5 µM, 10 µM, 15 µM, and 150 µM topotecan; 0.1 µM, 0.5 µM, 1 µM, and 10 µM TW-37) and for 1 vehicle control (0.1% DMSO). The supernatant was transferred from this pool of ROs or RPE cells for a set of triplicate wells into a 96-well flat-bottom plate.

CyQUANT™ LDH Cytotoxicity Assay Kit (C20300 Invitrogen) was used to assess the cytotoxicity of the chemical-treated, Spontaneous, and Maximum LDH Activity organoids and RPE cells. 50 µl of Reaction Mixture (prepared according to the protocol of CyQUANT™ Kit) were added to each sample well and mixed. The plate was incubated at RT for 30 minutes and protected from light. Then, 50 µl of Stop Solution was added to each sample well and mixed by gentle tapping to avoid creating bubbles that could prevent accurate absorbance readings. If any, bubbles in wells were broken with a syringe needle before reading. The absorbance was measured at 490 and 680 nm in a Varioskan™ LUX multimode microplate reader (Thermo Fisher Scientific). To determine LDH activity, the 680-nm absorbance value (background) was subtracted from the 490-nm absorbance value before calculating the percentage of Cytotoxicity (%), which was calculated using the following formula:

$$\% \text{ Cytotoxicity} = \left[\frac{\text{Compound treated LDH Activity-Spontaneous LDH Activity}}{\text{Maximum LDH Activity-Spontaneous LDH Activity}}\right] \times 100$$

2.10 Retinal organoid dissociation

After 72 hours of incubation with the three chemotherapeutic agents, hESC- and hiPSC-derived 90- & 150-day-old organoids were dissociated using MACS Neurosphere Dissociation Kit (P) (130-095-943 Miltenyi Biotec GmbH) following the manufacturer's protocol. Firstly, organoids were collected in 15 ml Falcon tubes, the medium was removed, and 500 µl of enzyme mix (stock solution: 3.84 ml pre-heated Buffer X; 40 µl Buffer Y; 100 µl Enzyme P; 20 µl Enzyme A) was added per sample. Tubes were incubated for 10 minutes at 37°C. After incubation, organoids were mechanically dissociated using fire-polished glass Pasteur pipettes of decreasing diameter by pipetting up and down 10-15 times slowly to avoid forming air bubbles. Samples were incubated again at 37°C for 5 minutes. Organoids were mechanically dissociated for a second time using the glass Pasteur pipettes. Single-cell suspension was applied to a 40 µm Pre-Separation Filter (CC8111-0042 Starlabs) placed on a 50 ml Falcon tube, followed by 5 ml of HBSS (14175053 Life Technologies). The cell suspension was centrifuged at 300×g for 10 minutes at RT. Following the supernatant removal, cells were resuspended in a 1 ml maintenance medium and processed immediately for further applications, including determining the cell number.

2.11 Soft agar colony formation assay

Retinal organoids at days 90 and 150 of differentiation were dissociated, as described above. Single-cell suspensions in organoids' maintenance medium with 0.48% LB-agar (22700-025 Invitrogen) were added to 12-well plates precoated with 0.5% LB-agar in maintenance medium at a concentration of 1000/well. Cells were maintained in a 37°C humidified incubator with 5% CO_2 for 80 days. Colony images were taken at RT using a bright-field microscope (Zeiss AxioVert1).

2.12 Cell-cycle phase distribution and apoptosis analyses

As described before, after 72 hours of incubation, vehicle control, drug-treated retinal organoids, and RPE cells were dissociated into single cells. The cell-cycle assay was performed with the BD Cycletest™ Plus DNA Reagent Kit (340242 BD Biosciences). This reagent kit involves dissolving the cell membrane lipids with a non-ionic detergent, eliminating the cell cytoskeleton and nuclear proteins with trypsin (solution A), digesting the cellular RNA with an enzyme, and stabilising the

nuclear chromatin with spermine (solution B). Then, propidium iodide (solution C) is stoichiometrically bound to the clean, isolated nuclei, which are then run on a flow cytometer equipped with electronic doublet-discrimination capability. In contrast, the apoptosis assay was performed with the BD PE Annexin V Apoptosis Detection Kit I (559763 BD Biosciences), following the protocol provided with the kits. The method of the BD PE Annexin V Apoptosis Detection Kit I precedes the loss of the cell membrane integrity, which accompanies the latest stages of cell death resulting from either apoptosis or necrosis. Hence, staining with PE Annexin V is used in conjunction with the vital dye 7-Amino-Actinomycin (7-AAD) to identify early apoptotic cells (7-AAD negative, PE Annexin V positive). Viable cells with intact membranes exclude 7-AAD, while the membranes of dead and damaged cells are permeable to 7-AAD. Samples were analysed by flow cytometry; 10,000 events were collected per sample using a Special Order BD LSRFortessa™ Cell Analyzer.

2.13 RNA extraction

RNA extraction was performed using the ReliaPrep™ RNA Miniprep System (Z6011 Promega), following an optimised protocol based on the manufacturer's instructions. First, 350 µl of BL buffer supplemented with 1-Thioglycerol were added to each pellet. The cells were mixed by pipetting, 120 µl of 100% isopropanol were added, and the samples were vortexed for 5 seconds. The lysed cells were transferred to mini-columns and centrifuged. Unless stated otherwise, all centrifugation steps were completed at 14,000 x g for 30 seconds. The flow-through was discarded, and the columns were washed with 500 µl of RNA wash solution. 24 µl of Yellow Core Buffer, 3 µl of 0.09M MnCl2, and 3 µl of DNase I were combined per sample in the stated order to make up the DNase I incubation mix and mixed by gentle pipetting. 30 µl of DNase I incubation mix were added to each mini-column to degrade contaminating DNA. After a 15-minute incubation at room temperature, 200 µl of Column Wash Solution were added, and the samples were centrifuged for 15 seconds. Following a further wash with 500 µl of RNA Wash solution and centrifugation, the collection tubes were discarded, and the mini-columns were placed in a new collection tube. A final wash with 300 µl of RNA Wash Solution was done, centrifuging the tubes for 2 minutes, following incubation with the wash solution for 1 minute. The columns were transferred to the elution tubes, and 20 µl of Nuclease-Free water were used to elute the mRNA bound to each column. The

Nuclease-Free water was incubated on the column for 3 minutes before centrifuging the samples for 1 minute. The concentration of the mRNA from the elution tubes was assessed using the RNA broad range option on a Qubit™ 3 Fluorometer (Q33216 Invitrogen).

2.14 cDNA conversion

cDNA conversion from extracted RNA was performed using the Promega-GoScript™ Reverse Transcription System (A5000 Promega), following an optimised protocol based on the manufacturer's instructions. The volume of RNA sample to use was calculated using the following formula: [0.2/(RNA sample concentration)]*1000. This was supplemented with 2 µl of random primers, and the total volume was brought up to 10 µl using Nuclease-Free water. The sample was incubated in a heated block at 70°C for 5 minutes, then at 4°C for 5 minutes. To prepare the reverse transcription reaction mix, the following components (multiplied by the number of samples plus 1 to account for pipetting errors) were combined in the order listed: 8 µl of GoScript™ 5X Reaction buffer, 6 µl of 25 mM MgCl2, 2 µl of PCR nucleotide Mix, 1 µl of Recombinant RNasin Ribonuclease Inhibitor, 2 µl of GoScript™ Reverse Transcriptase, and 11 µl of Nuclease-Free Water. 30 µl of the reverse transcription reaction mix were added and mixed by pipetting to each RNA and primer mix. The samples were first incubated for 5 minutes at 25°C for the primers to anneal to the RNA, then for 1 hour at 42°C for the extension, and finally at 70°C for 15 minutes to inactivate the enzyme. The cDNA was stored at -20°C for future use.

2.15 Quantitative RT-PCR

Real-time quantitative polymerase chain reactions were performed using the Promega-GoTaq® qPCR kit (A6001 Promega) following an optimised protocol based on the manufacturer's instructions. Primers synthesised by Sigma-Aldrich (**Table 2-3**) were used to set up the qPCRs. Every reaction included 5 µl of GoTaq® qPCR Master Mix (2X), 0.5 µL of template cDNA, and forward and reverse primers at 3 µM each. The volume was adjusted to 10 µl with Nuclease-Free Water. Samples were amplified on an Applied Biosystems™ QuantStudio™ 7 Flex (4485701 Applied Biosystems) according to the manufacturer's instructions and the following cycling program: 50°C for 2 minutes, 95°C for 10 minutes; 40 cycles of denaturation at 95°C

for 15 seconds, annealing and extension at 60°C for 1 minute; melt curve stage at 95°C for 15 seconds, 60°C for 1 minute and 95°C for 15 seconds. The data were analysed using the 2-ΔΔCt method and plotted using GraphPad Prism v9.3.1 (GraphPad Software, LLC).

Table 2-3. Forward, reverse primers and expected product sizes used for screened genes.

Gene	Forward Primer	Reverse Primer	Product size
GAPDH	5'- TGCACCACCACCTGCTTAGC	5'- GGCATGGACTGTGGTCATGAG	87 bp
Ezrin	5'- GTTTTCCCCAGTTGTAATAGTGCC	5'- TCCGTAATTCAATCAGTCCTGC	101 bp
RPE65	5'- TGCGTATGGACTTGGCTT	5'- TCCTGCTCCTGGGCTCACC	190 bp
Transthyretin	5'- GATGGGATTTCATGTAACCAAGAG	5'- CTGCCTGGACTTCTAACATAGC	84 bp
TYR	5'- ATTGGGACTGGCGGGATG	5'- GCATAAAGACTGATGGCTGTTG	164 bp
ZO1	5'- GTCCAGAATCTCGGAAAAGTGCC	5'- CTTTCAGCGCACCATACCAACC	132 bp

2.16 Transepithelial Electrical Resistance (TEER) in RPE cells

RPE cells were incubated at RT for 15 minutes prior to performing the measurements using a Millicell ERS-2 Voltohmmeter (MERS00002 Millipore). The resistance of the samples was measured by immersing the electrode at a 90° angle so that the shorter tip was in the transwell insert and the longer tip was in the outer well. Unit area resistance ($\Omega \cdot cm^2$) was calculated by subtracting the resistance reading across the blank from the resistance reading across the sample for each measurement. Then the result was multiplied by the effective membrane area of the transwell insert of a 24-well plate (0.33 cm^2).

2.17 POSs-RPE Phagocytosis assay

2.17.1 FITC labelling of POSs

Bovine rod photoreceptor outer segments (POSs; 98740 InVision BioResources) were labelled by adding 0.4 mg/ml fluorescein isothiocyanate (FITC, 20 mg/ml stock in EtOH, 1:50 dilution; F7367 Sigma Aldrich), resuspended thoroughly, followed by centrifugation at 3000 RCF for 4 minutes. The pellet was resuspended in 10 ml of the final stage RPE medium. POSs were incubated on a shaker at RT for 1 hour, protected from light. They were centrifuged again, washed three times with PBS, resuspended in 1 ml of RPE medium, and then counted and adjusted the concentration accordingly to 10^6 POSs/ml. FITC labelling was

confirmed under a fluorescent microscope. POSs were stored in 2.5% (73 mM) sucrose (S0389 Sigma Aldrich) in PBS.

2.17.2 Phagocytosis by flow cytometry

Once the POSs vials were thawed, RPE medium + 10% FBS was added to the POSs and centrifuged again before resuspending in the same medium in the volume required. The 4°C control transwell plate was incubated at 4°C POSs for 10 minutes. POSs concentration was adjusted to 40 million per ml. 75 µl FITC-POSs suspension was added per transwell insert. Samples and 4°C controls were protected from light and incubated for 4 hours at 37°C and 4°C, respectively. After incubation, cells were washed twice with PBS and dissociated into single-cell suspension with TrypLE™ Select Enzyme (10X). Once TrypLE™ Select Enzyme (10X) was aspirated, 200 µl of flow buffer (2% FBS in PBS) and DRAQ5™ (1:40; ab108410 Abcam) were added. Cells were removed from inserts and transferred to small 1.5 ml Eppendorf tubes for a 10-minute incubation at 37°C. 200 µl 0.4% Trypan blue (93595-50ML Sigma Aldrich) was added to samples and incubated for 10 minutes. Samples were centrifuged at 350 RCF for 5 minutes, washed with PBS, and resuspended in flow buffer before transferring them to flow tubes. Samples were analysed by Fluorescence-Activated Cell Sorting (FACS), and 10,000 events were collected per sample using a Special Order BD LSRFortessa™ Cell Analyzer.

2.18 Statistical analysis

One-way ANOVA test (Šídák's multiple comparisons test) was used to compare the mean ± SEM values between drug-treated and untreated controls in hESC-, patient-specific hiPSC-derived retinal organoids, and RPE cells for all the analyses, except for RO cell cycle-phase distribution analyses. The Shapiro-Wilk normality test assessed the normal distribution of the data. An unpaired two-tailed Student’s t-test was used to compare the mean ± SEM values between pRB-depleted and control hESC- and patient-specific hiPSC-derived retinal organoids for the cell cycle-phase distribution analysis (**Figure 3-9** and **Figure 3-13**). All the statistical analyses were performed with GraphPad Prism v9.3.1 (GraphPad Software, LLC). Values of $p \leq 0.05$ were considered statistically significant (*$p \leq 0.05$, **$p \leq 0.01$, ***$p \leq 0.001$, ****$p \leq 0.0001$).

Chapter 3

3 Generation and characterisation of hESC- and patient hiPSC-derived retinal organoids

3.1 Introduction

The human retina is the light-sensitive element of the eye comprising three layers of neurons, two layers of synapses and Müller glial cells (Blond and Léveillard, 2019). The neural retina's five central neural cell populations include rod and cone PRs, HCs, BCs, ACs and RGCs (Stenfelt et al., 2017). The retina collects the visual information processed as images through an internal circuitry where other neuronal cell populations collaborate (Busskamp et al., 2010). The visual information collection begins with phototransduction, where the light enters the eye and photons are absorbed by the PR outer segments for the isomerisation of the chromophore conjugated with the visual pigment (Sung and Chuang, 2010). After this initial process, the information is relayed to the BCs to finally provide excitation to the RGCs, which integrate the signal from BCs and ACs and forward it as electrical responses via the optic nerve (Sung and Chuang, 2010).

Retinoblastoma (Rb) is retinal cancer that affects children younger than five years, with a prevalence of 1:15,000 individuals worldwide (Stenfelt et al., 2017, Valverde et al., 2005, Saengwimol et al., 2018). The biallelic inactivation of the *RB1* tumour suppressor gene, and the subsequent loss of the retinoblastoma protein (pRB), accounts for up to 98% of Rb cases, while the rest have been reported to have an amplification of the *MDM2, MDM4, SKP2* and/or *MYCN* oncogenes (Kaewkhaw and Rojanaporn, 2020, Benavente and Dyer, 2015). High cure rates of up to 95% have been achieved in developed countries when correct diagnosis and treatment for the confinement of the malignant mass to the eye have been given in the early stages (Parulekar, 2010). Nonetheless, around 50% of the cases will die of disseminated Rb in developing countries (Chantada, 2011).

Although there has been some progress in treatments for Rb, patients can still suffer neurocognitive development, cataracts, hearing loss and cosmetic deformities (Belson et al., 2019, Ing et al., 2012). Enucleation has traditionally been the treatment of choice to reduce mortality in patients with severe Rb, significantly diminishing the quality of life (Wong et al., 2022). Current strategies for treating Rb include two or three chemotherapeutic drugs with alkylating and DNA-damaging

agents with cytoskeletal inhibitors, some of them with reported toxicity (Sachdeva and O'Brien, 2012).

pRB expression pattern in the developing retina is predominantly abundant in RPCs in the G1-, S-, and early to mid-G2/M-phases at an early stage of development [foetal week (Fwk) 5] (Lee et al., 2005, Lee et al., 2006). Additionally, pRB expression is not detected in the earliest identifiable RGC, AC, and BC precursors by Fwk 9 migrating away from the ventricular layer, but then it is seen when these precursor cells undergo further differentiation. However, it is not detected in the earliest RXRγ^{+} cone precursors or the earliest Nrl^{+} rod precursors (Lee et al., 2006). Then, pRB expression rises to high levels in cones and low levels in rods at a mid-stage of development (Fwk 12). Finally, as further differentiation of cell types occurs at a mature stage of development (Fwk 18), pRB expression is prominent in mature Müller glial cells when they exit the cell cycle (Lee et al., 2006). pRB does not mediate the initial proliferative arrest of retinal neurons, but it may induce arrest in RPCs or maintain an arrest in postmitotic precursors. The role of pRB in RGCs, HCs, cone and rod PRs, and Müller glial cells resides in maintaining their differentiation state. Through development, the complex pattern of pRB expression in retinal cell types is crucial for identifying the retinal cell that depends on the *RB1* gene to suppress tumour formation (Spencer et al., 2005).

pRB loss and retinal cell type-specific circuitries are correlated with the proliferation and development of Rb-like tumours. The maturing L/M-cone precursor circuitry was found to be needed for tumour proliferation in Rb as these cone populations were enriched (Xu et al., 2014). A cone precursor cell has been proposed to be the cell of origin in human Rb, as cone lineage factors (TRβ2, RXRγ), highly expressed oncoproteins (MDM2 and MYCN), and p27 downregulation likely mediated by SKP2 contribute to pRB loss (Xu et al., 2014). Furthermore, a recent publication from our group (Collin et al., 2021) also suggested a proliferating cone precursor cell as the origin cell for human Rb. The study's proof-of-principle single-cell RNA-Seq analysis of human tumours showed that cone precursors escaped cell cycle arrest and/or p53-mediated apoptosis. Other groups (Liu et al., 2020, Yang et al., 2021b, Wu et al., 2022) also suggested ARR3^{+} maturing cone precursors as the cell of origin for human Rb, as their transcriptome sequencing profiling results for Rb cells showed abundant cone precursor markers.

Reprogramming differentiated mouse cells to an embryonic-like state by introducing the now well-known Yamanaka factors (Oct3/4, Sox2, c-Myc, and Klf4) (Takahashi and Yamanaka, 2006) was a milestone that unlocked new possibilities in stem cell research. Later, Yamanaka and colleagues (Takahashi et al., 2007) reproduced the induction of pluripotent stem cells by reprogramming human dermal fibroblasts using the same four factors. These findings allowed the generation of any human cell type from reprogrammed hESCs and hiPSCs. Pluripotent stem cells can be conditioned towards a specific organ (or organoid) fate by mimicking early human embryonic development. An organoid is an artificial self-organising tissue resembling an organ that satisfies criteria such as having a 3D structure, multiple cell types and a specialised function. Reprogrammed PSCs can give rise to the three primary germ layers to form ectoderm, mesoderm and endoderm organoids (Lancaster and Huch, 2019). The potential of these methods is relevant for regenerative medicine, disease modelling, drug screening and repurposing, and toxicity assessment. Consequently, Yoshiki Sasai's pioneering work (Sasai, 2013) on establishing a 3D *in vitro* organoid model to study the development of tissues and organs was a milestone, particularly in retinal disease modelling by induced organogenesis.

Retinal organoids are functional 3D cellular structures that exhibit all the critical retinal cell types and are organised in a laminated structure resembling the human retina. These complex structures recapitulate the retina's development, morphology and maturation (Fernando et al., 2022). Work from our group (Hallam et al., 2018, Mellough et al., 2019b, Chichagova et al., 2019, Dorgau et al., 2022) and others (Cora et al., 2019, Zhong et al., 2014, Capowski et al., 2019, Fernando et al., 2022, Saha et al., 2022, Samimi et al., 2022, Wahlin et al., 2017) has revealed that PSC-derived ROs have light-sensitive PRs at the apical layer as part of the functionality of these organoid structures. As the human retina displays unique features that differ from mammalian retinas, numerous features of human biology and disease mechanisms are also dissimilar. Hence, human ROs are a suitable model that accurately represents the human retina's specific characteristics.

Over the last decade, several protocols have been published regarding the generation of 2D and 3D retinal tissue from hESCs and hiPSCs (Meyer et al., 2009) and 3D optic cup morphogenesis from mESCs (Eiraku et al., 2011). Then, further advances reported the development of optic cups with stratified neural retina

containing cone and rod PRs (Nakano et al., 2012) and 3D optic cups with all major retinal cell types (Zhong et al., 2014, Lakowski et al., 2018, Kuwahara et al., 2019, Kuwahara et al., 2015, Meyer et al., 2009) from hESCs and hiPSCs. Protocols for the differentiation of retinal organoids containing all the necessary structures for phototransduction with light-sensitive PRs have been established in our group (Hallam et al., 2018, Mellough et al., 2019b, Chichagova et al., 2019, Dorgau et al., 2022) and others (Cora et al., 2019, Zhong et al., 2014, Capowski et al., 2019, Fernando et al., 2022, Saha et al., 2022, Samimi et al., 2022, Wahlin et al., 2017) (as described in the introduction section **1.4.4 Retinal organoids** of this thesis).

Retinal organoid differentiation from hESCs and hiPSCs is a powerful tool with promising results for retinal disease modelling. Establishing a 3D system using ROs is crucial for developmental research and disease progression modelling. Generating specific cell types that are affected is essential for drug screening with clinical relevance for retinal disorders like AMD (Yang et al., 2014), Rb, RP (Buskin et al., 2018), STGD1 (Khan et al., 2020), and glaucoma (Teotia et al., 2017). Examples of disease modelling using retinal organoids have been discussed in the introduction section (**1.5 Retinal disease modelling**) of this thesis document.

The complex expression pattern of pRB during retinal development in a cell type and species-specific manner, in addition to the absence of a relevant animal model, contributes to an incomplete understanding of Rb biology. To this end, establishing an *in vitro* Rb disease model using ROs from hESCs and patient hiPSCs would provide new insights to understand Rb's pathomechanisms better and find new treatments through drug screening. To date, some groups have developed human Rb disease models using ROs. A research study by (Liu et al., 2020) used hESC-derived ROs with biallelic mutagenesis of the *RB1* gene, exhibiting canonical Rb tumorigenesis *in vivo*. Moreover, their single-cell sequencing data suggested that Rb originated from ARR3^{+} maturing cone precursors. Nonetheless, this study did not consider the patient-specific genetic background nor the epigenetic starting point of the hiPSCs, which can influence the development of Rb. In a research study, (Saengwimol et al., 2018) derived ROs from patient chemotherapy-naïve tumours, showing that primarily cone signal circuitry (M/L^{+} cells) and glial tumour microenvironment (GFAP^{+} cells) were present. Their findings confirmed organoid

histological features similar to retinal tumours and seeds, which retained DNA copy-number alterations and gene and protein expression of the parental tissue.

In a subsequent study, (Norrie et al., 2021) developed hiPSC-derived ROs from 15 patients with germline *RB1* mutations. Additionally, they dissociated the ROs after 45 days and injected them into the vitreous of eyes of immunocompromised mice for Rb tumour growth. Their Rb patient, the hiPSC-derived RO model, provided insights into the tumourigenic mechanism that follows *RB1* inactivation and the cellular origin of Rb. Establishing a well-characterised *in vitro* Rb RO model is essential for developing reliable systems helpful in testing new chemotherapeutics for individual patients. Interestingly, (Kanber et al., 2022) published a study using hESC-derived ROs after *RB1* inactivation by CRISPR/Cas9 mutagenesis. Their results showed depletion in most retinal cell types except for proliferative cones after day 130 of differentiation, supporting these as a human Rb cell of origin. Nonetheless, *RB1* knock-out organoid disintegration after day 126 of differentiation was a limitation of this study that the authors attributed to a lack of pRB, as it was not observed in wild-type or heterozygous *RB1* ROs. Remarkably, in our recent study (Rozanska et al., 2022), we were able to characterise and maintain in culture homozygous mutant *RB1* ROs beyond day 150 of differentiation.

Recently, (Blixt et al., 2022) generated the first *in vitro* Rb model using $RB1^{+/+}$ hESC-derived retinal organoids that overexpressed *MYCN*. They also induced tumourigenic growth using an animal model by overexpressing *MYCN* in RB1-proficient chicken retinas. The relevance of this study relies on establishing an alternative Rb disease model that does not exhibit the *RB1* inactivation that is frequently observed in established *in vitro* Rb models. As this overexpressing *MYCN* *in vitro* model was tested *in vivo* in a chicken model, they provided insights into the cellular and molecular pathogenesis of Rb in the absence of *RB1* mutations, which is of clinical significance for designing and testing novel Rb drugs.

The previous studies have provided evidence for the application of patient-specific *RB1* hiPSC-derived ROs for drug discovery, repurposing, and screening. However, it is vital to establish an *in vitro* human *RB1* organoid model that is characterised in detail, which is the main topic of this chapter.

3.2 Aims

The main aim of this chapter was to characterise hESC- and patient hiPSC-derived retinal organoids. The H9 RB1-null hESC line was obtained in collaboration with Prof. Nissim Benvenisty (Avior et al., 2017). Dr Agata Rozanska, from our group, has generated patient *RB1*$^{-/-}$ hiPSC, and the isogenic control (*RB1*$^{+/+}$ hiPSC) through CRISPR/Cas9 gene-editing from the heterozygous patient *RB1*$^{+/-}$ hiPSC line (Rozanska et al., 2022). Immunohistochemistry, fluorescence microscopy and positive cell quantification from IF images were used to characterise the hESC- and patient hiPSC-derived ROs, revealing cell-type composition and retinal lamination variations. The most affected retinal cell types were identified by a combination of proliferation, apoptosis, and cell type-specific markers.

3.3 Results

3.3.1 The steady-state level of pRB is highest at the early stage of differentiation and decreases with time

Once the hESC and patient hiPSC lines were established, ROs were generated following the protocol developed in our group (Hallam et al., 2018) (**2.2 Retinal organoids differentiation** section of this thesis). Characterisation of hESC- and hiPSC-derived ROs was completed by immunofluorescence (IF) analysis to assess the characteristics of a potential Rb disease model by analysing the expression of the neural retina, proliferation, pRB and apoptosis markers. The emergence of retinal cell types within the laminated neural retina was assessed at three different time points during the differentiation process on days 35, 90, and 150. Representative bright-field images of all cell lines differentiated into ROs for days 35, 90 and 150 showed a well-distinguished neural retina epithelium (**Figure 3-1**).

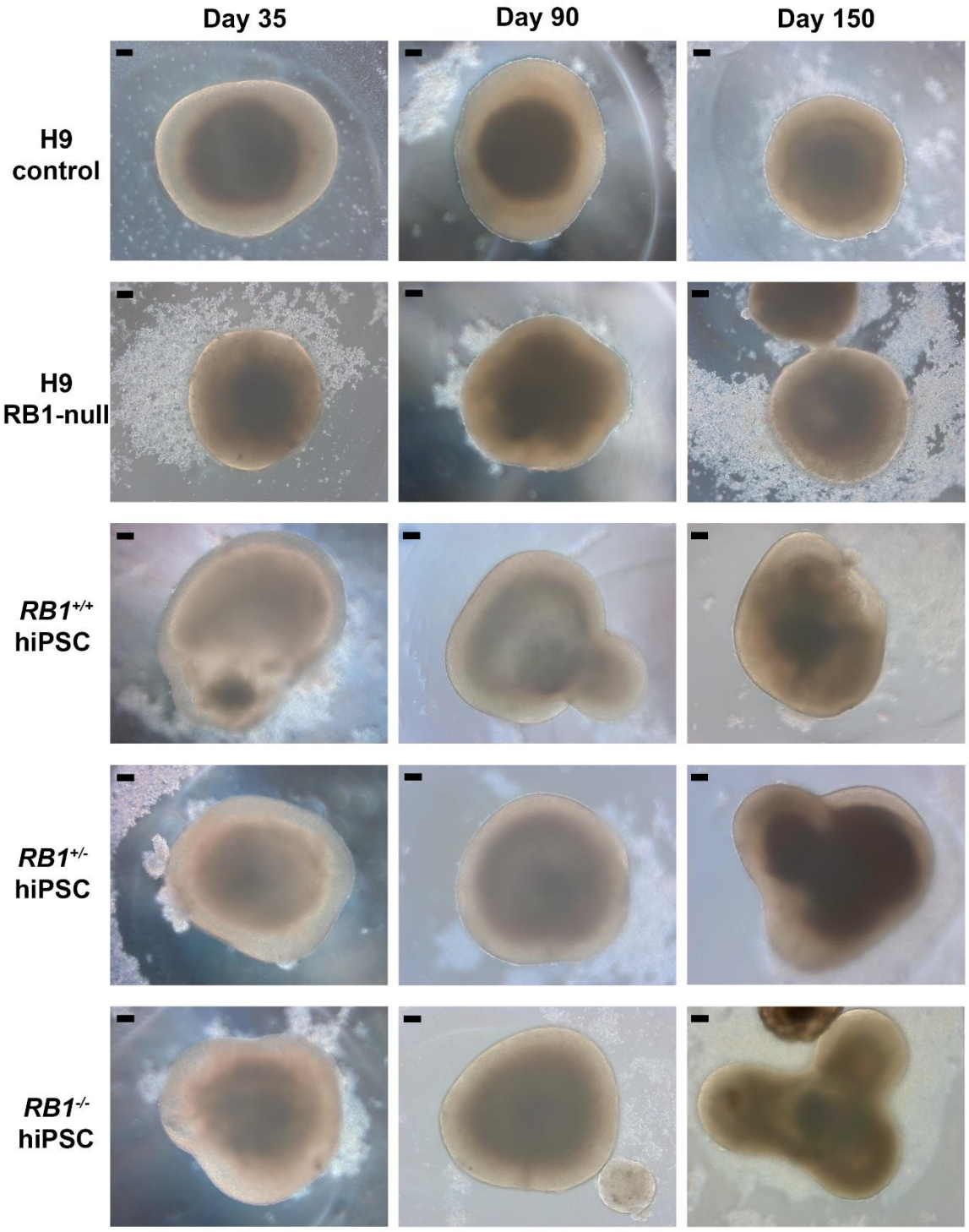

Figure 3-1. Generation of hESC- and patient hiPSC-derived retinal organoids. Light microscopy representative phase-contrast images of H9 control hESC-, H9 RB1-null hESC-, *RB1*$^{+/+}$ hiPSC-, *RB1*$^{+/-}$ hiPSC-, and *RB1*$^{-/-}$ hiPSC-derived retinal organoids on days 35, 90 and 150 of differentiation. 5X images. Scale bars; 100 µm.

Immunofluorescence analysis of pRB was performed in wild-type (H9 hESC- and *RB1*$^{+/+}$ hiPSC-derived) ROs on three time points of differentiation as part of the characterisation. The quantification analysis of the immunofluorescence images using MATLAB™ software showed that in wild-type ROs, the steady state of pRB is highest at the early differentiation stage (day 35) and then decreases with time (**Figure 3-2A, C**). H9 control hESC-derived ROs showed around 60% of pRB^{+} cells on day 35, 43% on day 90, and only 3% on day 150 (**Figure 3-2A**). Then, the bar graph for hiPSC-derived ROs revealed lower levels on day 35 of around 52% of pRB^{+} cells for patient *RB1*$^{+/+}$ hiPSC-derived ROs, and approximately a fraction of 35% for *RB1*$^{+/-}$ hiPSC-derived ROs. Then, pRB^{+} cell percentage values decreased to 28% in *RB1*$^{+/+}$ ROs and 15% in *RB1*$^{+/-}$ ROs on day 90. Finally, by day 150 of differentiation, results showed around 13% and 6% of pRB^{+} cells for *RB1*$^{+/+}$ and *RB1*$^{+/-}$ hiPSC-ROs, respectively (**Figure 3-2C**). No pRB expression was detected throughout the differentiation of H9 RB1-null hESC- and *RB1*$^{-/-}$ hiPSC-derived ROs, while reduced expression was observed in the heterozygous *RB1*$^{+/-}$ hiPSC-derived ROs (**Figure 3-2B, D**).

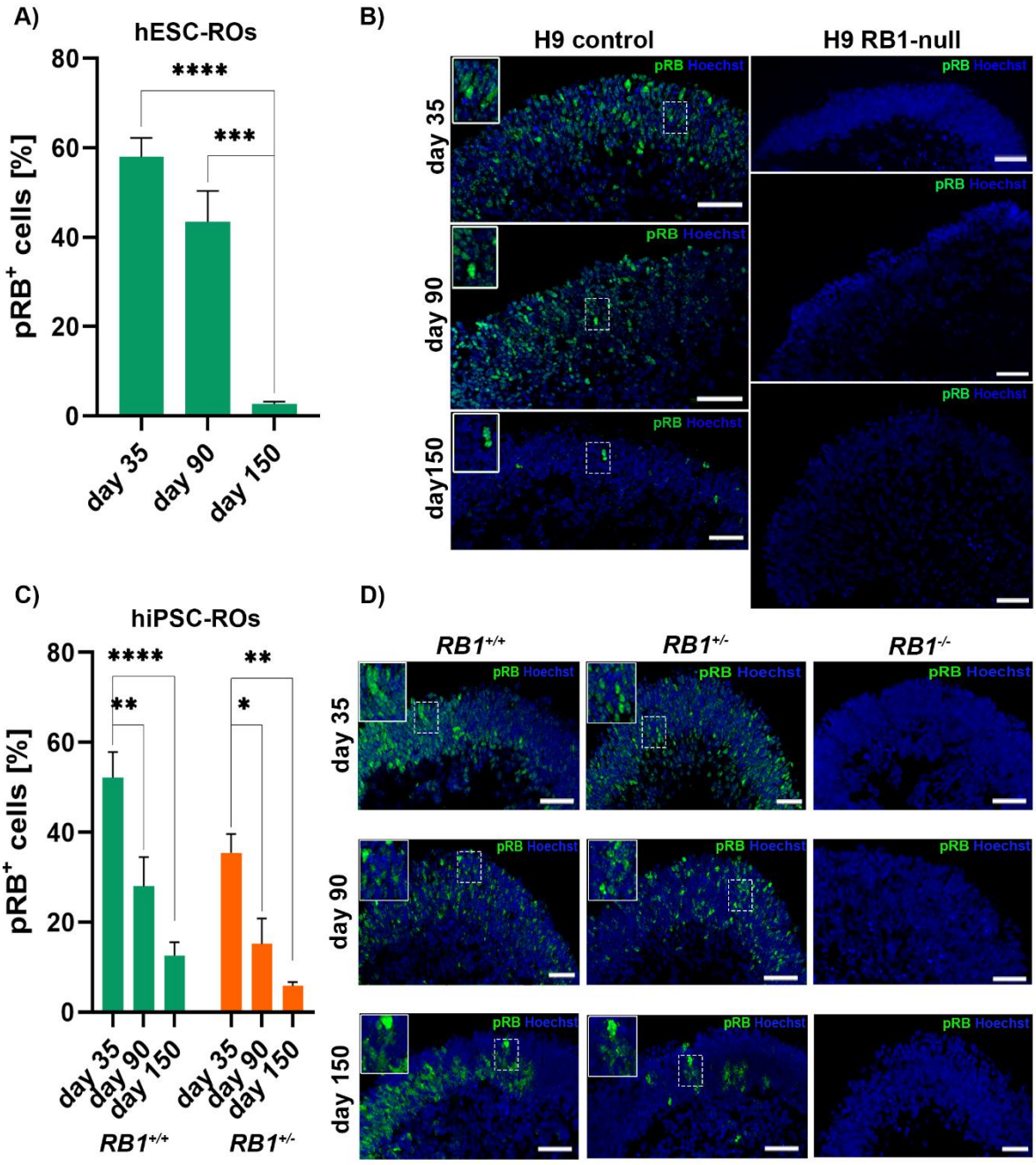

Figure 3-2. Immunofluorescence analysis for pRB of hESC- and patient hiPSC-derived retinal organoids throughout differentiation stages.
Bar charts showing the fraction of pRB$^+$ cells in H9 hESC- (**A**) and patient *RB1*$^{+/+}$ and *RB1*$^{+/-}$ hiPSC-ROs (**C**) at days 35, 90 and 150 of differentiation. Representative immunofluorescent staining of pRB (green) counterstained with Hoechst for H9 control hESC-, H9 RB1-null hESC- (**B**), and patient *RB1*$^{+/+}$, *RB1*$^{+/-}$, and *RB1*$^{-/-}$ hiPSC-ROs (**D**) at days 35, 90 and 150 of differentiation. Insets show higher magnification images. 12 ROs were used as biological replicates. 10 sections of ROs were cut and imaged. Data are presented as mean ± SEM (n = 10 sections from each biological replicate). Scale bars; 50 µm.

3.3.2 Expression of pRB in different retinal cell types in H9 control hESC-derived retinal organoids

To identify the presence of pRB in different cell types, retinal lineage and proliferation markers were co-stained with pRB marker in H9 control hESC-derived ROs on days 35, 90 and 150 of differentiation (**Figure 3-3**, **Figure 3-4**). Qualitative analysis showed pRB expression in the post-mitotic precursor (CRX^+), retinal progenitor ($VSX2^+$), RGC ($SNCG^+$), and proliferating ($Ki67^+$) cells during the early stage (day 35) of differentiation (**Figure 3-3A**). The analysis on later time points of development showed co-expression of pRB marker with retinal progenitor ($VSX2^+$), rods and cones ($RCVRN^+$), cone precursor ($RXR\gamma^+$, $ARR3^+$), L- and M-cone ($OPN1LW/MW^+$), rod PR (RHO^+), HC ($PROX1^+$), BC ($PKC\alpha^+$), Müller glial ($VIMENTIN^+$), and proliferation ($Ki67^+$) cell markers on day 90 (**Figure 3-3B**) and 150 (**Figure 3-4**) of differentiation. These results revealed the near-to-ubiquitous expression of pRB in different retina cell types. Nonetheless, no co-localisation of pRB was observed with the apoptotic ($CASP3^+$) cell marker by days 90 and 150 of differentiation.

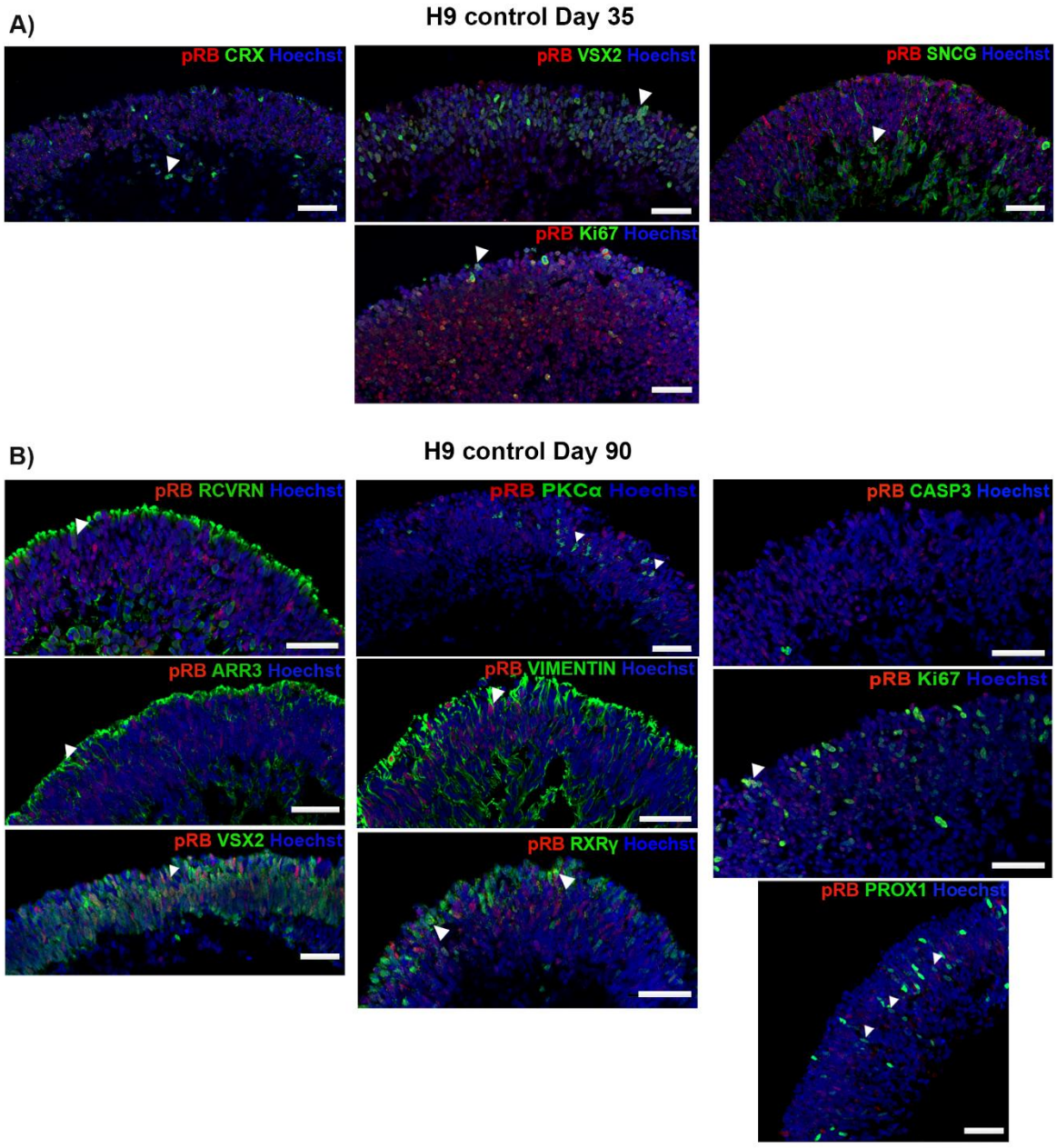

Figure 3-3. Immunofluorescence analysis of H9 control hESC-derived ROs at days 35 and 90 of differentiation.
Representative immunofluorescence analysis of H9 control hESC-derived ROs for pRB (red) counterstained with Hoechst. **A.** CRX, VSX2, SNCG, and Ki67 (green), at day 35. **B.** RCVRN, ARR3, VSX2, PKCα, VIMENTIN, RXRγ, CASP3, Ki67, and PROX1 (green), at day 90 of differentiation. White arrowheads show co-localisation of the pRB marker with the specified marker. 12 ROs were used as biological replicates. 10 sections of ROs were cut and imaged from each biological replicate. Scale bars; 50 μm.

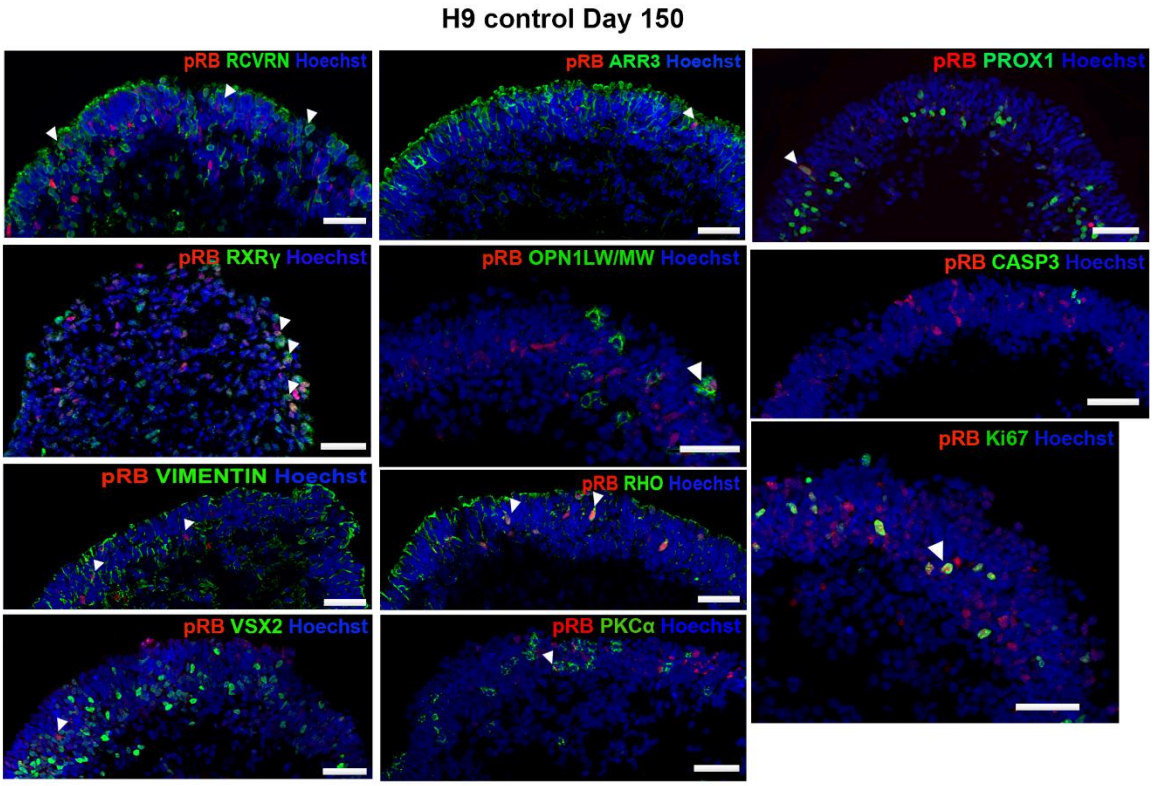

Figure 3-4. Immunofluorescence analysis of H9 control hESC-ROs at day 150 of differentiation.
Representative immunofluorescence analysis of H9 control hESC-derived ROs for pRB (red) co-stained with RCVRN, RXRγ, VIMENTIN, VSX2, ARR3, OPN1LW/MW, RHO, PKCα, PROX1, CASP3, and Ki67 (green), counterstained with Hoechst at day 150 of differentiation. White arrowheads show co-localisation of the pRB marker with the specified marker. 12 ROs were used as biological replicates. 10 sections of ROs were cut and imaged from each biological replicate. Scale bars; 50 μm.

3.3.3 pRB inactivation results in a significant increase in proliferating cone precursor, horizontal, retinal ganglion cells, and a decrease in amacrine cells during retinal organoid maturation

Given the reported role of pRB on cell proliferation, apoptosis, and retinal development, the impact of pRB inactivation was assessed by characterisation of hESC- and patient hiPSC-derived ROs in different stages of development. At the early stage of differentiation (day 35), there was a significant decrease in the percentage of PR precursors (CRX^+) and RGCs ($SNCG^+$), an increase in the fraction of proliferating ($Ki67^+$) cells and no change in retinal progenitors ($VSX2^+$) in H9 RB1-null hESC- compared to control H9 hESC-derived ROs (**Figure 3-5A**). The results for early differentiated retinal cell types co-expressing Ki67 proliferation marker revealed a significant increase in the fraction of proliferating RGCs ($SNCG^+Ki67^+$) and retinal progenitors ($VSX2^+Ki67^+$) but not a significant change in proliferating PR precursors (CRX^+Ki67^+) in H9 RB1-null hESC- compared to H9 hESC-derived ROs (**Figure 3-5A**). In the H9 control hESC-ROs, putative RGCs were mainly located at the basal aspect. Nonetheless, in the H9 RB1-null hESC-ROs, RGCs were found throughout the RO structure and concentrated in the apical layer where typically PR precursors reside (**Figure 3-5B**).

Figure 3-5. Immunohistochemical analysis of hESC-derived retinal organoids at day 35 of differentiation.
A. Bar charts showing the retinal cell types (left) and $Ki67^+$ co-expressing fractions (right). **B.** Representative immunofluorescence analysis for CRX, SNCG, VSX2, pRB (red) and Ki67 (green), counterstained with Hoechst at day 35. 12 ROs were used as biological replicates. 10 sections of ROs were cut and imaged. Data are presented as mean ± SEM (n = 10 sections from each biological replicate). Values of $p \leq 0.05$ were considered statistically significant (*$p \leq 0.05$, **$p \leq 0.01$, ***$p \leq 0.001$, ****$p \leq 0.0001$). White arrowheads point at the co-localisation of Ki67 with the specified marker. Scale bars; 50 µm.

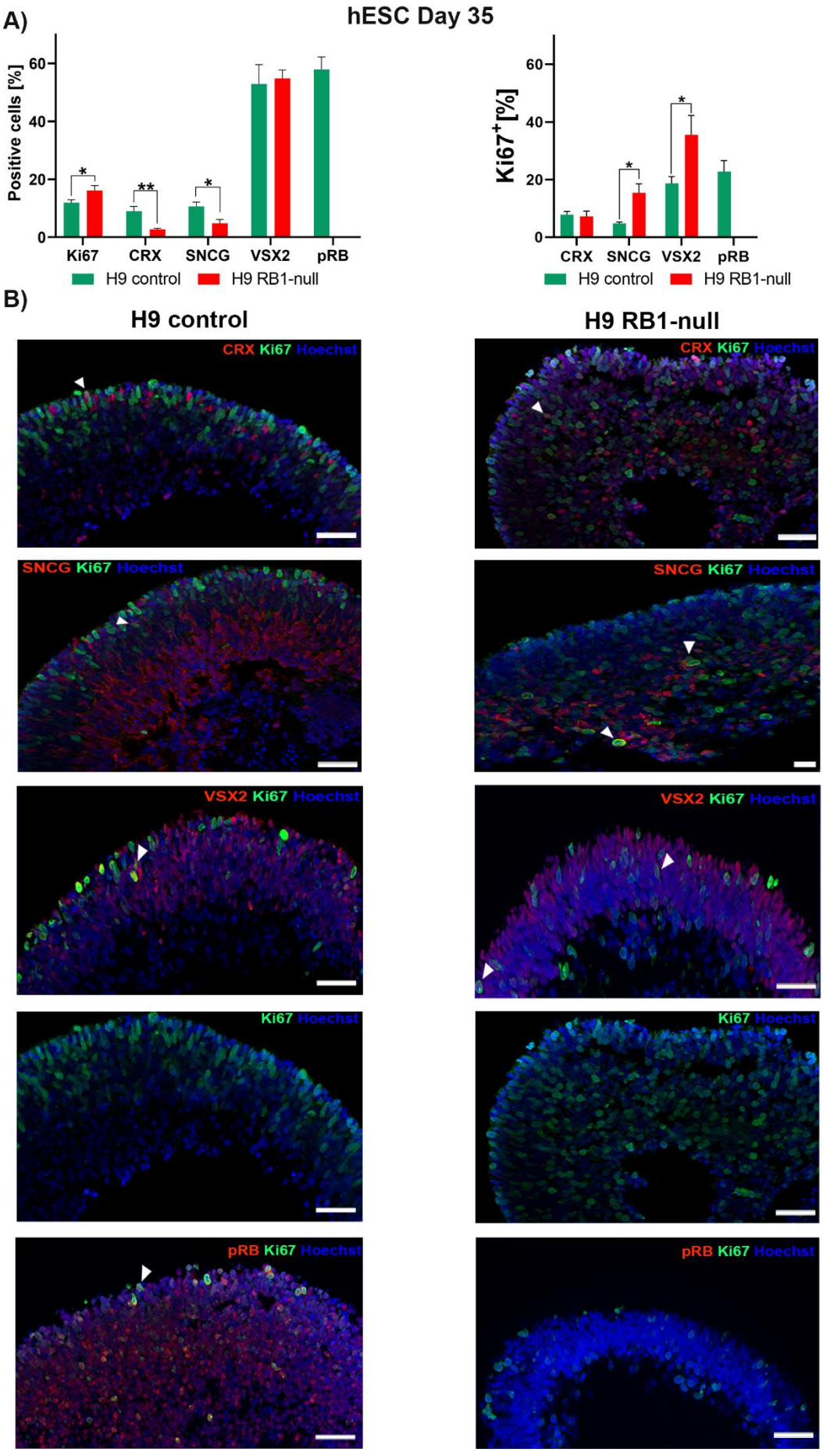
A)
hESC Day 35
Positive cells [%]
60
40
20
0
*
**
*
Ki67
CRX
SNCG
VSX2
pRB
H9 control
H9 RB1-null
Ki67+ [%]
60
40
20
0
*
*
CRX
SNCG
VSX2
pRB
H9 control
H9 RB1-null
B)
H9 control
H9 RB1-null
CRX Ki67 Hoechst
CRX Ki67 Hoechst
SNCG Ki67 Hoechst
SNCG Ki67 Hoechst
VSX2 Ki67 Hoechst
VSX2 Ki67 Hoechst
Ki67 Hoechst
Ki67 Hoechst
pRB Ki67 Hoechst
pRB Ki67 Hoechst

The mid-stage differentiation (day 90) was characterised by a significantly decreased fraction of ACs ($AP2\alpha^+$) in H9 RB1-null hESC- compared to H9 control hESC-derived ROs. The immunohistochemistry analysis also revealed a significantly increased fraction of RGCs ($SNCG^+$), apoptotic ($CASP3^+$), and proliferating ($Ki67^+$) cells in H9 RB1-null hESC-derived ROs. However, results showed no significant difference in rod precursor (NRL^+), HC ($PROX1^+$), cone precursor ($RXR\gamma^+$), and retinal progenitor ($VSX2^+$) cell fractions. In parallel, a significant increase was detected in the percentage of proliferating retinal progenitors ($VSX2^+Ki67^+$), proliferating RGCs ($SNCG^+Ki67^+$), and proliferating cone precursors ($RXR\gamma^+Ki67^+$) in H9 RB1-null hESC-derived ROs. No changes were observed in the percentage of proliferating rod PRs (NRL^+Ki67^+), proliferating HCs ($PROX1^+Ki67^+$), proliferating ACs ($AP2\alpha^+Ki67^+$), and proliferating apoptotic ($CASP3^+Ki67^+$) cells (**Figure 3-6A**). As observed at an early stage of differentiation, RGCs were found throughout the different layers of the retinal structure of the H9 RB1-null hESC-derived ROs. Retinal cone arrestin-3^+ ($ARR3^+$) cells were found at the apical layer of hESC-derived ROs (**Figure 3-6B**).

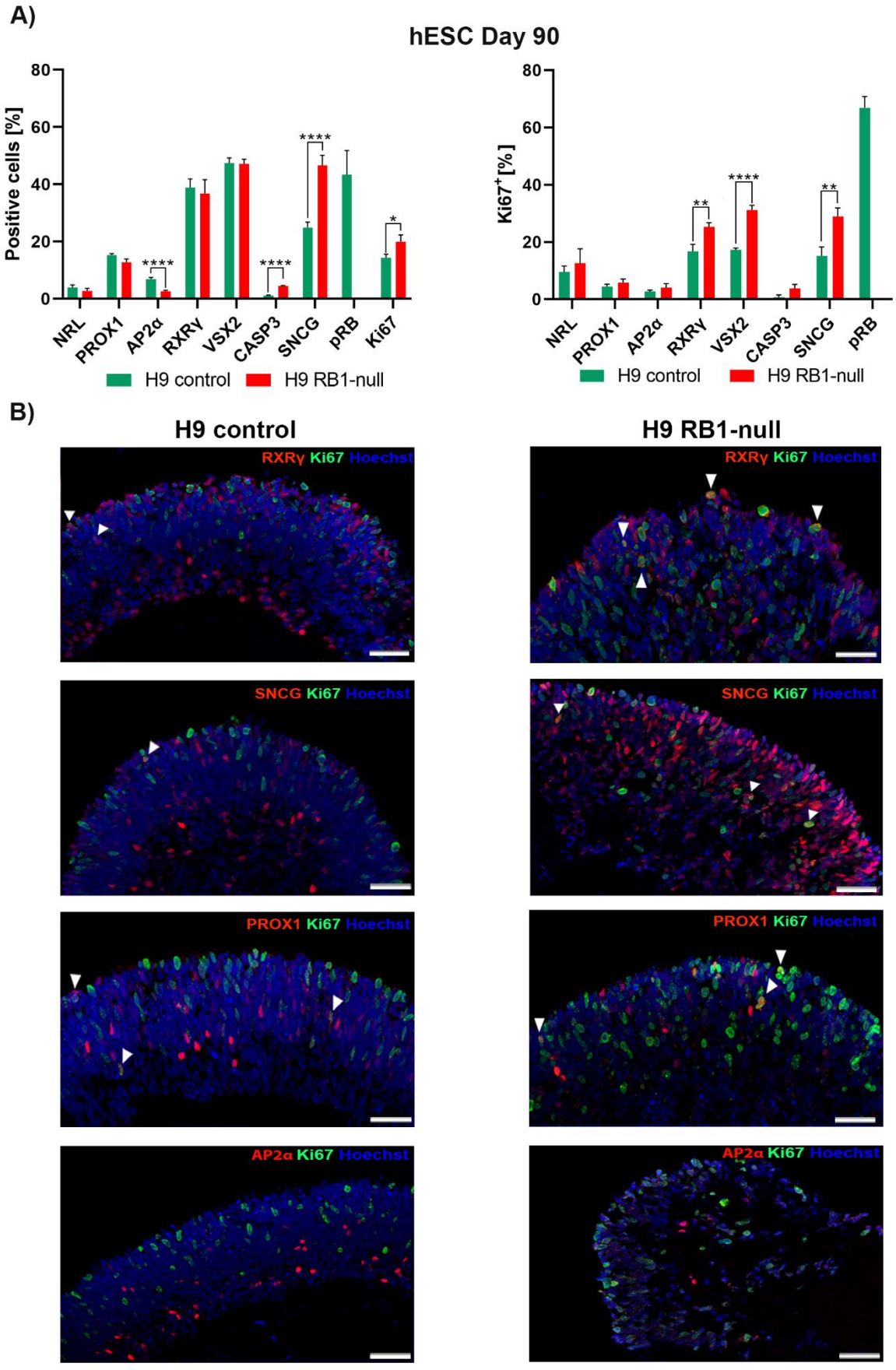
A)
hESC Day 90
Positive cells [%]
Ki67+ [%]
NRL
PROX1
AP2α
RXRγ
VSX2
CASP3
SNCG
pRB
Ki67
H9 control
H9 RB1-null
B)
H9 control
H9 RB1-null
RXRγ Ki67 Hoechst
SNCG Ki67 Hoechst
PROX1 Ki67 Hoechst
AP2α Ki67 Hoechst

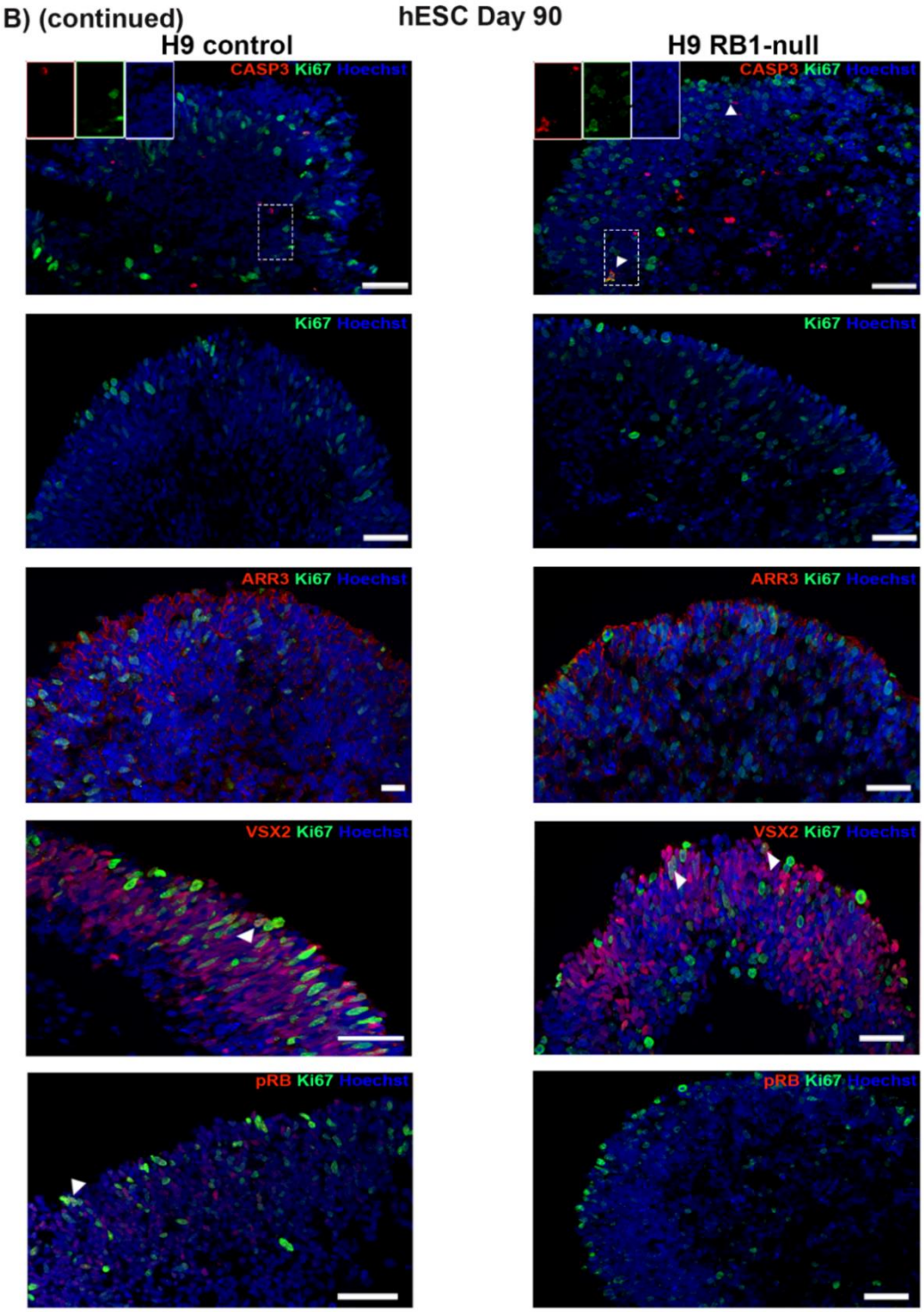

Figure 3-6. Immunohistochemical analysis of hESC-derived retinal organoids at day 90 of differentiation.

A. Bar charts showing the retinal cell types (left) and Ki67^{+} co-expressing fractions (right). **B**. Representative immunofluorescence analysis for RXRγ, SNCG, PROX1, AP2α, CASP3, Ki67, ARR3, VSX2, and pRB counterstained with Hoechst at day 90. 12 ROs were used as biological replicates. 10 sections of ROs were cut and imaged. Data are presented as mean ± SEM (n = 10 sections from each biological replicate). Values of $p \leq 0.05$ were considered statistically significant (*$p \leq 0.05$, **$p \leq 0.01$, ***$p \leq 0.001$, ****$p \leq 0.0001$). White arrowheads point at the co-localisation of Ki67 with the specified marker. Scale bars; 50 µm.

Analysis at a mature stage of differentiation (day 150) revealed a significantly increased percentage of cone precursors (RXRγ$^+$), RGCs (SNCG$^+$), apoptotic (CASP3$^+$), and proliferating (Ki67$^+$) cells in H9 RB1-null hESC-derived ROs. Conversely, results showed a significantly decreased fraction of ACs (AP2α$^+$), mature S- (OPN1SW$^+$), L- and M-cones (OPN1LW/MW$^+$), and rod PRs (RHO$^+$) in H9 RB1-null hESC-derived ROs. However, no significant difference was observed in cone precursor (NRL$^+$), HC (PROX1$^+$), and retinal progenitor (VSX2$^+$) cell fractions. Moreover, results showed significantly increased fractions of proliferative HCs (PROX1$^+$Ki67$^+$), cone precursors (RXRγ$^+$Ki67$^+$), retinal progenitors (VSX2$^+$Ki67$^+$), and RGCs (SNCG$^+$Ki67$^+$) in H9 RB1-null hESC-derived ROs. Interestingly, no significant difference was observed in the cell fraction of the proliferative rod precursor (NRL$^+$Ki67$^+$) (**Figure 3-7A**). RGCs were noted in the apical and different retinal layers in H9 RB1-null hESC-derived ROs, as reported in previous time points of development (**Figure 3-7B**).

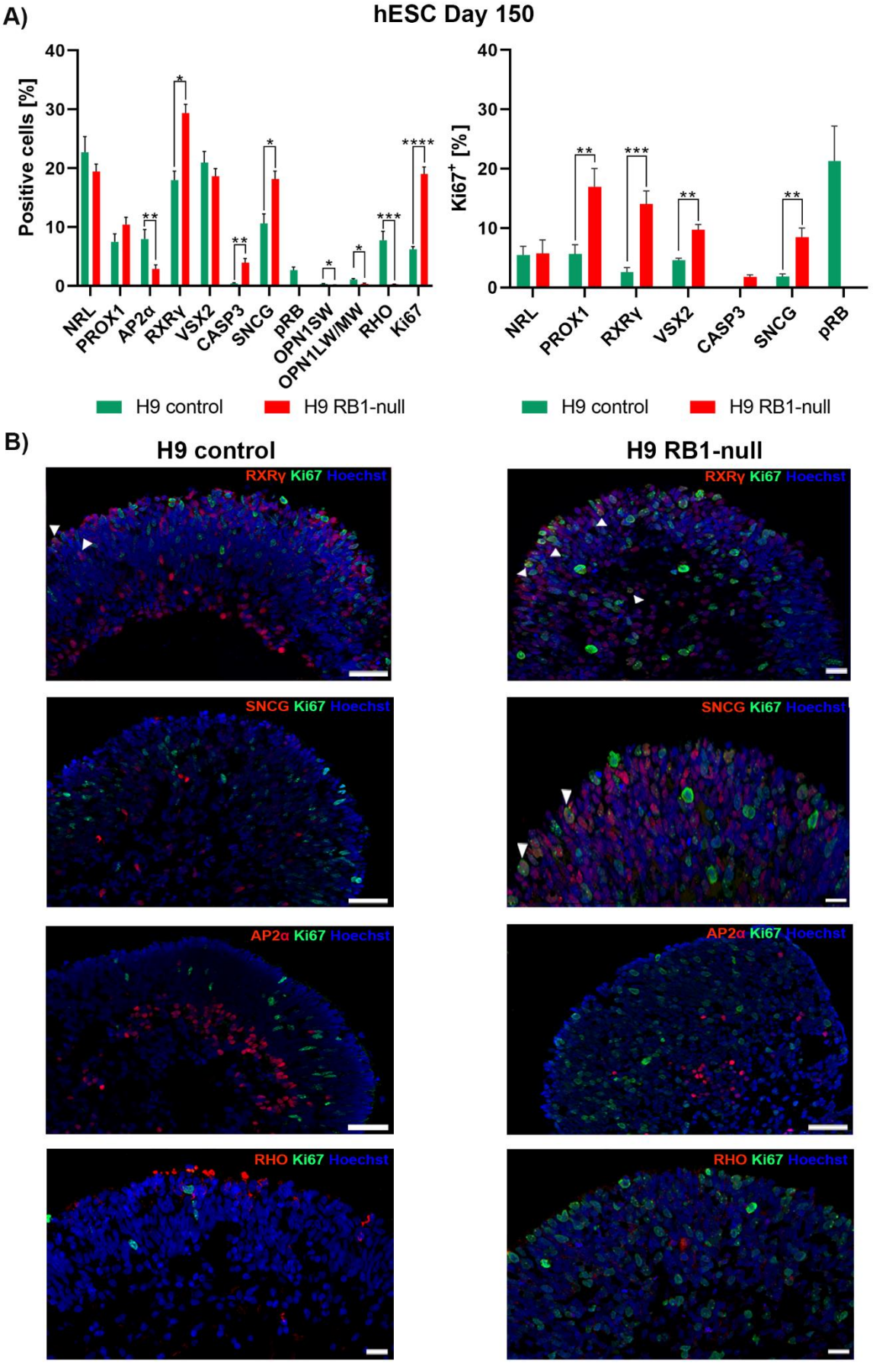
A)
hESC Day 150
Positive cells [%]
40
30
20
10
0
NRL
PROX1
AP2α
RXRγ
VSX2
CASP3
SNCG
pRB
OPN1SW
OPN1LW/MW
RHO
Ki67
Ki67+ [%]
PROX1
RXRγ
VSX2
CASP3
SNCG
pRB
H9 control
H9 RB1-null
B)
H9 control
H9 RB1-null
RXRγ Ki67 Hoechst
SNCG Ki67 Hoechst
AP2α Ki67 Hoechst
RHO Ki67 Hoechst

B) (continued) hESC Day 150

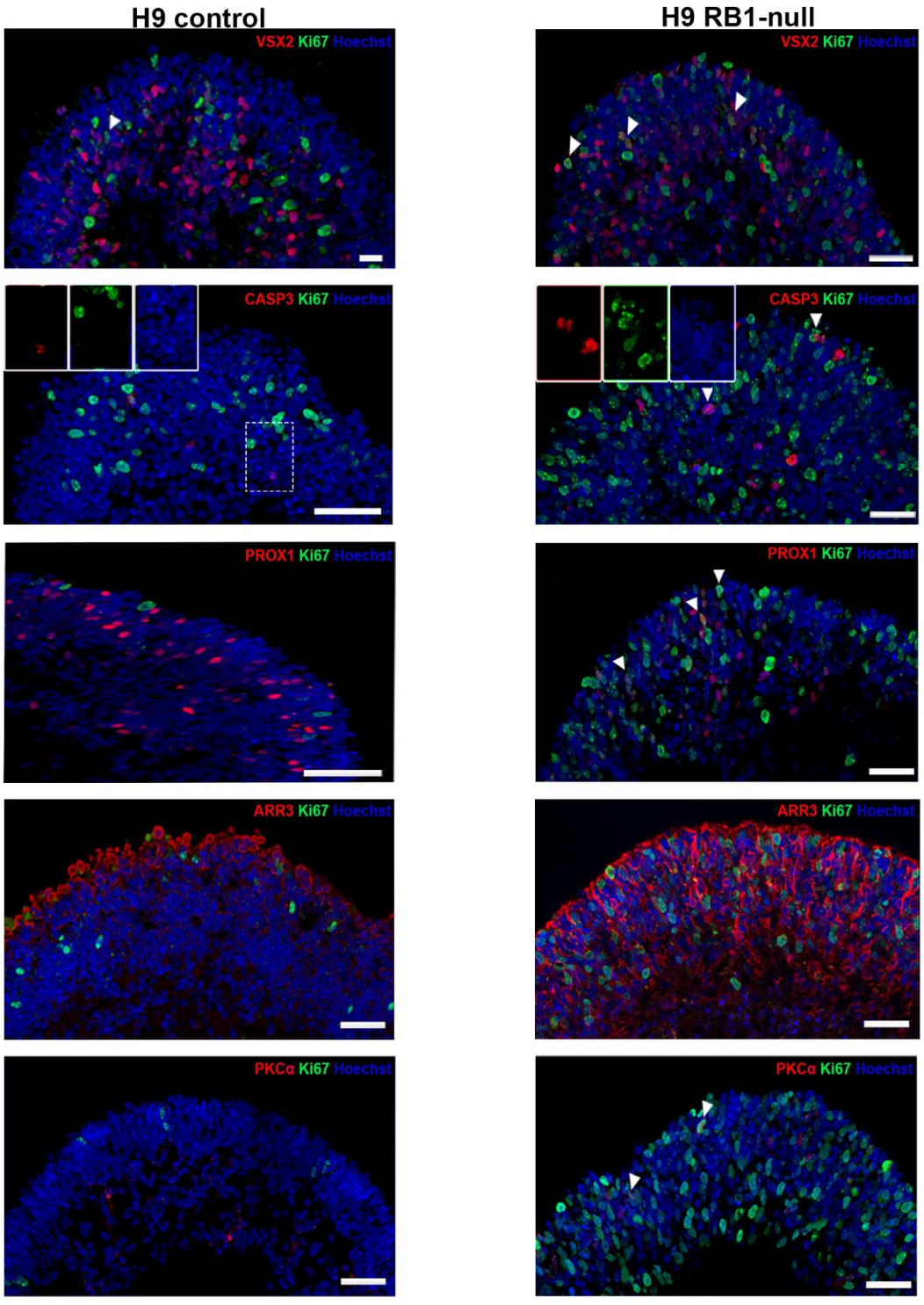

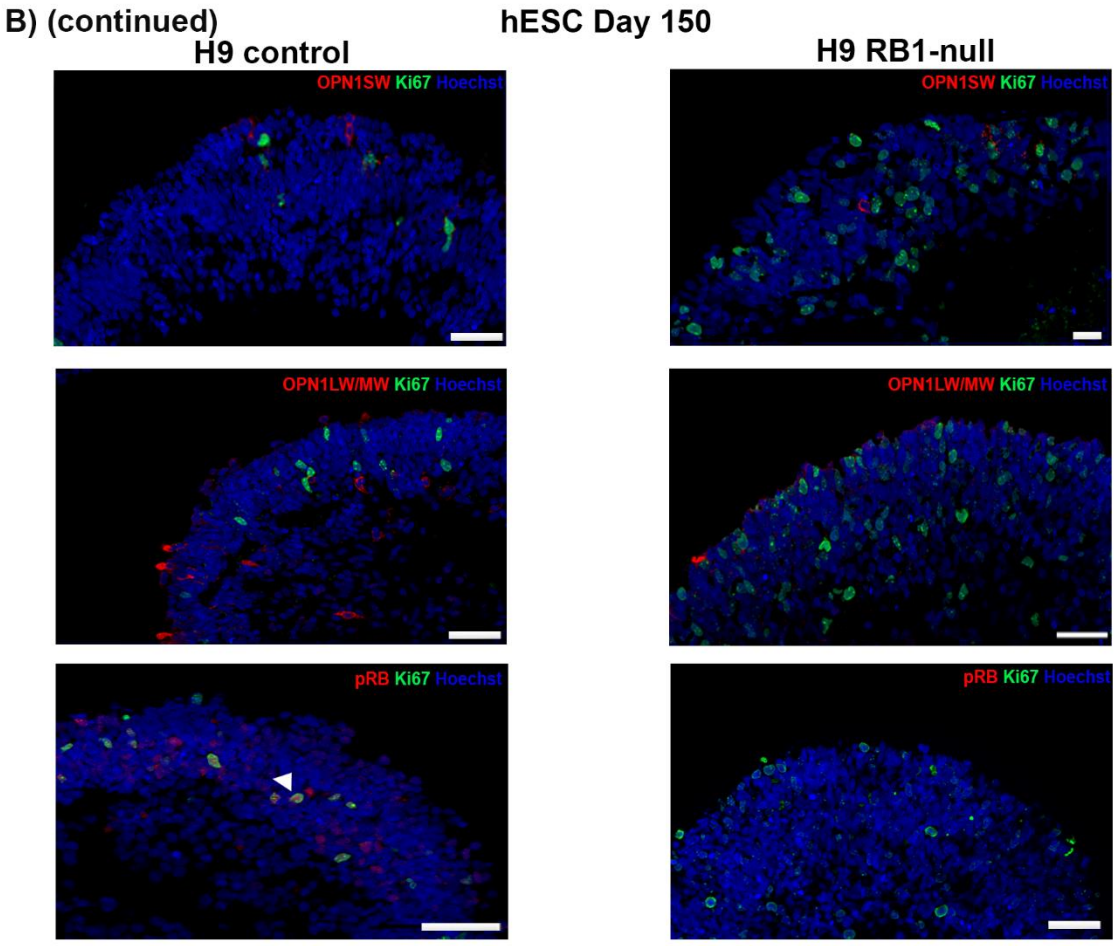

Figure 3-7. Immunohistochemical analysis of hESC-derived retinal organoids at day 150 of differentiation.
A. Bar charts showing the retinal cell types (left) and Ki67^{+} co-expressing fractions (right). **B.** Representative immunofluorescence analysis for RXRγ, SNCG, PROX1, AP2α, CASP3, Ki67, ARR3, and VSX2, counterstained with Hoechst at day 90. 12 ROs were used as biological replicates. 10 sections of ROs were cut and imaged. Data are presented as mean ± SEM (n = 10 sections from each biological replicate). Values of $p \leq 0.05$ were considered statistically significant (*$p \leq 0.05$, **$p \leq 0.01$, ***$p \leq 0.001$, ****$p \leq 0.0001$). White arrowheads point at the co-localisation of Ki67 with the specified marker. Scale bars; 50 μm.

In addition to the immunofluorescence analysis of the proliferation marker (Ki67) in pRB-depleted hESC-derived ROs, the cell-cycle phase distribution analyses based on propidium iodide (PI) staining were performed for mid-stage and late-stage retinal development. Representative data for RO cell population gating for cell cycle assay is included (**Figure 3-8**). These analyses confirmed a significantly enriched fraction of cells in the S-phase (5.26%) in 90-day-old H9 RB1-null hESC-derived ROs compared to wild-type (1.91%) (**Figure 3-9A**). Likewise, the analyses for day 150 of differentiation reported the enriched fraction of cells in the S-phase (5.31%) in H9 RB1-null hESC-derived ROs compared to wild-type (1.48%) (**Figure 3-9B**).

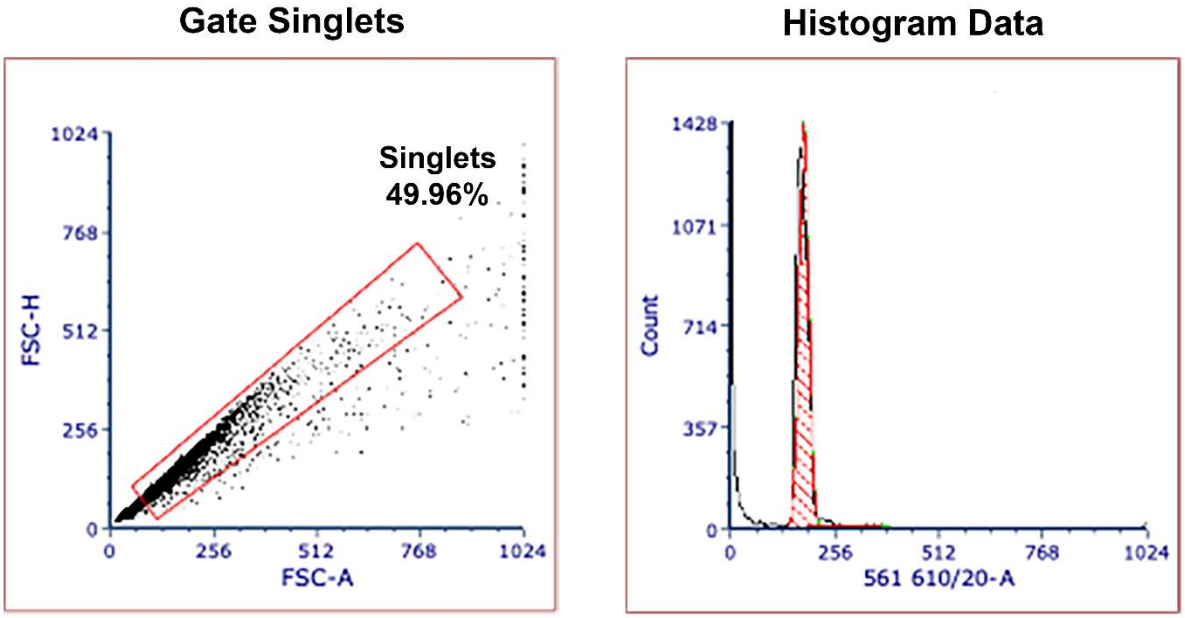

DNA Cycle Statistics

Cycle	G1 Mean	G1 CV	%G1	G2 Mean	G2 CV	%G2	%S	G2/G1	%Total	B.A.D.
Diploid	181.39	6.38	93.60	383.46	5.05	0.54	5.86	2.11	100.00	0.00

Figure 3-8. Cell population gating for cell cycle assay in hESC- and hiPSC-derived retinal organoids at day 90 and day 150 of differentiation.
Representative dot-plot, histogram graph, and DNA cycle statistics table of the cell population gating of single-cell suspensions from hESC- and hiPSC-derived ROs.

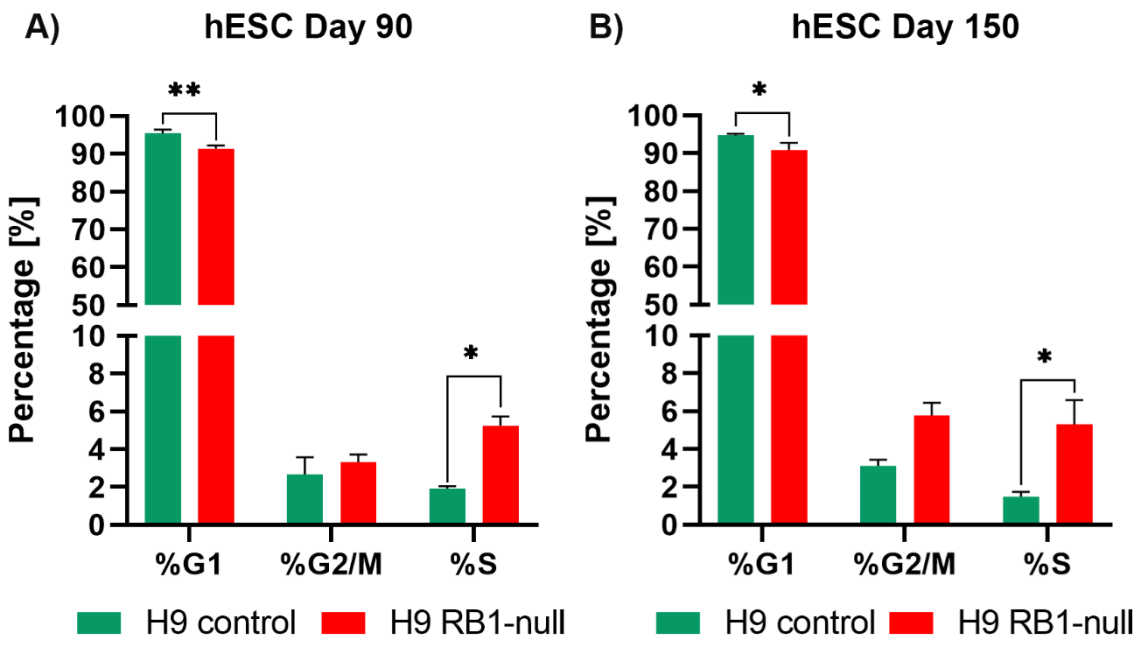

Figure 3-9. Cell cycle phase distribution analysis of hESC-derived retinal organoids at day 90 and day 150 of differentiation.
Bar charts showing the percentage of the G1-, G2/M-, and S-phase of the cell cycle of hESC ROs at day 90 (**A**) and day 150 (**B**) of differentiation**.** 24 ROs per cell line treatment were used as a batch of biological replicates. Data are presented as mean ± SEM (n = 3 repeats from each independently cultured batch of biological replicates). Values of $p \leq 0.05$ were considered statistically significant (*$p \leq 0.05$, **$p \leq 0.01$, ***$p \leq 0.001$, ****$p \leq 0.0001$).

In summary, a common feature of H9 RB1-null hESC-derived ROs was the increased presence of proliferating retinal progenitors ($VSX2^+Ki67^+$) from day 35 and the increased fraction of proliferating cone precursors ($RXR\gamma^+Ki67^+$) from day 90. RGCs ($SNCG^+$) were more frequent and located in the apical layer and throughout the retinal structure in the H9 RB1-null hESC-derived ROs. Also, H9 RB1-null hESC-ROs were characterised by a significant increase in the fraction of proliferating RGCs ($SNCG^+Ki67^+$) throughout retinal development and proliferating HCs ($PROX1^+Ki67^+$) at a mature stage as well as a substantial decrease in ACs ($AP2\alpha^+$) from day 90 of differentiation. The expression of mature S- and M-cone and rod PR markers ($OPN1SW^+$, $OPN1LW/MW^+$ and RHO^+, respectively) was significantly reduced in 150-day-old H9 RB1-null hESC-derived ROs. Simultaneously, a low but significant increase was reported in the fraction of apoptotic ($CASP3^+$) cells in the day 90 and day 150 H9 RB1-null hESC-derived ROs, confirming the increase of the cleaved Caspase-3 steady-state levels. Finally, cell cycle phase distribution analyses

reported the enriched fraction of cells in the S-phase in the H9 RB1-null hESC-derived ROs at mid-stage (day 90) and mature stage (day 150) of development.

3.3.4 The mitotic and tumorigenic activity is limited to the homozygous RB1$^{+/+}$ but not heterozygous RB1$^{+/-}$ hiPSC-RO phenotype

Similar to H9 RB1-null hESC-derived ROs, the analysis showed a significant increase in the percentage of SNCG^{+}, VSX2^{+} and Ki67^{+} cells in the *RB1$^{-/-}$* hiPSC-derived ROs throughout the early differentiation time course. The fraction of pRB^{+} cells was significantly decreased in heterozygous (*RB1$^{+/-}$*) compared to isogenic control (*RB1$^{+/+}$*) hiPSC-derived ROs. There was no difference in the percentage of PR precursors (CRX^{+}) or proliferating PR precursors (CRX^{+}Ki67^{+}) in any patient hiPSC-derived ROs at this stage. Although the fraction of SNCG^{+} and VSX2^{+} cells was increased in both the heterozygous (*RB1$^{+/-}$*) and the homozygous (*RB1$^{-/-}$*) hiPSC-derived ROs, only the homozygous ROs were characterised by an increased percentage of proliferating SNCG^{+} and proliferating VSX2^{+} marked by Ki67 staining (**Figure 3-10A**).

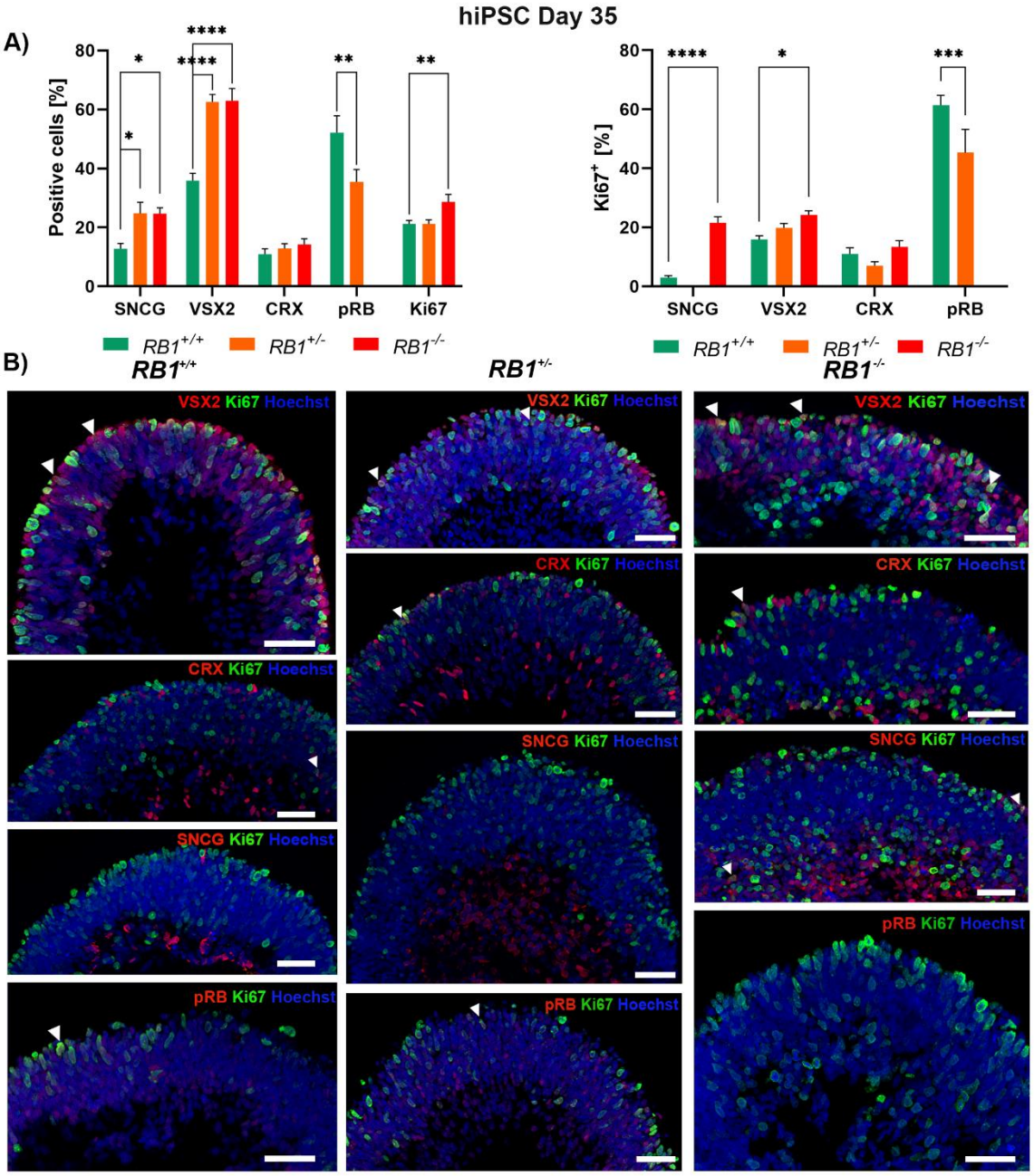

Figure 3-10. Immunohistochemical analysis of patient hiPSC-derived retinal organoids at day 35 of differentiation.
A. Bar charts showing the retinal cell types (left) and Ki67$^+$ co-expressing fractions (right). **B.** Representative immunofluorescence analysis for VSX2, CRX, SNCG, pRB and Ki67, counterstained with Hoechst at day 35. One hiPSC-derived clone per cell line was used for RO differentiation. 12 ROs were used as biological replicates. 10 sections of ROs were cut and imaged. Data are presented as mean ± SEM (n = 10 sections from each biological replicate). Values of $p \leq 0.05$ were considered statistically significant (*$p \leq 0.05$, **$p \leq 0.01$, ***$p \leq 0.001$, ****$p \leq 0.0001$). White arrowheads point at the co-localisation of Ki67 with the specified marker. Scale bars; 50 µm.

The quantitative immunofluorescence analysis at day 90 of differentiation for patient hiPSC-derived ROs indicated a significantly increased fraction of retinal progenitor (VSX2$^+$) cells in both heterozygous (*RB1*$^{+/-}$) and homozygous (*RB1*$^{-/-}$) compared to the isogenic control (*RB1*$^{+/+}$) hiPSC-derived ROs. Moreover, there is a significant increase in the percentage of RGCs (SNCG$^+$), apoptotic (CASP3$^+$) and proliferating (Ki67$^+$) cells exclusively in homozygous (*RB1*$^{-/-}$) hiPSC-derived ROs. There was a low yet significant decrease in the fraction of HCs (PROX1$^+$) in heterozygous *RB1*$^{+/-}$ hiPSC-derived ROs. Notably, the fraction of rod precursor (NRL$^+$) and cone precursor (RXRγ$^+$) cells was unaffected by heterozygous or homozygous mutation in the *RB1* gene. Interestingly, the ACs (AP2α$^+$) were undetectable in homozygous (*RB1*$^{-/-}$) ROs, while they were observed in the INL in heterozygous (*RB1*$^{+/-}$) and isogenic (*RB1*$^{+/+}$) patient hiPSC-derived ROs. Although the percentage of VSX2$^+$ cells was increased in both heterozygous- and homozygous-derived ROs at day 90 of differentiation, only homozygous *RB1*$^{-/-}$ hiPSC-derived ROs were characterised by the enrichment of proliferating retinal progenitors (VSX2$^+$Ki67$^+$), proliferating HCs (PROX1$^+$Ki67$^+$), proliferating cone precursors (RXRγ$^+$Ki67$^+$), proliferating RGCs (SNCG$^+$Ki67$^+$), and proliferating apoptotic (CASP3$^+$Ki67$^+$) cells. No changes were observed in the fraction of proliferating rod precursors (NRL$^+$Ki67$^+$) in any patient hiPSC-derived ROs (**Figure 3-11A**).

As previously reported in H9 RB1-null hESC-derived ROs, RGCs were primarily found in the apical layer and throughout the retinal structure in patient *RB1*$^{-/-}$ hiPSC-derived ROs. Cone precursors (ARR3$^+$) were observed in the apical site, while Müller glial (VIMENTIN$^+$) cells spanned across different retinal layers as part of the structure of the ROs (**Figure 3-11B**).

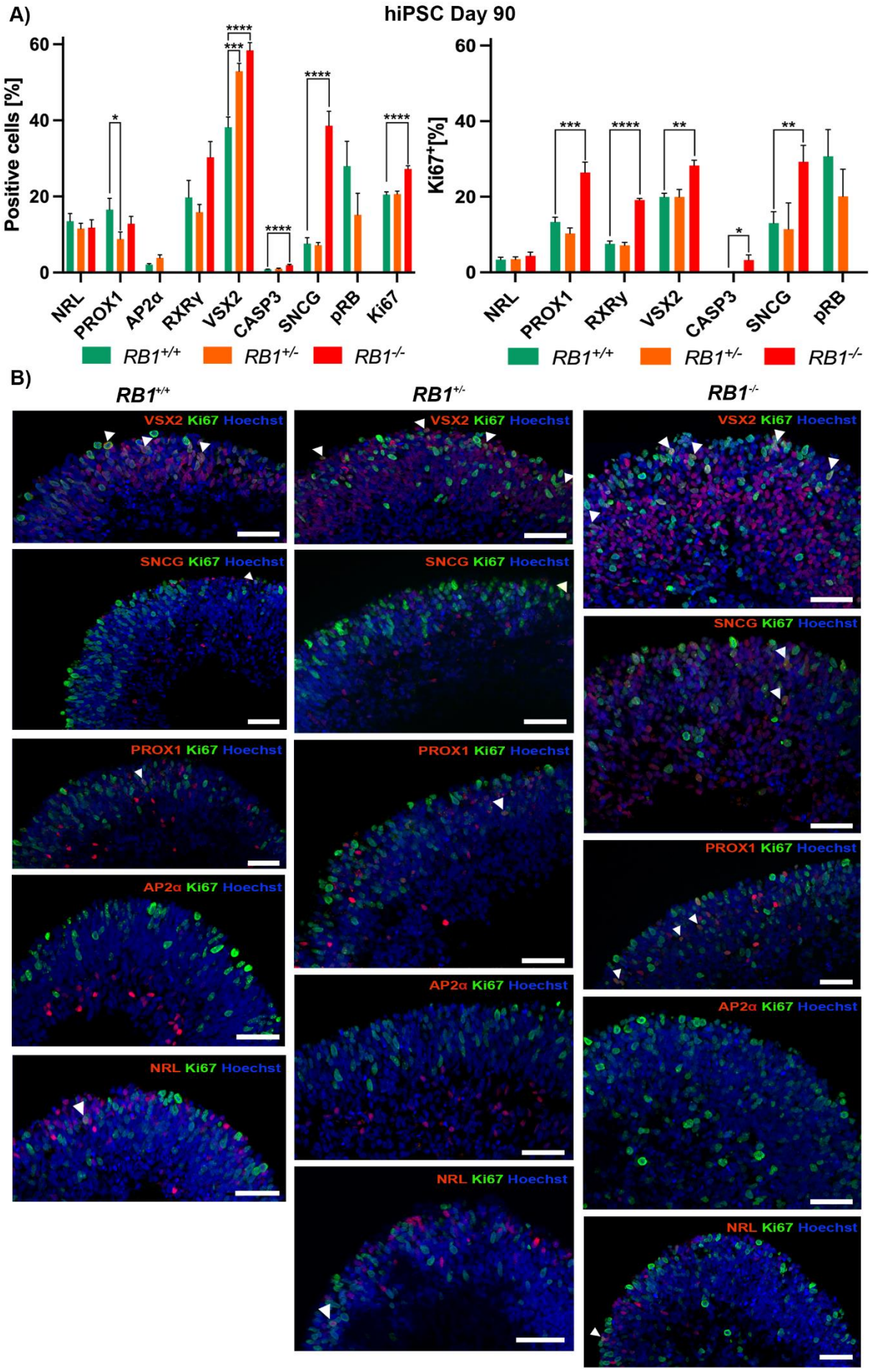
A)
hiPSC Day 90
Positive cells [%]
Ki67+[%]
NRL
PROX1
AP2α
RXRγ
VSX2
CASP3
SNCG
pRB
Ki67
RB1+/+
RB1+/-
RB1-/-
B)
RB1+/+
RB1+/-
RB1-/-
VSX2 Ki67 Hoechst
SNCG Ki67 Hoechst
PROX1 Ki67 Hoechst
AP2α Ki67 Hoechst
NRL Ki67 Hoechst

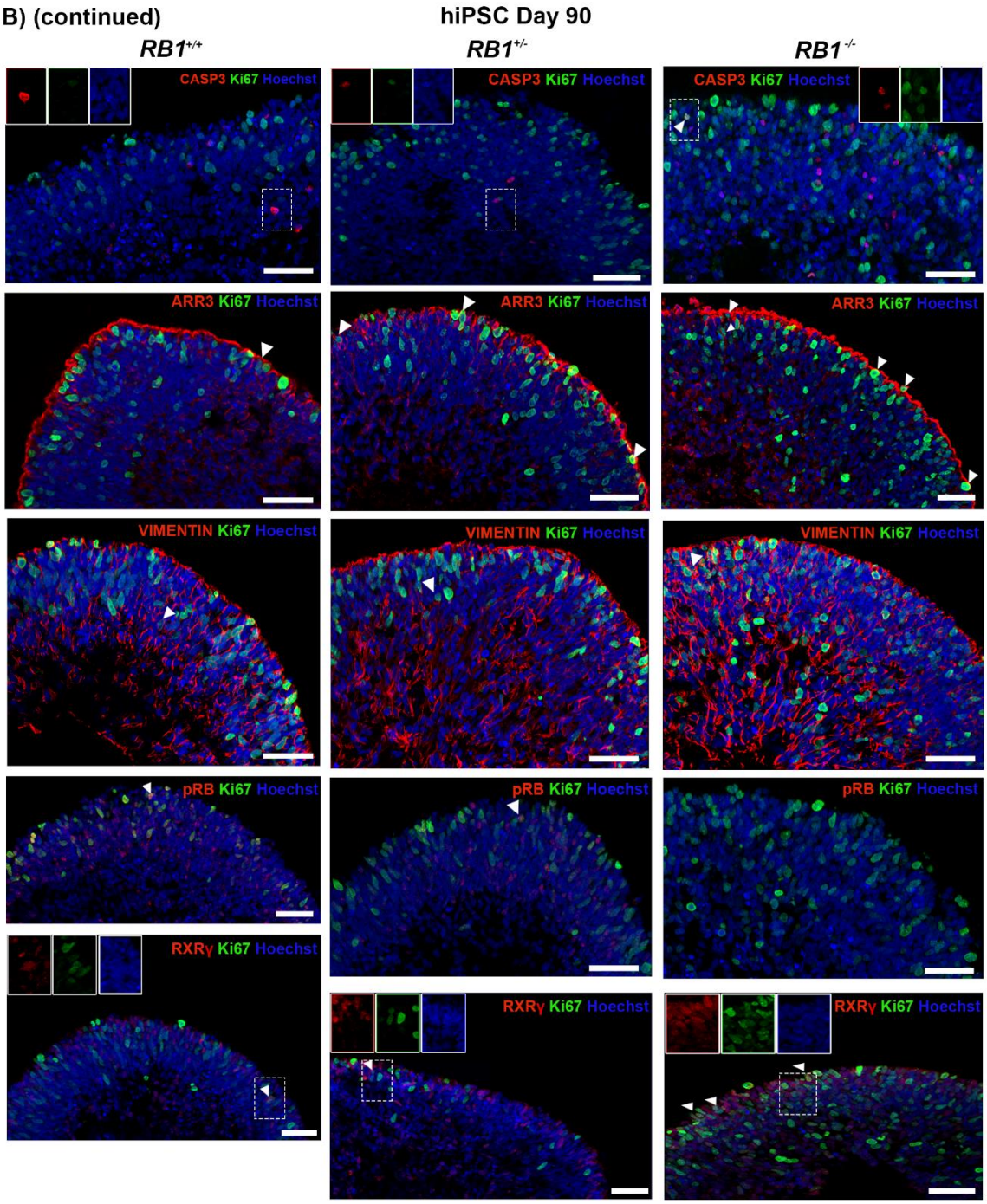

Figure 3-11. Immunohistochemical analysis of patient hiPSC-derived retinal organoids at day 90 of differentiation.
A. Bar charts showing the retinal cell types (left) and Ki67^{+} co-expressing fractions (right). **B.** Representative immunofluorescence analysis for RXRγ, SNCG, PROX1, AP2α, CASP3, Ki67, ARR3, and VSX2, counterstained with Hoechst at day 90. One hiPSC-derived clone per cell line was used for RO differentiation. 12 ROs were used as biological replicates. 10 sections of ROs were cut and imaged. Data are presented as mean ± SEM (n = 10 sections from each biological replicate). Values of $p \leq 0.05$ were considered statistically significant (*$p \leq 0.05$, **$p \leq 0.01$, ***$p \leq 0.001$, ****$p \leq 0.0001$). White arrowheads point at the co-localisation of Ki67 with the specified marker. Scale bars; 50 µm.

Quantitative analysis at day 150 of differentiation indicated a significantly increased fraction of cone precursors (RXRγ^{+}), RGCs (SNCG^{+}), HCs (PROX1^{+}), retinal progenitors (VSX2^{+}), apoptotic (CASP3^{+}), and proliferating (Ki67^{+}) cells in patient *RB1*$^{-/-}$ hiPSC-derived ROs (**Figure 3-12A**). No difference was observed in the fraction of pRB^{+} cells in the heterozygous (*RB1*$^{+/-}$) compared to the isogenic (*RB1*$^{+/+}$) hiPSC-derived ROs. Remarkably, a complete lack of ACs (AP2α^{+}) was observed in *RB1*$^{-/-}$ hiPSC-derived ROs, which was reported since mid-stage differentiation (day 90). ACs were found in the INL in the isogenic (*RB1*$^{+/+}$) control and heterozygous *RB1*$^{+/-}$ hiPSC-derived ROs (**Figure 3-12B**). RGCs were observed in the apical layer and distributed across the different layers of the ROs in the homozygous *RB1*$^{-/-}$ hiPSC-derived ROs as in previous time points of development. Furthermore, results revealed significantly increased fractions of proliferating cone precursors (RXRγ^{+}Ki67^{+}), proliferating RGCs (SNCG^{+}Ki67^{+}), proliferating HCs (PROX1^{+}Ki67^{+}), and proliferating retinal progenitors (VSX2^{+}Ki67^{+}), in patient homozygous *RB1*$^{-/-}$ hiPSC-derived ROs. Finally, the fraction of proliferating cells expressing pRB (pRB^{+}Ki67^{+}) was significantly decreased in heterozygous *RB1*$^{+/-}$ hiPSC-derived ROs (**Figure 3-12A**).

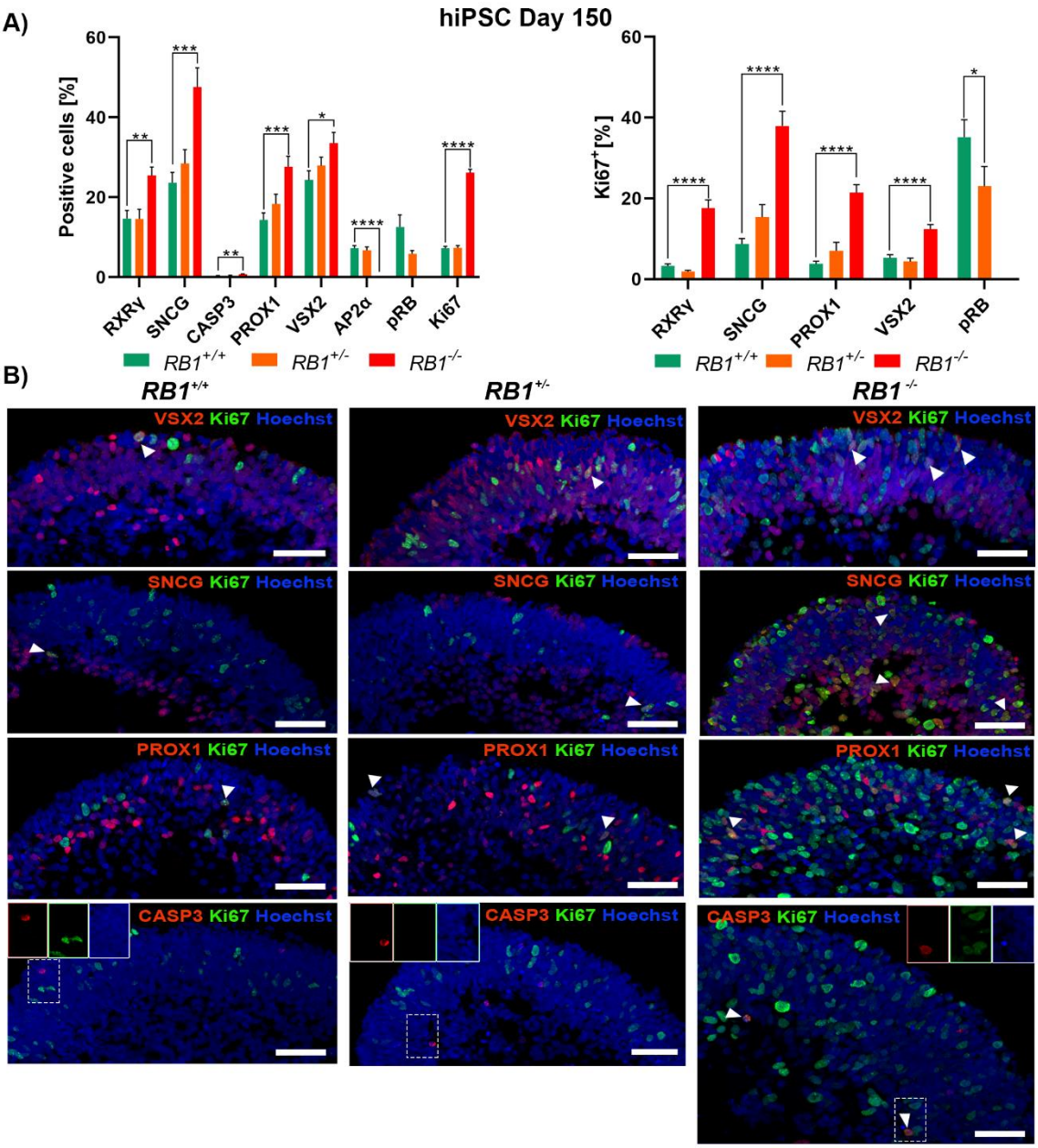
A)
hiPSC Day 150
Positive cells [%]
RXRγ
SNCG
CASP3
PROX1
VSX2
AP2α
pRB
Ki67
RB1+/+
RB1+/-
RB1-/-
Ki67+ [%]
B)
RB1+/+
RB1+/-
RB1-/-
VSX2 Ki67 Hoechst
SNCG Ki67 Hoechst
PROX1 Ki67 Hoechst
CASP3 Ki67 Hoechst

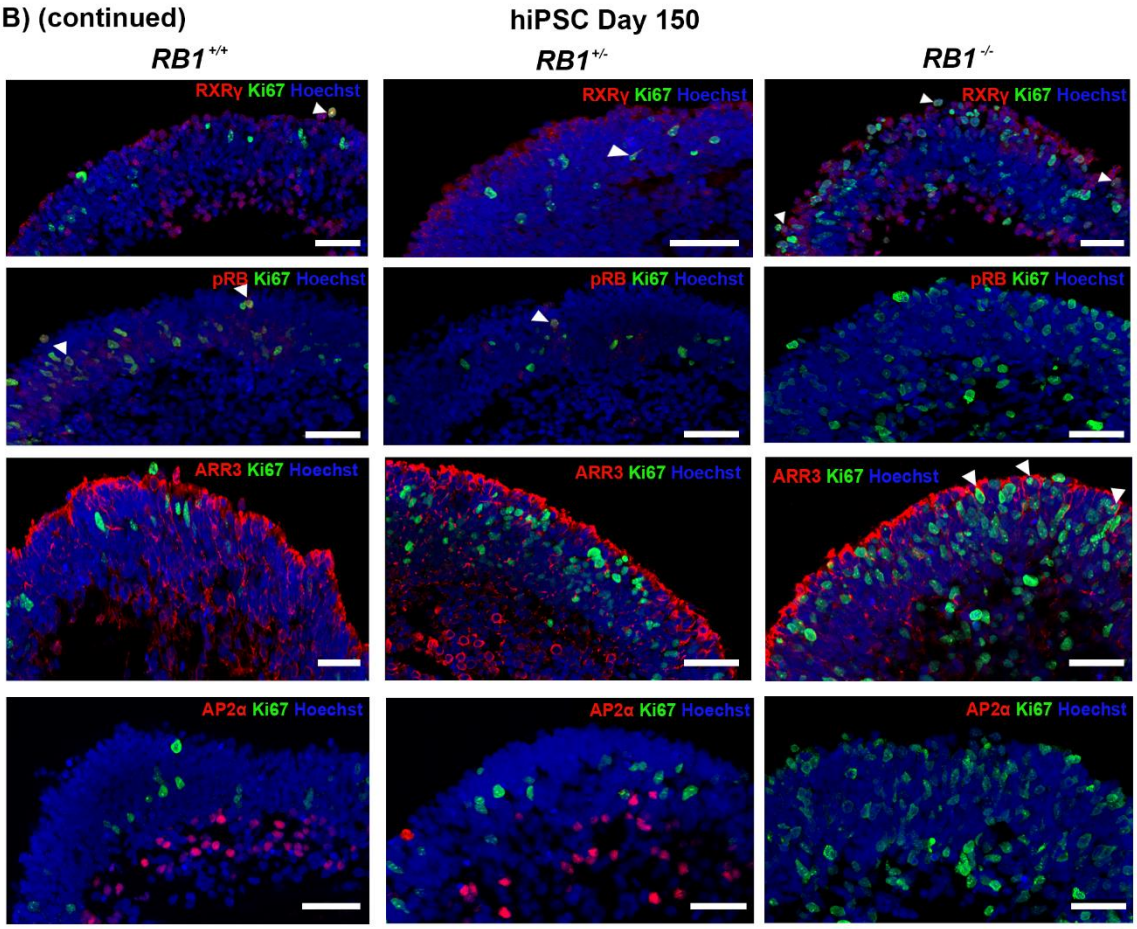

Figure 3-12. Immunohistochemical analysis of patient hiPSC-derived retinal organoids at day 150 of differentiation.
A. Bar charts showing the retinal cell types (left) and Ki67^{+} co-expressing fractions (right). **B.** Representative immunofluorescence analysis for VSX2, SNCG, PROX1, CASP3, RXRγ, pRB, ARR3, AP2α, and Ki67 counterstained with Hoechst at day 150. One hiPSC-derived clone per cell line was used for RO differentiation. 12 ROs were used as biological replicates. 10 sections of ROs were cut and imaged. Data are presented as mean ± SEM (n = 10 sections from each biological replicate). Values of $p \leq 0.05$ were considered statistically significant (*$p \leq 0.05$, **$p \leq 0.01$, ***$p \leq 0.001$, ****$p \leq 0.0001$). White arrowheads point at the co-localisation of Ki67 with the specified marker. Scale bars; 50 µm.

Additionally, the cell cycle phase distribution analyses based on PI staining were performed for the mid-stage and the late stage of retinal development. The results of the analyses confirmed a significantly enriched fraction of cells in the S-phase (3.93%; 4.82%) and G2/M-phase (7.33%; 6.94%) in 90-day-old patient *RB1*$^{+/-}$ and *RB1*$^{-/-}$ hiPSC-derived ROs, respectively, compared to isogenic control (1.64; 2.71%) (**Figure 3-13A**). Similarly, the analyses for day 150 of differentiation reported the enriched fraction of cells in the S-phase (6%) in patient *RB1*$^{-/-}$ hiPSC-derived ROs only compared to isogenic control (0.93%) (**Figure 3-13B**).

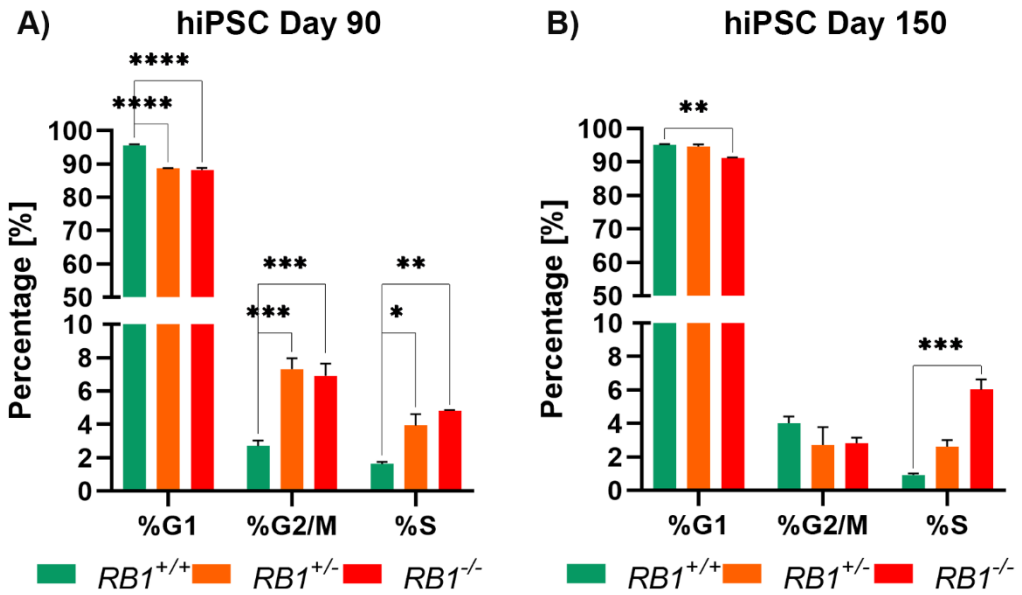

Figure 3-13. Cell cycle phase distribution analysis of patient hiPSC-derived retinal organoids at day 90 and day 150 of differentiation.
Bar charts showing the percentage of the G1-, G2/M-, and S-phase of the cell cycle of patient hiPSC-derived ROs at day 90 (**A**) and day 150 (**B**) of differentiation**.** One hiPSC-derived clone per cell line was used for RO differentiation. 24 ROs per cell line treatment were used as a batch of biological replicates. Data are presented as mean ± SEM (n = 3 repeats from each independently cultured batch of biological replicates). Values of $p \leq 0.05$ were considered statistically significant (*$p \leq 0.05$, **$p \leq 0.01$, ***$p \leq 0.001$, ****$p \leq 0.0001$).

In summary, the homozygous *RB1*$^{-/-}$ patient hiPSC-derived ROs revealed a high level of proliferating retinal progenitors (VSX2^{+}Ki67^{+}), cone precursors (RXRγ^{+}Ki67^{+}), proliferating RGCs (SNCG^{+}Ki67^{+}), proliferating HCs (PROX1^{+}Ki67^{+}) and a complete lack of ACs (AP2α^{+}). Interestingly, an increased fraction of retinal progenitor (VSX2^{+}) cells was observed in the heterozygous *RB1*$^{+/-}$ hiPSC-derived ROs at days 35 and 90 of differentiation. Nevertheless, the higher mitotic and tumourigenic activity was restricted exclusively to the homozygous mutant, indicating that the inactivation of both copies of *RB1* is needed to initiate tumourigenesis. Lastly, cell cycle phase distribution analyses confirmed the enriched fraction of cells in the S-phase in the patient *RB1*$^{-/-}$ hiPSC-derived ROs at mid-stage (day 90) and late stage (day 150) of development as previously seen in pRB-deficient hESC-derived ROs.

3.3.5 Formation of sphere-like aggregates of pRB-depleted retinal organoids in soft colony agar assays indicate transformation in vitro

Soft agar colony assay was performed from dissociated 90- and 150-day-old hESC- and patient hiPSC-derived ROs (**Figure 3-14**). Results revealed small and large sphere-like aggregates only in the H9 RB1-null hESC- and *RB1*$^{-/-}$ hiPSC-derived ROs, indicating cell growth in an anchorage-independent manner and cell transformation *in vitro*. These results suggest that the higher mitotic activity was restricted to the H9 RB1-null hESC- and *RB1*$^{-/-}$ hiPSC-derived ROs, meaning that inactivation of both copies of *RB1* is needed to initiate tumourigenesis.

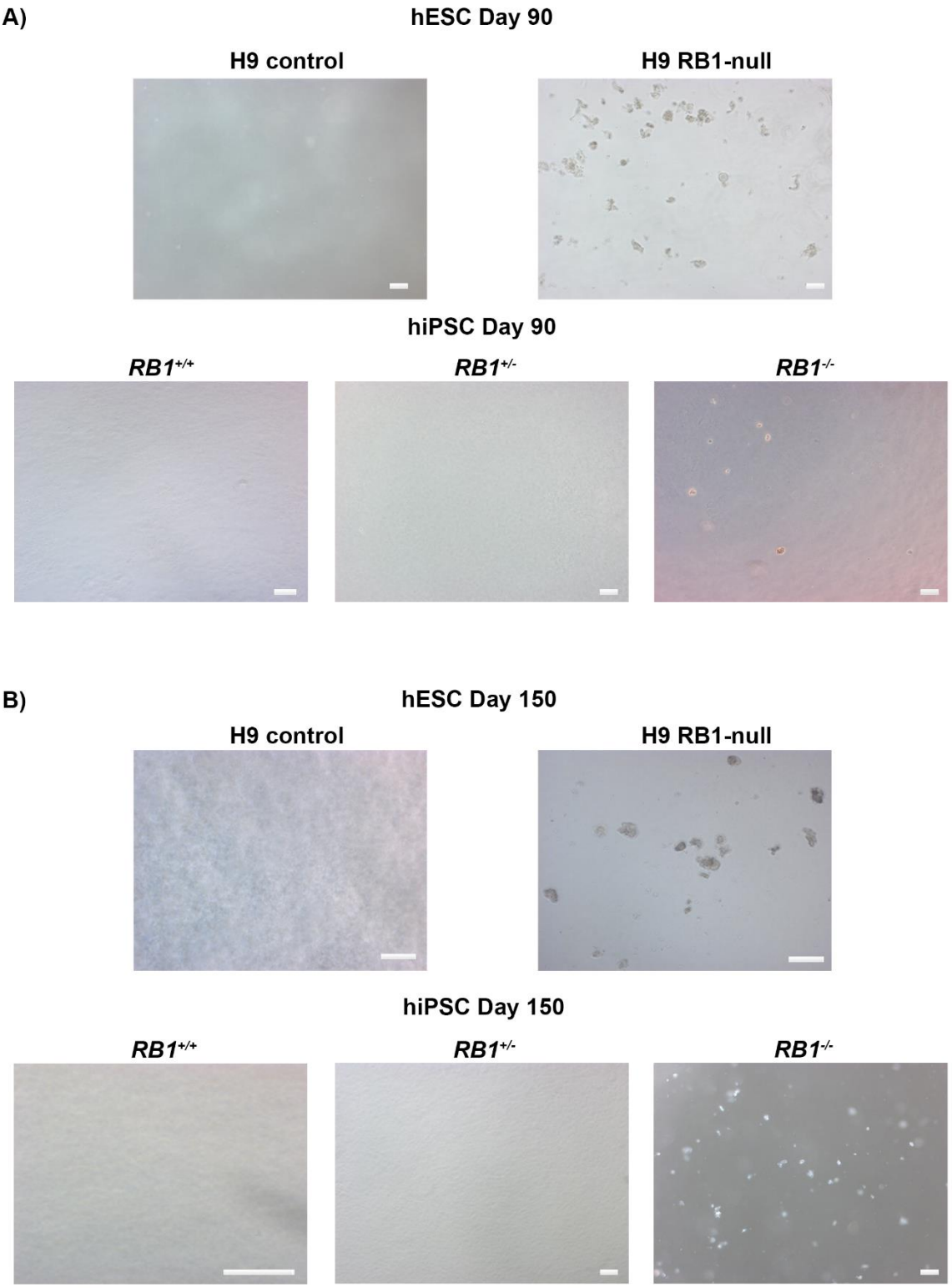

Figure 3-14. Tumourigenic characteristics of pRB-depleted hESC- and patient hiPSC-derived retinal organoids.

Bright-field images of soft agar colony formation assay showing the ability of pRB-depleted retinal cells originating from day 90 (**A**) and day 150 (**B**) H9 RB1-null hESC- and patient *RB1*$^{-/-}$ hiPSC-derived retinal organoids to grow in suspension. Scale bars; 100 µm.

3.4 Discussion

pRB is a functional tumour suppressor and regulator of the cell cycle progression that is affected in multiple malignancies (Di Fiore et al., 2013), including Rb (Sachdeva and O'Brien, 2012). Inactivation of both copies of the *RB1* gene is a causative factor of Rb. Current management protocols include systemic, intravitreal, intraarterial and periocular chemotherapeutic treatments (Yanık et al., 2015), aiming to salvage the ocular globe and the patient's visual function (Saengwimol et al., 2018). The current chemotherapeutic drugs include melphalan, topotecan, etoposide, vincristine, and carboplatin (Yanık et al., 2015). Promising new Rb treatment agents include novel molecules such as TW-37, which is reported to inhibit tumour growth by inducing apoptosis (Zeitlin et al., 2008). Enucleation is performed in recurrent tumour growths, and preserving the eye-sight proves challenging due to extended retinal damage (Dimaras et al., 2015, Dyer, 2016, Berry et al., 2017, Kong et al., 2020). Understanding Rb malignancies at the molecular, cellular, genetic, and epigenetic levels is crucial for designing new and efficacious therapies for tumour growth treatment.

As RO differentiation is a well-established method in Lako's group (Hallam et al., 2018, Mellough et al., 2019b), two Rb disease models were developed (Rozanska et al., 2022) through CRISPR/Cas9 inactivation of the *RB1* gene in PSCs. ROs were derived from hESCs and patient hiPSCs from a child with heterozygous *RB1* mutation (c.2082delC) who developed bilateral tumour growths before the age of 4. Isogenic wild-type ($RB1^{+/+}$) and homozygous ($RB1^{-/-}$) hiPSC lines were genetically engineered to compare patient phenotypes within the same genetic background. Thus, hESC- and hiPSC-derived ROs were differentiated using the protocol developed in our group (Hallam et al., 2018). Immunofluorescence analyses were performed to characterise the retinal cell populations in the ROs. The emergence of the laminated neural retina was assessed at several time points, including the early stage (day 35), mid-stage (day 90), and mature stage (day 150) of differentiation, where the pRB-depleted ROs exhibited a lack of pRB expression throughout development.

Results for the characterisation of hESC- and hiPSC-derived ROs at an early stage (day 35) of differentiation revealed common features for pRB-depleted ROs: **1)** a significant increase in proliferating RGCs ($SNCG^+Ki67^+$); and **2)** an increase in proliferating retinal progenitors ($VSX2^+Ki67^+$). It is possible to speculate that the inactivation of *RB1* at an early stage of development deregulated cell differentiation and proliferation, which resulted in the increase in at least one or more specific retinal cell types and proliferating cells in the pRB-depleted ROs. RGCs are the earliest-born neurons, and it could be that the inactivation of *RB1* led to an increase in the proliferation of this cell type and early retinal progenitors.

Subsequently, results for mid-stage (day 90) and late-stage (day 150) development revealed common features in pRB-depleted ROs: **1)** a significant increase of RGCs ($SNCG^+$), apoptotic ($CASP3^+$ confirmed the increase of the cleaved-caspase-3 steady-state levels), and proliferating ($Ki67^+$) cells; **2)** a decrease of ACs ($AP2\alpha^+$) in H9 RB1-null hESC-derived ROs and surprisingly no $AP2\alpha^+$ cells in homozygous ($RB1^{-/-}$) hiPSC-derived ROs; and **3)** an increase of proliferating cone precursors ($RXR\gamma^+Ki67^+$) and RGCs ($SNCG^+Ki67^+$).

In summary, both pRB-depleted models shared the following key features throughout development: **1)** increased fraction of proliferating cone precursors ($RXR\gamma^+Ki67^+$), RGCs ($SNCG^+Ki67^+$) and retinal progenitors ($VSX2^+Ki67^+$); **2)** an increased percentage of proliferating ($Ki67^+$) and apoptotic ($CASP3^+$) cells; **3)** decreased fraction of ACs ($AP2\alpha^+$) from day 90 of differentiation; and **4)** a lack of *RB1* expression in homozygous ($RB1^{-/-}$) and a significant decrease of the pRB^+ cell fraction in the heterozygous ($RB1^{+/-}$) hiPSC-derived ROs.

The pRB-depleted ROs generated from both models showed similar features to Rb tumours. Notably, we reported cell growth in an anchorage-independent manner in our soft colony formation assays from dissociated pRB-depleted ROs, indicative of cell transformation *in vitro*, but not those derived from wild-type or heterozygous ($RB1^{+/-}$) hiPSC-derived ROs. A publication from one group (Zheng et al., 2020) did not report any Rb cells nor tumourigenicity from their human $RB1^{-/-}$ RO models when performing the soft agar assay. None of the cells from wild-type and $RB1^{-/-}$ ROs exhibited anchorage-independent growth and failed to form clones in the agar. The authors hypothesise the lack of tumour formation in their $RB1^{-/-}$ RO model

is due to the hESC origin and lack of cells sensitive to *RB1* depletion. However, our work (Rozanska et al., 2022) reported the characterisation and tumourigenicity of pRB-depleted ROs derived from hESCs and patient hiPSCs. Additionally, their haematoxylin and eosin (H&E) staining did not reveal any rosette-like structure similar to Flexner–Wintersteiner and Homer Wright rosettes. Nonetheless, our work (Rozanska et al., 2022) via transmission electron microscopy (TEM) did report mitochondrial cristae aberrations and rosette-like structures in H&E staining of pRB-depleted ROs. Interestingly, another group (Li et al., 2022) reported similar results to ours by demonstrating the same ultrastructural features, tightly packed clusters of cells and rosette-like structures of *RB1*$^{-/-}$ ROs as seen in Rb tumours.

Furthermore, (Saengwimol et al., 2018) reported the presence of RXRγ in chemotherapy-naïve tumour organoids and its relevance for maintaining and developing L/M-cones. They co-stained RXRγ, OPN1SW and OPN1LW/MW with Ki67 markers and reported neoplastic L/M-cones but rarely detected S-cones and described them as non-proliferative. These findings agree with the results presented in this study of decreased S-cones and no proliferation in H9 RB1-null hESC-derived ROs. The authors did not report any Nrl^{+} or RHO^{+} cells in tumour organoids, while our study showed that Nrl^{+} cells were detected on days 90 and 150 and RHO on day 150 in H9 RB1-null hESC-derived ROs. However, differences presented in our results compared to data shown by the authors rely on the underlying completely different origin of ROs as theirs came from chemotherapy-naïve tumours while ours were PSC-derived.

Proliferating cone precursors (RXRγ^{+}Ki67^{+}) were a common feature of pRB-depleted ROs, which suggests that this specific proliferating cell type forms the cell of origin for human Rb. Multiple scRNA-seq studies performed on pRB-depleted ROs and Rb tumours from different groups (Liu et al., 2020, Kanber et al., 2022, Li et al., 2022, Yang et al., 2021b, Wu et al., 2022) have also suggested an Rb cell of origin stemming from a maturing cone precursor (ARR3^{+}) which agree with data from our work on Rb tumours (Collin et al., 2021) and organoids (Rozanska et al., 2022) suggesting that these G2/M precursors escaped cell cycle arrest and/or p53-mediated apoptosis. A common finding of these scRNA-seq studies was the excessive cluster of cone precursors in the pRB-depleted ROs that expressed abundant cone precursor markers, *ARR3* and *RXRG*. Furthermore, (Liu et al., 2020)

theorised that the retinoma-like cells could be in a transition stage between premalignant cone precursors and tumour cells, which was later suggested by our scRNA-seq data (Rozanska et al., 2022) and by (Li et al., 2022).

In contrast, (Norrie et al., 2021) hypothesised an Rb cellular identity bias towards RPCs or rods due to the presence of highly proliferative tumour cells with the retinal progenitor identity, giving rise to more differentiated tumour cells with rod and other neuron features. In fact, our study (Rozanska et al., 2022) showed that RPCs prevail following *in vitro* pRB-depletion, suggesting a role of pRB in retinal cell differentiation. However, single-cell lineage tracing studies would be required to fully address the hypothesis of an RPC/rod identity for Rb.

Increased fractions of proliferating RGCs ($SNCG^{+}Ki67^{+}$) and HCs ($PROX1^{+}Ki67^{+}$) were observed during the development of pRB-depleted ROs in our study (Rozanska et al., 2022). However, we provided evidence through scRNA-seq that the fraction of HCs and RGCs was decreased and that markers for these cells were expressed in Rb cell clusters. Additional analyses revealed that the starting cone precursors acquire expression of RGC and HC markers upon entry into the cell cycle. (Liu et al., 2021) in their multi-omics research study identified two different molecular subtypes of human Rb from patients' tumours. Both Rb subtypes exhibited maturing cone precursor ($ARR3^{+}$) markers in agreement with a cone precursor cell origin of human Rb. Further analyses indicated that subtype 2 tumours also had an *MDM4* and *MYCN* amplification and overexpression of markers attributed to RGCs and neuronal markers (including *SOX11, DCX, STMN2*) associated with other retinal cell types. These findings involving the expression of neuronal/RGC markers in the less differentiated cone cells in Rb tumours support our results of acquired HC and RGC markers in cone precursors from pRB-depleted ROs.

scRNA-seq analyses have revealed that cone precursors express RGC and HC markers in patient Rb tumours and human pRB-depleted ROs. Interestingly, it has been suggested in the murine model that an HC, as a fully differentiated neuron, is the cell of origin in mouse Rb (Ajioka et al., 2007). In their study, Rb tumours in p107-single mice did not expand by a stem cell mechanism but by a differentiated HC clonal expansion. In addition, (Pajovic et al., 2011) showed that the cell originating Rb in a murine model had features of differentiated Müller glial cells with

progenitor properties. Moreover, (Xu et al., 2014) suggested that human and mouse retinal tumours derive from different intrinsically death-resistant phenotypes, which would support the notion that human Rbs have a different precursor cell of origin from the murine Rb model. In fact, we reported (Rozanska et al., 2022) an increased fraction of proliferating HCs ($PROX1^{+}Ki67^{+}$) in both pRB-depleted RO models at a late stage of development. This could be explained by starting cone precursors acquiring HC markers upon entry into the cell cycle, as scRNA-seq analyses revealed. Therefore, these results point to a cell of origin different from an interneuron for human Rb.

Kanber *et al.* generated homozygous, heterozygous and isogenic *RB1* hESC-derived ROs through CRISPR/Cas9 mutagenesis (Kanber et al., 2022) similar to our pRB-depleted RO model (Rozanska et al., 2022). The authors reported enrichment and proliferation of cone precursors and maturing cone PRs, supporting the idea of these cone cells as the cell of origin of human Rb. These results agree with work from our group (Rozanska et al., 2022, Collin et al., 2021). This study also described the decrease of rods and ACs, and the expression of S- and L/M-opsins restricted only to a few cells, which agrees with our results. Finally, their transcriptome analysis revealed an upregulation of *RBL1* (p107), *MDM2, DEK, SYK* and *HELLS* as a gain of the Rb expression signature. These results primarily agree with work from our group (Collin et al., 2021) reporting high expression of *DEK,* low expression of *MDM2* but high *MDM4* expression in Rb tumours, and *DEK, SYK* and retinoma marker *HELLS* (Rozanska et al., 2022) in pRB-depleted ROs. However, their study was limited to pRB-depleted hESC-derived ROs that could not be kept beyond 130 days of differentiation as they described aberrant organoid differentiation and disintegration. Our study had pRB-depleted hESC- and patient hiPSC-derived ROs in continuous culture after 150 days of differentiation.

Interestingly, (Norrie et al., 2021) recapitulated human Rb formation by combining *in vitro* 3D RO culture and an *in vivo* murine model. They reported the generation of hiPSCs from 15 patients with germline *RB1* mutations and the subsequent RO differentiation up to day 45 before dissociating and intravitreally injecting them into immunocompromised mice. Tumour formation was observed, and it was indistinguishable from human Rb tumours. Nonetheless, limitations to this study include only hiPSC-derived ROs that were kept in culture until day 45, and the

requirement of a detailed characterisation *in vitro* of the patient *RB1* hiPSC-derived ROs for drug testing, which was covered in our study (Rozanska et al., 2022) as characterised hESC- and hiPSC-derived ROs were kept viable beyond day 150.

In a recent research study using patient hiPSCs, (Li et al., 2022) generated heterozygous and homozygous *RB1* mutant hiPSC-derived ROs. Their results exhibited tumourigenesis *in vitro* and a significant increase in proliferating and maturing cone precursors ($ARR3^{+}Ki67^{+}$) in the $RB1^{-/-}$ ROs, as we also showed. Consistent with Rb profiles in spatiotemporal transcriptomes, they reported highly expressed PR fate-determining markers, *CRX* and *OTX2* in the mutant $RB1^{-/-}$ ROs. Moreover, the *OTX2* marker was also observed as a key gene implicated in two Rb tumours in the scRNA-seq analysis from our group (Collin et al., 2021). The authors also reported abundant Flexner-Wintersteiner rosette-like structures in the pRB-depleted ROs, similar to our results (Rozanska et al., 2022) as pathological hallmarks of differentiated Rb. Together with our publication, these results demonstrate the feasibility of Rb organoids for studying tumourigenesis and developing novel Rb chemotherapeutics, as these organoid models recapitulate the development of Rb tumours.

Remarkably, some differences were observed between our hESC- and hiPSC-derived RO disease models. These minor differences observed between our RO models cannot be attributed to differences in *RB1* inactivation, as pRB depletion was confirmed in both cases. They are likely due to the epigenetic starting point of hESC versus hiPSC lines, hiPSC clonal variations or the patient's genetic background. This matter could be addressed in a following study with a larger number of hiPSC clones from a larger number of patients with *RB1* mutations.

Still, both RO models shared the same pattern of increased apoptotic and proliferating cone precursor cells. Our work (Rozanska et al., 2022) in pRB-depleted ROs showing a decrease in HCs, ACs, and RGCs might indicate that pRB dysfunction could interfere with retinal cell differentiation or survival. Reducing specific cell populations in the absence of pRB could be a compensatory response to an increase in the proliferation of cone precursor cells, which agrees with (Zheng et al., 2020), where the authors reported that pRB is required for PR and BC differentiation. Interestingly, the accumulation of RPCs (Rozanska et al., 2022) and

the lack of ACs (AP2α^{+}) in patient *RB1*$^{-/-}$ hiPSC-derived ROs from day 90 may respond to a block in differentiation. A previous study (Li et al., 2010) showed the incompatibility between TFAP2A (AP2α) protein expression in ACs and survival in Rb cell lines and tumours. Our study's analyses of scRNA-Seq data (Rozanska et al., 2022) suggested that this block in differentiation might occur either before or after the development of transient neurogenic RPCs (T1), which are thought to give rise to these retinal cell lineages. Furthermore, the enhanced accumulation of RPCs in pRB-depleted ROs was at the expense of ACs, HCs, and RGCs, suggesting a key role for pRB in retinal cell differentiation, as data revealed a block in AC differentiation observed in Rb tumours and pRB-depleted ROs.

Moreover, a cell proliferation increase in Rb ROs agrees with an essential increase in the steady-state level of E2F1 (Saavedra et al., 2002), as we reported (Rozanska et al., 2022). Another common observation in our disease models was the cell accumulation and entry to the S-phase. These features are promoted in a loss of pRB, as studies reported in ROs (Zheng et al., 2020) and mouse cerebral organoids (Matsui et al., 2017), which we confirmed in our pRB-depleted hESC- and patient hiPSC-derived ROs. Cell-cycle phase distribution analyses supported an enriched fraction of cells in the S-phase during the mid and late stages of retinal development.

Lastly, a research study by (Blixt et al., 2022) established an Rb disease model system using chicken retina and tumourigenic human *RB1*-proficient hESC-derived ROs by overexpressing *MYCN*. Results showed tumourigenic cells expressing markers of cone PR and HC progenitors. However, a cone PR of various degrees of maturation was the dominating phenotype, which is consistent with our results.

3.5 Conclusion

We have developed and fully characterised hESC- and patient *RB1* hiPSC-derived RO models and shown that both are defined by a significant increase in the fraction of apoptotic cells (CASP3^{+}), proliferating RGCs (SNCG^{+}Ki67^{+}) and proliferating cone precursors (RXRγ^{+}Ki67^{+}). pRB-depleted ROs exhibited an enriched fraction of cells in the S-phase during the mid and late stages of retinal development. Additionally, these ROs formed sphere-like aggregates indicating cell

growth in an anchorage-independent manner and cell transformation *in vitro*. These results suggest that the higher mitotic activity was restricted to the pRB-depleted ROs, meaning that the inactivation of both copies of *RB1* is needed to initiate tumourigenesis. Importantly, we have demonstrated that these two models robustly recapitulate Rb's development and malignant transformation *in vivo*. This work was peer-reviewed and published in (Rozanska et al., 2022).

Chapter 4

4 Drug screening of hESC- and patient hiPSC-derived retinal organoids

4.1 Introduction

New chemotherapeutic agents and repurposed drugs are needed to develop novel treatments that are more effective and specific for Rb management. The availability of preclinical models is restricted to mimicking the retinal response and clinical observations of chemotherapeutic treatments. A thorough pharmacological characterisation is needed to select adequate candidates for Rb treatment according to their specific tumour cytotoxicity (Schaiquevich et al., 2022). Nonetheless, multiple factors should be considered for clinical application, including the antitumour activity, drug penetration across the ocular and brain barriers, toxicity profile, and access to formulations (Cancela et al., 2021). Chemotherapy agents broadly used alone or in combination based on the favourable ocular disposition to treat Rb with a variable degree of success include melphalan, topotecan, carboplatin, and Bcl-2 inhibitors such as TW-37 (Saengwimol et al., 2018).

Melphalan is an alkylating agent that forms DNA inter-strand crosslinks leading to a cytotoxic response and apoptosis (Vasquez, 2010, Mougenot et al., 2006). It has been used to treat a variety of malignancies, including breast and ovarian cancer, lymphomas, neuroblastomas, acute leukaemias, and multiple myeloma, due to its extensive antitumor efficacy (Sarosy et al., 1988, Bayraktar et al., 2013). It is the most often used chemotherapeutic drug delivered intraarterially and intravitreally for recurrent vitreous seeds after Rb treatment. Unfortunately, adverse effects such as retinal toxicity, chorioretinopathy, electroretinographic abnormalities, RPE alterations, and retinal vasculitis, among other complications in darkly pigmented iris (physical association to melanin), including pupillary synechiae, iris atrophy, and cataracts are associated with melphalan administration (Paez-Escamilla et al., 2017, Xue et al., 2019).

Topotecan is a topoisomerase I enzyme inhibitor and anticancer drug that targets DNA replication. It was developed as a semisynthetic version of camptothecin (Dennis et al., 1997) that induces a p53 response in Rb cells (Laurie et al., 2006). The antineoplastic activity was first observed in small-cell lung cancer, haematologic malignancies, paediatric neuroblastoma, and rhabdomyosarcoma

(Takimoto and Arbuck, 1997). Pharmacologic studies of topotecan combined with carboplatin, cisplatin, doxorubicin, and etoposide have been completed in patients with solid tumours with documented primary antineoplastic responses but with exhibited toxicologic effects (Rowinsky and Kaufmann, 1997). Currently, it is well established for Rb treatment in systemic and intravitreal chemotherapies as it causes less cytotoxic effects, but it may also be less effective than melphalan for managing persistent vitreous seeds (Winter et al., 2019, Paez-Escamilla et al., 2017, Rao et al., 2018b).

TW-37 is a novel small molecule inhibitor of the Bcl-2 family (B-cell leukaemia anti-apoptotic proteins) that induces cell apoptosis, inhibits tumour growth, particularly in melanoma-derived tumours, and reduces the microvessel density in angiogenesis (Zeitlin et al., 2008). The Bcl-2 family proteins are crucial in balancing cell proliferation and apoptosis regulation (Lei et al., 2017) and can be divided into two categories: anti-apoptosis and pro-apoptotic. Preclinical studies revealed that TW-37 reduced the tumour size in xenograft models and cell proliferation of pancreatic and B-cell lymphomas (Mohammad et al., 2007). Thus, TW-37, as an inhibitor of the Bcl-2 family, highlights its efficacy against chemotherapy-resistant tumours. The most valuable features shared by these Bcl-2 inhibitors are their low overall cytotoxicity compared to conventional chemotherapeutic agents and their synergising ability with other drugs to inhibit tumour cell survival (Zeitlin et al., 2008).

Current chemotherapy treatments for Rb management include the following delivery routes (Yanık et al., 2015):

1. **Systemic**: comprises a drug injection into a vein or oral intake. Chemotherapeutic agents such as melphalan, topotecan, vincristine, etoposide, and carboplatin are widely used. Their application is limited to treating retinal seeds that exhibit massive infiltration, as penetration of drugs is challenging in systemic delivery.
2. **Intravitreal**: direct injection of melphalan and/or topotecan (Schaiquevich et al., 2022) into the vitreous humour that increases the bioavailability of drugs in-site. This method achieves the highest concentration of the drug in the confined intraocular space, allowing improved control of vitreous seeds.

3. **Intraarterial**: a melphalan injection that can also be combined with topotecan and carboplatin into the ophthalmic artery. This approach can halt the development of new tumours in patients with genetic Rb.
4. **Periocular:** a carboplatin injection that usually allows a higher local drug concentration. The delivery route can be either subconjunctival or subtenon's space location, circumventing the blood-retinal barrier.

Vitreous seeding is a substantial problem in Rb treatment since the vitreous is an avascular tissue, meaning that the transition of drugs via intraarterial administration is restricted (Winter et al., 2019). If vitreous seeding is recurrent, it may lead to enucleation of the affected eye (Süsskind et al., 2016). Over the last decade, there has been a shift in Rb treatment from systemic chemotherapy infusion to intravitreal injection due to the low bioavailability of drugs in retinal tissue and adverse toxic effects (Winter et al., 2019).

Finally, large libraries of compounds should be assessed using high-throughput screens of several cell lines for accounting for the diverse drug response observed in patients (Schaiquevich et al., 2022). To this end, validating a 3D *in vitro* RO model for Rb is an essential step in novel drug discovery, allowing for assessing drug response and cytotoxicity before translation to clinical application.

4.2 Aims

The main aim of this chapter was to validate the hESC- and patient hiPSC-derived retinal organoid models for drug testing applications. This study used two hESC lines (H9 control and H9 RB1-null hESC) and three patient-specific hiPSC lines (*RB1*$^{-/-}$, *RB1*$^{+/-}$, *RB1*$^{+/+}$ hiPSC) for RO differentiation as described in **3** of this thesis document. Three clinically used chemotherapeutic agents (melphalan, topotecan, and TW-37) were tested on both pRB-depleted RO models. Drug responses of the ROs were evaluated for cytotoxicity, immunohistochemistry, fluorescence microscopy, and soft agar assay. Positive cell quantification from immunofluorescence images was used to assess the effects of the chemotherapeutic agents on proliferating and apoptotic cone precursor cells. Identification of the most affected retinal cell types after the drug treatments was assessed by proliferation, apoptosis, and cone precursor cell type-specific markers.

4.3 Results

4.3.1 Dose-dependent significant increase of cytotoxicity and cell death in drug-treated retinal organoids

To assess the application of hESC- (**Figure 4-1**) and patient hiPSC-derived (**Figure 4-2**) ROs for testing therapeutic agents, organoids were incubated for 72 hours with varying doses of three drugs used in current treatments of Rb tumours: melphalan, topotecan, and TW-37. Melphalan is an alkylating agent that is highly effective against Rb, but high concentrations (Winter et al., 2016) are needed to reach its metronomic IC50 (50% inhibitory concentration) *in vitro*, attainable only after intraarterial or intravitreal chemotherapy (Dalvin et al., 2019). Topotecan is a topoisomerase inhibitor, which prevents topoisomerase-I from re-ligating the nicked DNA strand, resulting in DNA damage and cell death (Rao et al., 2018a). It is effective against Rb in combination with melphalan. Bcl-2 inhibitors such as TW-37 compete with pro-apoptotic proteins (such as Bid, Bim, and Bad) and induce apoptosis (Zeitlin et al., 2008).

Results indicated cell death (assessed by LDH release percentage) specific to be in 32 µM melphalan, 10-15 µM topotecan and 1-10 µM TW-37 treatments in 90-day-old H9 RB1-null hESC-derived ROs (**Figure 4-1A-C**). Then, cell death was specific in 16-32 µM melphalan and 10 µM topotecan treatments in 150-day-old H9 RB1-null hESC-derived ROs (**Figure 4-1D-F**).

Figure 4-1. Cytotoxicity assessment of chemotherapeutic agents for Rb treatment in 90- and 150-day-old H9 control and H9 RB1-null hESC-derived retinal organoids.
Bar graphs showing cytotoxicity of the specified agent [melphalan; 8, 16, 32, 320 µM (**A, D**), topotecan; 5, 10, 15, 150 µM (**B, E**), TW-37; 0.1, 0.5, 1,10 µM (**C, F**) alongside vehicle-treated sample; 0.1% DMSO] measured by LDH release into the supernatant of hESC-derived organoids. The 100% cytotoxicity value corresponds to the Maximum LDH activity of Triton-X-100. 12 ROs per treatment were used as biological replicates. Data presented as mean ± SEM (n = 5 wells from each biological replicate). Values of $p \leq 0.05$ were considered statistically significant (*$p \leq 0.05$, **$p \leq 0.01$, ***$p \leq 0.001$, ****$p \leq 0.0001$). **G.** Table summarises positive cytotoxicity response for drug-treated hESC-derived ROs at specified concentrations in days 90 and 150 of differentiation ('X' indicates statistically significant change at the specified condition compared to the vehicle control; cells with a green background colour indicating specific effects of the specified drug in H9 RB1-null hESC-derived ROs).

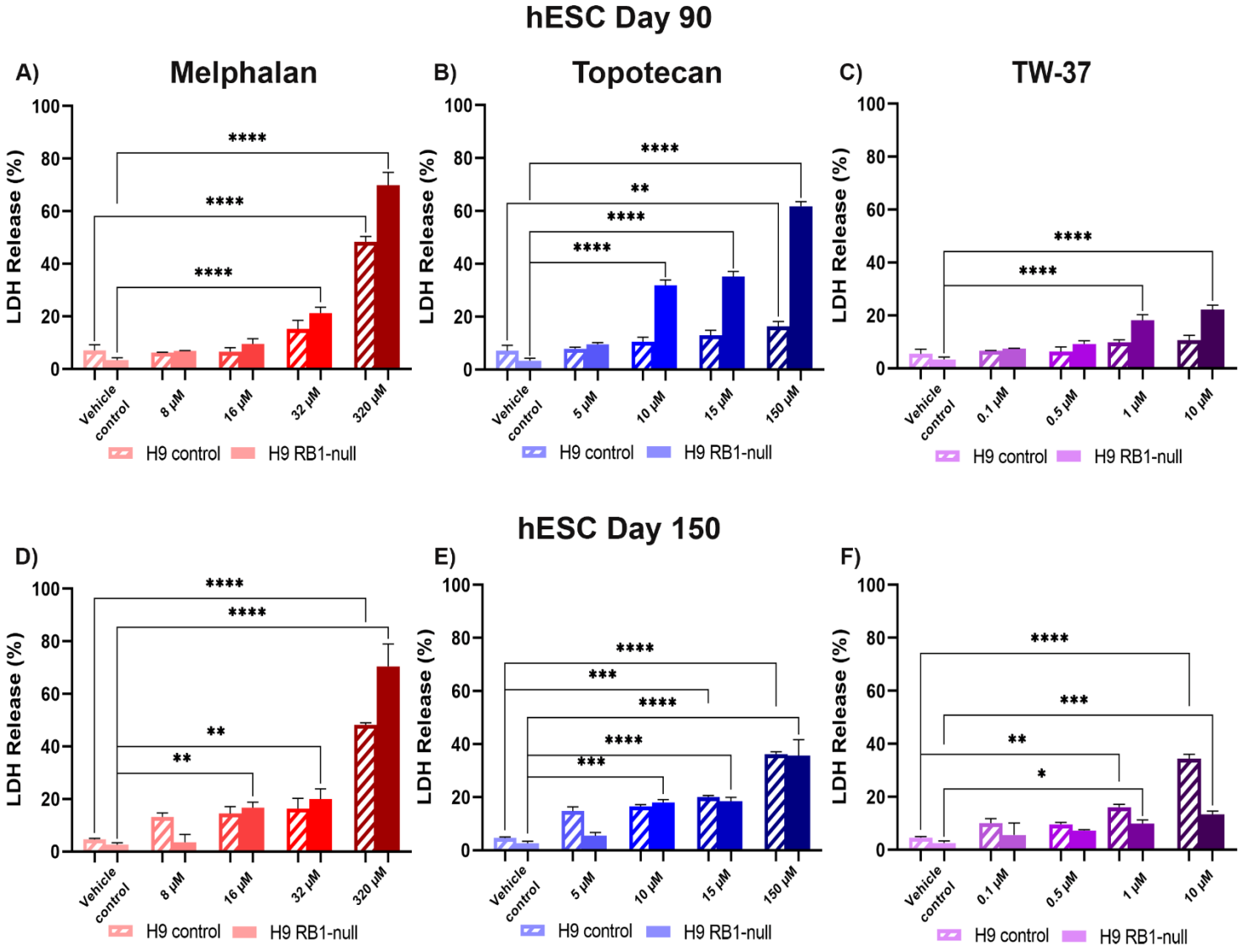

G)

Day 90		H9	H9 RB1-null
Melphalan	8 µM		
	16 µM		
	32 µM		X
	320 µM	X	X
Topotecan	5 µM		
	10 µM		X
	15 µM		X
	150 µM	X	X
TW-37	0.1 µM		
	0.5 µM		
	1 µM		X
	10 µM		X

Day 150		H9	H9 RB1-null
Melphalan	8 µM		
	16 µM		X
	32 µM		X
	320 µM	X	X
Topotecan	5 µM		
	10 µM		X
	15 µM	X	X
	150 µM	X	X
TW-37	0.1 µM		
	0.5 µM		
	1 µM	X	X
	10 µM	X	X

Cytotoxicity analyses for day 90 (**Figure 4-2A-C**) patient *RB1*$^{-/-}$ hiPSC-derived ROs revealed specific cell death in 16 µM melphalan, 5-10 µM topotecan and 1 µM TW-37 treatments. Results for day 150 (**Figure 4-2D-F**) patient *RB1*$^{-/-}$ hiPSC-ROs revealed specific cell death in 16-32 µM melphalan, 10-150 µM topotecan, and 0.5-1 µM TW-37 treatments. Thus, data for the mature stage (day 150) confirm the specificity of the cytotoxic effects of Rb chemotherapeutic agents when administered within the clinical range in pRB-depleted patient hiPSC-derived ROs.

Regarding results for day 90 (**Figure 4-2A-C**), patient *RB1*$^{+/-}$ hiPSC-derived ROs, 16 µM melphalan and 5-10 µM topotecan treatments caused specific cytotoxicity. Then, data for day 150 patient *RB1*$^{+/-}$ hiPSC-derived ROs (**Figure 4-2D-F**) revealed no specific cell death for any treatments.

Figure 4-2. Cytotoxicity assessment of chemotherapeutic agents for Rb treatment in 90- and 150-day-old patient hiPSC-derived retinal organoids.
Bar graphs showing cytotoxicity of the specified agent [melphalan; 8, 16, 32, 320 µM (**A, D**), topotecan; 5, 10, 15, 150 µM (**B, E**), TW-37; 0.1, 0.5, 1,10 µM (**C, F**) alongside vehicle-treated sample; 0.1% DMSO] measured by LDH release into the supernatant of patient *RB1*$^{+/+}$, *RB1*$^{+/-}$ and *RB1*$^{-/-}$ hiPSC-derived organoids. The 100% cytotoxicity value corresponds to the Maximum LDH activity of Triton-X-100. One hiPSC-derived clone per cell line was used for RO differentiation. 12 ROs per treatment were used as biological replicates. Data presented as mean ± SEM (n = 5 wells from each biological replicate). Values of $p \leq 0.05$ were considered statistically significant (*$p \leq 0.05$, **$p \leq 0.01$, ***$p \leq 0.001$, ****$p \leq 0.0001$). **G.** Table summarises positive cytotoxicity response for drug-treated hiPSC-derived ROs at specified concentrations in days 90 and 150 of differentiation ('X' indicates statistically significant change at the specified condition compared to the vehicle control; cells with a green background colour indicating specific effects of the specified drug in *RB1*$^{-/-}$ hiPSC-ROs).

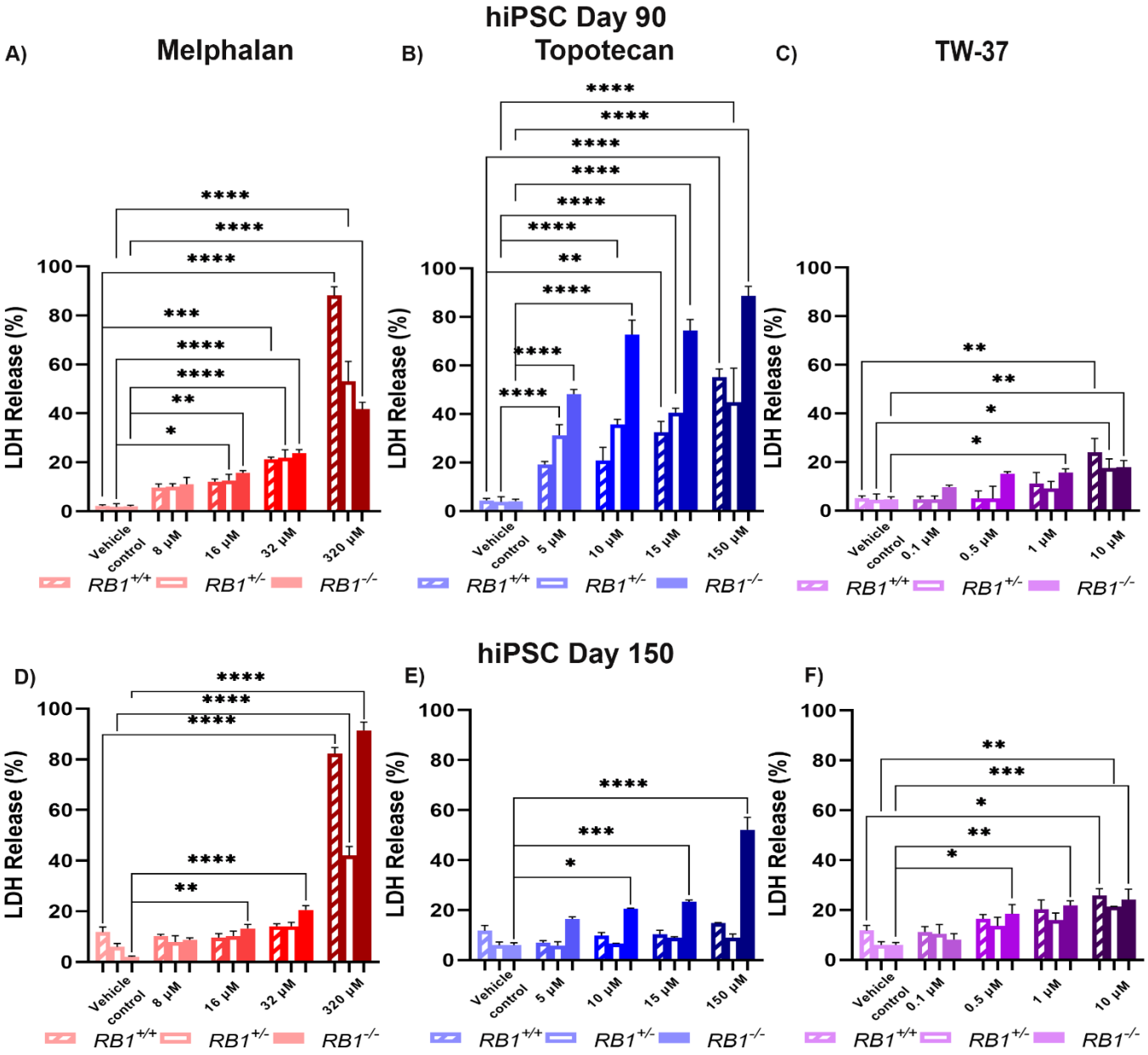

G)

Day 90		RB1 +/+	RB1 +/-	RB1 -/-
Melphalan	8 µM			
	16 µM		X	X
	32 µM	X	X	X
	320 µM	X	X	X
Topotecan	5 µM		X	X
	10 µM		X	X
	15 µM	X	X	X
	150 µM	X	X	X
TW-37	0.1 µM			
	0.5 µM			
	1 µM			X
	10 µM	X	X	X

Day 150		RB1 +/+	RB1 +/-	RB1 -/-
Melphalan	8 µM			
	16 µM			X
	32 µM			X
	320 µM	X	X	X
Topotecan	5 µM			
	10 µM			X
	15 µM			X
	150 µM			X
TW-37	0.1 µM			
	0.5 µM			X
	1 µM			X
	10 µM	X	X	X

4.3.2 Rb chemotherapeutic agents cause a significant decrease of proliferating cone precursor cells in pRB-depleted retinal organoids

To assess if these chemotherapeutic agents were acting on proliferating cone precursors in both hESC- and patient hiPSC-derived ROs, quantitative immunofluorescence analysis was performed. Results for day 90 (**Figure 4-3A**) and 150 (**Figure 4-4A**) hESC-derived ROs revealed that 16-32 µM melphalan, 10-150 µM topotecan and 0.5-10 µM TW-37 are the most effective doses in H9 RB1-null hESC-derived ROs as they significantly reduced the fraction of proliferating cone precursors to similar levels found within the H9 control hESC-derived ROs.

No significant changes were detected in the proliferating cone precursors of the normal wild-type organoids, H9 hESC-derived ROs (**Figure 4-3A, Figure 4-4A**). Interestingly, 320 µM melphalan, as the 10-fold increase to the maximal clinical dose, completely disrupted the structure of hESC-derived ROs in both time points of differentiation (day 90 and 150). Thus, analyses for the highest dose of melphalan were restricted to LDH cytotoxicity assay, as described in section **4.3.1 Dose-dependent significant increase of cytotoxicity and cell death in drug-treated retinal organoids** of this thesis document.

Together these data point to 16 µM melphalan, 10 µM topotecan, and 1 µM TW-37 as most effective in specifically lowering the level of proliferating cone precursors in the H9 RB1-null hESC-derived RO model while retaining the wild-type ROs unaffected.

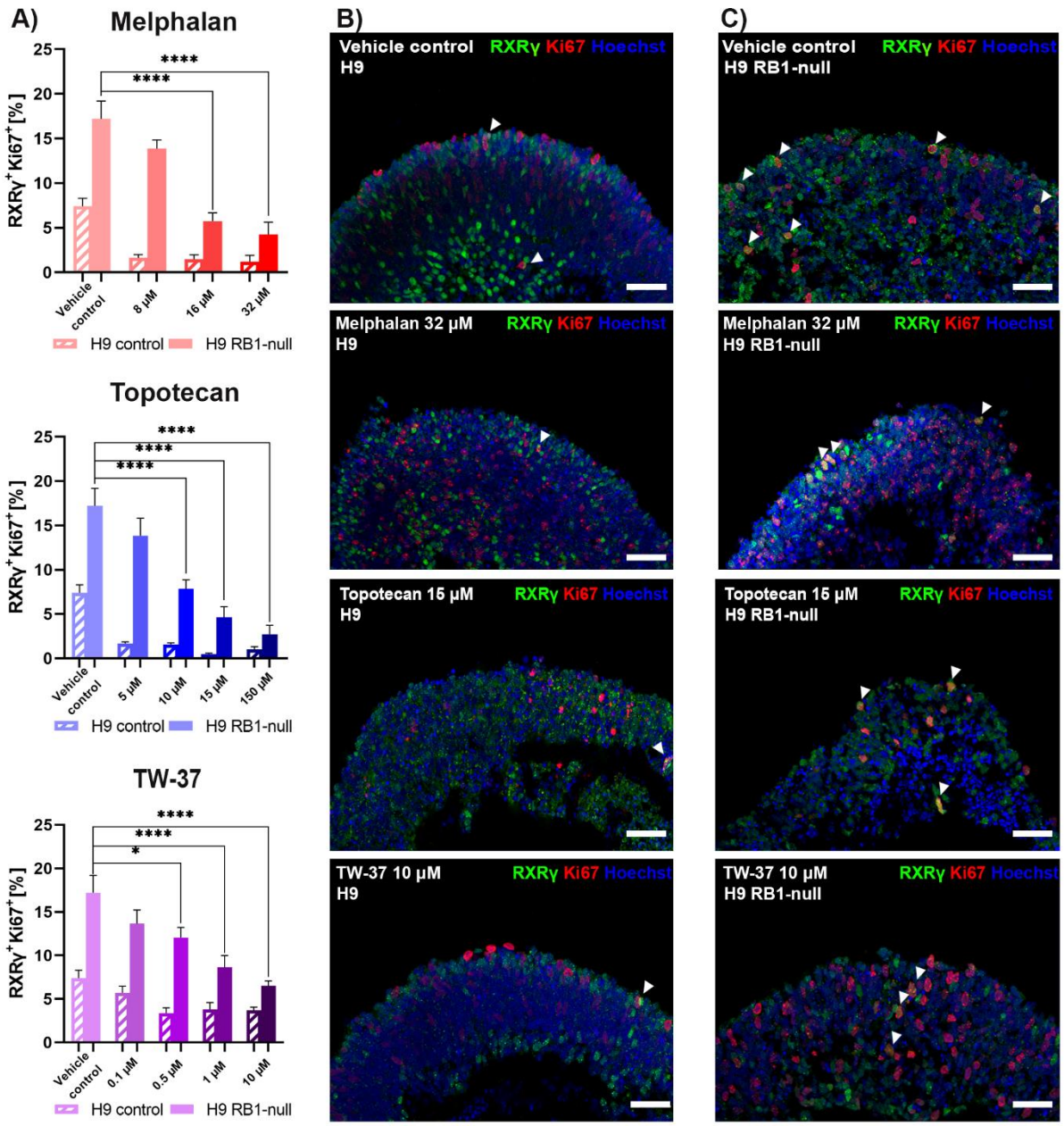

Figure 4-3. Proliferating cone precursor assessment of chemotherapeutic agents for Rb treatment in 90-day-old H9 control and H9 RB1-null hESC-derived retinal organoids.

A. Bar graphs showing the percentage of proliferating cone precursors ($RXR\gamma^{+}Ki67^{+}$) in immunostained sections of treated organoid agent (melphalan; 8, 16, 32 μM, topotecan; 5, 10, 15, 150 μM, TW-37; 0.1, 0.5, 1, 10 μM alongside vehicle-treated sample; 0.1% DMSO). 12 ROs per treatment were used as biological replicates. 5 sections of ROs were cut and imaged. Data presented as mean ± SEM (n = 5 sections from each biological replicate). Values of $p \leq 0.05$ were considered statistically significant (*$p \leq 0.05$, **$p \leq 0.01$, ***$p \leq 0.001$, ****$p \leq 0.0001$). **B-C.** Representative immunostaining of RXRγ (green) and Ki67 (red) counterstained with Hoechst for H9 control (**B**) and H9 RB1-null (**C**) hESC-derived ROs; vehicle-treated sample, melphalan 32 μM, topotecan 15 μM, and TW-37 10 μM. White arrowheads point at the co-localisation of Ki67 with the cone precursor (RXRγ) marker. Scale bars; 50 μm.

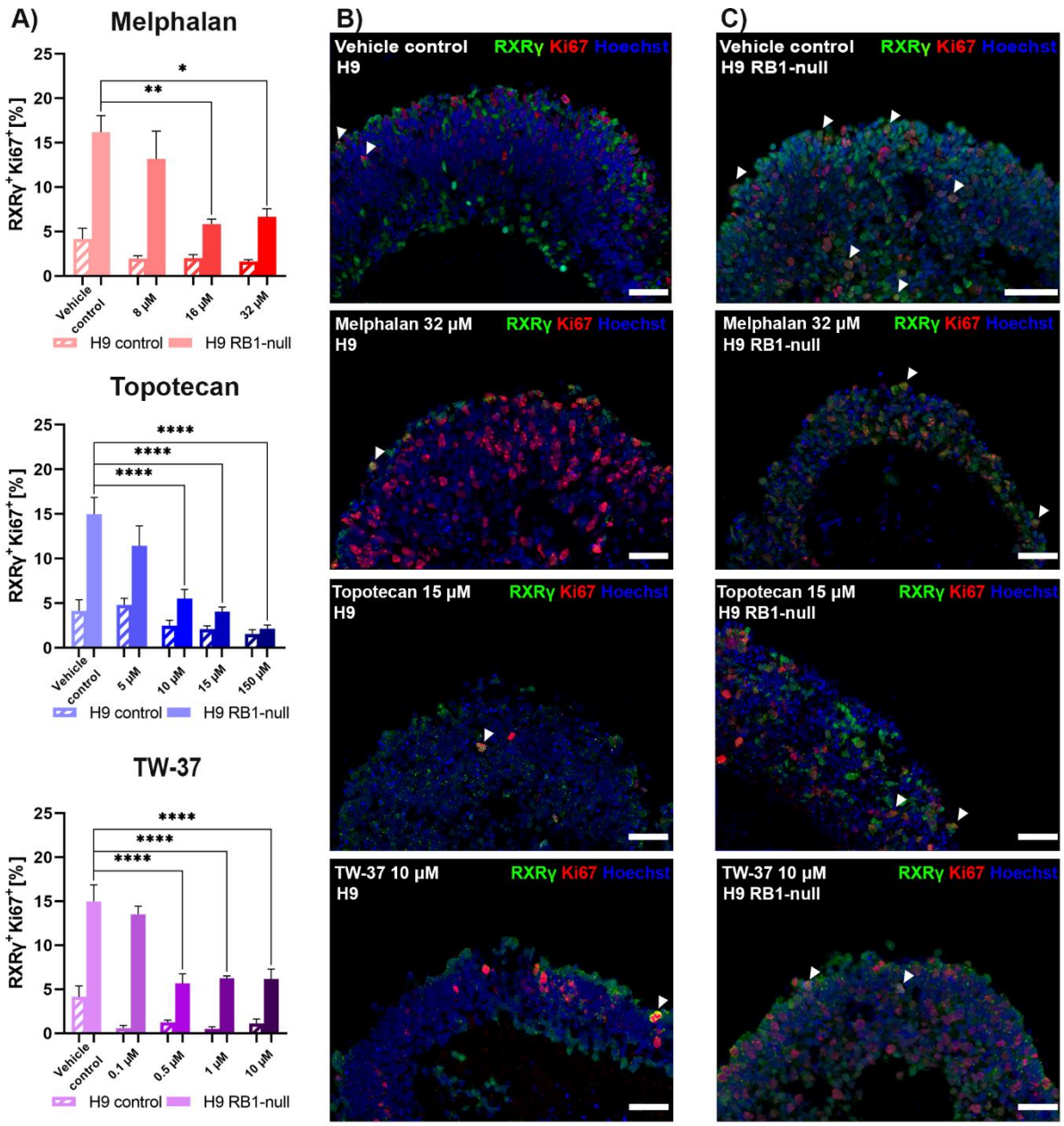

Figure 4-4. Proliferating cone precursor assessment of chemotherapeutic agents for Rb treatment in 150-day-old H9 control and H9 RB1-null hESC-derived retinal organoids.

A. Bar graphs showing the percentage of proliferating cone precursors ($RXR\gamma^{+}Ki67^{+}$) in immunostained sections of treated organoid agent (melphalan; 8, 16, 32 μM, topotecan; 5, 10, 15, 150 μM, TW-37; 0.1, 0.5, 1, 10 μM alongside vehicle-treated sample; 0.1% DMSO). 12 ROs per treatment were used as biological replicates. 5 sections of ROs were cut and imaged. Data presented as mean ± SEM (n = 5 sections from each biological replicate). Values of $p \leq 0.05$ were considered statistically significant (*$p \leq 0.05$, **$p \leq 0.01$, ***$p \leq 0.001$, ****$p \leq 0.0001$). **B-C.** Representative immunostaining of RXRγ (green) and Ki67 (red) counterstained with Hoechst for H9 control (**B**) and H9 RB1-null (**C**) hESC-derived ROs; vehicle-treated sample, melphalan 32 μM, topotecan 15 μM, and TW-37 10 μM. White arrowheads point at the co-localisation of Ki67 with the cone precursor (RXRγ) marker. Scale bars; 50 μm.

In addition to the above concentrations, 8 μM melphalan and 5 μM topotecan treatments significantly reduced the percentage of RXRγ^{+}Ki67^{+} cells on day 90 (**Figure 4-5A**) and day 150 (**Figure 4-6A**) patient *RB1*$^{-/-}$ hiPSC-derived organoids. No significant changes were detected in the proliferating cone precursors of hiPSC-derived wild-type ROs (**Figure 4-5A, Figure 4-6A**). Also, the 320 μM melphalan treatment completely disrupted the structure of patient hiPSC-derived ROs on days 90 and 150 of differentiation.

These assays, in combination, revealed that 16 μM melphalan, 10 μM topotecan, and 1 μM TW-37 are the most efficient treatments for specifically reducing the fraction of proliferating cone precursors in patient *RB1*$^{-/-}$ hiPSC-derived ROs while retaining the healthy tissue unaffected.

Figure 4-5. Proliferating cone precursor assessment of chemotherapeutic agents for Rb treatment in 90-day-old patient hiPSC-derived retinal organoids.
A. Bar graphs showing the percentage of proliferating cone precursors (RXRγ^{+}Ki67^{+}) in immunostained sections of treated organoid agent (melphalan; 8, 16, 32 μM, topotecan; 5, 10, 15, 150 μM, TW-37; 0.1, 0.5, 1, 10 μM alongside vehicle-treated sample; 0.1% DMSO). One hiPSC-derived clone per cell line was used for RO differentiation. 12 ROs per treatment were used as biological replicates. 5 sections of ROs were cut and imaged. Data presented as mean ± SEM (n = 5 sections from each biological replicate). Values of $p \leq 0.05$ were considered statistically significant (*$p \leq 0.05$, **$p \leq 0.01$, ***$p \leq 0.001$, ****$p \leq 0.0001$). **B-D.** Representative immunostaining of RXRγ (green) and Ki67 (red) counterstained with Hoechst for patient *RB1*$^{+/+}$ (B), *RB1*$^{+/-}$ (**C**), and *RB1*$^{-/-}$ (**D**) hiPSC-derived ROs; vehicle-treated sample, melphalan 32 μM, topotecan 15 μM, and TW-37 10 μM. White arrowheads point at the co-localisation of Ki67 with the cone precursor (RXRγ) marker. Scale bars; 50 μm.

Figure 4-6. Proliferating cone precursor assessment of chemotherapeutic agents for Rb treatment in 150-day-old patient hiPSC-derived retinal organoids.
A. Bar graphs showing the percentage of proliferating cone precursors (RXRγ^{+}Ki67^{+}) in immunostained sections of treated organoid agent (melphalan; 8, 16, 32 μM, topotecan; 5, 10, 15, 150 μM, TW-37; 0.1, 0.5, 1, 10 μM alongside vehicle-treated sample; 0.1% DMSO). One hiPSC-derived clone per cell line was used for RO differentiation. 12 ROs per treatment were used as biological replicates. 5 sections of ROs were cut and imaged. Data presented as mean ± SEM (n = 5 sections from each biological replicate). Values of $p \leq 0.05$ were considered statistically significant (*$p \leq 0.05$, **$p \leq 0.01$, ***$p \leq 0.001$, ****$p \leq 0.0001$). **B-D**. Representative immunostaining of RXRγ (green) and Ki67 (red) counterstained with Hoechst for patient *RB1*$^{+/+}$ (B), *RB1*$^{+/-}$ (**C**), and *RB1*$^{-/-}$ (**D**) hiPSC-derived ROs; vehicle-treated sample, melphalan 32 μM, topotecan 15 μM, and TW-37 10 μM. White arrowheads point at the co-localisation of Ki67 with the cone precursor (RXRγ) marker. Scale bars; 50 μm.

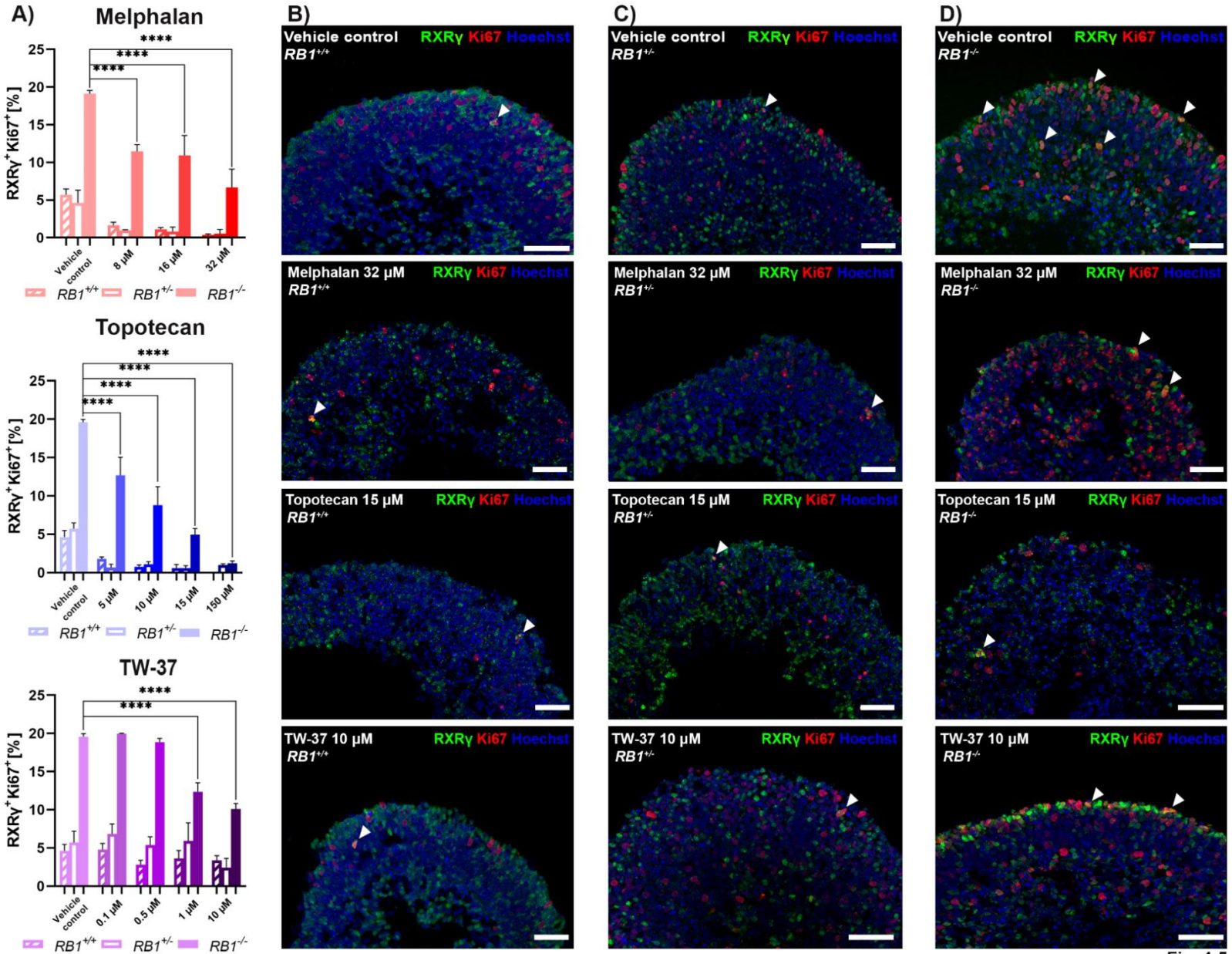
A)
Melphalan
RXRγ+Ki67+ [%]
Vehicle control
8 µM
16 µM
32 µM
RB1+/+
RB1+/-
RB1-/-
Topotecan
5 µM
10 µM
15 µM
150 µM
TW-37
0.1 µM
0.5 µM
1 µM
10 µM
B)
C)
D)
Vehicle control RXRγ Ki67 Hoechst
Melphalan 32 µM RXRγ Ki67 Hoechst
Topotecan 15 µM RXRγ Ki67 Hoechst
TW-37 10 µM RXRγ Ki67 Hoechst

Fig. 4-5

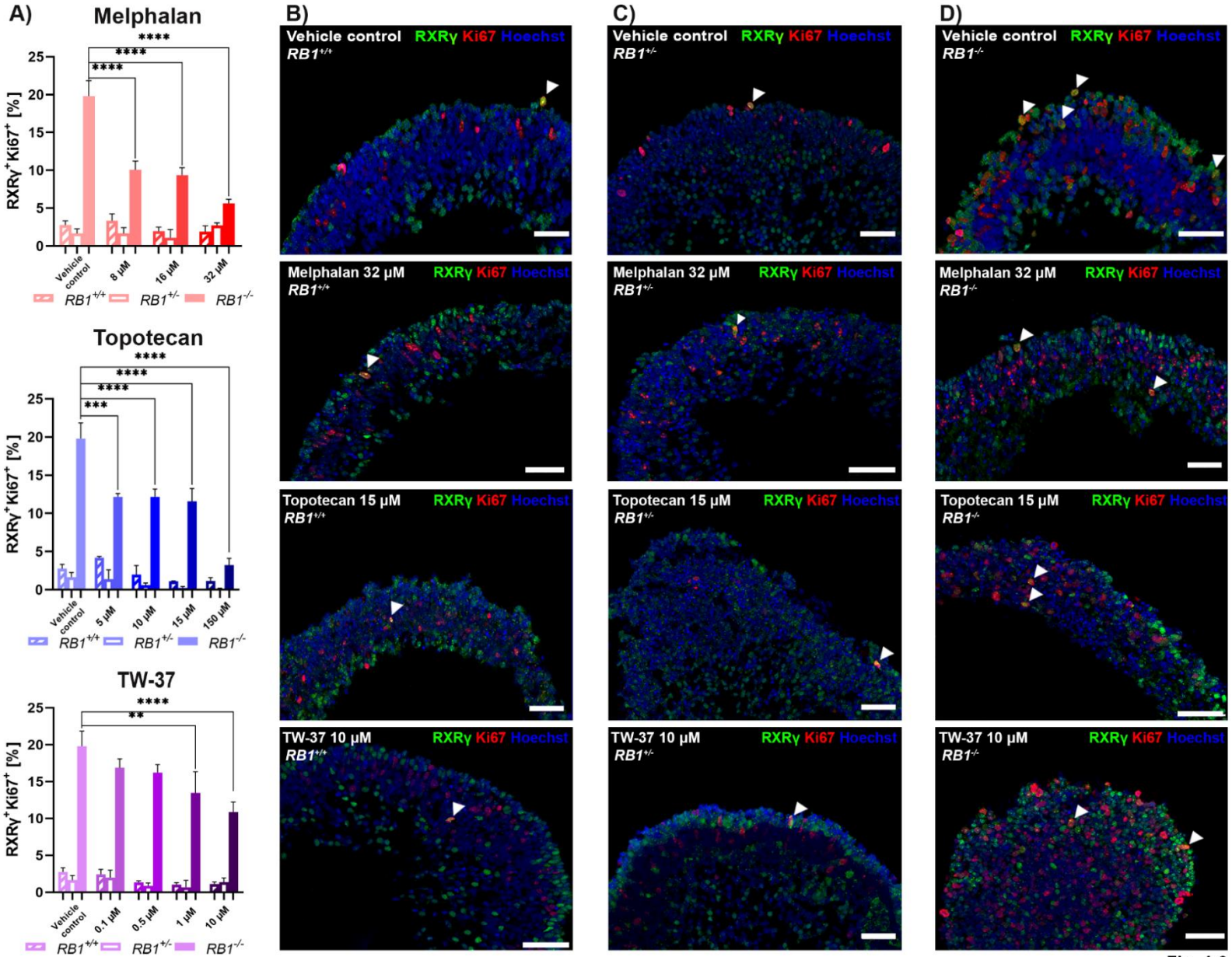
A)
Melphalan
RXRγ+Ki67+ [%]
Vehicle control
8 µM
16 µM
32 µM
RB1+/+
RB1+/-
RB1-/-
Topotecan
5 µM
10 µM
15 µM
150 µM
TW-37
0.1 µM
0.5 µM
1 µM
10 µM
B)
C)
D)
Vehicle control RXRγ Ki67 Hoechst
Melphalan 32 µM RXRγ Ki67 Hoechst
Topotecan 15 µM RXRγ Ki67 Hoechst
TW-37 10 µM RXRγ Ki67 Hoechst

Fig. 4-6

4.3.3 Rb chemotherapeutic agents cause a significant increase of apoptotic cone precursor cells in drug-treated pRB-depleted retinal organoids

To assess the drug specificity for cone precursors, cell killing in day 90 and 150 hESC- and patient hiPSC-derived ROs was evaluated by quantitative immunofluorescence analysis of RXRγ^{+}CASP3^{+} RO immunostained sections. Results for day 90 (**Figure 4-7A**) and day 150 (**Figure 4-8A**) H9 RB1-null hESC-derived ROs revealed that 32 µM melphalan and 150 µM topotecan did cause a significant increase in the fraction of apoptotic cone precursor (RXRγ^{+}CASP3^{+}) cells. In addition to these drug concentrations, 10-15 µM topotecan treatments significantly increased the percentage of RXRγ^{+}CASP3^{+} cells on day 150 H9 RB1-null hESC ROs.

Data for day 90 (**Figure 4-9A**) and day 150 (**Figure 4-10A**) patient *RB1*$^{-/-}$ hiPSC-derived ROs suggest that 32 µM melphalan and 10-15 µM topotecan significantly increased the fraction of apoptotic cone precursor (RXRγ^{+}CASP3^{+}) cells. Additionally, 10 µM TW-37 treatment did cause an increase of RXRγ^{+}CASP3^{+} cells in day 90 *RB1*$^{-/-}$ hiPSC-derived ROs, which did not reflect by day 150. The levels of apoptotic cone precursor cells of hESC- or hiPSC-derived wild-type and heterozygous mutant ROs treated with Rb chemotherapeutic agents within the clinical range remained very similar to vehicle control treatments in both time points. However, topotecan 150 µM treatment caused cytotoxicity in 90-day-old wild-type and heterozygous *RB1* hiPSC-derived ROs, suggesting non-specific toxic effects at this high dose manifested in similar levels of RXRγ^{+}CASP3^{+} cells (**Figure 4-9A**). Together, these results point to 32 µM melphalan and 10 µM topotecan as most effective for killing proliferating cone precursors in both pRB-depleted hESC and patient hiPSC models while retaining the healthy tissue unaffected.

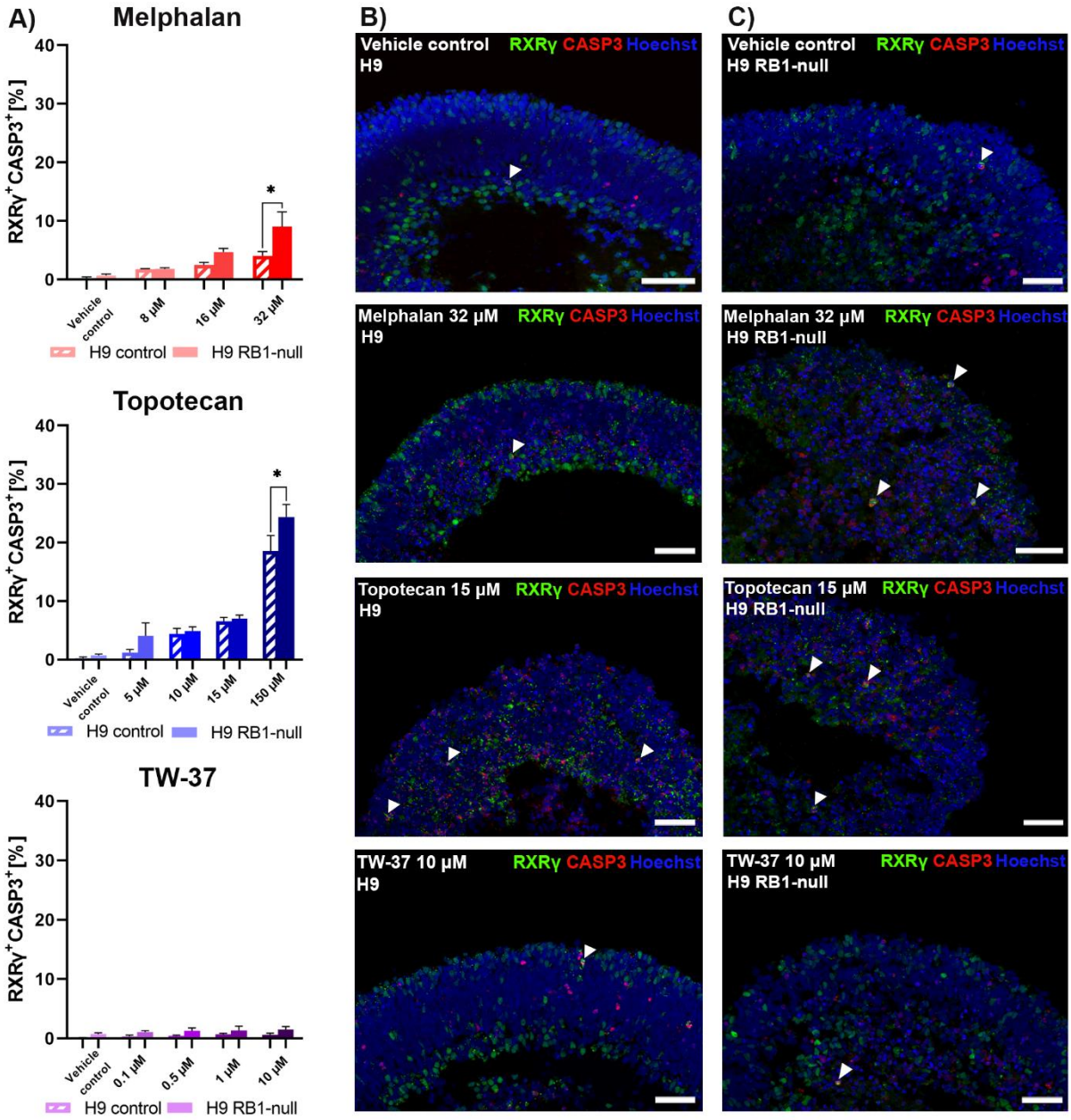

Figure 4-7. Apoptotic response of chemotherapeutic agents for Rb treatment in 90-day-old H9 control and H9 RB1-null hESC retinal organoids.
A. Bar graphs showing the percentage of apoptotic cone precursors ($RXR\gamma^+CASP3^+$) in immunostained sections of treated organoid agent (melphalan; 8, 16, 32 μM, topotecan; 5, 10, 15, 150 μM, TW-37; 0.1, 0.5, 1, 10 μM alongside vehicle-treated sample; 0.1% DMSO). 12 ROs per treatment were used as biological replicates. 5 sections of ROs were cut and imaged. Data presented as mean ± SEM (n = 5 sections from each biological replicate). Values of $p \leq 0.05$ were considered statistically significant (*$p \leq 0.05$, **$p \leq 0.01$, ***$p \leq 0.001$, ****$p \leq 0.0001$). **B-C.** Representative immunostaining of RXRγ (green) and CASP3 (red) counterstained with Hoechst for H9 control (**B**) and H9 RB1-null (**C**) hESC-derived ROs; vehicle-treated sample, melphalan 32 μM, topotecan 15 μM, and TW-37 10 μM. White arrowheads point at the co-localisation of RXRγ with the apoptosis (cleaved-caspase-3; CASP3) marker. Scale bars; 50 μm.

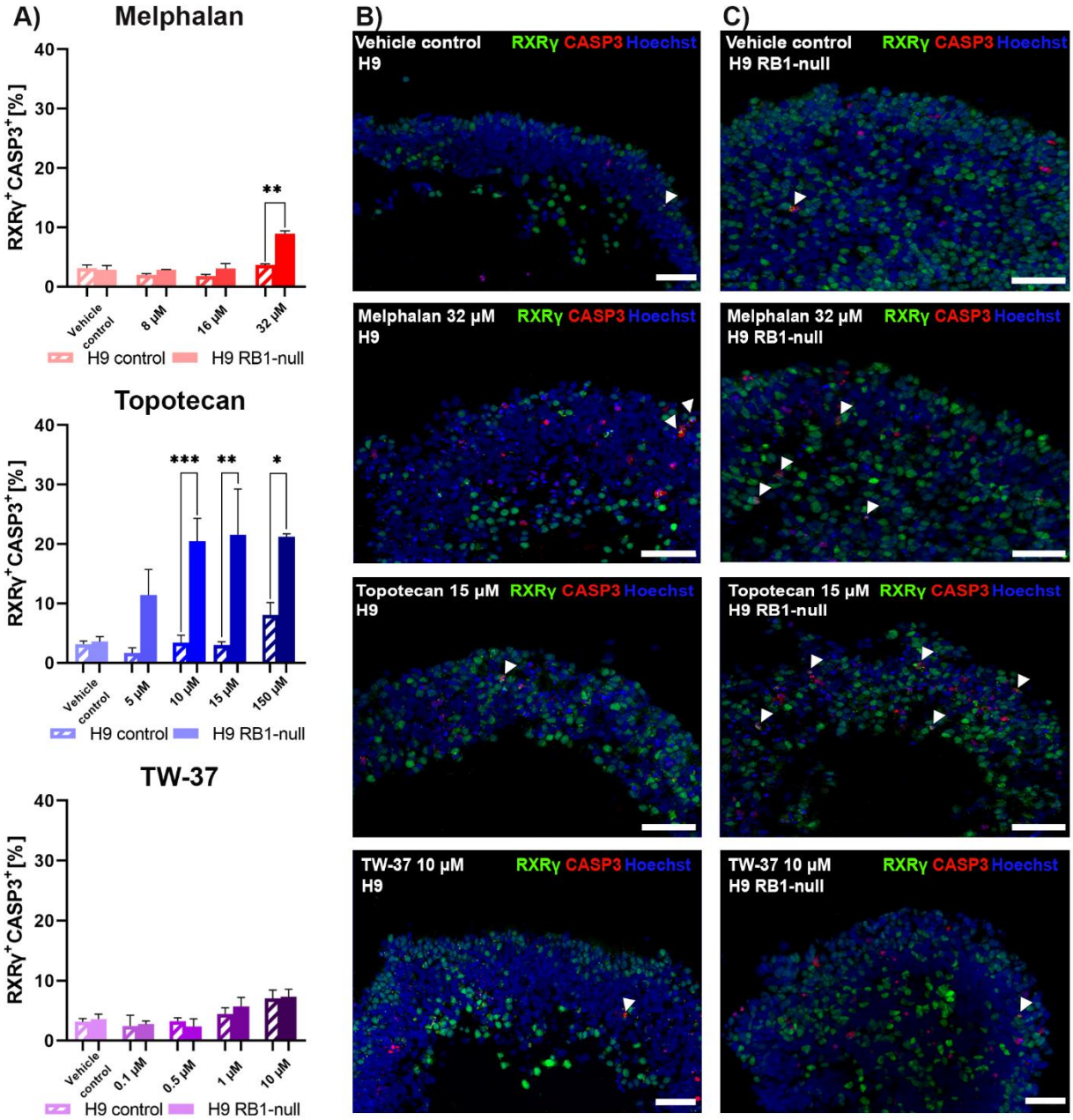

Figure 4-8. Apoptotic response of chemotherapeutic agents for Rb treatment in 150-day-old H9 control and H9 RB1-null hESC retinal organoids.

A. Bar graphs showing the percentage of apoptotic cone precursors ($RXR\gamma^{+}CASP3^{+}$) in immunostained sections of treated organoid agent (melphalan; 8, 16, 32 µM, topotecan; 5, 10, 15, 150 µM, TW-37; 0.1, 0.5, 1, 10 µM alongside vehicle-treated sample; 0.1% DMSO). 12 ROs per treatment were used as biological replicates. 5 sections of ROs were cut and imaged. Data presented as mean ± SEM (n = 5 sections from each biological replicate). Values of $p \leq 0.05$ were considered statistically significant (*$p \leq 0.05$, **$p \leq 0.01$, ***$p \leq 0.001$, ****$p \leq 0.0001$). **B-C.** Representative immunostaining of RXRγ (green) and CASP3 (red) counterstained with Hoechst for H9 control (**B**) and H9 RB1-null (**C**) hESC-derived ROs; vehicle-treated sample, melphalan 32 µM, topotecan 15 µM, and TW-37 10 µM. White arrowheads point at the co-localisation of RXRγ with the apoptosis (cleaved-caspase-3; CASP3) marker. Scale bars; 50 µm.

Figure 4-9. Apoptotic response of chemotherapeutic agents for Rb treatment in 90-day-old patient hiPSC-derived retinal organoids.
A. Bar graphs showing the percentage of apoptotic cone precursors ($RXR\gamma^{+}CASP3^{+}$) in immunostained sections of treated organoid agent (melphalan; 8, 16, 32 μM, topotecan; 5, 10, 15, 150 μM, TW-37; 0.1, 0.5, 1, 10 μM alongside vehicle-treated sample; 0.1% DMSO). One hiPSC-derived clone per cell line was used for RO differentiation. 12 ROs per treatment were used as biological replicates. 5 sections of ROs were cut and imaged. Data presented as mean ± SEM (n = 5 sections from each biological replicate). Values of $p \leq 0.05$ were considered statistically significant (*$p \leq 0.05$, **$p \leq 0.01$, ***$p \leq 0.001$, ****$p \leq 0.0001$). **B-D.** Representative immunostaining of RXRγ (green) and CASP3 (red) counterstained with Hoechst for patient *RB1*$^{+/+}$ (**B**), *RB1*$^{+/-}$ (**C**), and *RB1*$^{-/-}$ (**D**) hiPSC-derived ROs; vehicle-treated sample, melphalan 32 μM, topotecan 15 μM, and TW-37 10 μM. White arrowheads point at the co-localisation of RXRγ with the apoptosis (cleaved-caspase-3; CASP3) marker. Scale bars; 50 μm.

Figure 4-10. Apoptotic response of chemotherapeutic agents for Rb treatment in 150-day-old patient hiPSC-derived retinal organoids.
A. Bar graphs showing the percentage of apoptotic cone precursors ($RXR\gamma^{+}CASP3^{+}$) in immunostained sections of treated organoid agent (melphalan; 8, 16, 32 μM, topotecan; 5, 10, 15, 150 μM, TW-37; 0.1, 0.5, 1, 10 μM alongside vehicle-treated sample; 0.1% DMSO). One hiPSC-derived clone per cell line was used for RO differentiation. 12 ROs per treatment were used as biological replicates. 5 sections of ROs were cut and imaged. Data presented as mean ± SEM (n = 5 sections from each biological replicate). Values of $p \leq 0.05$ were considered statistically significant (*$p \leq 0.05$, **$p \leq 0.01$, ***$p \leq 0.001$, ****$p \leq 0.0001$). **B-D.** Representative immunostaining of RXRγ (green) and CASP3 (red) counterstained with Hoechst for patient *RB1*$^{+/+}$ (**B**), *RB1*$^{+/-}$ (**C**), and *RB1*$^{-/-}$ (**D**) hiPSC-derived ROs; vehicle-treated sample, melphalan 32 μM, topotecan 15 μM, and TW-37 10 μM. White arrowheads point at the co-localisation of RXRγ with the apoptosis (cleaved-caspase-3; CASP3) marker. Scale bars; 50 μm.

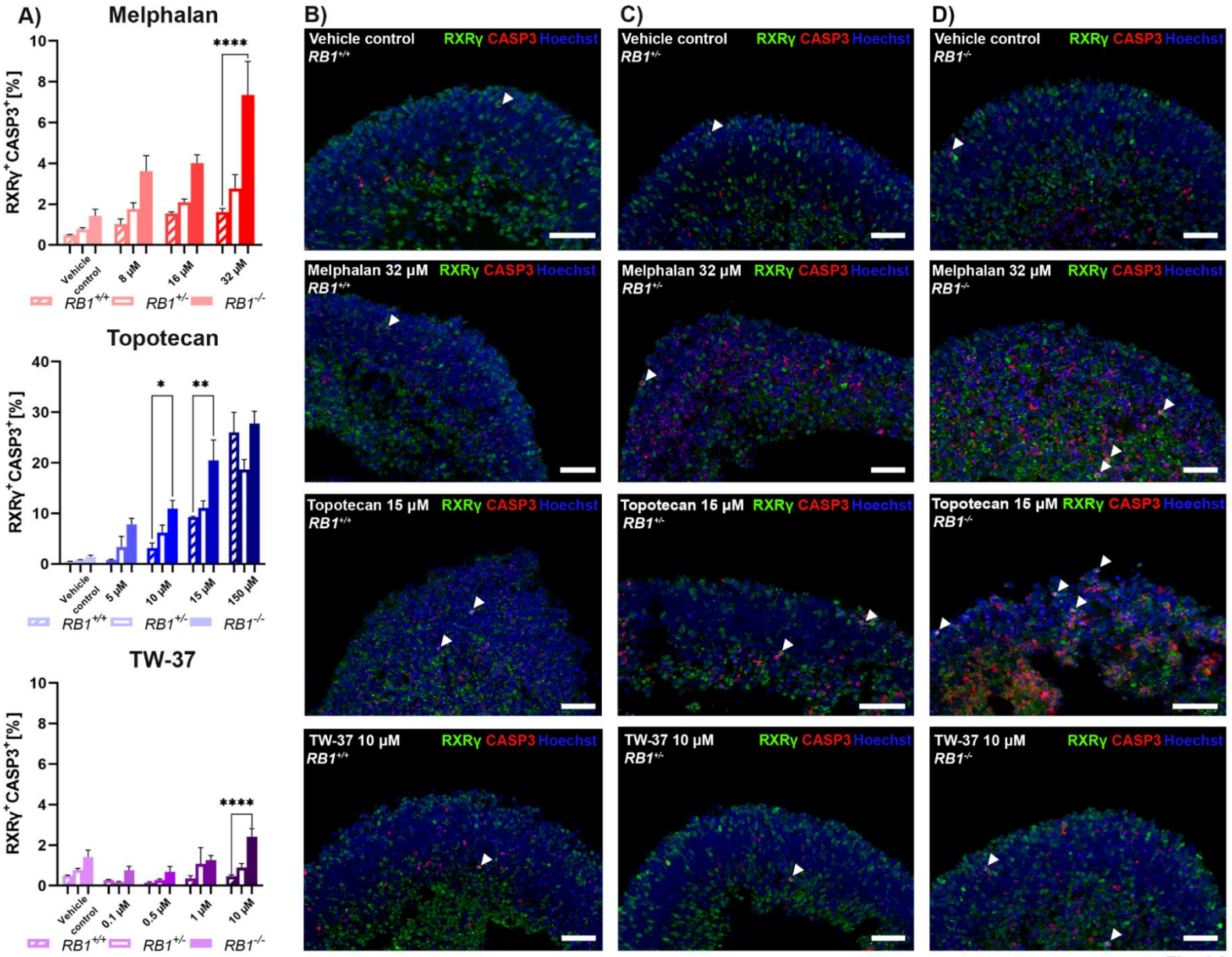
A)
Melphalan
RXRγ+CASP3+[%]
****
Vehicle control
8 µM
16 µM
32 µM
RB1+/+
RB1+/-
RB1-/-
Topotecan
*
**
Vehicle control
5 µM
10 µM
15 µM
150 µM
TW-37
****
0.1 µM
0.5 µM
1 µM
10 µM
B)
C)
D)
Vehicle control RXRγ CASP3 Hoechst
Melphalan 32 µM RXRγ CASP3 Hoechst
Topotecan 15 µM RXRγ CASP3 Hoechst
TW-37 10 µM RXRγ CASP3 Hoechst

Fig. 4-9

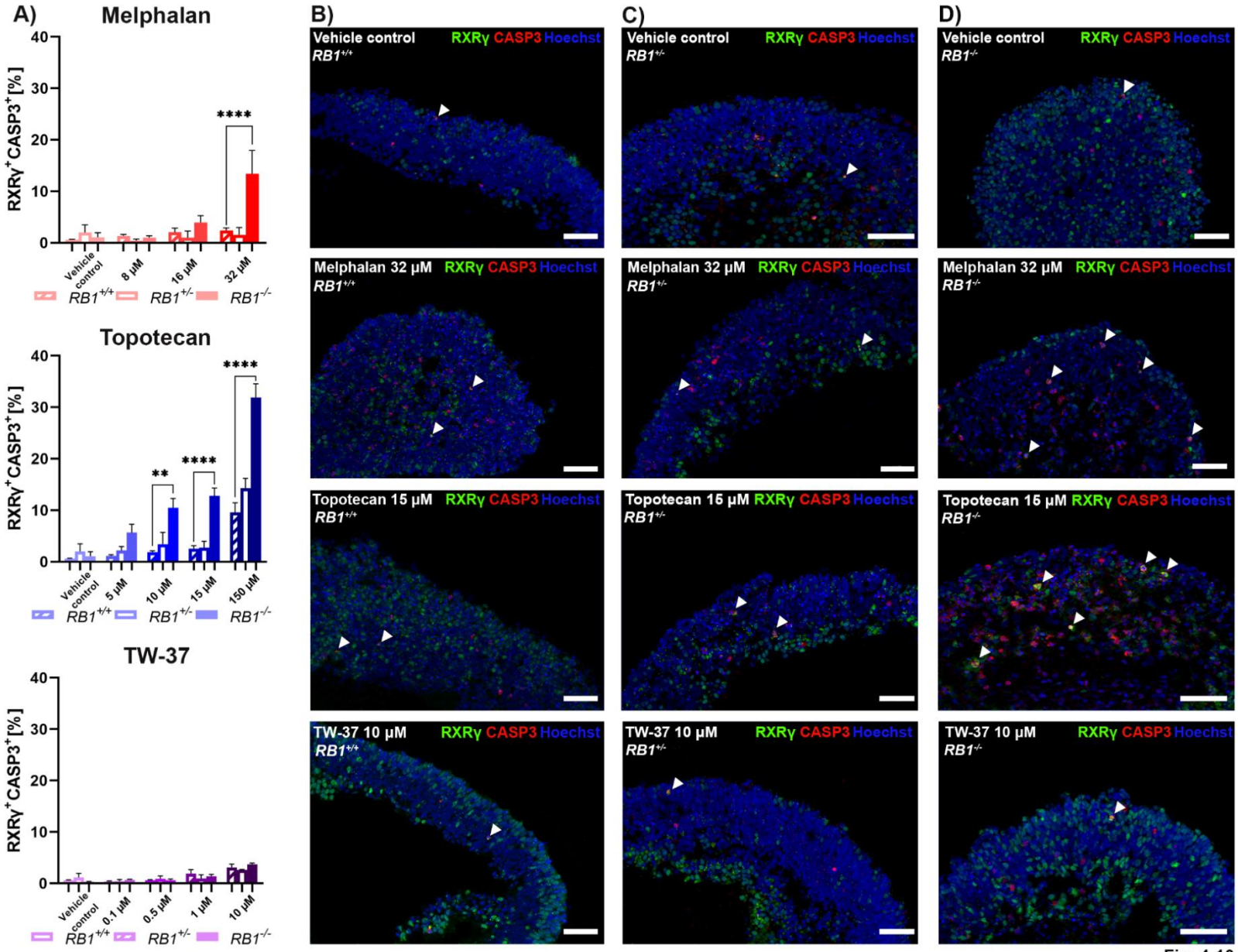
A)
Melphalan
RXRγ+CASP3+[%]
40
30
20
10
0
****
Vehicle control
8 µM
16 µM
32 µM
RB1+/+
RB1+/-
RB1-/-
Topotecan
RXRγ+CASP3+[%]
40
30
20
10
0
**
****
****
Vehicle control
5 µM
10 µM
15 µM
150 µM
RB1+/+
RB1+/-
RB1-/-
TW-37
RXRγ+CASP3+[%]
40
30
20
10
0
Vehicle control
0.1 µM
0.5 µM
1 µM
10 µM
RB1+/+
RB1+/-
RB1-/-
B)
C)
D)
Vehicle control RXRγ CASP3 Hoechst
RB1+/+
RB1+/-
RB1-/-
Melphalan 32 µM RXRγ CASP3 Hoechst
RB1+/+
RB1+/-
RB1-/-
Topotecan 15 µM RXRγ CASP3 Hoechst
RB1+/+
RB1+/-
RB1-/-
TW-37 10 µM RXRγ CASP3 Hoechst
RB1+/+
RB1+/-
RB1-/-

Fig. 4-10

4.3.4 Assessing the formation of sphere-like aggregates of drug-treated pRB-depleted retinal organoids in soft colony agar assays

Soft agar colony assay was performed from dissociated drug-treated 90- and 150-day-old hESC- and patient hiPSC-derived ROs. Results revealed small and large sphere-like aggregates in the vehicle- and drug-treated H9 RB1-null hESC- and *RB1*$^{-/-}$ hiPSC-derived ROs, indicating the prevalence of cell growth in an anchorage-independent manner and cell transformation *in vitro*. Quantitative analysis revealed that 32 µM melphalan, 15 µM topotecan and 1 µM TW-37 treatments were the most efficient conditions to significantly reduce the number and size of the sphere-like aggregates derived from both pRB-depleted RO models in both time points (**Figure 4-11A-D**). No sphere-like aggregate formation was observed in 90- and 150-day-old H9 hESC-derived ROs (**Figure 4-12**) or patient *RB1*$^{+/+}$ and *RB1*$^{+/-}$ hiPSC-derived ROs (**Figure 4-13**). These results suggest that the higher mitotic activity observed in vehicle-treated controls, although reduced in drug-treated samples, was restricted to H9 RB1-null hESC- and *RB1*$^{-/-}$ hiPSC-derived ROs.

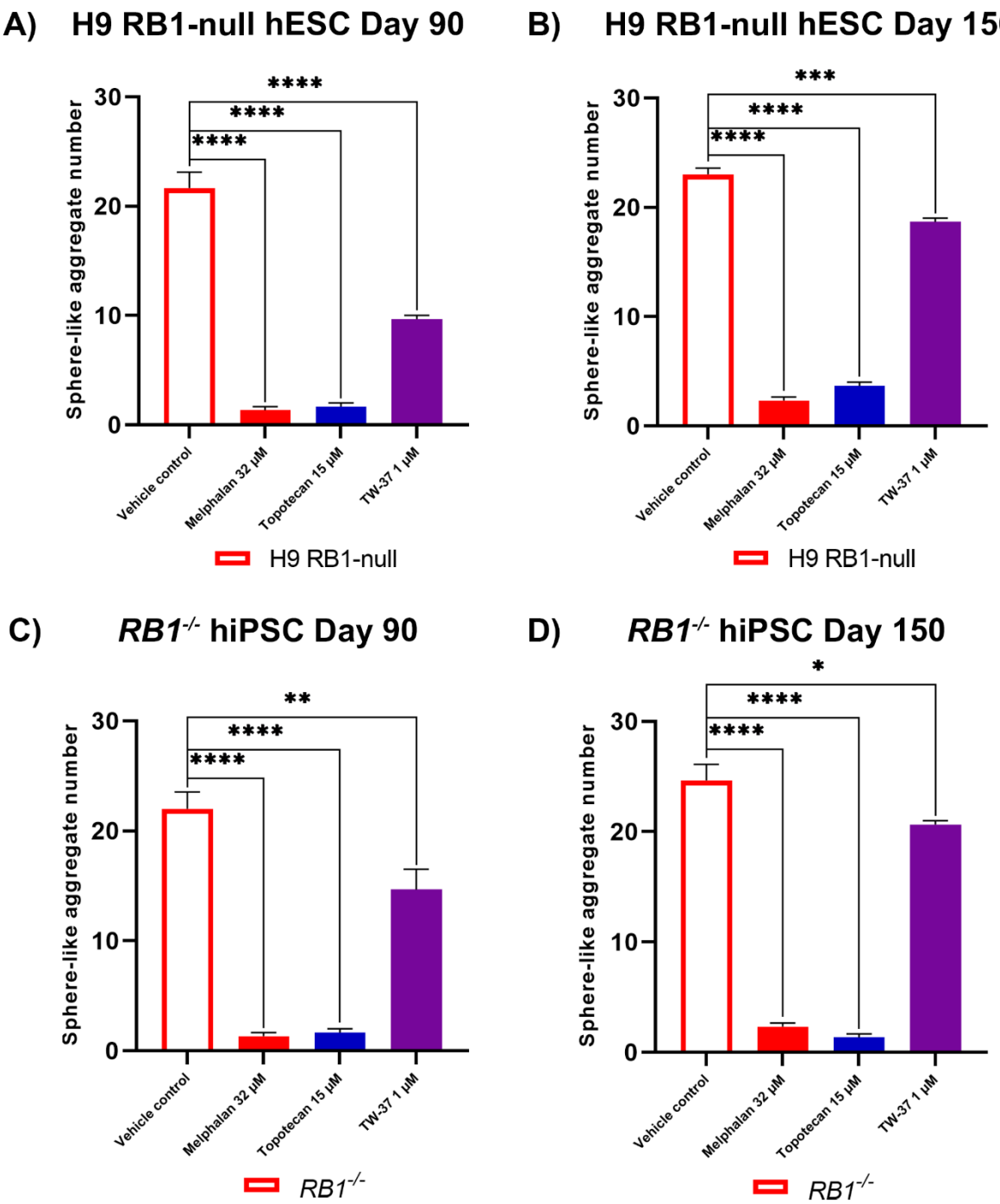

Figure 4-11. Assessment of sphere-like aggregate formation in drug-treated pRB-depleted retinal organoids.

Bar graphs showing the number of sphere-like aggregates of pRB-depleted retinal cells originating from 90- (**A**) and 150-day-old (**B**) H9 RB1-null hESC-derived ROs and 90- (**C**) and 150-day-old (**D**) patient *RB1*$^{-/-}$ hiPSC-derived ROs drug-treated to grow in suspension as part of soft agar colony formation assay (vehicle-treated 0.1% DMSO, 32 µM melphalan, 15 µM topotecan, and 1 µM TW-37). One hiPSC-derived clone per cell line was used for RO differentiation. 12 ROs per treatment were used as biological replicates. Data presented as mean ± SEM (n = 3 wells from each biological replicate). 1000 cells were plated per well in 12-well plates in triplicates. Values of $p \leq 0.05$ were considered statistically significant (*$p \leq 0.05$, **$p \leq 0.01$, ***$p \leq 0.001$, ****$p \leq 0.0001$).

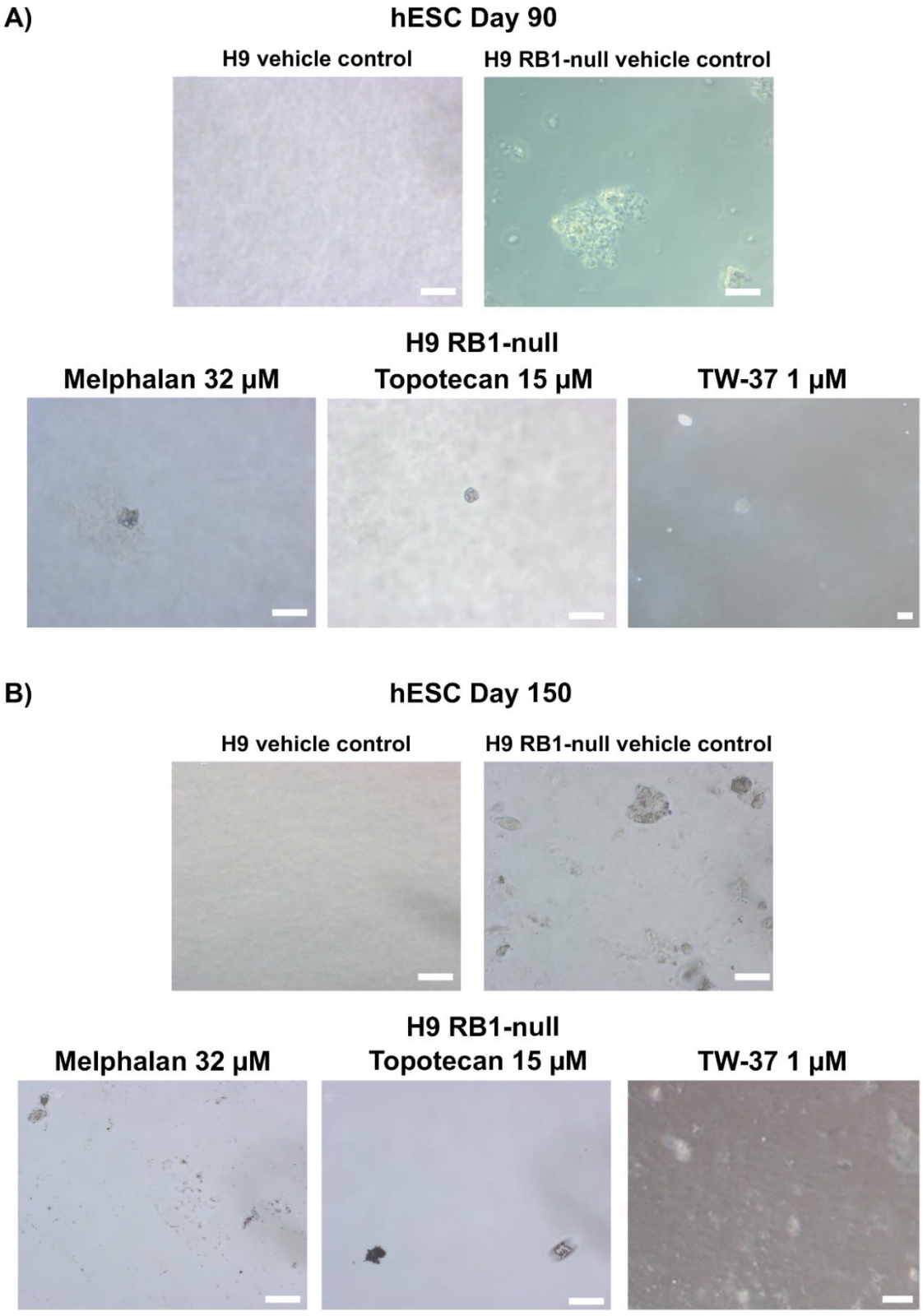

Figure 4-12. Sphere-like aggregate formation in drug-treated pRB-depleted hESC-derived retinal organoids.

Representative bright-field images of soft agar colony formation assay showing the ability of pRB-depleted retinal cells originating from 90- (**A**) and 150-day-old (**B**) drug-treated H9 RB1-null hESC-derived ROs to grow in suspension (vehicle-treated 0.1% DMSO, 32 µM melphalan, 15 µM topotecan, and 1 µM TW-37). Scale bars; 50 µm.

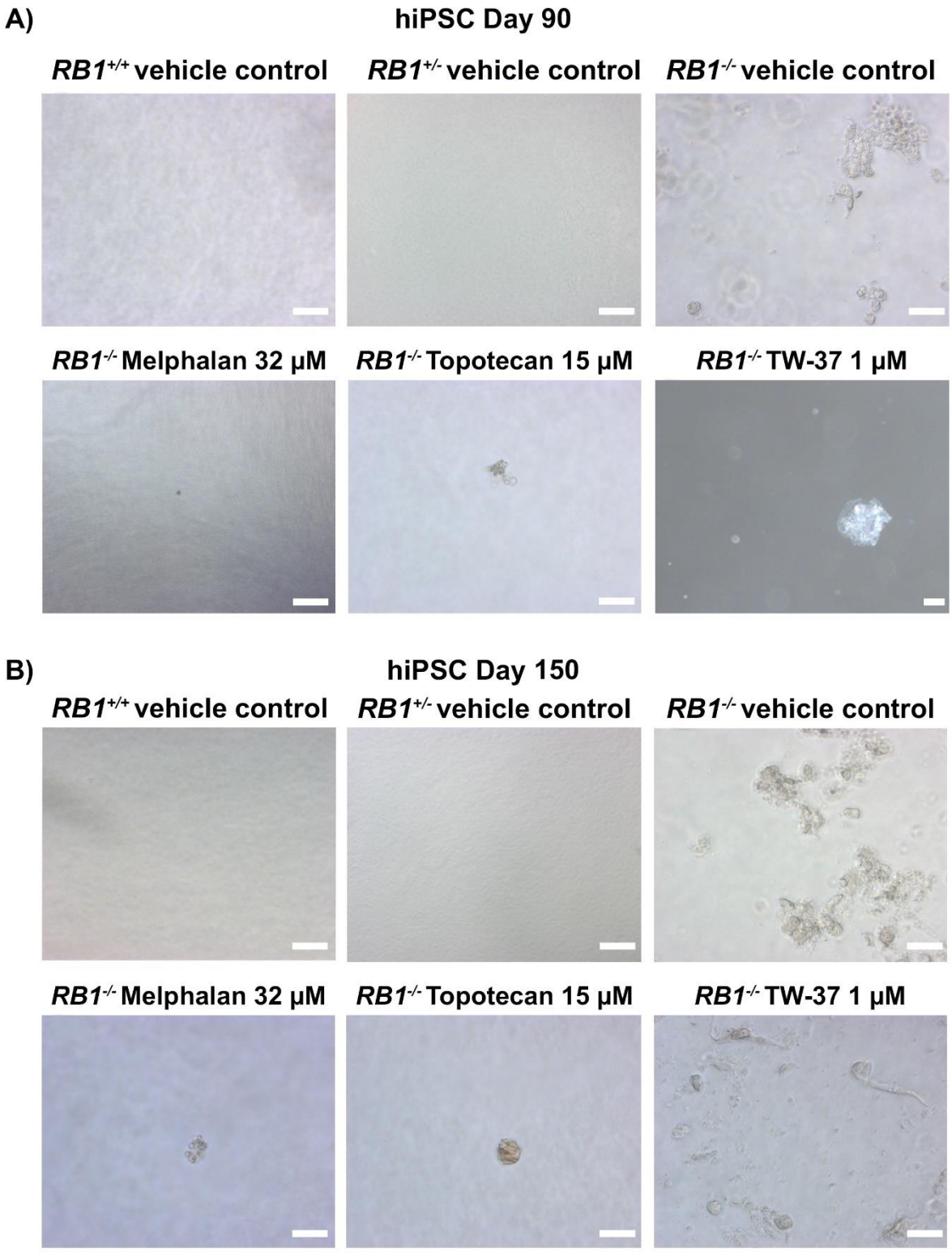

Figure 4-13. Sphere-like aggregate formation in drug-treated pRB-depleted patient hiPSC-derived retinal organoids.
Representative bright-field images of soft agar colony formation assay showing the ability of pRB-depleted retinal cells originating from 90- (**A**) and 150-day-old (**B**) drug-treated patient *RB1*$^{-/-}$ hiPSC-derived ROs to grow in suspension (vehicle-treated 0.1% DMSO, 32 µM melphalan, 15 µM topotecan, and 1 µM TW-37). Scale bars; 50 µm.

4.4 Discussion

pRB is a functional tumour suppressor and regulator of the cell cycle that plays a significant role in cell proliferation, differentiation, and apoptosis (Sachdeva and O'Brien, 2012). Inactivation of both copies of the *RB1* gene is a causative factor of Rb. Current treatments for Rb management include systemic, intravitreal, intraarterial, and periocular chemotherapy (Yanık et al., 2015), aiming to salvage the ocular globe and the patient's visual function (Saengwimol et al., 2018). The standard chemotherapeutic agents are melphalan, topotecan, etoposide, vincristine, and carboplatin (Yanık et al., 2015). Novel and small molecules such as TW-37 are promising drugs that induce apoptosis and inhibit tumour growth, potentially supporting the development of new treatments for Rb (Zeitlin et al., 2008). However, recurrent malignant growth might lead to extended retinal damage and even enucleation, representing a challenging condition for preserving eyesight (Dimaras et al., 2015, Dyer, 2016). Designing new efficient therapies for managing the progression of the disease requires a detailed understanding of retinal tumours at the molecular and cellular levels.

Results from **3 Generation and characterisation of hESC- and patient hiPSC-derived retinal organoids** of this document have provided robust evidence that H9 RB1-null hESC- and patient *RB1*$^{-/-}$ hiPSC-derived ROs mimic the development and malignant transformation that occurs *in vivo* resulting in Rb tumours. To this end, these pRB-depleted RO models were assessed for drug screening by incubating the ROs with three chemotherapeutic agents: melphalan, topotecan, and TW-37. The three chemotherapeutic drugs were administered in doses within the range in clinical application plus a 10-fold increase of the highest dose.

LDH cytotoxicity assay was performed on day 90 and 150 drug-treated hESC- and patient hiPSC-derived ROs. Results for day 90 revealed significant cell death in a dose-dependent manner in pRB-depleted ROs, while only the 10-fold increase of the maximal dose clinically used for topotecan and TW-37 was significant in wild-type control ROs. In addition, 320 µM melphalan treatment caused cytotoxicity in H9 hESC- and 32-320 µM melphalan in patient *RB1*$^{+/+}$ hiPSC-derived ROs. It is possible to speculate that retinal cells might be more drug-sensitive at this point since, at day

90 of differentiation, there is more proliferation progression as part of retinal development. Then, results for day 150 showed significant cell death levels in a dose-dependent manner in pRB-depleted ROs, while only the 10-fold increase of the highest dose clinically used for all three drugs was significant in wild-type control ROs. Data revealed that doses of the three drugs within the clinical range at day 150 do not cause significant cytotoxicity and retain the healthy tissue unaffected. The clinical relevance of these results suggests that at a mature stage of differentiation (day 150), drug responses are more specific due to the rise in proliferating cone precursors that these chemotherapeutic agents target.

All three compounds significantly decreased the percentage of proliferating cone precursors ($RXR\gamma^{+}Ki67^{+}$) to the levels found in H9 control hESC- and patient *RB1*$^{+/+}$ hiPSC-derived ROs. In addition, the drug-treated pRB-depleted ROs also exhibited an increase in the fraction of apoptotic cone precursor ($RXR\gamma^{+}CASP3^{+}$) cells. No significant changes were observed in the wild-type control hESC- and patient hiPSC-derived ROs, apart from melphalan and topotecan treatments at the highest concentration tested.

Interestingly, there was a lack of response in $RXR\gamma^{+}CASP3^{+}$ cells in any of the TW-37 treatments in 150-day-old pRB-depleted ROs. However, a significant decrease in proliferating cone precursors ($RXR\gamma^{+}Ki67^{+}$) was observed in the highest two concentrations of TW-37. Data suggested that TW-37 works in a limited fashion by significantly decreasing proliferating cone precursors but not increasing apoptotic cone precursors, as observed with melphalan and topotecan treatments.

pRB-depleted ROs might show better responses to chemotherapeutic drugs such as TW-37 in a different experimental design. Changes, including the drug incubation time and administration (7-day treatment) followed by continuous culture as described by (Liu et al., 2020), might improve the response of TW-37. Further work as triple staining of proliferating and apoptotic cone precursors ($RXR\gamma^{+}Ki67^{+}CASP3^{+}$) might also provide a better understanding of the killing efficacy and specificity of these chemotherapeutic agents.

Results for the soft colony agar assays confirmed that the sphere-like aggregates still did grow in an anchorage-independent manner from dissociated drug-treated H9 RB1-null hESC- and patient *RB1*$^{-/-}$ hiPSC-derived ROs. However,

the analyses revealed that all drug treatments within the clinical range significantly decreased the size and number of the sphere-like aggregates. Although *in vitro* cell transformation still undergoes in drug-treated pRB-depleted dissociated retinal cells from organoids, the chemotherapeutic agents partially kill some of the retinal 'seed' cells that give rise to Rb cells. These results agree with the significant decrease of proliferating cone precursors ($RXR\gamma^{+}Ki67^{+}$) observed in the same drug-treated pRB-depleted ROs in both time points.

As a proof of feasibility study, (Liu et al., 2020) performed drug screening in their pRB-depleted hESC-derived RO model at an early stage (day 60) and late stage (day 90) of differentiation. The study tested four chemotherapeutic agents currently used in the clinical application, including vincristine (5 nM), etoposide (0.5 μM), carboplatin (10 μM), and topotecan (10 nM) as a 7-day treatment followed by continuous culture to day 120. The drug responses were determined by flow cytometry, immunohistochemistry of $Ki67^{+,}$ and cleaved-caspase-3^{+} ($CASP3^{+}$) cells. Their results for all tested drugs except for etoposide in both time points showed a significant decrease in $Ki67^{+}$ and an increase in $CASP3^{+}$ cells. The experimental design, including the chemotherapeutic agents and doses, for this study's drug testing differs from the one developed in this chapter. However, the effects of topotecan on pRB-depleted hESC-derived ROs on day 90 of differentiation, characterised by the decrease of proliferating cells and increase of apoptotic cells, agree with the results of our topotecan drug testing by day 90.

In an Rb organoid differentiation and drug screening study, (Saengwimol et al., 2018) performed cell cycle analysis in 150-day-old Rb organoids as a response to melphalan, topotecan, and other anticancer drugs after 24 and 72 hours of incubation. The authors found that chemotherapy-naïve tumour organoids treated with a dose of 32 μM melphalan did not arrest in the S-phase but underwent apoptosis in the sub-G1 phase. They also described increased G1-phase fraction for all melphalan concentrations (Saengwimol et al., 2018). In the case of topotecan, they reported increased cell death and a reduced number of G0/G1-phase cells, which showed similar cell cycle profiles for the highest concentrations of melphalan and topotecan, comparable killing effects in treated Rb ROs. In addition to cell cycle phase distribution analysis, the study also reported a significant decrease of

proliferating cone precursor (RXRγ^{+}Ki67^{+}) cells in the 24-hour exposure of the 11 μM topotecan treatment alone and in combination with melphalan.

Data for our 150-day-old H9 RB1-null and patient *RB1*$^{-/-}$ hiPSC-ROs treated with 32 μM melphalan showed a significant decrease in proliferating cone precursors (RXRγ^{+}Ki67^{+}) and an increase in apoptotic cone precursors (RXRγ^{+}CASP3^{+}). These results agree with a publication from (Saengwimol et al., 2018) regarding proliferation and apoptotic patterns since 32 μM melphalan treatment in chemotherapy-naïve tumour organoids did not arrest in the S-phase but underwent apoptosis in the sub-G1 phase. Similar results of increased cell death and reduced number of G0/G1-phase cells were observed in the 11 μM topotecan treatment that approached our 10 μM topotecan treatment. Our 72-hour topotecan treatment for pRB-depleted ROs exhibited a significant cell death percentage, a decrease in RXRγ^{+}Ki67^{+} cells, and an increase in RXRγ^{+}CASP3^{+} cells. Notwithstanding, it is important to highlight the difference of origin between our *in vitro* hESC- and patient hiPSC-derived RO model mimicking the environment of the retina in contrast to their model comprising organoids derived from chemotherapy-naïve tumours.

Hypoxic conditions have been shown to promote proliferation and differentiation in neural stem cells (Zhu et al., 2005). Oxygen tension impacts neurons' viability and cell fate commitment during early neuronal development in mice (Chen et al., 2007) and humans (Pistollato et al., 2007). Mouse ESC- and iPSC-derived retinal organoids have been generated under normoxia (20% O_2) and hypoxia (5% O_2) conditions during the first 10 days of differentiation without significant morphological differences (Chen et al., 2016). However, results revealed that organoids in hypoxic conditions demonstrated significantly higher differentiation into optic vesicles and optic cups. Oxygen in 3D cell cultures, such as ROs, develops gradients as its diffusion is limited due to the gas-liquid phases where it diffuses through the solid phase of cell clusters (McMurtrey, 2016). Additionally, the oxygen concentration gradients result from the competition between diffusion and consumption (Griffith and Swartz, 2006). Nonuniform oxygen and nutrient concentration experienced in organoids cause the formation of hypoxic cores in the centre of the 3D structure (Ast and Mootha, 2019, Thakuri et al., 2017). Although hypoxic cores have been studied, the extent of the core formation remains poorly understood. Like oxygen diffusion, drug concentration gradients are formed during

their application to the 3D organoid culture. As cone precursors are the cells of interest for drug screening in our pRB-depleted RO models, the chemotherapeutic agents' effects aim for the apical layer in the periphery of the organoid structure. Drug penetration research would be needed to study these drugs' effects in other retinal cell types located in deeper layers and the hypoxic core of the RO models.

Although more work employing a more significant number of chemotherapeutic agents and ROs from patients with various mutations in the *RB1* gene is needed, initial results corroborated the validity of these *in vitro* models as suitable systems for drug and cytotoxicity screening prior to large clinical trials.

4.5 Conclusion

In summary, the drug response of our Rb hESC- and patient hiPSC-derived RO models has been assessed and characterised in terms of cytotoxicity, effects on proliferating cone precursors, and *in vitro* cell transformation. Results have shown that administration of Rb chemotherapeutic agents within the range used in a clinical application at day 150 of differentiation significantly reduced the proliferating cone precursor ($RXR\gamma^{+}Ki67^{+}$) cell fraction and increased the percentage of apoptotic cone precursor ($RXR\gamma^{+}CASP3^{+}$) cells while retaining the healthy tissue unaffected. Importantly, results in this chapter have shown that these two pluripotent stem cell-derived RO models recapitulate the development of Rb *in vivo* and can be successfully used for validating drug and toxicology testing with possible therapeutic implications.

Chapter 5

5 Generation, characterisation, and drug screening of hESC- and hiPSC-derived RPE

5.1 Introduction

The retinal pigment epithelium (RPE) is a polygonal pigmented cell monolayer located at the outermost layer of the retina and responsible for transporting metabolic end products from the subretinal space to the blood (Strauss, 2005, Yang et al., 2021c). The RPE monolayer is comprised of highly polarised hexagonal postmitotic cells located between the retina and the choroid (Milyushina et al., 2011), only separated from the choriocapillaris by Bruch's membrane (BrM) (Strauss, 2005, Lynn et al., 2017). These highly differentiated cells have a dark brown pigmentation attributed to their melanin content that protects the retina from ultraviolet light. The RPE cells also remove the excessive accumulation of free radicals from the photo-oxidative retinal environment (Lynn et al., 2017, Yang et al., 2021c). Moreover, the pigmented monolayer guards the inside and the outside of the retina as a cell barrier, exerting strict control over the entry and exit of metabolic products. Proteins such as ZO-1, claudin and occludin enable the formation of tight junctions between the RPE cells as part of the barrier function of the monolayer (Yang et al., 2021c).

Transporting nutrients (glucose, retinol, and fatty acids) and metabolic end products from the RPE to the PRs allows for the maintenance of the visual cycle (Sharma et al., 2021). Reisomerisation of all-*trans*-retinal back into 11-*cis*-retinal in the RPE preserves the PR excitability and the ion composition stabilisation. The structural integrity of PR and choriocapillaris endothelium is maintained by diverse growth, differentiation, and immunosuppressive factors secreted by the RPE (Strauss, 2005). Additionally, the RPE cells have a pivotal role in maintaining the retina as the PR outer segments (POSs) face the RPE's apical membrane (Tamiya et al., 2010). The pigmented monolayer is responsible for recycling PR outer disks through phagocytosis, which engulfs and eliminates exfoliated POSs to maintain the visual cells (Strauss, 2005).

The cell junctions and polarity of the RPE monolayer are crucial for preserving the integrity of the blood-retinal barrier. When the stability of the RPE cell polarity

and cell junctions is disrupted, the phagocytic activity and material exchange of the apical and basal structures of the RPE cells are affected as well (Yang et al., 2021c). Failure of any of the vital functions of the RPE sustaining health and function of the neural retina can result in retinal degeneration, loss of visual function, and blindness. The RPE's functional impairment might lead to retinopathy, including AMD, RP, and STGD1 (Lynn et al., 2017).

Clinical evidence reports RPE hyperplasia, hypertrophy and gliosis induced after 6 months of the end of chemotherapy treatment in an Rb patient. Active cancer recurrence arising from a focal scar after consolidative laser therapy is a progressive retinal opacification that mimics active Rb (Zolfaghari et al., 2018). RPE hyperplasia with gliosis is a rare side of RPE toxicity from intra-arterial or intravitreal chemotherapy and local laser therapy. Laser photocoagulation induces RPE hyperplasia around the laser site on the retina in a murine model (Zolfaghari et al., 2018). When there are alterations in the RPE, they usually appear flat and darkly pigmented and sporadically present with a subretinal cleft. (Shields et al., 2011, Shields et al., 2014) described in clinical reports that RPE mottling with gradual progression over time manifested in Rb patients following intra-arterial chemotherapy with 20–30 μg melphalan, indicating the side effects of Rb chemotherapeutics to the RPE. Similarly, (Muen et al., 2012) conducted a clinical study with 14 Rb patients treated with melphalan delivered through the intra-ophthalmic artery for tumour management. Results reported RPE atrophy and pigmentary clumping in 47% of patients treated with melphalan. (Xue et al., 2019) conducted a clinical study with 23 patients treated with intravitreal melphalan (20–33 μg), where patients were reported to manifest RPE atrophy, inflammation and toxicity. Finally, these relevant clinical studies provide supporting evidence of the RPE alterations caused by melphalan, which can ultimately impact the patient's visual acuity.

An *in vitro* study (Süsskind et al., 2016) using the ARPE19 cell line evaluated the cytotoxicity of melphalan, topotecan, and carboplatin on RPE cells. As clinical evidence has reported RPE alterations before, the study investigated these drugs' toxic cellular effects in a dose-dependent manner in a cell culture model. The results revealed a concentration-dependent increase with each drug in the number and size of gaps in the monolayer. Also, the authors described a decrease in proliferative

activity and cell viability and an increase in apoptosis after 24 hours of incubation with melphalan and topotecan. No cell density alterations were reported. Their conclusions point to a direct toxic effect of melphalan *in vivo* in the RPE after intra-arterial or intravitreal chemotherapy, as angiographic RPE alterations have been observed in patients. However, the ARPE19 disease model (Hazim et al., 2019) is not directly comparable to the RPE cells in terms of cell differentiation and characterisation of typical RPE cells.

Two pluripotent stem cell (PSC)-derived Rb organoid models were characterised in the previous chapters of this thesis and a recent publication from our group (Rozanska et al., 2022). These pRB-depleted ROs mimicked the crucial stages of tumourigenesis and displayed the critical features of Rb tumours. In this chapter, two PSC-RPE models were characterised and used as an *in vitro* platform to assess the effects of commonly used Rb chemotherapeutics on RPE cells. Since non-heritable Rb accounts for ≈ 60% of all Rbs (Sachdeva and O'Brien, 2012), both inactivating *RB1* mutations may occur locally within the retina. Thus, it might be plausible that the surrounding RPE cells are clear of *RB1* mutations. With this in mind, the experiments described in this chapter were designed to assess the impact of chemotherapeutic drugs on wild-type *RB1*$^{+/+}$ PSC-derived RPE cells.

5.2 Aims

The main aim of this chapter was to investigate the impact of the three chemotherapeutic agents (melphalan, topotecan and TW-37) on hESC- and hiPSC-derived RPE cells. To this end, this study generated the RPE cell monolayers from two cell lines following an optimised version of a differentiation protocol described in our group (Buskin et al., 2018): H9 hESCs and patient *RB1*$^{+/+}$ hiPSCs (Rozanska et al., 2022). The characterisation was assessed by immunohistochemistry, fluorescence microscopy, apical-basal polarity and tight junction markers, qPCR for gene expression analysis, and flow cytometric assays. Drug response analyses were determined by LDH cytotoxicity, cell cycle and apoptosis assays, phagocytic capacity and transepithelial electrical resistance (TEER). Together these experiments determined the impacts of these Rb chemotherapeutic drugs on RPE functionality.

5.3 Results

5.3.1 Drug testing in hESC- and hiPSC-derived RPE cells

Bright-field images of mature hESC- and hiPSC-derived RPE cells displayed the characteristic pigmented cobblestone morphology (**Figure 5-1**). Three drugs currently used for Rb tumour management, melphalan, topotecan, and TW-37, were tested in both H9 hESC- and hiPSC-derived RPE cells to assess the effects of these chemotherapeutic agents. Three doses within the range of clinical application plus a 10-fold increase of the maximum value within the range were selected to be tested. The RPE cells were incubated for 72 hours with varying doses of the chemotherapeutic agents as we previously tested in PSC-derived ROs (Rozanska et al., 2022), as described in **4 Drug screening of hESC- and patient hiPSC-derived retinal organoids** of this thesis.

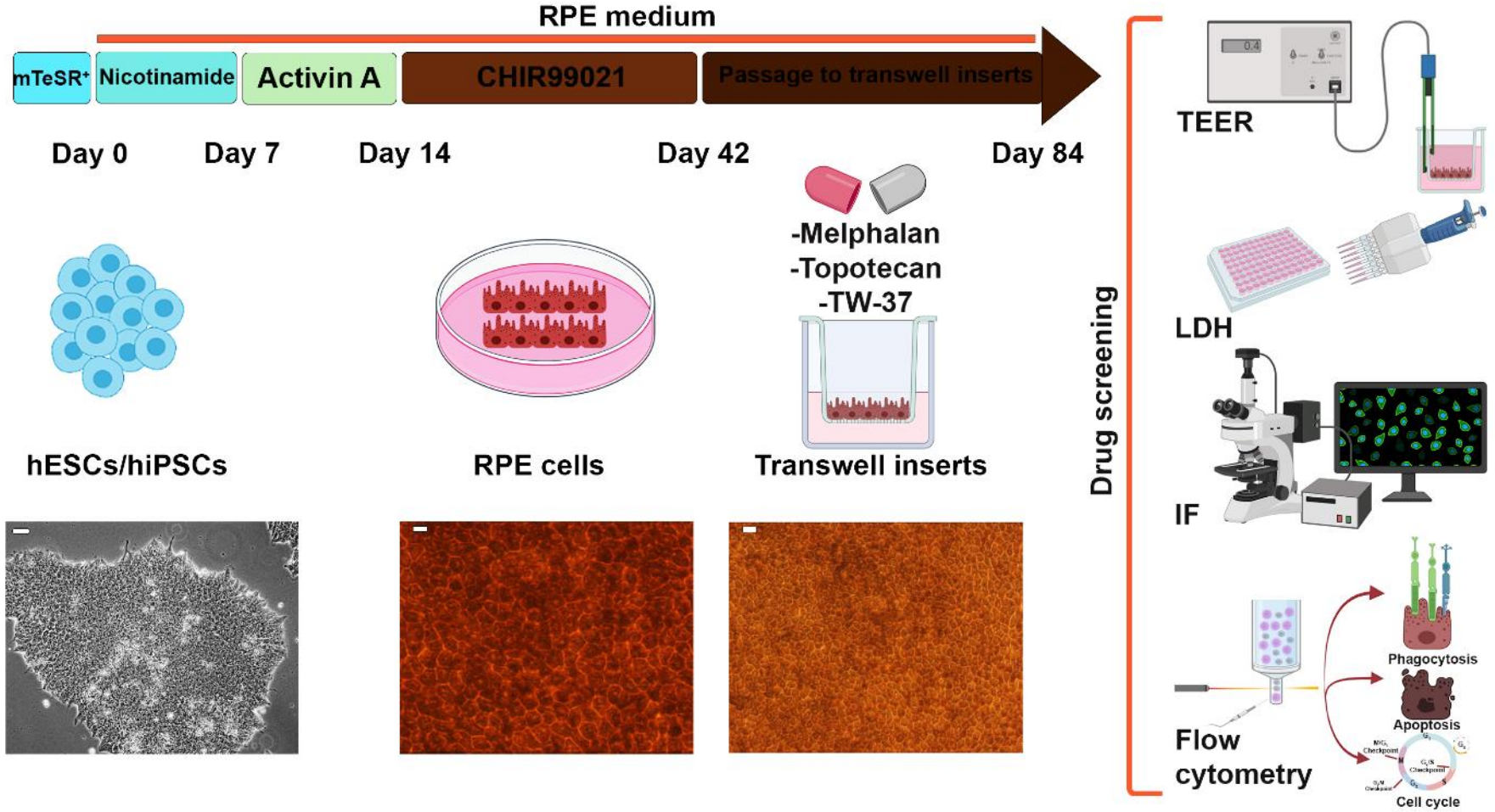

Figure 5-1. Characterisation and drug screening of H9 hESC- and hiPSC-derived RPE cells.
Schematic showing RPE cell differentiation from H9 hESC and hiPSC lines and drug screening of mature RPE cell lines with three chemotherapeutic agents, of which two first are commonly used in Rb treatment. The specified agents include varying doses of melphalan (8, 16, 32, 320 μM), topotecan (5, 10, 15, 150 μM), and TW-37 (0.1, 0.5, 1, 10 μM) alongside vehicle-treated sample (0.1% DMSO). Scale bars; 50 μm (left and right bright-field images); 20 μm (middle bright-field image).

Qualitative immunofluorescence analyses of all hESC- and hiPSC-RPE vehicle- and drug-treated groups demonstrated the maintenance of the apical (Ezrin) and basal (Collagen IV) polarity (**Figure 5-2**) in addition to the tight junction (ZO-1) marker (**Figure 5-3**). The typical apical-basal polarity and the tight junction network of the RPE phenotype were preserved after administration of the highest dose of melphalan, topotecan, and TW-37 used in the clinical application.

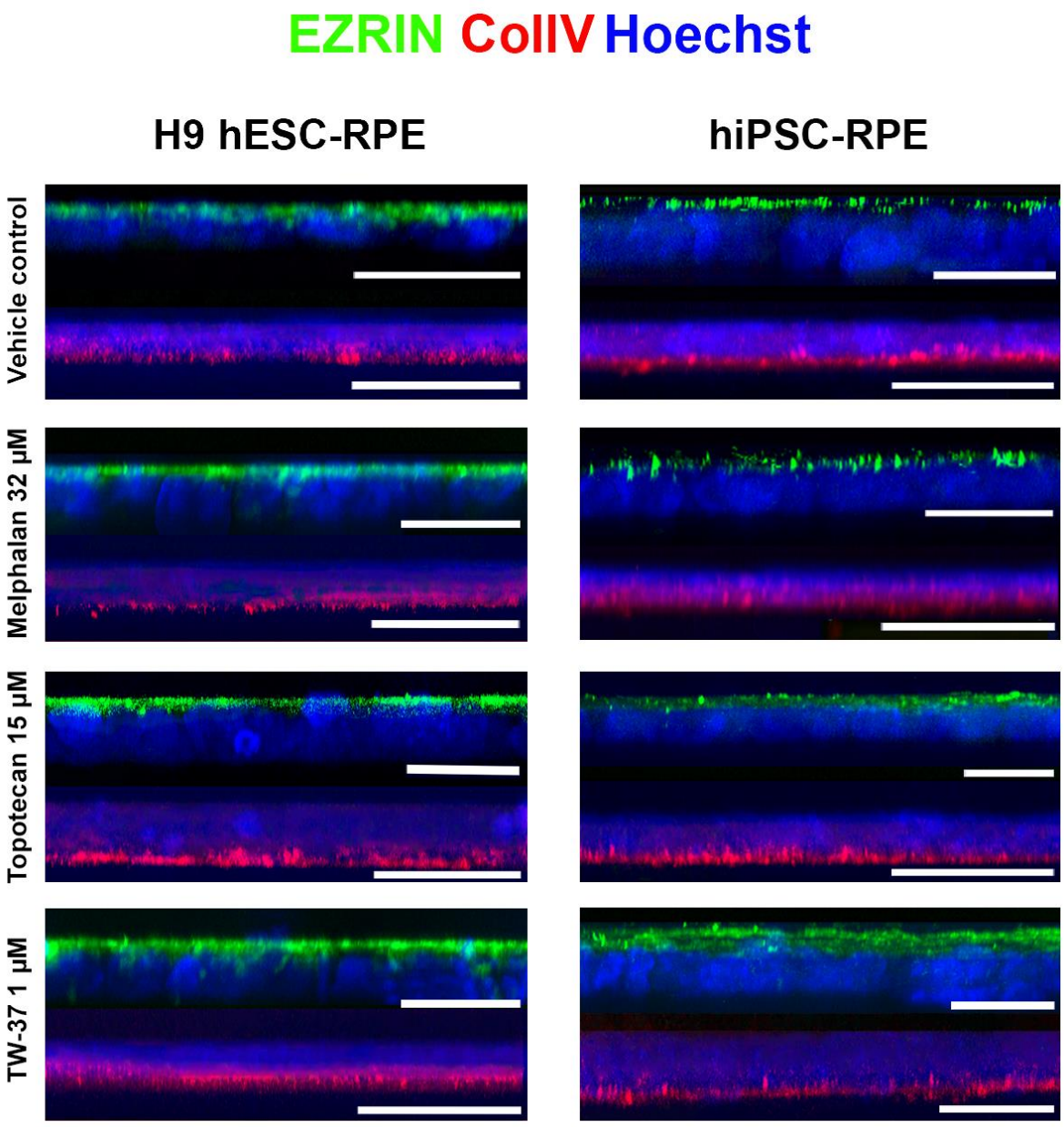

Figure 5-2. Immunofluorescence analysis for the apical-basal polarity of H9 hESC- and hiPSC-derived RPE cells.
Representative immunostaining of Ezrin (green) and CollV (red), counterstained with Hoechst for drug-treated H9 hESC- and hiPSC-derived RPE cells (vehicle-treated 0.1% DMSO, melphalan 32 µM, topotecan 15 µM, and TW-37 10 µM). 3 RPE transwell inserts (24-well plates) per treatment were used as biological replicates (n = 3). Scale bars; 20 µm.

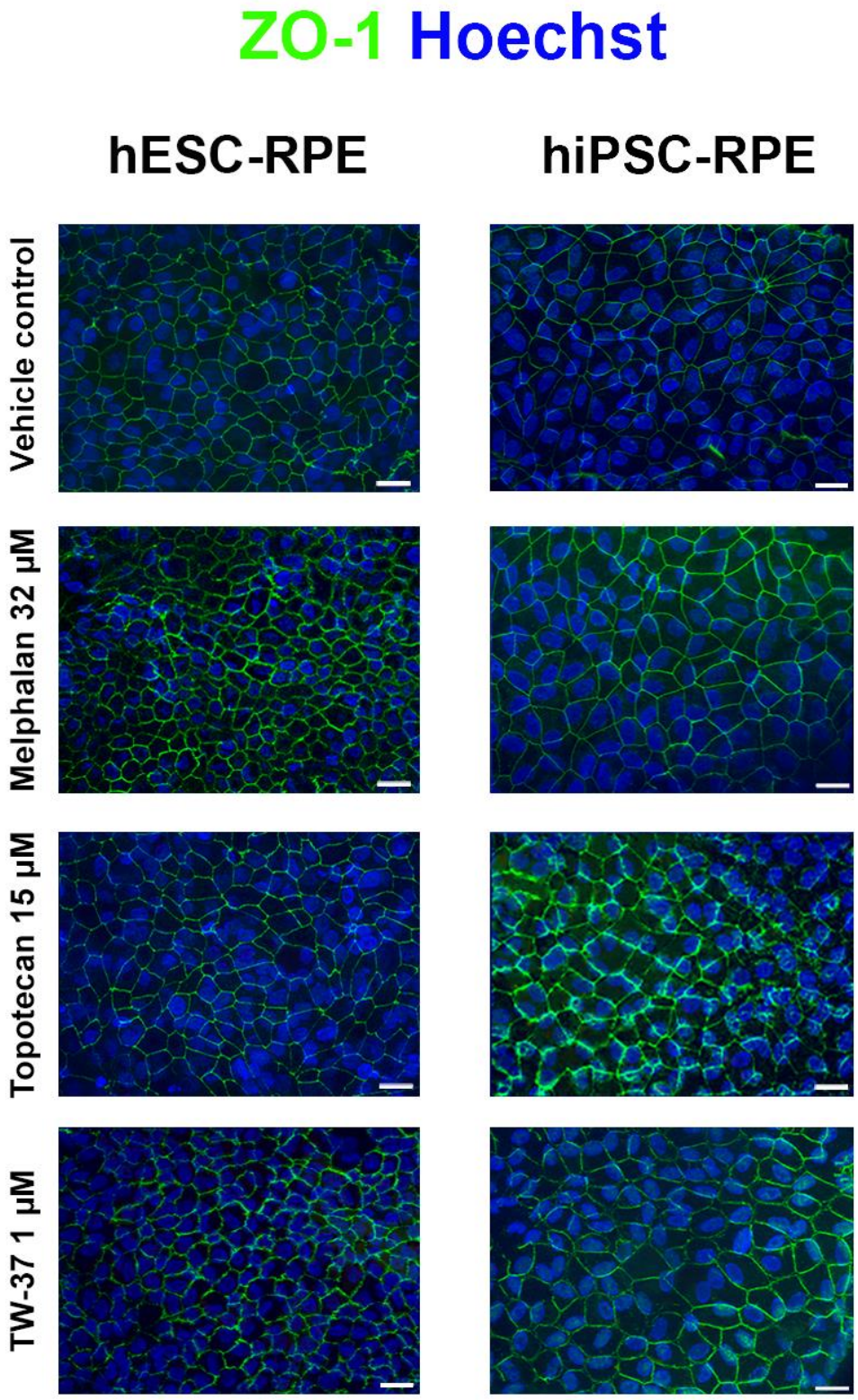

Figure 5-3. Immunofluorescence analysis for the tight junctions of H9 hESC- and hiPSC-derived RPE cells.
Representative immunostaining of ZO-1 (green) counterstained with Hoechst for drug-treated H9 hESC- and hiPSC-derived RPE cells (vehicle-treated 0.1% DMSO, melphalan 32 µM, topotecan 15 µM, and TW-37 1 µM). 3 RPE transwell inserts (24-well plates) per treatment were used as biological replicates (n = 3). Scale bars; 20 µm.

To quantitatively assess the impact of chemotherapeutic drugs on the RPE's barrier function, transepithelial electrical resistance (TEER) values were measured in mature-stage RPE transwell inserts (>8-week-old) before drug administration and after 72 hours of incubation (**Figure 5-4**). Data demonstrated a significant decrease in TEER of the hESC- and hiPSC-derived RPE monolayers in all the concentrations tested for all three drugs compared to the vehicle-only treatment. These results suggest that Rb chemotherapeutic treatments affect the RPE's barrier function.

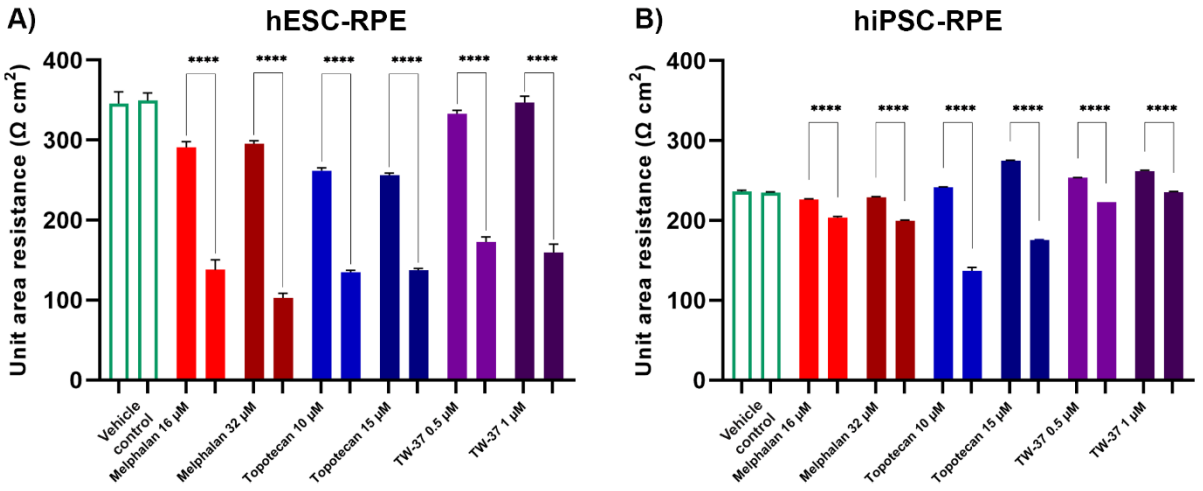

Figure 5-4. Transepithelial electrical resistance analysis of H9 hESC- and hiPSC-derived RPE cells.
Bar graphs showing transepithelial electrical resistance values ($\Omega \cdot cm^2$) of vehicle- and drug-treated (**A**) H9 hESC- and (**B**) hiPSC-derived RPE cells (vehicle-treated 0.1% DMSO, melphalan 16-32 µM, topotecan 10-15 µM, and TW-37 0.5-10 µM). 3 RPE transwell inserts (24-well plates) per treatment were used as biological replicates. Data presented as mean ± SEM (n = 3 inserts from each biological replicate). Values of $p \leq 0.05$ were considered statistically significant (*$p \leq 0.05$, **$p \leq 0.01$, ***$p \leq 0.001$, ****$p \leq 0.0001$).

As part of the quantitative assessment of the cell cycle phase distribution analysis, these three chemotherapeutic agents were tested in both hESC- and hiPSC-derived RPE cell models. Representative data for RPE cell population gating for cell cycle assay is included (**Figure 5-5**). The results revealed that for all drug treatments, there was no significant difference in the percentage of cells in any of the cell cycle phases (**Figure 5-6A-F**). At tested concentrations of each drug, no cell accumulation in the S-phase was detected, nor was the prevention of the cycle's progression to the G2/M-phase, indicating no cell cycle alterations compared to vehicle-treated controls.

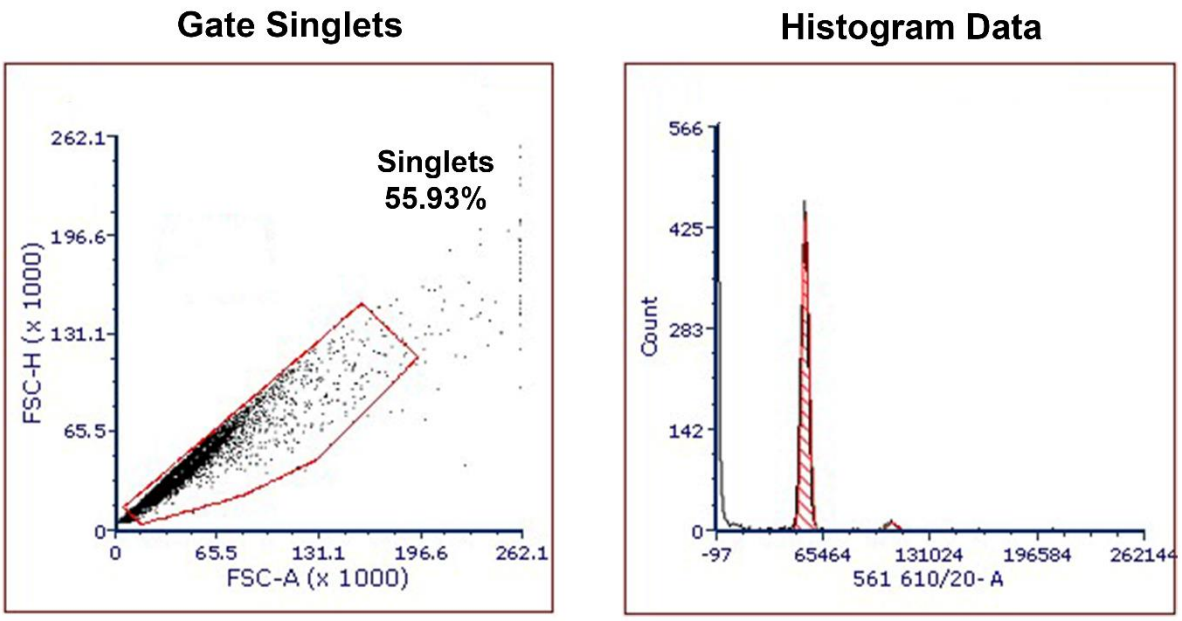

DNA Cycle Statistics

Cycle	G1 Mean	G1 CV	%G1	G2 Mean	G2 CV	%G2	%S	G2/G1	%Total	B.A.D.
Diploid	55120.92	3.87	96.13	108938.23	2.49	2.66	1.21	1.98	100.00	0.00

Figure 5-5. Cell population gating for cell cycle assay in H9 hESC- and hiPSC-derived RPE cells.
Representative dot-plot, histogram graph, and DNA cycle statistics table of the cell population gating of vehicle control- and drug-treated single-cell RPE suspensions.

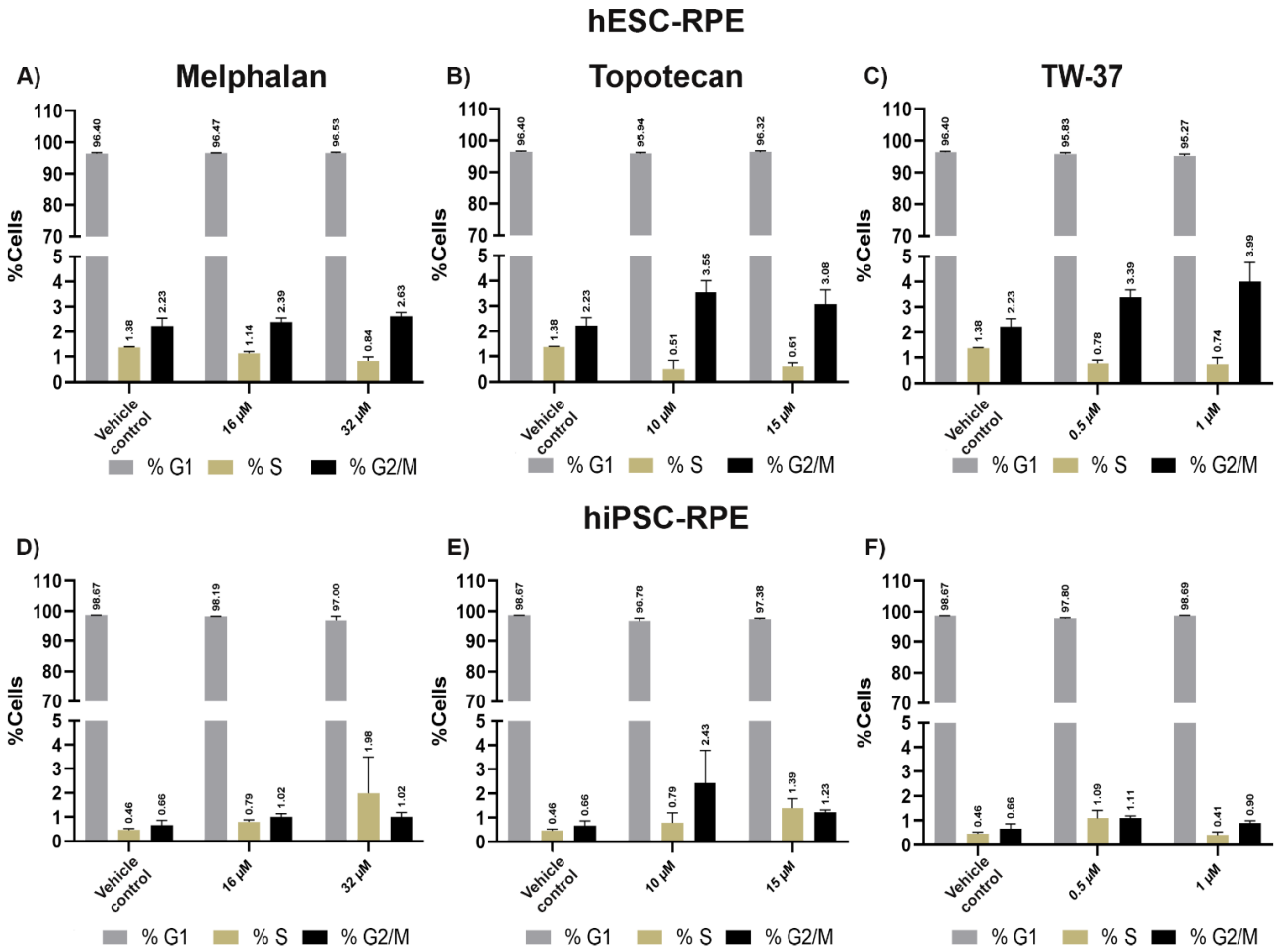

Figure 5-6. Cell-cycle phase distribution analysis of clinically used chemotherapeutic agents for Rb treatment in H9 hESC- and hiPSC-derived RPE cells.

Bar graphs showing the percentage of cells (%) of G1-, S-, and G2/M-phase in drug-treated H9 hESC- and hiPSC-derived RPE cells (melphalan, **A**, **D**; 16, 32 μM, topotecan, **B, E**; 10, 15 μM, TW-37, **C, F**; 0.5, 1 μM alongside vehicle-treated sample; 0.1% DMSO). 3 RPE wells (24-well plates) per treatment were used as biological replicates. Data presented as mean ± SEM (n = 3 wells from each biological replicate).

Drug cytotoxicity was assessed by lactate dehydrogenase (LDH) release into the supernatant and cell killing by apoptosis assay in hESC- (**Figure 5-8**) and hiPSC-derived (**Figure 5-9**) RPE cells. Representative data for RPE cell population gating for apoptosis assay is included (**Figure 5-7**). Melphalan and TW-37 were applied at a dose ten times higher than the maximal dose used in the clinical application (320 μM and 10 μM, respectively; **Figure 5-8A, C; Figure 5-9A, C**) did cause a significant increase in the cytotoxicity, while topotecan (150 μM; **Figure 5-9B**) did so only in hiPSC-derived RPE cells. The percentage of apoptotic cells in hESC- and hiPSC-derived RPE cells treated with two concentrations within the range used in clinical application remained very similar to vehicle-treated controls (**Figure 5-8; Figure 5-9**). These assays, in combination, pointed to 8-32 μM melphalan, 5-15 μM topotecan, and 0.1-1 μM TW-37 as the most effective doses in retaining the healthy RPE tissue unaffected in both hESC- and hiPSC-RPE models.

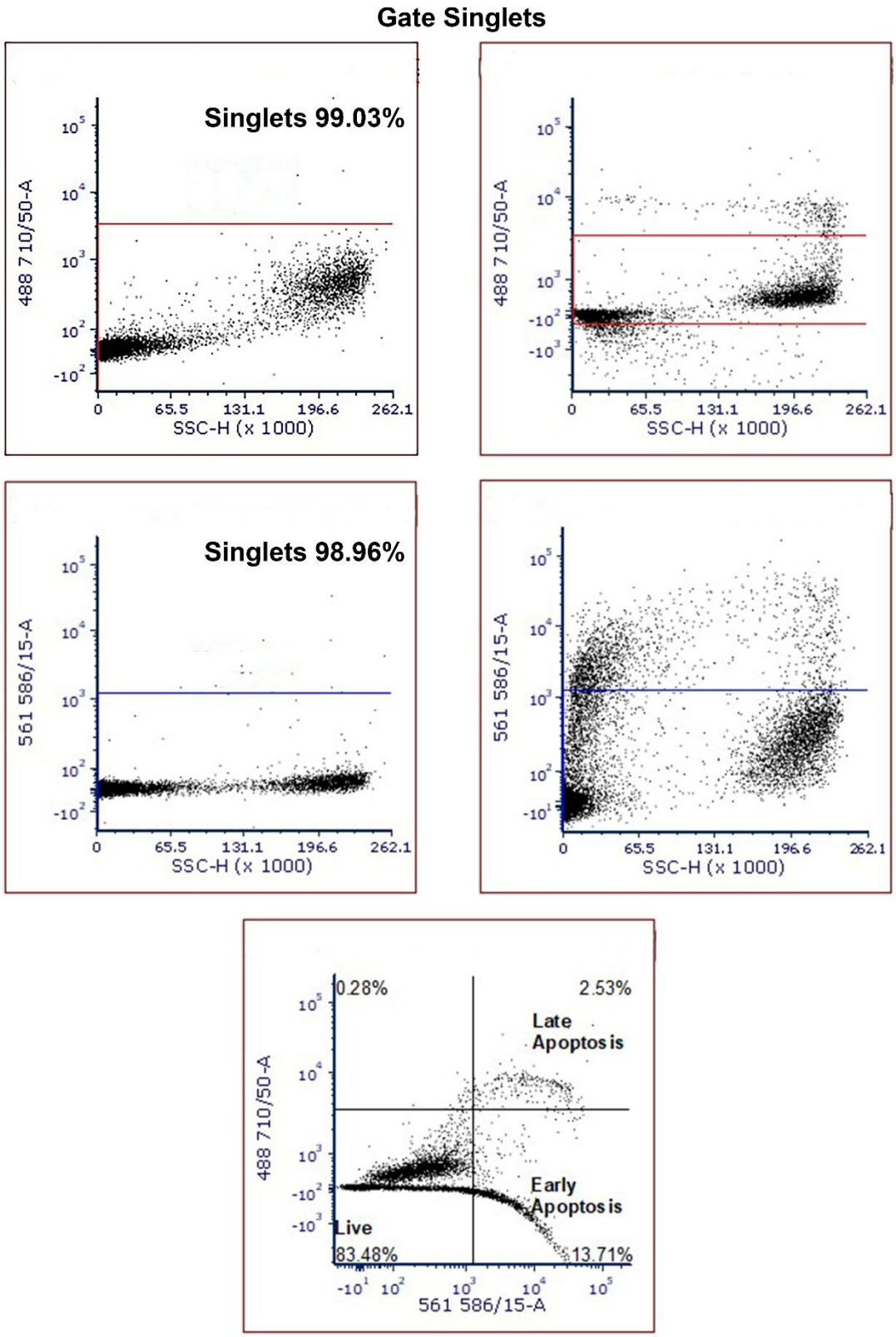

Figure 5-7. Cell population gating for apoptosis assay in H9 hESC- and hiPSC-derived RPE cells.
Representative dot-plots of the cell population gating of vehicle control- and drug-treated single-cell RPE suspensions.

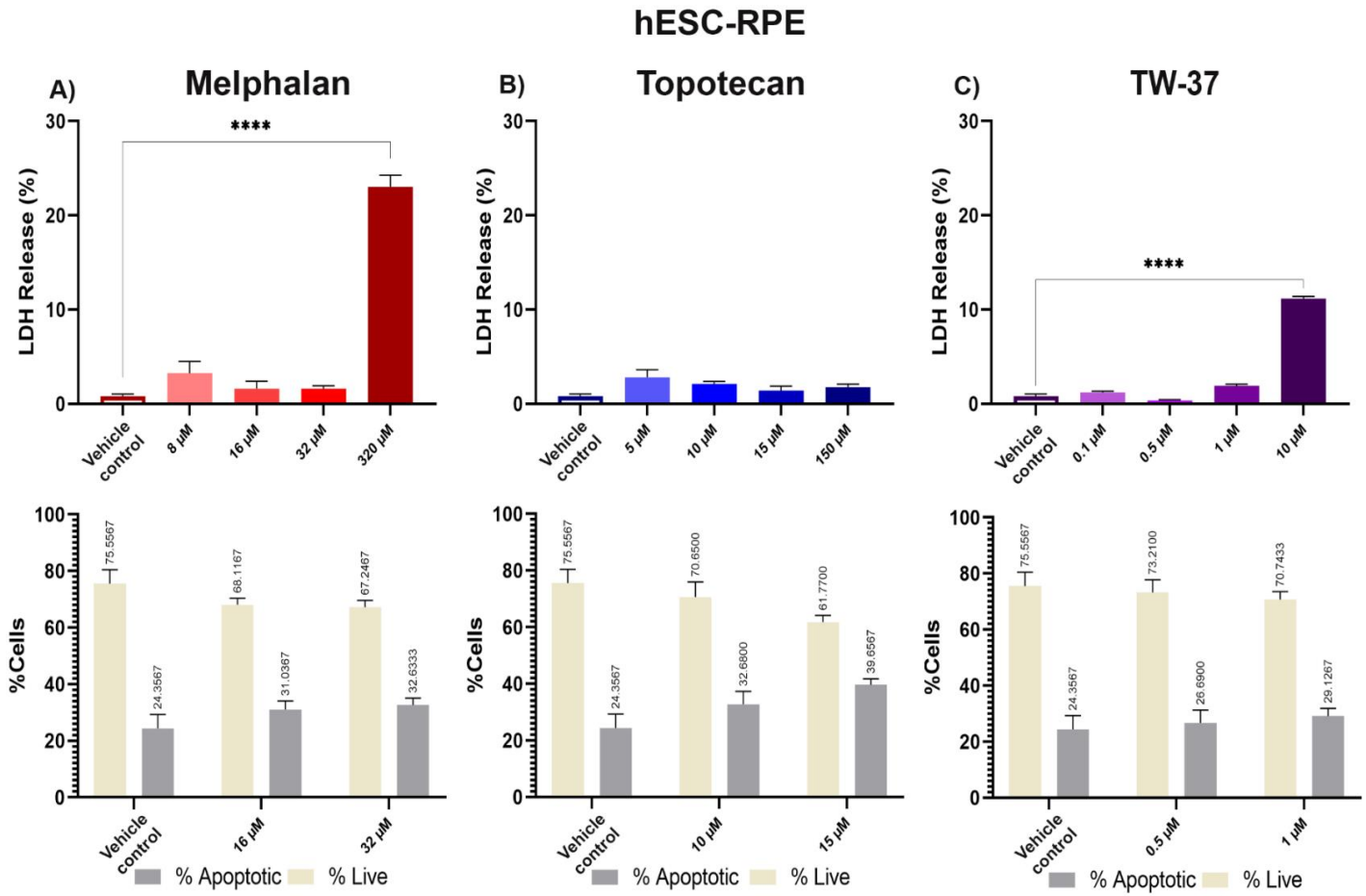

Figure 5-8. Assessment of clinically used chemotherapeutic agents for Rb treatment in H9 hESC-derived RPE cells. Bar graphs showing cytotoxicity of the specified agent measured by LDH release (%) into the supernatant and the percentage of apoptotic and live cells (%) in drug-treated H9 hESC-derived RPE cells (melphalan, **A**; 8, 16, 32 µM, topotecan, **B**; 5, 10, 15, 150 µM, TW-37, **C**; 0.1, 0.5, 1, 10 µM alongside vehicle-treated sample; 0.1% DMSO). The 100% cytotoxicity value corresponds to the Maximum LDH activity of Triton-X-100. 3 RPE transwell inserts (24-well plates) per treatment were used as biological replicates. Data presented as mean ± SEM (n = 3 inserts from each biological replicate). Values of $p \leq 0.05$ were considered statistically significant (*$p \leq 0.05$, **$p \leq 0.01$, ***$p \leq 0.001$, ****$p \leq 0.0001$).

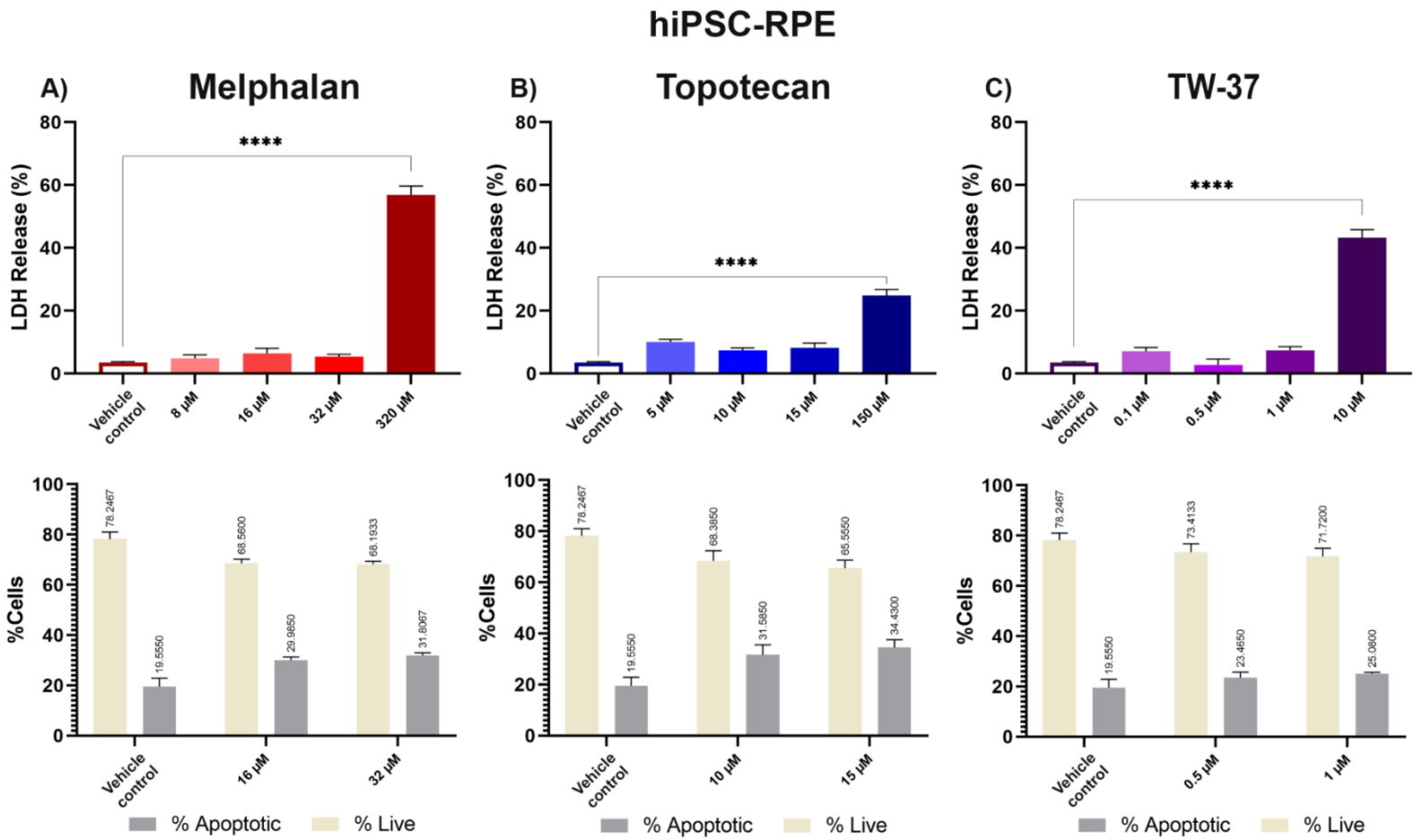

Figure 5-9. Assessment of clinically used chemotherapeutic agents for Rb treatment in hiPSC-derived RPE cells.
Bar graphs showing cytotoxicity of the specified agent measured by LDH release (%) into the supernatant and the percentage of apoptotic and live cells (%) in drug-treated hiPSC-derived RPE cells (melphalan, **A**; 8, 16, 32 µM, topotecan, **B**; 5, 10, 15, 150 µM, TW-37, **C**; 0.1, 0.5, 1, 10 µM alongside vehicle-treated sample; 0.1% DMSO). One hiPSC-derived clone was used for hiPSC-RPE differentiation. 3 RPE transwell inserts (24-well plates) per treatment were used as biological replicates. Data presented as mean ± SEM (n = 3 inserts from each biological replicate). Values of $p \leq 0.05$ were considered statistically significant (*$p \leq 0.05$, **$p \leq 0.01$, ***$p \leq 0.001$, ****$p \leq 0.0001$).

5.3.2 Gene expression regulation in drug-treated hESC- and hiPSC-derived RPE cells

To evaluate the impact of Rb drugs on RPE cells, we assessed the gene expression of several RPE markers by quantitative real-time PCR (qPCR) in drug-treated (**Figure 5-10**) hESC- and (**Figure 5-11**) hiPSC-derived RPE cells. The selected markers are essential genes in the RPE whose function of the encoded protein includes apical polarity maintenance (Ezrin, *EZR*); tight junction maintenance (*ZO-1*); melanin conversion pathway (*TYR*); transport of retinol (transthyretin, *TTR*) and retinol conversion in the visual cycle (*RPE65*). There were no changes in the expression of markers evaluated in hESC-RPE treated with Melphalan. However, a significant downregulation of *TYR, TTR, and RPE65* was observed in hiPSC-RPE treated with 32 µM melphalan and *EZR* with 16-32 µM melphalan treatments. The difference in gene expression was also observed between hESC- and hiPSC-derived RPE treated with topotecan. While both models displayed significant downregulation of *TYR, TTR* and *RPE65* expression, *EZR* expression was only downregulated in hiPSC-derived RPE cells. TW-37 also caused a different response in hESC- and hiPSC-RPE models. *EZR* was upregulated in hESC-derived RPE; *ZO-1, TYR* and *TTR* in hiPSC-derived RPE, whilst *TTR* was downregulated in hESC-derived RPE cells. These data demonstrate that amongst the three tested drugs, 10-15 µM topotecan treatments modulated the expression of genes involved in melanin and retinol pathways in both PSC-RPE models. The other two drugs caused changes in gene expression in one of the PSC-RPE models, suggesting donor-specific effects that may depend on the genetic background and the epigenetic starting point of hESC versus hiPSC lines.

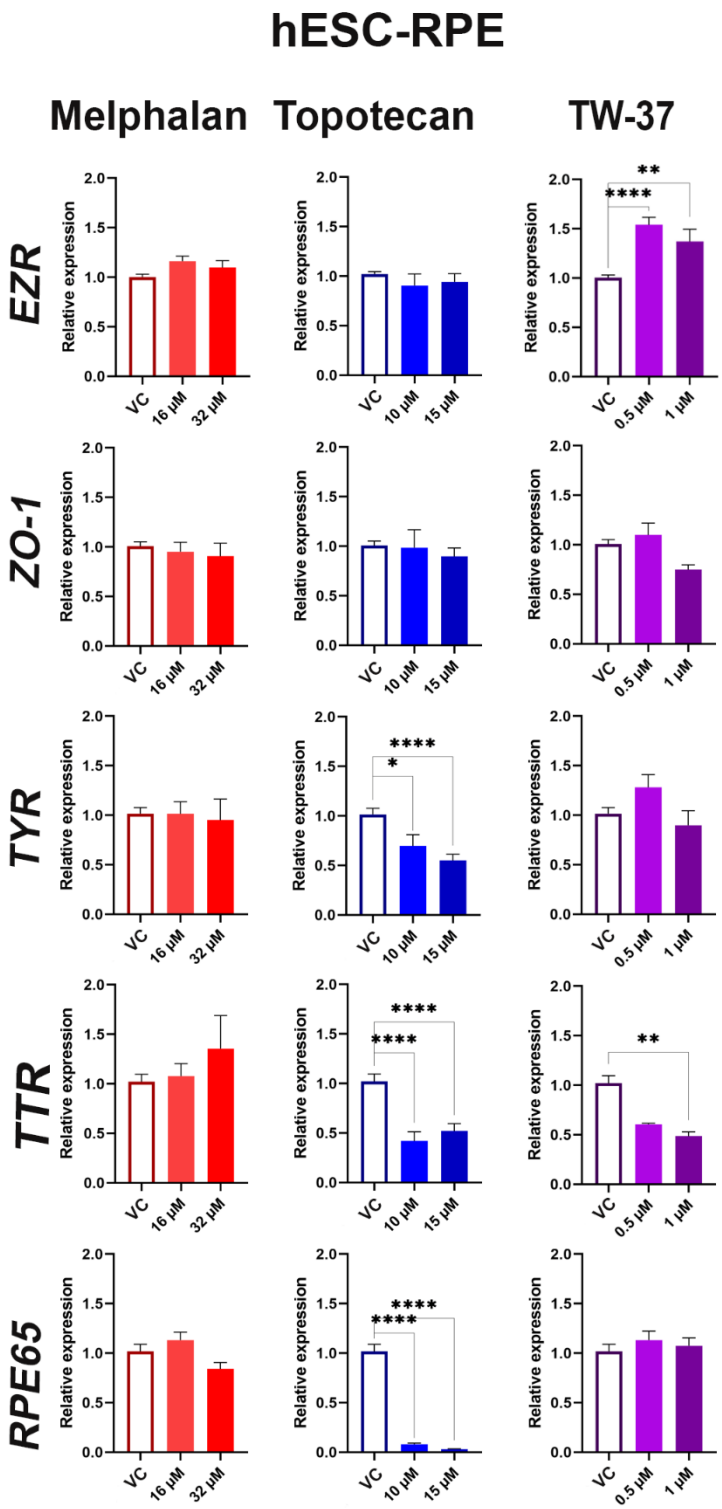

Figure 5-10. Quantitative real-time PCR validation of selected genes of clinically used chemotherapeutic agents for Rb treatment in H9 hESC-derived RPE cells.

Gene expression levels of *EZR, ZO-1, TYR, TTR,* and *RPE65* normalised relative to the housekeeping gene *GAPDH* in drug-treated H9 hESC-derived RPE cells (melphalan; 16, 32 µM, topotecan; 10, 15 µM, TW-37; 0.5, 1 µM, alongside vehicle-treated (VC) sample; 0.1% DMSO). RPE cell pellets from 3 wells (24-well plates) per treatment were used as biological replicates. All reactions were performed in triplicates. Data presented as mean ± SEM (n = 9 reactions). Values of $p \leq 0.05$ were considered statistically significant (*$p \leq 0.05$, **$p \leq 0.01$, ***$p \leq 0.001$, ****$p \leq 0.0001$).

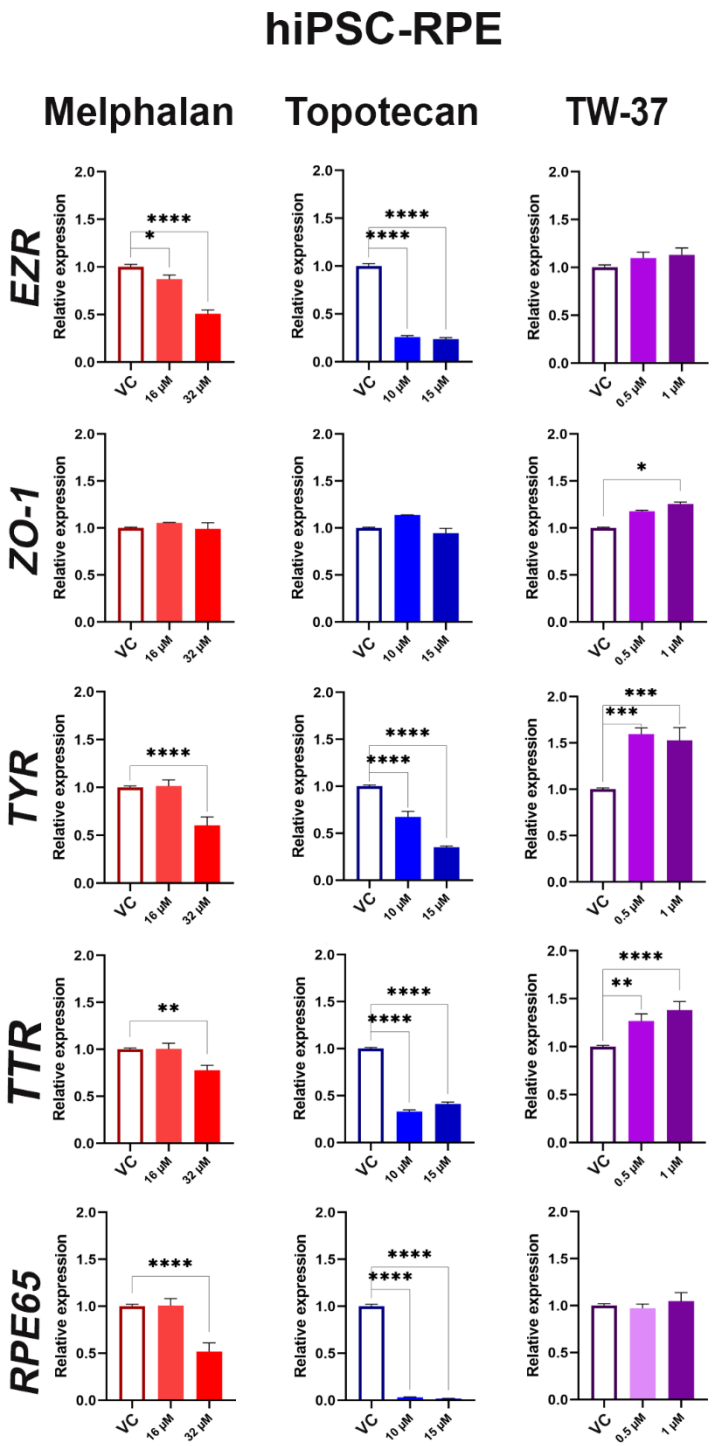

Figure 5-11. Quantitative real-time PCR validation of selected genes of clinically used chemotherapeutic agents for Rb treatment hiPSC-derived RPE cells.

Gene expression levels of *EZR, ZO-1, TYR, TTR,* and *RPE65* normalised relative to housekeeping gene *GAPDH* in drug-treated hiPSC-derived RPE cells (melphalan; 16, 32 µM, topotecan; 10, 15 µM, TW-37; 0.5, 1 µM, alongside vehicle-treated (VC) sample; 0.1% DMSO). One hiPSC-derived clone was used for hiPSC-RPE differentiation. RPE cell pellets from 3 wells (24-well plates) per treatment were used as biological replicates. All reactions were performed in triplicates. Data presented as mean ± SEM (n = 9 reactions). Values of $p \leq 0.05$ were considered statistically significant (*$p \leq 0.05$, **$p \leq 0.01$, ***$p \leq 0.001$, ****$p \leq 0.0001$).

5.3.3 Phagocytic activity is affected in drug-treated hESC- and hiPSC-derived RPE cells

Phagocytosis of shed photoreceptor outer segments (POSs) is one of the critical functions of the RPE for maintaining the retina. To assess this function, vehicle-treated and drug-treated hESC- and hiPSC-derived RPE cells were incubated with fluorescein isothiocyanate (FITC)-labelled bovine rod POSs. Single-cell RPE suspension samples were analysed by flow cytometry for the percentage of cells able to ingest POSs, and the number of POSs ingested by each cell was assessed through Median Fluorescence Intensity (MFI). Control experiments were used for the robustness of the data. PSC-RPE cells were incubated with FITC-labelled POSs at 4°C to block the POSs ability to phagocytose (**Figure 5-12**). Moreover, the RPE cells were treated with unlabelled POSs to assess background fluorescence. Trypan blue was added to quench any extracellular fluorescence and avoid false-positive fluorescence signals from free or unbound POSs. Data analysis was performed using FCS Express 7.

Drug-treated hESC- (**Figure 5-13A**) and hiPSC-derived (**Figure 5-13B**) RPE cells displayed no significant difference in the fraction of cells able to ingest POSs compared to vehicle-treated controls (0.1% DMSO). However, 16-32 μM melphalan and 10-15 μM topotecan treatments showed a significant decrease in $FITC^+$ POSs internalised by individual cells. In contrast, only 32 μM melphalan and 15 μM topotecan treatments caused a substantial reduction in POSs ingested in the hiPSC-derived RPE cells (**Figure 5-13A-B**). These results point to 16-32 μM melphalan and 10-15 μM topotecan treatments affecting the phagocytic activity of hESC-derived RPE cells, while only the highest concentrations within the clinical range, 32 μM melphalan and 15 μM topotecan, did so in the hiPSC-derived RPE cells. TW-37 treatments for RPE cells revealed no significant difference in POSs phagocytosis.

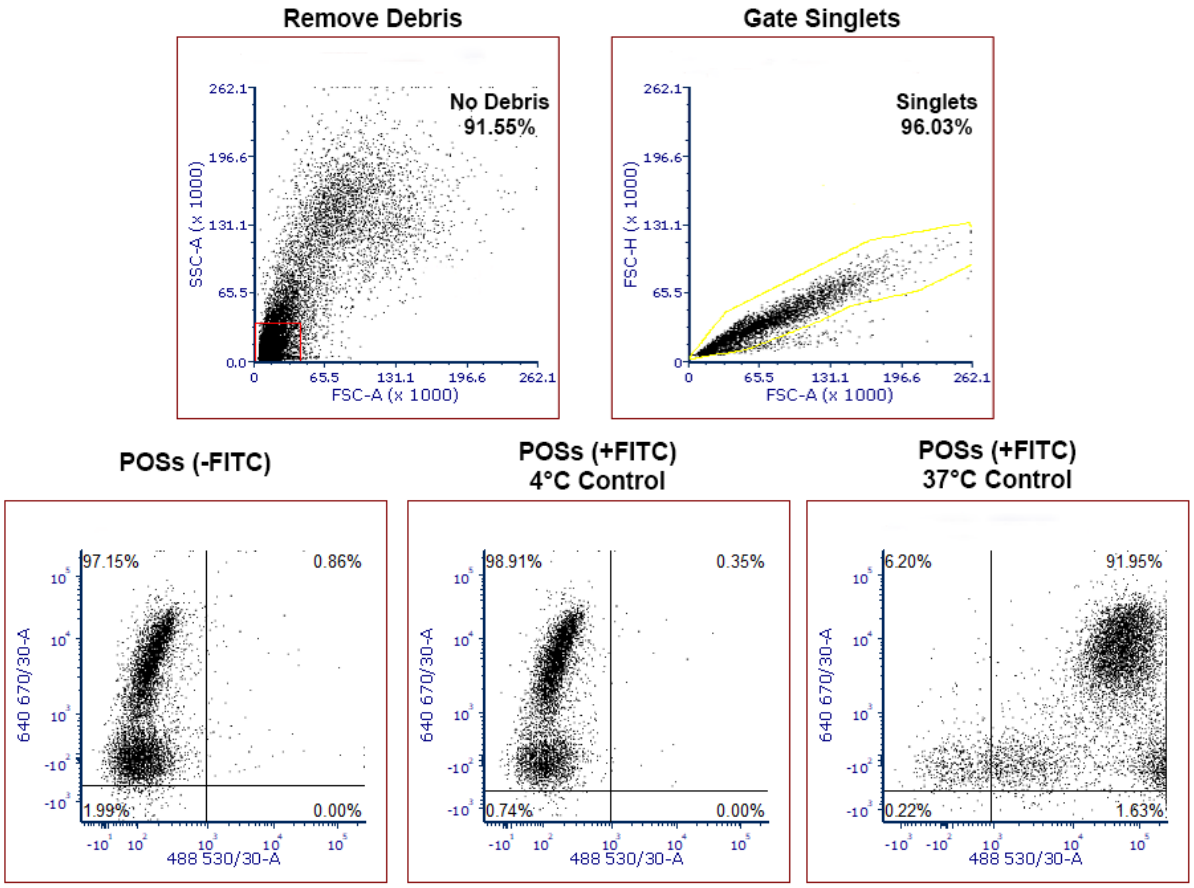

Figure 5-12. Cell population gating for phagocytosis assay in H9 hESC- and hiPSC-derived RPE cells.
Example dot-plots of the control cell population gating and single-cell RPE suspensions incubated with unlabelled, 4°C FITC-labelled, and 37°C FITC-labelled POSs.

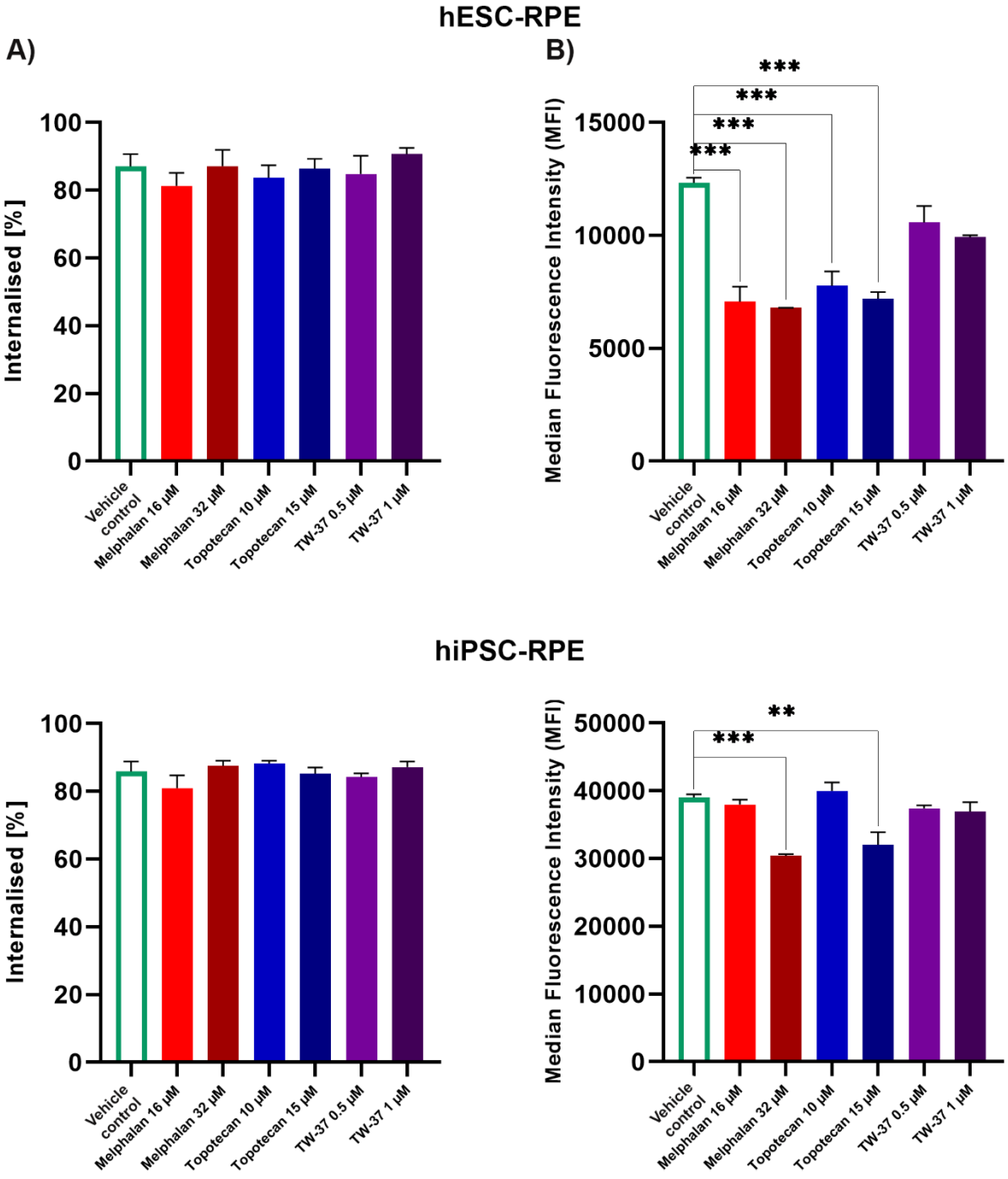

Figure 5-13. Phagocytic activity assessment of clinically used chemotherapeutic agents for Rb treatment in H9 hESC- and hiPSC-derived RPE cells.

Bar graphs showing the fraction of the total cell population that has internalised POSs and the median fluorescence intensity (MFI) values indicating the number of FITC-POSs internalised by individual cells in drug-treated (**A**) H9 hESC- and (**B**) hiPSC-derived RPE cells (melphalan; 16, 32 µM, topotecan; 10, 15 µM, TW-37; 0.5, 1 µM, alongside vehicle-treated sample; 0.1% DMSO). MFI indicates cell-surface receptor density involved in phagocytosis. One hiPSC-derived clone was used for hiPSC-RPE differentiation. 3 RPE transwell inserts (24-well plates) per treatment were used as biological replicates. Data presented as mean ± SEM (n = 3 inserts from each biological replicate). Values of $p \leq 0.05$ were considered statistically significant (*$p \leq 0.05$, **$p \leq 0.01$, ***$p \leq 0.001$, ****$p \leq 0.0001$).

5.4 Discussion

Alterations to the RPE and other adverse events, including RPE hyperplasia, gliosis, and mottling, have been clinically described in the eyes of some patients treated with melphalan and topotecan for Rb management (Xue et al., 2019, Zolfaghari et al., 2018, Süsskind et al., 2016). An *in vitro* study (Süsskind et al., 2016) was the first to report melphalan, topotecan, and carboplatin cytotoxicity on RPE cells. The authors used the ARPE19 cell line to investigate these drugs' toxic cellular effects in a dose-dependent manner. Nonetheless, the ARPE19 model (Hazim et al., 2019) is not directly comparable to the RPE cells as these cells are not well-differentiated, lack pigmentation, have an abnormal karyotype, and show low TEER. While they can phagocytose POSs, these cells have lower POS binding capability but faster kinetics to ingest the bound POSs and degrade the POS phagosomes compared to RPE cells. Although the ARPE19 cell line is widely used in eye research, the epithelial cell morphology and cytoskeletal organisation are not similar to the RPE cells (Hazim et al., 2019). Mature human PSC-derived RPE cells show significant advantages, including representative functionality for POS phagocytosis, TEER, and expression of markers specific to human RPE, as the appearance of pigmentation (Bennis et al., 2017), and thus represent a more likely model for testing the effects of Rb chemotherapeutic drugs.

Interestingly, a study (Singh et al., 2013) reported that hiPSC-derived RPE cells beyond passage (P) 3 fail to form monolayers and present alterations to morphological and functional characteristics and gene expression levels. However, all the assays described in this document for the hESC- and patient hiPSC-derived RPE models were carried out in P2 and P3 while retaining the RPE's key cytological and functional features. hESC- and hiPSC-derived RPE cells exhibited the typical cobblestone morphology and pigmentation, apical-basal polarity, and the expression of RPE-specific proteins. Both PSC-RPE models were incubated with three chemotherapeutic agents for 72 hours, namely melphalan, topotecan, and TW-37. The two highest concentrations clinically tested for all three drugs significantly decreased the TEER of both RPE monolayers. The functionality of the RPE is compromised when the integrity of the monolayer is susceptible to thinning or leakage, which ultimately can lead to the breakage of the barrier. Abnormal thinning of the RPE might lead to the early formation of geographic atrophy lesions (Folgar et

al., 2016), leaving individuals with poor visual acuity. When the blood-retinal barrier (BRB) is affected by injuries, immune and inflammatory components access the immune-privileged site of the retina, initiating an exacerbating cycle of neuroimmune responses that compromise retinal homeostasis and can lead to the development of disease phenotypes (Yang et al., 2020). BRB impairment can be a precursor of retinal diseases such as diabetic retinopathy, glaucoma, AMD, and retinal inflammatory disorders, including uveitis, central serous chorioretinopathy, and retinal vein occlusion (Yang et al., 2020).

High doses of melphalan and topotecan within the range used in the clinical application did affect the PSC-RPE ability to internalise POSs of PSC-RPE cells. Furthermore, these treatments downregulated the gene expression in the melanin and retinol pathways in RPE cells, which can impact pigmentation and the visual cycle. In contrast, hESC-derived RPE cells only did so for the apical-polarity maintenance gene. Importantly, our results revealed that in both RPE cell models, none of the drug treatments within the clinical range showed significant cytotoxic and apoptotic effects. No alterations were observed in the cell cycle and the apical-basal polarity. Clinical evidence in treated Rb patients has reported RPE hyperplasia due to chemotherapy. Still, the results indicate that it is unlikely to occur as the cell cycle remains unaffected.

High concentrations of melphalan and topotecan treatments may induce mechanical stress or a dynamic environment not near equilibrium, which compromises the durability and strength of the RPE monolayer (Rashid et al., 2016). These defects in the RPE cells make them susceptible to neovascularisation or the initiation of atrophic lesions that could lead to retinal disease. Thus, exposure of RPE cells to these Rb drugs should be avoided as much as possible for efficient drug delivery.

Future work to further assess these chemotherapeutic drugs and their effects on RPE cells would likely include a new experimental design where the RPE monolayers are incubated for recovery between cycles of drug exposure. Given this proposal, results would better reflect the overall alterations to the RPE by the administration of Rb chemotherapeutics as the design would more accurately mimic the potential dysfunctional environment. To this end, a 2D-3D patient hiPSC-derived retinal organoid and RPE coculture would provide new insights to better simulate the

in vivo niche of the retina and the RPE when chemotherapeutic agents are administered. To date, only 2D coculture of human Rb cell line Y79 and inserts of ARPE19 cell line has been achieved to test the toxicity of drugs used in breast cancer therapy (Mäenpää et al., 2004). However, as previously discussed, the ARPE19 cell line features are not comparable to PSC-derived RPE cells due to significant differences in cell organisation, representative functionality, and specificity.

5.5 Conclusion

In summary, our results demonstrate that although the most used Rb chemotherapeutic drugs do not cause RPE cytotoxicity, their administration to the RPE cells is correlated to changes in gene expression, phagocytic capacity, and barrier function. The most common delivery method in clinical application aiming to achieve the highest drug bioavailability is intravitreal injection. Given the results presented in this chapter, the application of other delivery methods is supported [e.g., intra-arterial chemotherapy (IAC) through the ophthalmic artery], which are likely to achieve a high concentration of the drugs reaching the tumour without exposing and/or damaging the adjacent healthy RPE monolayer. Finally, these findings demonstrate the feasibility of using PSC-derived RPE disease models to develop a robust platform for testing chemotherapeutic agents that could provide a roadmap for a personalised drug treatment regime.

Chapter 6

6 General discussion and Future Work

6.1 Discussion

Retinoblastoma (Rb) is retinal cancer affecting children younger than five years with a prevalence of around 1:15,000 infants worldwide (Stenfelt et al., 2017, Valverde et al., 2005, Saengwimol et al., 2018). The retinal malignancy is initiated by the biallelic inactivation of the tumour suppressor gene, *RB1,* and the retinoblastoma protein (pRB) loss, which accounts for up to 98% of Rb cases (Kaewkhaw and Rojanaporn, 2020). Current standard protocols include systemic, intravitreal, intraarterial and periocular chemotherapeutic treatments (Yanık et al., 2015). Available chemotherapy treatments for Rb management include two or three drugs with alkylating, DNA-damaging agents and/or cytoskeletal inhibitors such as melphalan, topotecan, etoposide, vincristine, and carboplatin (Yanık et al., 2015, Sachdeva and O'Brien, 2012). Novel and small molecules like TW-37 are promising Rb drugs that induce apoptosis and inhibit tumour growth (Zeitlin et al., 2008). Despite the progress in Rb treatments, standard Rb drugs are associated with cytotoxic adverse effects on the retina and alterations to the retinal pigment epithelium (RPE). Understanding Rb tumour initiation at the molecular, cellular, genetic, and epigenetic levels is essential for designing novel and efficacious treatments.

Our pRB-depleted hESC- and patient hiPSC-derived RO models shared the following key features throughout development that are displayed as well in Rb tumours: **1)** increased fraction of proliferating cone precursors ($RXR\gamma^{+}Ki67^{+}$), RGCs ($SNCG^{+}Ki67^{+}$) and retinal progenitors ($VSX2^{+}Ki67^{+}$); **2)** an increased percentage of proliferating ($Ki67^{+}$) and apoptotic ($CASP3^{+}$) cells; a block in differentiation that led to **3)** a decreased fraction of ACs ($AP2\alpha^{+}$) from day 90 of differentiation; and **4)** a lack of *RB1* expression in homozygous (*RB1*$^{-/-}$) and a significant decrease of the pRB^{+} cell fraction in the heterozygous (*RB1*$^{+/-}$) hiPSC-derived ROs.

These results showing a decrease of HCs, ACs, and RGCs in pRB-depleted ROs might indicate that pRB dysfunction could interfere with retinal cell differentiation and survival. Reducing specific cell populations in the absence of pRB could be a compensatory response to an increase in the proliferation of cone precursor cells,

which would agree with (Zheng et al., 2020), who reported that pRB is required for PR and BC differentiation.

scRNA-seq analyses *in vivo* (Collin et al., 2021) and *in vitro* (Rozanska et al., 2022) from our group suggested a maturing cone precursor as the cell of origin for human Rb, which other groups corroborated (Liu et al., 2020, Kanber et al., 2022, Li et al., 2022, Yang et al., 2021b, Wu et al., 2022). Results revealed proliferating cone precursors ($RXR\gamma^{+}Ki67^{+}$) as a common feature of pRB-depleted ROs. An RPC or rod cell of origin identity for human Rb has been suggested by (Norrie et al., 2021), but further work on single-cell lineage tracing studies would be required to address this hypothesis fully.

Data from our scRNA-seq analyses (Rozanska et al., 2022, Collin et al., 2021) revealed that starting cone precursors express RGC and HC markers in patient Rb tumours and human pRB-depleted ROs. (Liu et al., 2021) reported the expression of neuronal/RGC markers in the less differentiated cone cells in Rb tumours, which agrees with results from our scRNA-seq data and the increased fractions of proliferating RGCs ($SNCG^{+}Ki67^{+}$) and HCs ($PROX1^{+}Ki67^{+}$) reported during the development of pRB-depleted ROs. Interestingly, it has been suggested that the cell-originating Rb in a murine model had features of an HC (Ajioka et al., 2007) or differentiated Müller glial cells with progenitor properties (Pajovic et al., 2011). Furthermore, (Xu et al., 2014) hypothesised that human and mouse retinal tumours originate from various inherently death-resistant phenotypes, which would support the idea that human Rbs differ from the murine Rb model in terms of their precursor cell of origin. Additionally, mouse bulk RNA-seq studies pointed out that mouse Rb tumours resemble ACs, HCs (Qi and Cobrinik, 2017), PRs, and RPCs (Zhang et al., 2004, Donovan et al., 2006). In their *in vitro* study using murine retina cultures, (Singh et al., 2018) found that only pRb-depleted immature ($Arr3^{-}$) cone precursors entered the cell cycle and failed to move from the S- to the M-phase. These findings suggest that human Rb originated from a cell other than an interneuron, while murine Rb might have an interneuron cell of origin.

Once the pRB-depleted RO models were characterised, they were assessed for drug screening by incubating them with three Rb chemotherapeutic agents: melphalan, topotecan, and TW-37. The three drugs were administered in doses

within the range in clinical application plus a 10-fold increase of the highest dose of the range.

Cytotoxicity results for day 90 revealed significant cell death in a dose-dependent manner in pRB-depleted ROs. However, the highest melphalan dose within the clinical range caused cytotoxicity in wild-type ROs, which suggests that it is not specific to pRB-depleted ROs. It is possible to speculate that retinal cells might be more drug-sensitive at this point since there is more proliferation progression as part of retinal development. Day 150 results showed significant cell death levels in a dose-dependent manner in pRB-depleted ROs. Data revealed that doses of the three drugs within the clinical range did not cause significant cytotoxicity and retained the healthy tissue unaffected. This suggests that drug responses are more specific to target the proliferating cone precursors at a mature stage of differentiation (day 150).

All three compounds in both time points significantly decreased the percentage of proliferating cone precursors ($RXR\gamma^{+}Ki67^{+}$) in pRB-depleted ROs to the levels found in wild-type ROs. Simultaneously, the pRB-depleted ROs also exhibited an increase in the fraction of apoptotic cone precursor ($RXR\gamma^{+}CASP3^{+}$) cells, while no changes were observed in the wild-type control ROs within the clinical doses. These results agree with previously reported data by (Liu et al., 2020), showing a decrease in proliferating cells and an increase in apoptotic cells in pRB-depleted ROs after topotecan administration. Results for day 150 pRB-depleted ROs treated with 32 μM melphalan and 10 μM topotecan agree with (Saengwimol et al., 2018) regarding proliferation and apoptotic patterns in chemotherapy-naïve tumour organoids that did not arrest in the S-phase but underwent apoptosis in the sub-G1 phase.

A lack of response was observed in $RXR\gamma^{+}CASP3^{+}$ cells in all the TW-37 treatments in 150-day-old pRB-depleted ROs. This might suggest that TW-37 works in a limited fashion by significantly decreasing proliferating cone precursors but not increasing apoptotic cone precursors, as observed with the other two chemotherapeutic agents.

Soft colony agar assays confirmed that the sphere-like aggregates grew anchorage-independent from dissociated vehicle- and drug-treated pRB-depleted ROs. Results revealed that all Rb drug treatments within the clinical range significantly decreased the size and number of the sphere-like aggregates.

As part of modelling the Rb environment *in vitro*, we developed hESC- and patient hiPSC-derived RPE cell models that exhibited the typical pigmented cobblestone morphology, apical-basal polarity, and the expression of RPE-specific proteins. Clinically, the RPE exhibits alterations including cytotoxicity, hyperplasia, gliosis, and mottling in Rb patients treated with melphalan and topotecan (Xue et al., 2019, Zolfaghari et al., 2018, Süsskind et al., 2016).

Drug screening using Rb chemotherapeutics was performed in our PSC-RPE models. Results demonstrated that in both RPE monolayer models, none of the drug treatments within the clinical range showed significant cytotoxic and apoptotic effects. Also, no changes were observed in the cell cycle and the apical-basal polarity. However, analyses revealed a significantly decreased resistance of the RPE's barrier manifested by TEER values in both models when treated with the two highest doses for all three drugs. In parallel, high doses of melphalan and topotecan within the clinical range induced mechanical stress and decreased the RPE capacity to internalise POSs, compromising the RPE's functionality and integrity. Moreover, these treatments downregulated the gene expression in the melanin and retinol pathways in RPE cells, impacting cell pigmentation and the visual cycle. These defects in the RPE cells are insufficient to support evidence of RPE hyperplasia but make them susceptible to neovascularisation or atrophic lesions that could lead to retinal disease. Therefore, exposure of RPE cells to these chemotherapeutic agents should be avoided as much as possible for an efficient recommended intra-arterial drug delivery.

Together, these results demonstrate the feasibility of pRB-depleted ROs for studying tumourigenesis as they recapitulate the development of Rb tumours. Finally, the retinal organoid and the PSC-RPE models are powerful platforms for testing new Rb chemotherapeutic drugs.

6.2 Future directions

The findings of this study have suggested that a proliferating cone precursor might be the cell of origin for human Rb, which multiple scRNA-seq studies have supported. However, single-cell lineage tracing studies would be required to fully address discrepancies in the identity of the cell of origin for human Rb. In this thesis, the proliferating cone precursors are the cell target of interest for Rb chemotherapeutics testing in pRB-depleted RO models. Importantly, the drug's aim is

the apical layer in the periphery of the organoid structure. However, further research on drug penetration would be required to study these drugs' effects in other retinal cell types located in deeper layers and the hypoxic core of the RO models.

Although our pRB-depleted ROs showed positive responses to melphalan and topotecan treatments, results for TW-37 revealed a limited response. We suggest that pRB-depleted organoids might show better responses to chemotherapeutic drugs in a different and improved experimental design. Changes, including the drug incubation time and administration (7-day treatment) followed by continuous culture as described by (Liu et al., 2020), might improve the response of chemotherapeutic agents such as TW-37. Further work as triple staining of proliferating and apoptotic cone precursors ($RXR\gamma^{+}Ki67^{+}CASP3^{+}$) might also provide a better understanding of the killing efficacy and specificity of these chemotherapeutic agents.

Further assessment of the response of pRB-depleted ROs and RPE cells to Rb drugs should include a prolonged drug administration followed by a continuous culture that would allow a recovery time for the tissue. Given this different experimental approach, results would more accurately reflect the overall alterations to the drug-treated ROs and RPE cells. To this end, a 2D-3D RO and RPE coculture would be suitable to better simulate the *in vivo* environment of the retina and the RPE after Rb drug administration.

Although our results corroborated the validity of RO and PSC-RPE *in vitro* models as suitable systems for drug and cytotoxicity screening prior to large clinical trials, more work employing a larger number of chemotherapeutic agents and hiPSCs from patients with various mutations in the *RB1* gene is needed.

Finally, hESC and hiPSC technologies have provided advantages for developing reliable developmental and disease models that would serve as suitable platforms for drug testing. However, further improvements to differentiation protocols are required as, for example, variability between organoid batches is a pending issue that needs to be addressed. Additionally, the interaction between PRs from organoids and RPE cells requires further research to improve the understanding of the pathomechanisms of retinal degenerative diseases.

6.3 General conclusions

Retinal disease modelling via RO and RPE differentiation from hESCs and hiPSCs is a remarkable technology that has provided insights into cellular and molecular pathomechanisms as a roadmap for a personalised drug treatment regime. Our pRB-depleted hESC- and patient hiPSC-derived RO models recapitulate Rb's development and malignant transformation *in vivo*. Rb organoids were characterised by a significant increase in the fraction of proliferating cone precursors ($RXR\gamma^{+}Ki67^{+}$) and an enriched fraction of cells in the S-phase during the mid and late stages of retinal development. Also, they exhibited tumourigenesis features by forming sphere-like aggregates in soft agar, which indicate cell growth in an anchorage-independent manner and cell transformation *in vitro*.

The response of our RO models to Rb chemotherapeutic agents was assessed for validating drug and toxicology testing with possible therapeutic implications. Results have shown that administration of Rb drugs within the range used in a clinical application at day 150 of differentiation significantly reduced the proliferating cone precursor ($RXR\gamma^{+}Ki67^{+}$) cell percentage and increased the fraction of apoptotic cone precursor ($RXR\gamma^{+}CASP3^{+}$) cells while retaining the healthy tissue unaffected. Lastly, our hESC- and patient hiPSC-derived RPE models exhibited no cytotoxicity but alterations in gene expression, phagocytic capacity, and barrier function when exposed to Rb chemotherapeutic agents. Finally, using pRB-depleted RO and PSC-derived RPE models, this study recapitulated Rb's tumourigenesis *in vitro* and established a robust platform for testing novel Rb chemotherapeutic agents. This work was peer-reviewed and published in (Rozanska et al., 2022), and a second manuscript is currently under review (Cerna-Chavez et al.).

Appendices

Appendix A: List of publications

Rozanska A, **Cerna-Chavez R**, Queen R, Collin J, Zerti D, Dorgau B, Beh CS, Davey T, Coxhead J, Hussain R, Al-Aama J, Steel DH, Benvenisty N, Armstrong L, Parulekar M, Lako M. pRB-Depleted Pluripotent Stem Cell Retinal Organoids Recapitulate Cell State Transitions of Retinoblastoma Development and Suggest an Important Role for pRB in Retinal Cell Differentiation. *Stem Cells Transl Med*. 2022 Apr 29;11(4):415-433. doi: 10.1093/stcltm/szac008. PMID: 35325233; PMCID: PMC9052432.

Cerna-Chavez, R. and Rozanska, A. L. and Poretti, G. L. and Benvenisty, N. and Parulekar, M. and Lako, M. Retinal Pigment Epithelium Exhibits Gene Expression and Phagocytic Activity Alterations When Exposed to Retinoblastoma Chemotherapeutics. Available at SSRN: https://ssrn.com/abstract=4244886 or http://dx.doi.org/10.2139/ssrn.4244886

Serpa, T. and **Cerna-Chávez, R.** Una terminología trilingüe para la Medicina Regenerativa y la Ingeniería de Tejidos: un estudio basado en el uso de corpora en la composición de glosarios de lenguaje especializado en realidad aumentada. *Revista Digital Internacional de Lexicología, Lexicografía y Terminología*, 2020(3): p. 161-181.

Bibliography

A, H. & B, S. 2011. Potency of Various Types of Stem Cells and their Transplantation. *Journal of Stem Cell Research & Therapy,* 01.

AASEN, D. M. & VERGARA, M. N. 2019. New Drug Discovery Paradigms for Retinal Diseases: A Focus on Retinal Organoids. *Journal of Ocular Pharmacology and Therapeutics*.

ADAMS, J. M. & CORY, S. 2007. The Bcl-2 apoptotic switch in cancer development and therapy. *Oncogene,* 26**,** 1324-1337.

AERTS, I., LUMBROSO-LE ROUIC, L., GAUTHIER-VILLARS, M., BRISSE, H., DOZ, F. & DESJARDINS, L. 2006. Retinoblastoma. *Orphanet Journal of Rare Diseases,* 1**,** 31.

AFANASYEVA, T. A. V., CORRAL-SERRANO, J. C., GARANTO, A., ROEPMAN, R., CHEETHAM, M. E. & COLLIN, R. W. J. 2021. A look into retinal organoids: methods, analytical techniques, and applications. *Cellular and Molecular Life Sciences,* 78**,** 6505-6532.

AJIOKA, I., MARTINS, R. A. P., BAYAZITOV, I. T., DONOVAN, S., JOHNSON, D. A., FRASE, S., CICERO, S. A., BOYD, K., ZAKHARENKO, S. S. & DYER, M. A. 2007. Differentiated Horizontal Interneurons Clonally Expand to Form Metastatic Retinoblastoma in Mice. *Cell,* 131**,** 378-390.

AKHTAR, T., XIE, H., KHAN, M. I., ZHAO, H., BAO, J., ZHANG, M. & XUE, T. 2019. Accelerated photoreceptor differentiation of hiPSC-derived retinal organoids by contact co-culture with retinal pigment epithelium. *Stem Cell Research,* 39**,** 101491.

AMABILE, G. & MEISSNER, A. 2009. Induced pluripotent stem cells: current progress and potential for regenerative medicine. *Trends Mol Med,* 15**,** 59-68.

ANTHONY, P. P. 1990. Robbins' Pathologic Basis of Disease. *Journal of Clinical Pathology,* 43**,** 176.

ARTANDI, S. E. & DEPINHO, R. A. 2010. Telomeres and telomerase in cancer. *Carcinogenesis,* 31**,** 9-18.

AST, T. & MOOTHA, V. A.-O. X. 2019. Oxygen and mammalian cell culture: are we repeating the experiment of Dr. Ox?

AUGUSTYNIAK, J., BERTERO, A., COCCINI, T., BADERNA, D., BUZANSKA, L. & CALONI, F. 2019. Organoids are promising tools for species-specific in vitro toxicological studies. *Journal of Applied Toxicology,* 39**,** 1610-1622.

AVIOR, Y., LEZMI, E., YANUKA, D. & BENVENISTY, N. 2017. Modeling Developmental and Tumorigenic Aspects of Trilateral Retinoblastoma via Human Embryonic Stem Cells. *Stem Cell Reports,* 8**,** 1354-1365.

AZMI, A. S., WANG, Z., PHILIP, P. A., MOHAMMAD, R. M. & SARKAR, F. H. 2011. Emerging Bcl-2 inhibitors for the treatment of cancer. *Expert opinion on emerging drugs,* 16**,** 59-70.

BAERISWYL, V. & CHRISTOFORI, G. 2009. The angiogenic switch in carcinogenesis. *Seminars in Cancer Biology,* 19**,** 329-337.

BAKIR, B., CHIARELLA, A. M., PITARRESI, J. R. & RUSTGI, A. K. 2020. EMT, MET, Plasticity, and Tumor Metastasis. *Trends in Cell Biology,* 30**,** 764-776.

BAKKEN, T. E., VAN VELTHOVEN, C. T. J., MENON, V., HODGE, R. D., YAO, Z., NGUYEN, T. N., GRAYBUCK, L. T., HORWITZ, G. D., BERTAGNOLLI, D., GOLDY, J., YANNY, A. M., GARREN, E., PARRY, S.,

CASPER, T., SHEHATA, S. I., BARKAN, E. R., SZAFER, A., LEVI, B. P., DEE, N., SMITH, K. A., SUNKIN, S. M., BERNARD, A., PHILLIPS, J., HAWRYLYCZ, M. J., KOCH, C., MURPHY, G. J., LEIN, E., ZENG, H. & TASIC, B. 2021. Single-cell and single-nucleus RNA-seq uncovers shared and distinct axes of variation in dorsal LGN neurons in mice, non-human primates, and humans. *eLife,* 10**,** e64875.

BALASUBRAMANIAN, R. & GAN, L. 2014. Development of Retinal Amacrine Cells and Their Dendritic Stratification. *Current Ophthalmology Reports,* 2**,** 100-106.

BALUK, P., HASHIZUME, H. & MCDONALD, D. M. 2005. Cellular abnormalities of blood vessels as targets in cancer. *Current Opinion in Genetics & Development,* 15**,** 102-111.

BARRALLO-GIMENO, A. & NIETO, M. A. 2005. The Snail genes as inducers of cell movement and survival: implications in development and cancer. *Development,* 132**,** 3151-3161.

BAYRAKTAR, U. D., BASHIR, Q., QAZILBASH, M., CHAMPLIN, R. E. & CIUREA, S. O. 2013. Fifty years of melphalan use in hematopoietic stem cell transplantation. *Biology of blood and marrow transplantation : journal of the American Society for Blood and Marrow Transplantation,* 19**,** 344-356.

BELSON, P. J., EASTWOOD, J.-A., BRECHT, M.-L., HAYS, R. D. & PIKE, N. A. 2019. A Review of Literature on Health-Related Quality of Life of Retinoblastoma Survivors. *Journal of Pediatric Oncology Nursing,* 37**,** 116-127.

BENAVENTE, C. A. & DYER, M. A. 2015. Genetics and Epigenetics of Human Retinoblastoma. *Annual Review of Pathology: Mechanisms of Disease,* 10**,** 547-562.

BENNIS, A., JACOBS, J. G., CATSBURG, L. A. E., TEN BRINK, J. B., KOSTER, C., SCHLINGEMANN, R. O., VAN MEURS, J., GORGELS, T., MOERLAND, P. D., HEINE, V. M. & BERGEN, A. A. 2017. Stem Cell Derived Retinal Pigment Epithelium: The Role of Pigmentation as Maturation Marker and Gene Expression Profile Comparison with Human Endogenous Retinal Pigment Epithelium.

BERRY, J. L., BECHTOLD, M., SHAH, S., ZOLFAGHARI, E., REID, M., JUBRAN, R. & KIM, J. W. 2017. Not All Seeds Are Created Equal: Seed Classification Is Predictive of Outcomes in Retinoblastoma. *Ophthalmology,* 124**,** 1817-1825.

BERX, G. & VAN ROY, F. 2009. Involvement of Members of the Cadherin Superfamily in Cancer. *Cold Spring Harbor Perspectives in Biology,* 1.

BIERIE, B. & MOSES, H. L. 2006. TGFβ: the molecular Jekyll and Hyde of cancer. *Nature Reviews Cancer,* 6**,** 506-520.

BIRCH, J. & GIL, J. 2020. Senescence and the SASP: many therapeutic avenues. *Genes & Development,* 34**,** 1565-1576.

BLASCO, M. A. 2005. Telomeres and human disease: ageing, cancer and beyond. *Nature Reviews Genetics,* 6**,** 611-622.

BLIXT, M. K. E., HELLSAND, M., KONJUSHA, D., ZHANG, H., STENFELT, S., ÅKESSON, M., RAFATI, N., TARARUK, T., STÅLHAMMAR, G., ALL-ERIKSSON, C., RING, H. & HALLBÖÖK, F. 2022. MYCN induces cell-specific tumorigenic growth in RB1-proficient human retinal organoid and chicken retina models of retinoblastoma. *Oncogenesis,* 11**,** 34.

BLOND, F. & LÉVEILLARD, T. 2019. Functional Genomics of the Retina to Elucidate its Construction and Deconstruction. *International Journal of Molecular Sciences,* 20.

BOIJE, H., SHIRAZI FARD, S., EDQVIST, P.-H. & HALLBÖÖK, F. 2016. Horizontal Cells, the Odd Ones Out in the Retina, Give Insights into Development and Disease. *Frontiers in Neuroanatomy,* 10.

BOYER, L. A., LEE, T. I., COLE, M. F., JOHNSTONE, S. E., LEVINE, S. S., ZUCKER, J. P., GUENTHER, M. G., KUMAR, R. M., MURRAY, H. L., JENNER, R. G., GIFFORD, D. K., MELTON, D. A., JAENISCH, R. & YOUNG, R. A. 2005. Core Transcriptional Regulatory Circuitry in Human Embryonic Stem Cells. *Cell,* 122**,** 947-956.

BROOKS, M. J., CHEN, H. Y., KELLEY, R. A., MONDAL, A. K., NAGASHIMA, K., DE VAL, N., LI, T., CHAITANKAR, V. & SWAROOP, A. 2019. Improved Retinal Organoid Differentiation by Modulating Signaling Pathways Revealed by Comparative Transcriptome Analyses with Development In Vivo. *Stem Cell Reports*.

BUCHHOLZ, D. E., HIKITA, S. T., ROWLAND, T. J., FRIEDRICH, A. M., HINMAN, C. R., JOHNSON, L. V. & CLEGG, D. O. 2009. Derivation of Functional Retinal Pigmented Epithelium from Induced Pluripotent Stem Cells. *Stem Cells,* 27**,** 2427-2434.

BUCHKOVICH, K., DUFFY, L. A. & HARLOW, E. 1989. The retinoblastoma protein is phosphorylated during specific phases of the cell cycle. *Cell,* 58**,** 1097-1105.

BUSKIN, A., ZHU, L., CHICHAGOVA, V., BASU, B., MOZAFFARI-JOVIN, S., DOLAN, D., DROOP, A., COLLIN, J., BRONSTEIN, R., MEHROTRA, S., FARKAS, M., HILGEN, G., WHITE, K., PAN, K.-T., TREUMANN, A., HALLAM, D., BIALAS, K., CHUNG, G., MELLOUGH, C., DING, Y., KRASNOGOR, N., PRZYBORSKI, S., ZWOLINSKI, S., AL-AAMA, J., ALHARTHI, S., XU, Y., WHEWAY, G., SZYMANSKA, K., MCKIBBIN, M., INGLEHEARN, C. F., ELLIOTT, D. J., LINDSAY, S., ALI, R. R., STEEL, D. H., ARMSTRONG, L., SERNAGOR, E., URLAUB, H., PIERCE, E., LÜHRMANN, R., GRELLSCHEID, S.-N., JOHNSON, C. A. & LAKO, M. 2018. Disrupted alternative splicing for genes implicated in splicing and ciliogenesis causes PRPF31 retinitis pigmentosa. *Nature Communications,* 9**,** 4234.

BUSSKAMP, V., DUEBEL, J., BALYA, D., FRADOT, M., VINEY, T. J., SIEGERT, S., GRONER, A. C., CABUY, E., FORSTER, V., SEELIGER, M., BIEL, M., HUMPHRIES, P., PAQUES, M., MOHAND-SAID, S., TRONO, D., DEISSEROTH, K., SAHEL, J. A., PICAUD, S. & ROSKA, B. 2010. Genetic Reactivation of Cone Photoreceptors Restores Visual Responses in Retinitis Pigmentosa. *Science,* 329**,** 413.

BYSTRÖM, B., VIRTANEN, I., ROUSSELLE, P., GULLBERG, D. & PEDROSA-DOMELLÖF, F. 2006. Distribution of Laminins in the Developing Human Eye. *Investigative Ophthalmology & Visual Science,* 47**,** 777-785.

CACERES, P. S. & RODRIGUEZ-BOULAN, E. 2020. Retinal pigment epithelium polarity in health and blinding diseases. *Current Opinion in Cell Biology,* 62**,** 37-45.

CANCELA, M. B., ZUGBI, S., WINTER, U., MARTINEZ, A. L., SAMPOR, C., SGROI, M., FRANCIS, J. H., GARIPPA, R., ABRAMSON, D. H.,

CHANTADA, G. & SCHAIQUEVICH, P. 2021. A decision process for drug discovery in retinoblastoma. *Investigational New Drugs,* 39**,** 426-441.
CAPOWSKI, E. E., SAMIMI, K., MAYERL, S. J., PHILLIPS, M. J., PINILLA, I., HOWDEN, S. E., SAHA, J., JANSEN, A. D., EDWARDS, K. L., JAGER, L. D., BARLOW, K., VALIAUGA, R., ERLICHMAN, Z., HAGSTROM, A., SINHA, D., SLUCH, V. M., CHAMLING, X., ZACK, D. J., SKALA, M. C. & GAMM, D. M. 2019. Reproducibility and staging of 3D human retinal organoids across multiple pluripotent stem cell lines. *Development,* 146**,** dev171686.
CASCALHO, M. & PLATT, J. L. 2008. 81 - Challenges and potentials of xenotransplantation. *In:* RICH, R. R., FLEISHER, T. A., SHEARER, W. T., SCHROEDER, H. W., FREW, A. J. & WEYAND, C. M. (eds.) *Clinical Immunology (Third Edition).* Edinburgh: Mosby.
CAVALLARO, U. & CHRISTOFORI, G. 2004. Cell adhesion and signalling by cadherins and Ig-CAMs in cancer. *Nature Reviews Cancer,* 4**,** 118-132.
CEKIC, C., SAG, D., DAY, Y.-J. & LINDEN, J. 2013. Extracellular adenosine regulates naive T cell development and peripheral maintenance. *Journal of Experimental Medicine,* 210**,** 2693-2706.
CEPKO, C. L., AUSTIN, C. P., YANG, X., ALEXIADES, M. & EZZEDDINE, D. 1996. Cell fate determination in the vertebrate retina. *Proceedings of the National Academy of Sciences,* 93**,** 589-595.
CHAI, P., JIA, R., LI, Y., ZHOU, C., GU, X., YANG, L., SHI, H., TIAN, H., LIN, H., YU, J., ZHUANG, A., GE, S., JIA, R. & FAN, X. 2022. Regulation of epigenetic homeostasis in uveal melanoma and retinoblastoma. *Progress in Retinal and Eye Research,* 89**,** 101030.
CHANTADA, G. L. 2011. Retinoblastoma: Lessons and challenges from developing countries. Ellsworth Lecture 2011. *Ophthalmic Genetics,* 32**,** 196-203.
CHAO, D. T. & KORSMEYER, S. J. 1998. BCL-2 FAMILY: Regulators of Cell Death. *Annual Review of Immunology,* 16**,** 395-419.
CHAO, D. T., LINETTE, G. P., BOISE, L. H., WHITE, L. S., THOMPSON, C. B. & KORSMEYER, S. J. 1995. Bcl-XL and Bcl-2 repress a common pathway of cell death. *The Journal of experimental medicine,* 182**,** 821-828.
CHEN, H.-L., PISTOLLATO, F., HOEPPNER, D. J., NI, H.-T., MCKAY, R. D. G. & PANCHISION, D. M. 2007. Oxygen Tension Regulates Survival and Fate of Mouse Central Nervous System Precursors at Multiple Levels. *Stem Cells,* 25**,** 2291-2301.
CHEN, H. Y., KAYA, K. D., DONG, L. & SWAROOP, A. 2016. Three-dimensional retinal organoids from mouse pluripotent stem cells mimic in vivo development with enhanced stratification and rod photoreceptor differentiation.
CHEN, K. & RAJEWSKY, N. 2007. The evolution of gene regulation by transcription factors and microRNAs. *Nature Reviews Genetics,* 8**,** 93-103.
CHICHAGOVA, V., DORGAU, B., FELEMBAN, M., GEORGIOU, M., ARMSTRONG, L. & LAKO, M. 2019. Differentiation of Retinal Organoids from Human Pluripotent Stem Cells. *Current Protocols in Stem Cell Biology,* 50**,** e95.
CHICHAGOVA, V., HILGEN, G., GHAREEB, A., GEORGIOU, M., CARTER, M., SERNAGOR, E., LAKO, M. & ARMSTRONG, L. 2020. Human iPSC

differentiation to retinal organoids in response to IGF1 and BMP4 activation is line- and method-dependent. *STEM CELLS,* 38**,** 195-201.
CHRISTMAN, J. K. 2002. 5-Azacytidine and 5-aza-2′-deoxycytidine as inhibitors of DNA methylation: mechanistic studies and their implications for cancer therapy. *Oncogene,* 21**,** 5483-5495.
CINKORNPUMIN, J. K., KWON, S. Y., GUO, Y., HOSSAIN, I., SIROIS, J., RUSSETT, C. S., TSENG, H.-W., OKAE, H., ARIMA, T., DUCHAINE, T. F., LIU, W. & PASTOR, W. A. 2020. Naive Human Embryonic Stem Cells Can Give Rise to Cells with a Trophoblast-like Transcriptome and Methylome. *Stem Cell Reports,* 15**,** 198-213.
CLEVERS, H. C. 2019. Organoids: Avatars for Personalized Medicine. *The Keio Journal of Medicine,* 68**,** 95-95.
COBRINIK, D. 2005. Pocket proteins and cell cycle control. *Oncogene,* 24**,** 2796-2809.
COBRINIK, D., LEE MH FAU - HANNON, G., HANNON G FAU - MULLIGAN, G., MULLIGAN G FAU - BRONSON, R. T., BRONSON RT FAU - DYSON, N., DYSON N FAU - HARLOW, E., HARLOW E FAU - BEACH, D., BEACH D FAU - WEINBERG, R. A., WEINBERG RA FAU - JACKS, T. & JACKS, T. 1996. Shared role of the pRB-related p130 and p107 proteins in limb development.
COLLIN, J., MELLOUGH, C. B., DORGAU, B., PRZYBORSKI, S., MORENO-GIMENO, I. & LAKO, M. 2016. Using Zinc Finger Nuclease Technology to Generate CRX-Reporter Human Embryonic Stem Cells as a Tool to Identify and Study the Emergence of Photoreceptors Precursors During Pluripotent Stem Cell Differentiation. *Stem Cells,* 34**,** 311-321.
COLLIN, J., QUEEN, R., ZERTI, D., DORGAU, B., HUSSAIN, R., COXHEAD, J., COCKELL, S. & LAKO, M. 2019. Deconstructing Retinal Organoids: Single Cell RNA-Seq Reveals the Cellular Components of Human Pluripotent Stem Cell-Derived Retina. *Stem cells (Dayton, Ohio),* 37**,** 593-598.
COLLIN, J., QUEEN, R., ZERTI, D., STEEL, D. H., BOWEN, C., PARULEKAR, M. & LAKO, M. 2021. Dissecting the Transcriptional and Chromatin Accessibility Heterogeneity of Proliferating Cone Precursors in Human Retinoblastoma Tumors by Single Cell Sequencing—Opening Pathways to New Therapeutic Strategies? *Investigative Ophthalmology & Visual Science,* 62**,** 18-18.
CORA, V., HADERSPECK, J., ANTKOWIAK, L., MATTHEUS, U., NECKEL, H. P., MACK, F. A., BOLZ, S., UEFFING, M., PASHKOVSKAIA, N., ACHBERGER, K. & LIEBAU, S. 2019. A Cleared View on Retinal Organoids. *Cells,* 8.
CORSON, T. W. & GALLIE, B. L. 2007. One hit, two hits, three hits, more? Genomic changes in the development of retinoblastoma. *Genes, Chromosomes and Cancer,* 46**,** 617-634.
COWAN, C. S., RENNER, M., DE GENNARO, M., GROSS-SCHERF, B., GOLDBLUM, D., HOU, Y., MUNZ, M., RODRIGUES, T. M., KROL, J., SZIKRA, T., CUTTAT, R., WALDT, A., PAPASAIKAS, P., DIGGELMANN, R., PATINO-ALVAREZ, C. P., GALLIKER, P., SPIRIG, S. E., PAVLINIC, D., GERBER-HOLLBACH, N., SCHUIERER, S., SRDANOVIC, A., BALOGH, M., PANERO, R., KUSNYERIK, A., SZABO, A., STADLER, M. B., ORGÜL, S., PICELLI, S., HASLER, P. W., HIERLEMANN, A., SCHOLL, H. P. N., ROMA, G., NIGSCH, F. & ROSKA, B. 2020. Cell

Types of the Human Retina and Its Organoids at Single-Cell Resolution. *Cell,* 182**,** 1623-1640.e34.
DAL BO, M., BOMBEN, R., HERNÁNDEZ, L. & GATTEI, V. 2015. The MYC/miR-17-92 axis in lymphoproliferative disorders: A common pathway with therapeutic potential.
DALGARD, C. L., GONZALEZ, M., DENIRO, J. E. & O'BRIEN, J. M. 2009. Differential MicroRNA-34a Expression and Tumor Suppressor Function in Retinoblastoma Cells. *Investigative Ophthalmology & Visual Science,* 50**,** 4542-4551.
DALVIN, L. A., KUMARI, M., ESSUMAN, V. A., SHOHELLY SHIPA, S., ANCONA-LEZAMA, D., LUCIO-ALVAREZ, J. A., JABBOUR, P. & SHIELDS, C. L. 2019. Primary Intra-Arterial Chemotherapy for Retinoblastoma in the Intravitreal Chemotherapy Era: Five Years of Experience. *Ocular Oncology and Pathology,* 5**,** 139-146.
DANKO, C. G., MCILVAIN, V. A., QIN, M., KNOX, B. E. & PERTSOV, A. M. 2007. Bioinformatic identification of novel putative photoreceptor specific cis-elements. *BMC Bioinformatics,* 8**,** 407.
DAS, D., BHATTACHARJEE, K., BARTHAKUR, S. S., TAHILIANI, P. S., DEKA, P., BHATTACHARJEE, H., DEKA, A. & PAUL, R. 2014. A new rosette in retinoblastoma. *Indian Journal of Ophthalmology,* 62.
DASKALAKIS, M., BLAGITKO-DORFS, N. & HACKANSON, B. 2010. Decitabine. *In:* MARTENS, U. M. (ed.) *Small Molecules in Oncology.* Berlin, Heidelberg: Springer Berlin Heidelberg.
DE BLANDER, H., MOREL, A.-P., SENARATNE, A. P., OUZOUNOVA, M. & PUISIEUX, A. 2021. Cellular Plasticity: A Route to Senescence Exit and Tumorigenesis. *Cancers* [Online], 13.
DE PALMA, M., MURDOCH, C., VENNERI, M. A., NALDINI, L. & LEWIS, C. E. 2007. Tie2-expressing monocytes: regulation of tumor angiogenesis and therapeutic implications. *Trends in Immunology,* 28**,** 519-524.
DEBERARDINIS, R. J., LUM, J. J., HATZIVASSILIOU, G. & THOMPSON, C. B. 2008. The Biology of Cancer: Metabolic Reprogramming Fuels Cell Growth and Proliferation. *Cell Metabolism,* 7**,** 11-20.
DEMB, J. B. & SINGER, J. H. 2015. Functional Circuitry of the Retina. *Annual Review of Vision Science,* 1**,** 263-289.
DENARDO, D. G., ANDREU, P. & COUSSENS, L. M. 2010. Interactions between lymphocytes and myeloid cells regulate pro- versus anti-tumor immunity. *Cancer and Metastasis Reviews,* 29**,** 309-316.
DENNIS, M. J., BEIJNEN, J. H., GROCHOW, L. B. & VAN WARMERDAM, L. J. 1997. An overview of the clinical pharmacology of topotecan. *Seminars in oncology,* 24**,** S5-12-S5-18.
DI FIORE, R., D'ANNEO, A., TESORIERE, G. & VENTO, R. 2013. RB1 in cancer: Different mechanisms of RB1 inactivation and alterations of pRb pathway in tumorigenesis. *Journal of Cellular Physiology,* 228**,** 1676-1687.
DIMARAS, H. & CORSON, T. W. 2019. Retinoblastoma, the visible CNS tumor: A review. *Journal of Neuroscience Research,* 97**,** 29-44.
DIMARAS, H., CORSON, T. W., COBRINIK, D., WHITE, A., ZHAO, J., MUNIER, F. L., ABRAMSON, D. H., SHIELDS, C. L., CHANTADA, G. L., NJUGUNA, F. & GALLIE, B. L. 2015. Retinoblastoma. *Nature reviews. Disease primers,* 1**,** 15021-15021.

DIMARAS, H., KHETAN, V., HALLIDAY, W., ORLIC, M., PRIGODA, N. L., PIOVESAN, B., MARRANO, P., CORSON, T. W., EAGLE, R. C., JR., SQUIRE, J. A. & GALLIE, B. L. 2008. Loss of RB1 induces non-proliferative retinoma: increasing genomic instability correlates with progression to retinoblastoma. *Human Molecular Genetics,* 17**,** 1363-1372.

DIMARAS, H., KIMANI, K., DIMBA, E. A. O., GRONSDAHL, P., WHITE, A., CHAN, H. S. L. & GALLIE, B. L. 2012. Retinoblastoma. *The Lancet,* 379**,** 1436-1446.

DISTEFANO, T., CHEN, H. Y., PANEBIANCO, C., KAYA, K. D., BROOKS, M. J., GIESER, L., MORGAN, N. Y., POHIDA, T. & SWAROOP, A. 2018. Accelerated and Improved Differentiation of Retinal Organoids from Pluripotent Stem Cells in Rotating-Wall Vessel Bioreactors. *Stem Cell Reports,* 10**,** 300-313.

DONOVAN, S. L., SCHWEERS, B., MARTINS, R., JOHNSON, D. & DYER, M. A. 2006. Compensation by tumor suppressor genes during retinal development in mice and humans. *BMC Biology,* 4**,** 14.

DORGAU, B., FELEMBAN, M., HILGEN, G., KIENING, M., ZERTI, D., HUNT, N. C., DOHERTY, M., WHITFIELD, P., HALLAM, D., WHITE, K., DING, Y., KRASNOGOR, N., AL-AAMA, J., ASFOUR, H. Z., SERNAGOR, E. & LAKO, M. 2019. Decellularised extracellular matrix-derived peptides from neural retina and retinal pigment epithelium enhance the expression of synaptic markers and light responsiveness of human pluripotent stem cell derived retinal organoids. *Biomaterials,* 199**,** 63-75.

DORGAU, B., FELEMBAN, M., SHARPE, A., BAUER, R., HALLAM, D., STEEL, D. H., LINDSAY, S., MELLOUGH, C. & LAKO, M. 2018. Laminin γ3 plays an important role in retinal lamination, photoreceptor organisation and ganglion cell differentiation. *Cell Death & Disease,* 9**,** 615.

DORGAU, B., GEORGIOU, M., CHAUDHARY, A., MOYA-MOLINA, M., COLLIN, J., QUEEN, R., HILGEN, G., DAVEY, T., HEWITT, P., SCHMITT, M., KUSTERMANN, S., POGNAN, F., STEEL, D. H., SERNAGOR, E., ARMSTRONG, L. & LAKO, M. 2022. Human Retinal Organoids Provide a Suitable Tool for Toxicological Investigations: A Comprehensive Validation Using Drugs and Compounds Affecting the Retina. *Stem Cells Translational Medicine,* 11**,** 159-177.

DRAPER, G. J., SANDERS, B. M., BROWNBILL, P. A. & HAWKINS, M. M. 1992. Patterns of risk of hereditary retinoblastoma and applications to genetic counselling. *British Journal of Cancer,* 66**,** 211-219.

DRESCHER, U., KREMOSER, C., HANDWERKER, C., LÖSCHINGER, J., NODA, M. & BONHOEFFER, F. 1995. In vitro guidance of retinal ganglion cell axons by RAGS, a 25 kDa tectal protein related to ligands for Eph receptor tyrosine kinases. *Cell,* 82**,** 359-370.

DVORAK, H. F. 1986. Tumors: Wounds That Do Not Heal. *New England Journal of Medicine,* 315**,** 1650-1659.

DYER, M. A. 2016. Lessons from Retinoblastoma: Implications for Cancer, Development, Evolution, and Regenerative Medicine. *Trends in molecular medicine,* 22**,** 863-876.

DYSON, N. J. 2016. RB1: a prototype tumor suppressor and an enigma. *Genes & Development,* 30**,** 1492-1502.

DZUTSEV, A., BADGER, J. H., PEREZ-CHANONA, E., ROY, S., SALCEDO, R., SMITH, C. K. & TRINCHIERI, G. 2017. Microbes and Cancer. *Annual Review of Immunology,* 35**,** 199-228.

EAGLE JR, R. C. 2009. High-Risk Features and Tumor Differentiation in Retinoblastoma: A Retrospective Histopathologic Study. *Archives of Pathology & Laboratory Medicine,* 133**,** 1203-1209.

EAGLE, R. C., SHIELDS, J. A., DONOSO, L. & MILNER, R. S. 1989. Malignant Transformation of Spontaneously Regressed Retinoblastoma, Retinoma/Retinocytoma Variant. *Ophthalmology,* 96**,** 1389-1395.

EDQVIST, P.-H. D., LEK, M., BOIJE, H., LINDBÄCK, S. M. & HALLBÖÖK, F. 2008. Axon-bearing and axon-less horizontal cell subtypes are generated consecutively during chick retinal development from progenitors that are sensitive to follistatin. *BMC Developmental Biology,* 8**,** 46.

EDQVIST, P. H. D., MYERS, S. M. & HALLBÃ¶Ã¶K, F. 2009. Early identification of retinal subtypes in the developing, pre-laminated chick retina using the transcription factors Prox1, Lim1, Ap2a, Pax6, Isl1, Isl2, Lim3 and Chx10. *European Journal of Histochemistry,* 50**,** 147-154.

EIRAKU, M., TAKATA, N., ISHIBASHI, H., KAWADA, M., SAKAKURA, E., OKUDA, S., SEKIGUCHI, K., ADACHI, T. & SASAI, Y. 2011. Self-organizing optic-cup morphogenesis in three-dimensional culture. *Nature,* 472**,** 51-56.

ELDRED, K. C., HADYNIAK, S. E., HUSSEY, K. A., BRENERMAN, B., ZHANG, P.-W., CHAMLING, X., SLUCH, V. M., WELSBIE, D. S., HATTAR, S., TAYLOR, J., WAHLIN, K., ZACK, D. J. & JOHNSTON, R. J. 2018. Thyroid hormone signaling specifies cone subtypes in human retinal organoids. *Science,* 362**,** eaau6348.

ELSHATORY, Y., DENG, M., XIE, X. & GAN, L. 2007. Expression of the LIM-homeodomain protein Isl1 in the developing and mature mouse retina. *Journal of Comparative Neurology,* 503**,** 182-197.

EULER, T., HAVERKAMP, S., SCHUBERT, T. & BADEN, T. 2014. Retinal bipolar cells: Elementary building blocks of vision. *Nature reviews. Neuroscience,* 15**,** 507-19.

EWENS, K. G., BHATTI, T. R., MORAN, K. A., RICHARDS-YUTZ, J., SHIELDS, C. L., EAGLE, R. C. & GANGULY, A. 2017. Phosphorylation of pRb: mechanism for RB pathway inactivation in MYCN-amplified retinoblastoma. *Cancer Medicine,* 6**,** 619-630.

FAIN, G. & SAMPATH, A. P. 2018. Rod and cone interactions in the retina. *F1000Research,* 7**,** F1000 Faculty Rev-657.

FERNANDO, M., LEE, S., WARK, J. R., XIAO, D., LIM, B. Y., O'HARA-WRIGHT, M., KIM, H. J., SMITH, G. C., WONG, T., TEBER, E. T., ALI, R. R., YANG, P., GRAHAM, M. E. & GONZALEZ-CORDERO, A. 2022. Differentiation of brain and retinal organoids from confluent cultures of pluripotent stem cells connected by nerve-like axonal projections of optic origin. *Stem Cell Reports,* 17**,** 1476-1492.

FERON, O. 2009. Pyruvate into lactate and back: From the Warburg effect to symbiotic energy fuel exchange in cancer cells. *Radiotherapy and Oncology,* 92**,** 329-333.

FERRER, M., CORNEO, B., DAVIS, J., WAN, Q., MIYAGISHIMA, K. J., KING, R., MAMINISHKIS, A., MARUGAN, J., SHARMA, R., SHURE, M., TEMPLE, S., MILLER, S. & BHARTI, K. 2014. A Multiplex High-

Throughput Gene Expression Assay to Simultaneously Detect Disease and Functional Markers in Induced Pluripotent Stem Cell-Derived Retinal Pigment Epithelium. *Stem Cells Translational Medicine,* 3**,** 911-922.

FIDLER, I. J. 2003. The pathogenesis of cancer metastasis: the 'seed and soil' hypothesis revisited. *Nature Reviews Cancer,* 3**,** 453-458.

FINKBEINER, C., ORTUÑO-LIZARÁN, I., SRIDHAR, A., HOOPER, M., PETTER, S. & REH, T. A. 2022. Single-cell ATAC-seq of fetal human retina and stem-cell-derived retinal organoids shows changing chromatin landscapes during cell fate acquisition. *Cell Reports,* 38**,** 110294.

FOLGAR, F. A., YUAN, E. L., SEVILLA, M. B., CHIU, S. J., FARSIU, S., CHEW, E. Y. & TOTH, C. A. 2016. Drusen Volume and Retinal Pigment Epithelium Abnormal Thinning Volume Predict 2-Year Progression of Age-Related Macular Degeneration. *Ophthalmology,* 123**,** 39-50.e1.

GALLINA, D., TODD, L. & FISCHER, A. J. 2014. A comparative analysis of Müller glia-mediated regeneration in the vertebrate retina. *Experimental Eye Research,* 123**,** 121-130.

GAO, L., NATH, S. C., JIAO, X., ZHOU, R., NISHIKAWA, S., KRAWETZ, R., LI, X. & RANCOURT, D. E. 2019. Post-Passage rock inhibition induces cytoskeletal aberrations and apoptosis in Human embryonic stem cells. *Stem Cell Research,* 41**,** 101641.

GEORGIOU, M., YANG, C., ATKINSON, R., PAN, K.-T., BUSKIN, A., MOLINA, M. M., COLLIN, J., AL-AAMA, J., GOERTLER, F., LUDWIG, S. E. J., DAVEY, T., LÜHRMANN, R., NAGARAJA-GRELLSCHEID, S., JOHNSON, C. A., ALI, R., ARMSTRONG, L., KOROLCHUK, V., URLAUB, H., MOZAFFARI-JOVIN, S. & LAKO, M. 2022. Activation of autophagy reverses progressive and deleterious protein aggregation in PRPF31 patient-induced pluripotent stem cell-derived retinal pigment epithelium cells. *Clinical and Translational Medicine,* 12**,** e759.

GIACINTI, C. & GIORDANO, A. 2006. RB and cell cycle progression. *Oncogene,* 25**,** 5220-5227.

GONZALEZ-CORDERO, A., KRUCZEK, K., NAEEM, A., FERNANDO, M., KLOC, M., RIBEIRO, J., GOH, D., DURAN, Y., BLACKFORD, S. J. I., ABELLEIRA-HERVAS, L., SAMPSON, R. D., SHUM, I. O., BRANCH, M. J., GARDNER, P. J., SOWDEN, J. C., BAINBRIDGE, J. W. B., SMITH, A. J., WEST, E. L., PEARSON, R. A. & ALI, R. R. 2017. Recapitulation of Human Retinal Development from Human Pluripotent Stem Cells Generates Transplantable Populations of Cone Photoreceptors. *Stem Cell Reports,* 9**,** 820-837.

GORGOULIS, V., ADAMS, P. D., ALIMONTI, A., BENNETT, D. C., BISCHOF, O., BISHOP, C., CAMPISI, J., COLLADO, M., EVANGELOU, K., FERBEYRE, G., GIL, J., HARA, E., KRIZHANOVSKY, V., JURK, D., MAIER, A. B., NARITA, M., NIEDERNHOFER, L., PASSOS, J. F., ROBBINS, P. D., SCHMITT, C. A., SEDIVY, J., VOUGAS, K., VON ZGLINICKI, T., ZHOU, D., SERRANO, M. & DEMARIA, M. 2019. Cellular Senescence: Defining a Path Forward. *Cell,* 179**,** 813-827.

GRASEMANN, C., GRATIAS, S., STEPHAN, H., SCHÜLER, A., SCHRAMM, A., KLEIN-HITPASS, L., RIEDER, H., SCHNEIDER, S., KAPPES, F., EGGERT, A. & LOHMANN, D. R. 2005. Gains and overexpression identify DEK and E2F3 as targets of chromosome 6p gains in retinoblastoma. *Oncogene,* 24**,** 6441-6449.

GRIFFITH, L. G. & SWARTZ, M. A. 2006. Capturing complex 3D tissue physiology in vitro.
GRIVENNIKOV, S. I., GRETEN, F. R. & KARIN, M. 2010. Immunity, Inflammation, and Cancer. *Cell,* 140**,** 883-899.
GUO, T., TSAI, D., BAI, S., MORLEY, J. W., SUANING, G. J., LOVELL, N. H. & DOKOS, S. 2014. Understanding the Retina: A Review of Computational Models of the Retina from the Single Cell to the Network Level. 42**,** 419-436.
GUPTA, G. P., MINN, A. J., KANG, Y., SIEGEL, P. M., SERGANOVA, I., CORDÓN-CARDO, C., OLSHEN, A. B., GERALD, W. L. & MASSAGUÉ, J. 2005. Identifying Site-specific Metastasis Genes and Functions. *Cold Spring Harbor Symposia on Quantitative Biology,* 70**,** 149-158.
GUPTA, P. B., PASTUSHENKO, I., SKIBINSKI, A., BLANPAIN, C. & KUPERWASSER, C. 2019. Phenotypic Plasticity: Driver of Cancer Initiation, Progression, and Therapy Resistance. *Cell Stem Cell,* 24**,** 65-78.
GUZMAN, F., FAZELI, Y., KHUU, M., SALCIDO, K., SINGH, S. & BENAVENTE, C. A. 2020. Retinoblastoma Tumor Suppressor Protein Roles in Epigenetic Regulation. *Cancers,* 12.
HAIGIS, K., SAGE J FAU - GLICKMAN, J., GLICKMAN J FAU - SHAFER, S., SHAFER S FAU - JACKS, T. & JACKS, T. 2006. The related retinoblastoma (pRb) and p130 proteins cooperate to regulate homeostasis in the intestinal epithelium.
HALLAM, D., COLLIN, J., BOJIC, S., CHICHAGOVA, V., BUSKIN, A., XU, Y., LAFAGE, L., OTTEN, E. G., ANYFANTIS, G., MELLOUGH, C., PRZYBORSKI, S., ALHARTHI, S., KOROLCHUK, V., LOTERY, A., SARETZKI, G., MCKIBBIN, M., ARMSTRONG, L., STEEL, D., KAVANAGH, D. & LAKO, M. 2017. An Induced Pluripotent Stem Cell Patient Specific Model of Complement Factor H (Y402H) Polymorphism Displays Characteristic Features of Age-Related Macular Degeneration and Indicates a Beneficial Role for UV Light Exposure. *Stem cells (Dayton, Ohio),* 35**,** 2305-2320.
HALLAM, D., HILGEN, G., DORGAU, B., ZHU, L., YU, M., BOJIC, S., HEWITT, P., SCHMITT, M., UTENG, M., KUSTERMANN, S., STEEL, D., NICHOLDS, M., THOMAS, R., TREUMANN, A., PORTER, A., SERNAGOR, E., ARMSTRONG, L. & LAKO, M. 2018. Human-Induced Pluripotent Stem Cells Generate Light Responsive Retinal Organoids with Variable and Nutrient-Dependent Efficiency. *STEM CELLS,* 36**,** 1535-1551.
HAMEL, C. 2006. Retinitis pigmentosa. *Orphanet Journal of Rare Diseases,* 1**,** 40.
HANAHAN, D. 2022. Hallmarks of Cancer: New Dimensions. *Cancer Discovery,* 12**,** 31-46.
HANAHAN, D. & FOLKMAN, J. 1996. Patterns and Emerging Mechanisms of the Angiogenic Switch during Tumorigenesis. *Cell,* 86**,** 353-364.
HANAHAN, D. & WEINBERG, R. A. 2000. The Hallmarks of Cancer. *Cell,* 100**,** 57-70.
HANAHAN, D. & WEINBERG, ROBERT A. 2011. Hallmarks of Cancer: The Next Generation. *Cell,* 144**,** 646-674.
HAZIM, R. A., KARUMBAYARAM, S., JIANG, M., DIMASHKIE, A., LOPES, V. S., LI, D., BURGESS, B. L., VIJAYARAJ, P., ALVA-ORNELAS, J. A., ZACK,

J. A., KOHN, D. B., GOMPERTS, B. N., PYLE, A. D., LOWRY, W. E. & WILLIAMS, D. S. 2017. Differentiation of RPE cells from integration-free iPS cells and their cell biological characterization. *Stem Cell Research & Therapy,* 8**,** 217.

HAZIM, R. A., VOLLAND, S., YEN, A., BURGESS, B. L. & WILLIAMS, D. S. 2019. Rapid differentiation of the human RPE cell line, ARPE-19, induced by nicotinamide. *Experimental Eye Research,* 179**,** 18-24.

HELMINK, B. A., KHAN, M. A. W., HERMANN, A., GOPALAKRISHNAN, V. & WARGO, J. A. 2019. The microbiome, cancer, and cancer therapy. *Nature Medicine,* 25**,** 377-388.

HENDRICKSON, A. 2005. Organization of the Adult Primate Fovea. *In:* PENFOLD, P. L. & PROVIS, J. M. (eds.) *Macular Degeneration.* Berlin, Heidelberg: Springer Berlin Heidelberg.

HEZEL, A. F. & BARDEESY, N. 2008. LKB1; linking cell structure and tumor suppression. *Oncogene,* 27**,** 6908-6919.

HIRAMI, Y., OSAKADA, F., TAKAHASHI, K., OKITA, K., YAMANAKA, S., IKEDA, H., YOSHIMURA, N. & TAKAHASHI, M. 2009. Generation of retinal cells from mouse and human induced pluripotent stem cells. *Neuroscience Letters,* 458**,** 126-131.

HOSHINO, A., RATNAPRIYA, R., BROOKS, M. J., CHAITANKAR, V., WILKEN, M. S., ZHANG, C., STAROSTIK, M. R., GIESER, L., LA TORRE, A., NISHIO, M., BATES, O., WALTON, A., BERMINGHAM-MCDONOGH, O., GLASS, I. A., WONG, R. O. L., SWAROOP, A. & REH, T. A. 2017. Molecular Anatomy of the Developing Human Retina. *Developmental Cell,* 43**,** 763-779.e4.

HSU, P. P. & SABATINI, D. M. 2008. Cancer Cell Metabolism: Warburg and Beyond. *Cell,* 134**,** 703-707.

HU, H.-G., SCHOLTEN, I., GRUSS, C. & KNIPPERS, R. 2007. The distribution of the DEK protein in mammalian chromatin. *Biochemical and Biophysical Research Communications,* 358**,** 1008-1014.

HU, J., KADY, N., MACABASCO, A., GORIN, M. B., MATYNIA, A. & RADU, R. A. 2020. Complement Dysregulation is Evidenced in iPSC-derived RPE Cells from Stargardt Disease patients. *Investigative Ophthalmology & Visual Science,* 61**,** 1507-1507.

HU, Q. J., DYSON, N. & HARLOW, E. 1990. The regions of the retinoblastoma protein needed for binding to adenovirus E1A or SV40 large T antigen are common sites for mutations. *The EMBO Journal,* 9**,** 1147-1155.

HUBERMAN, A. D. & NIELL, C. M. 2011. What can mice tell us about how vision works? *Trends in Neurosciences,* 34**,** 464-473.

IKUSHIMA, H. & MIYAZONO, K. 2010. TGFβ signalling: a complex web in cancer progression. *Nature Reviews Cancer,* 10**,** 415-424.

ING, C., DIMAGGIO, C., WHITEHOUSE, A., HEGARTY, M. K., BRADY, J., VON UNGERN-STERNBERG, B. S., DAVIDSON, A., WOOD, A. J. J., LI, G. & SUN, L. S. 2012. Long-term Differences in Language and Cognitive Function After Childhood Exposure to Anesthesia. *Pediatrics,* 130**,** e476.

JACKSON, S. P. & BARTEK, J. 2009. The DNA-damage response in human biology and disease. *Nature,* 461**,** 1071-1078.

JADHAV, A. P., ROESCH, K. & CEPKO, C. L. 2009. Development and neurogenic potential of Müller glial cells in the vertebrate retina. *Progress in Retinal and Eye Research,* 28**,** 249-262.

JAGER, R. D., MIELER, W. F. & MILLER, J. W. 2008. Age-Related Macular Degeneration. *New England Journal of Medicine,* 358**,** 2606-2617.

JEFFREY, P. D., RUSSO, A. A., POLYAK, K., GIBBS, E., HURWITZ, J., MASSAGUÉ, J. & PAVLETICH, N. P. 1995. Mechanism of CDK activation revealed by the structure of a cyclinA-CDK2 complex. *Nature,* 376**,** 313-320.

JOHNSON, S. M., GROSSHANS H FAU - SHINGARA, J., SHINGARA J FAU - BYROM, M., BYROM M FAU - JARVIS, R., JARVIS R FAU - CHENG, A., CHENG A FAU - LABOURIER, E., LABOURIER E FAU - REINERT, K. L., REINERT KL FAU - BROWN, D., BROWN D FAU - SLACK, F. J. & SLACK, F. J. 2005. RAS is regulated by the let-7 microRNA family.

JONES, P. A. & BAYLIN, S. B. 2002. The fundamental role of epigenetic events in cancer. *Nature Reviews Genetics,* 3**,** 415-428.

JONES, R. G. & THOMPSON, C. B. 2009. Tumor suppressors and cell metabolism: a recipe for cancer growth. *Genes & Development,* 23**,** 537-548.

JUUTI-UUSITALO, K., NIEMINEN, M., TREUMER, F., AMPUJA, M., KALLIONIEMI, A., KLETTNER, A. & SKOTTMAN, H. 2015. Effects of Cytokine Activation and Oxidative Stress on the Function of the Human Embryonic Stem Cell–Derived Retinal Pigment Epithelial Cells. *Investigative Ophthalmology & Visual Science,* 56**,** 6265-6274.

KAELIN, W. G., EWEN, M. E. & LIVINGSTON, D. M. 1990. Definition of the minimal simian virus 40 large T antigen- and adenovirus E1A-binding domain in the retinoblastoma gene product. *Molecular and Cellular Biology,* 10**,** 3761-3769.

KAEWKHAW, R., KAYA, K. D., BROOKS, M., HOMMA, K., ZOU, J., CHAITANKAR, V., RAO, M. & SWAROOP, A. 2015. Transcriptome Dynamics of Developing Photoreceptors in Three-Dimensional Retina Cultures Recapitulates Temporal Sequence of Human Cone and Rod Differentiation Revealing Cell Surface Markers and Gene Networks. *Stem Cells,* 33.

KAEWKHAW, R. & ROJANAPORN, D. 2020. Retinoblastoma: Etiology, Modeling, and Treatment. *Cancers,* 12**,** 2304.

KAMIHARA, J., BOURDEAUT, F., FOULKES, W. D., MOLENAAR, J. J., MOSSÉ, Y. P., NAKAGAWARA, A., PARAREDA, A., SCOLLON, S. R., SCHNEIDER, K. W., SKALET, A. H., STATES, L. J., WALSH, M. F., DILLER, L. R. & BRODEUR, G. M. 2017. Retinoblastoma and Neuroblastoma Predisposition and Surveillance. *Clinical Cancer Research,* 23**,** e98.

KANBER, D., WOESTEFELD, J., DÖPPER, H., BOZET, M., BRENZEL, A., ALTMÜLLER, J., KILPERT, F., LOHMANN, D., POMMERENKE, C. & STEENPASS, L. 2022. RB1-Negative Retinal Organoids Display Proliferation of Cone Photoreceptors and Loss of Retinal Differentiation. *Cancers,* 14.

KANG, H. J., CHOI, Y. S., HONG, S.-B., KIM, K.-W., WOO, R.-S., WON, S. J., KIM, E. J., JEON, H. K., JO, S.-Y., KIM, T. K., BACHOO, R., REYNOLDS, I. J., GWAG, B. J. & LEE, H.-W. 2004. Ectopic Expression of the Catalytic Subunit of Telomerase Protects against Brain Injury Resulting from Ischemia and NMDA-Induced Neurotoxicity. *The Journal of Neuroscience,* 24**,** 1280.

KARASAWA, Y. & OKISAKA, S. 2004. Inhibition of Histone Deacetylation by Butyrate Induces Morphological Changes in Y79 Retinoblastoma Cells. *Japanese Journal of Ophthalmology,* 48**,** 542-551.

KARMAKAR, A., AHAMAD KHAN, M. M., KUMARI, N., DEVARAJAN, N. & GANESAN, S. K. 2022. Identification of Epigenetically Modified Hub Genes and Altered Pathways Associated With Retinoblastoma. *Frontiers in Cell and Developmental Biology,* 10.

KARNOUB, A. E. & WEINBERG, R. A. 2007. Chemokine Networks and Breast Cancer Metastasis. *Breast Disease,* 26**,** 75-85.

KASTAN, M. B. 2008. DNA Damage Responses: Mechanisms and Roles in Human Disease: 2007 G.H.A. Clowes Memorial Award Lecture. *Molecular Cancer Research,* 6**,** 517-524.

KENNEDY, K. M. & DEWHIRST, M. W. 2009. Tumor metabolism of lactate: the influence and therapeutic potential for MCT and CD147 regulation. *Future Oncology,* 6**,** 127-148.

KHAN, M., ARNO, G., FAKIN, A., PARFITT, D. A., DHOOGE, P. P. A., ALBERT, S., BAX, N. M., DUIJKERS, L., NIBLOCK, M., HAU, K. L., BLOCH, E., SCHIFF, E. R., PICCOLO, D., HOGDEN, M. C., HOYNG, C. B., WEBSTER, A. R., CREMERS, F. P. M., CHEETHAM, M. E., GARANTO, A. & COLLIN, R. W. J. 2020. Detailed Phenotyping and Therapeutic Strategies for Intronic ABCA4 Variants in Stargardt Disease. *Molecular Therapy - Nucleic Acids,* 21**,** 412-427.

KHAN, M., WALTERS, L. L., LI, Q., THOMAS, D. G., MILLER, J. M. L., ZHANG, Q., SCIALLIS, A. P., LIU, Y., DLOUHY, B. J., FORT, P. E., ARCHER, S. M., DEMIRCI, H., DOU, Y. & RAO, R. C. 2015. Characterization and pharmacologic targeting of EZH2, a fetal retinal protein and epigenetic regulator, in human retinoblastoma. *Laboratory Investigation,* 95**,** 1278-1290.

KIM, J., KOO, B.-K. & KNOBLICH, J. A. 2020. Human organoids: model systems for human biology and medicine. *Nature Reviews Molecular Cell Biology,* 21**,** 571-584.

KIM, S., LOWE, A., DHARMAT, R., LEE, S., OWEN, L. A., WANG, J., SHAKOOR, A., LI, Y., MORGAN, D. J., HEJAZI, A. A., CVEKL, A., DEANGELIS, M. M., ZHOU, Z. J., CHEN, R. & LIU, W. 2019. Generation, transcriptome profiling, and functional validation of cone-rich human retinal organoids. *Proceedings of the National Academy of Sciences,* 116**,** 10824.

KLIMANSKAYA, I., HIPP, J., REZAI, K. A., WEST, M., ATALA, A. & LANZA, R. 2004. Derivation and Comparative Assessment of Retinal Pigment Epithelium from Human Embryonic Stem Cells Using Transcriptomics. *Cloning and Stem Cells,* 6**,** 217-245.

KLYMKOWSKY, M. W. & SAVAGNER, P. 2009. Epithelial-Mesenchymal Transition: A Cancer Researcher's Conceptual Friend and Foe. *The American Journal of Pathology,* 174**,** 1588-1593.

KNUDSEN, E. S. & WANG, J. Y. 1997. Dual mechanisms for the inhibition of E2F binding to RB by cyclin-dependent kinase-mediated RB phosphorylation. *Molecular and Cellular Biology,* 17**,** 5771-5783.

KNUDSON, A. G. 1971. Mutation and Cancer: Statistical Study of Retinoblastoma. *Proceedings of the National Academy of Sciences,* 68**,** 820.

KOLB, H. 1997. Amacrine cells of the mammalian retina: Neurocircuitry and functional roles. *Eye,* 11**,** 904-923.
KONG, L., SUN, Y., CHEN, M., DAI, Y. & LIU, Z. 2020. Downregulation of microRNA-320a inhibits proliferation and induces apoptosis of retinoblastoma cells via targeting TUSC3.
KORKOLA, J. & GRAY, J. W. 2010. Breast cancer genomes—form and function. *Current Opinion in Genetics & Development,* 20**,** 4-14.
KOWALD, A., PASSOS, J. F. & KIRKWOOD, T. B. L. 2020. On the evolution of cellular senescence. *Aging Cell,* 19**,** e13270.
KUWAHARA, A., OZONE, C., NAKANO, T., SAITO, K., EIRAKU, M. & SASAI, Y. 2015. Generation of a ciliary margin-like stem cell niche from self-organizing human retinal tissue. *Nature Communications,* 6**,** 6286.
KUWAHARA, A., YAMASAKI, S., MANDAI, M., WATARI, K., MATSUSHITA, K., FUJIWARA, M., HORI, Y., HIRAMINE, Y., NUKAYA, D., IWATA, M., KISHINO, A., TAKAHASHI, M., SASAI, Y. & KIMURA, T. 2019. Preconditioning the Initial State of Feeder-free Human Pluripotent Stem Cells Promotes Self-formation of Three-dimensional Retinal Tissue. *Scientific Reports,* 9**,** 18936.
LABHISHETTY, V., CHOLEWIAK, S. A. & BANKS, M. S. 2019. Contributions of foveal and non-foveal retina to the human eye's focusing response. *Journal of Vision,* 19**,** 18-18.
LAKOWSKI, J., WELBY, E., BUDINGER, D., DI MARCO, F., DI FOGGIA, V., BAINBRIDGE, J. W. B., WALLACE, K., GAMM, D. M., ALI, R. R. & SOWDEN, J. C. 2018. Isolation of Human Photoreceptor Precursors via a Cell Surface Marker Panel from Stem Cell-Derived Retinal Organoids and Fetal Retinae. *STEM CELLS,* 36**,** 709-722.
LAMBA, D. A., KARL, M. O., WARE, C. B. & REH, T. A. 2006. Efficient generation of retinal progenitor cells from human embryonic stem cells. *Proceedings of the National Academy of Sciences,* 103**,** 12769.
LAMBERT, A. W. & WEINBERG, R. A. 2021. Linking EMT programmes to normal and neoplastic epithelial stem cells. *Nature Reviews Cancer,* 21**,** 325-338.
LANCASTER, M. A. & HUCH, M. 2019. Disease modelling in human organoids. *Disease Models & Mechanisms,* 12**,** dmm039347.
LAURIE, N., MOHAN, A., MCEVOY, J., REED, D., ZHANG, J., SCHWEERS, B., AJIOKA, I., VALENTINE, V., JOHNSON, D., ELLISON, D. & DYER, M. A. 2009. Changes in Retinoblastoma Cell Adhesion Associated with Optic Nerve Invasion. *Molecular and Cellular Biology,* 29**,** 6268.
LAURIE, N. A., DONOVAN, S. L., SHIH, C.-S., ZHANG, J., MILLS, N., FULLER, C., TEUNISSE, A., LAM, S., RAMOS, Y., MOHAN, A., JOHNSON, D., WILSON, M., RODRIGUEZ-GALINDO, C., QUARTO, M., FRANCOZ, S., MENDRYSA, S. M., KIPLIN GUY, R., MARINE, J.-C., JOCHEMSEN, A. G. & DYER, M. A. 2006. Inactivation of the p53 pathway in retinoblastoma. *Nature,* 444**,** 61-66.
LEE, E. Y. H. P., CHANG, C.-Y., HU, N., WANG, Y.-C. J., LAI, C.-C., HERRUP, K., LEE, W.-H. & BRADLEY, A. 1992. Mice deficient for Rb are nonviable and show defects in neurogenesis and haematopoiesis. *Nature,* 359**,** 288-294.

LEE, J.-O., RUSSO, A. A. & PAVLETICH, N. P. 1998. Structure of the retinoblastoma tumour-suppressor pocket domain bound to a peptide from HPV E7. *Nature,* 391**,** 859-865.

LEE, T. C., ALMEIDA, D., CLAROS, N., ABRAMSON, D. H. & COBRINIK, D. 2006. Cell Cycle–Specific and Cell Type–Specific Expression of Rb in the Developing Human Retina. *Investigative Ophthalmology & Visual Science,* 47**,** 5590-5598.

LEE, T. C., CLAROS, N., ALMEIDA, D., ABRAMSON, D. H., KHANNA, H., SWAROOP, A. & COBRINIK, D. 2005. Expression of the Retinoblastoma Protein in Human Retinal Development. *Investigative Ophthalmology & Visual Science,* 46**,** 3150-3150.

LEI, S., DING, Y., FU, Y., WU, S., XIE, X., WANG, C. & LIANG, H. 2017. The preclinical analysis of TW-37 as a potential anti-colorectal cancer cell agent. *PLOS ONE,* 12**,** e0184501.

LI, X., GLUBRECHT DD FAU - GODBOUT, R. & GODBOUT, R. 2010. AP2 transcription factor induces apoptosis in retinoblastoma cells.

LI, X., ZHANG, L., TANG, F. & WEI, X. 2021. Retinal Organoids: Cultivation, Differentiation, and Transplantation. *Frontiers in Cellular Neuroscience,* 15.

LI, Y.-P., WANG, Y.-T., WANG, W., ZHANG, X., SHEN, R.-J., JIN, K., JIN, L.-W. & JIN, Z.-B. 2022. Second hit impels oncogenesis of retinoblastoma in patient-iPSC-derived retinal organoids: Direct evidence for Knudson's theory. *PNAS Nexus*.

LIBBY, R. T., CHAMPLIAUD, M.-F., CLAUDEPIERRE, T., XU, Y., GIBBONS, E. P., KOCH, M., BURGESON, R. E., HUNTER, D. D. & BRUNKEN, W. J. 2000. Laminin Expression in Adult and Developing Retinae: Evidence of Two Novel CNS Laminins. *The Journal of Neuroscience,* 20**,** 6517.

LIMNIOS, I. J., CHAU, Y.-Q., SKABO, S. J., SURRAO, D. C. & O'NEILL, H. C. 2021. Efficient differentiation of human embryonic stem cells to retinal pigment epithelium under defined conditions. *Stem Cell Research & Therapy,* 12**,** 248.

LIU, H., TANG, X., SRIVASTAVA, A., PÉCOT, T., DANIEL, P., HEMMELGARN, B., REYES, S., FACKLER, N., BAJWA, A., KLADNEY, R., KOIVISTO, C., CHEN, Z., WANG, Q., HUANG, K., MACHIRAJU, R., SÁENZ-ROBLES, MARIA T., CANTALUPO, P., PIPAS, J. M. & LEONE, G. 2015. Redeployment of Myc and E2f1–3 drives Rb-deficient cell cycles. *Nature Cell Biology,* 17**,** 1036-1048.

LIU, H. A.-O., ZHANG, Y. A.-O., ZHANG, Y. A.-O. X., LI, Y. A.-O., HUA, Z. A.-O. X., ZHANG, C. A.-O., WU, K. A.-O., YU, F. A.-O., ZHANG, Y. A.-O., SU, J. A.-O. & JIN, Z. A.-O. X. 2020. Human embryonic stem cell-derived organoid retinoblastoma reveals a cancerous origin.

LIU, J., OTTAVIANI, D., SEFTA, M., DESBROUSSES, C., CHAPEAUBLANC, E., ASCHERO, R., SIRAB, N., LUBIENIECKI, F., LAMAS, G., TONON, L., DEHAINAULT, C., HUA, C., FRÉNEAUX, P., REICHMAN, S., KARBOUL, N., BITON, A., MIRABAL-ORTEGA, L., LARCHER, M., BRULARD, C., ARRUFAT, S., NICOLAS, A., ELAROUCI, N., POPOVA, T., NÉMATI, F., DECAUDIN, D., GENTIEN, D., BAULANDE, S., MARIANI, O., DUFOUR, F., GUIBERT, S., VALLOT, C., ROUIC, L. L.-L., MATET, A., DESJARDINS, L., PASCUAL-PASTO, G., SUÑOL, M., CATALA-MORA, J., LLANO, G. C., COUTURIER, J., BARILLOT, E., SCHAIQUEVICH, P.,

GAUTHIER-VILLARS, M., STOPPA-LYONNET, D., GOLMARD, L., HOUDAYER, C., BRISSE, H., BERNARD-PIERROT, I., LETOUZÉ, E., VIARI, A., SAULE, S., SASTRE-GARAU, X., DOZ, F., CARCABOSO, A. M., CASSOUX, N., POUPONNOT, C., GOUREAU, O., CHANTADA, G., DE REYNIÈS, A., AERTS, I. & RADVANYI, F. 2021. A high-risk retinoblastoma subtype with stemness features, dedifferentiated cone states and neuronal/ganglion cell gene expression. *Nature Communications,* 12**,** 5578.

LIU, Y., LIANG, G., ZHOU, T. & LIU, Z. 2019. Silencing UHRF1 Inhibits Cell Proliferation and Promotes Cell Apoptosis in Retinoblastoma Via the PI3K/Akt Signalling Pathway. *Pathology & Oncology Research*.

LLONCH, S., CARIDO, M. & ADER, M. 2018. Organoid technology for retinal repair. *Developmental Biology,* 433**,** 132-143.

LOHMANN, D. 2011. Retinoblastoma. *In:* SCHWAB, M. (ed.) *Encyclopedia of Cancer.* Berlin, Heidelberg: Springer Berlin Heidelberg.

LORBER, B., HSIAO, W. K. & MARTIN, K. 2016. Three-dimensional printing of the retina. *Current opinion in ophthalmology,* 27**,** 262-267.

LOWE, A., HARRIS, R., BHANSALI, P., CVEKL, A. & LIU, W. 2016. Intercellular Adhesion-Dependent Cell Survival and ROCK-Regulated Actomyosin-Driven Forces Mediate Self-Formation of a Retinal Organoid. *Stem Cell Reports,* 6**,** 743-756.

LU, Y., SHIAU, F., YI, W., LU, S., WU, Q., PEARSON, J. D., KALLMAN, A., ZHONG, S., HOANG, T., ZUO, Z., ZHAO, F., ZHANG, M., TSAI, N., ZHUO, Y., HE, S., ZHANG, J., STEIN-O'BRIEN, G. L., SHERMAN, T. D., DUAN, X., FERTIG, E. J., GOFF, L. A., ZACK, D. J., HANDA, J. T., XUE, T., BREMNER, R., BLACKSHAW, S., WANG, X. & CLARK, B. S. 2020. Single-Cell Analysis of Human Retina Identifies Evolutionarily Conserved and Species-Specific Mechanisms Controlling Development. *Developmental Cell,* 53**,** 473-491.e9.

LUND, R. D., WANG, S., KLIMANSKAYA, I., HOLMES, T., RAMOS-KELSEY, R., LU, B., GIRMAN, S., BISCHOFF, N., SAUVÉ, Y. & LANZA, R. 2006. Human Embryonic Stem Cell–Derived Cells Rescue Visual Function in Dystrophic RCS Rats. *Cloning and Stem Cells,* 8**,** 189-199.

LYNN, S. A., WARD, G., KEELING, E., SCOTT, J. A., CREE, A. J., JOHNSTON, D. A., PAGE, A., CUAN-URQUIZO, E., BHASKAR, A., GROSSEL, M. C., TUMBARELLO, D. A., NEWMAN, T. A., LOTERY, A. J. & RATNAYAKA, J. A. 2017. Ex-vivo models of the Retinal Pigment Epithelium (RPE) in long-term culture faithfully recapitulate key structural and physiological features of native RPE. *Tissue & cell,* 49**,** 447-460.

MACPHERSON, D. & DYER, M. A. 2007. Retinoblastoma: From the Two-Hit Hypothesis to Targeted Chemotherapy. *Cancer Research,* 67**,** 7547-7550.

MADHAVAN, J., CORAL, K., MALLIKARJUNA, K., CORSON, T. W., AMIT, N., KHETAN, V., GEORGE, R., BISWAS, J., GALLIE, B. L. & KUMARAMANICKAVEL, G. 2007. High Expression of KIF14 in Retinoblastoma: Association with Older Age at Diagnosis. *Investigative Ophthalmology & Visual Science,* 48**,** 4901-4906.

MÄENPÄÄ, H., TOIMELA, T., MANNERSTRÖM, M., SARANSAARI, P. & TÄHTI, H. 2004. Toxicity of Selected Cationic Drugs in Retinoblastomal Cultures and in Cocultures of Retinoblastomal and Retinal Pigment Epithelial Cell Lines. *Neurochemical Research,* 29**,** 305-311.

MAIDA, Y., YASUKAWA, M., FURUUCHI, M., LASSMANN, T., POSSEMATO, R., OKAMOTO, N., KASIM, V., HAYASHIZAKI, Y., HAHN, W. C. & MASUTOMI, K. 2009. An RNA-dependent RNA polymerase formed by TERT and the RMRP RNA. *Nature,* 461**,** 230-235.

MALEK, G., MACE, B., SALOUPIS, P., SCHMECHEL, D., RICKMAN, D., SULLIVAN, P. & RICKMAN, C. B. Initial Observations of Key Features of Age-Related Macular Degeneration in APOE Targeted Replacement Mice. *In:* HOLLYFIELD, J. G., ANDERSON, R. E. & LAVAIL, M. M., eds. Retinal Degenerative Diseases, 2006// 2006 Boston, MA. Springer US, 109-117.

MAO, X., AN, Q., XI, H., YANG, X.-J., ZHANG, X., YUAN, S., WANG, J., HU, Y., LIU, Q. & FAN, G. 2019. Single-Cell RNA Sequencing of hESC-Derived 3D Retinal Organoids Reveals Novel Genes Regulating RPC Commitment in Early Human Retinogenesis. *Stem Cell Reports,* 13**,** 747-760.

MASLAND, R. H. 2012. The tasks of amacrine cells. *Visual neuroscience,* 29**,** 3-9.

MASUTOMI, K., POSSEMATO, R., WONG, J. M. Y., CURRIER, J. L., TOTHOVA, Z., MANOLA, J. B., GANESAN, S., LANSDORP, P. M., COLLINS, K. & HAHN, W. C. 2005. The telomerase reverse transcriptase regulates chromatin state and DNA damage responses. *Proceedings of the National Academy of Sciences,* 102**,** 8222-8227.

MATSUI, T., NIETO-ESTÉVEZ, V., KYRYCHENKO, S., SCHNEIDER, J. W. & HSIEH, J. 2017. Retinoblastoma protein controls growth, survival and neuronal migration in human cerebral organoids. *Development,* 144**,** 1025.

MAYR, C., HEMANN, M. T. & BARTEL, D. P. 2007. Disrupting the Pairing Between let-7 and Hmga2 Enhances Oncogenic Transformation. *Science,* 315**,** 1576-1579.

MCEVOY, J., FLORES-OTERO, J., ZHANG, J., NEMETH, K., BRENNAN, R., BRADLEY, C., KRAFCIK, F., RODRIGUEZ-GALINDO, C., WILSON, M., XIONG, S., LOZANO, G., SAGE, J., FU, L., LOUHIBI, L., TRIMARCHI, J., PANI, A., SMEYNE, R., JOHNSON, D. & DYER, MICHAEL A. 2011. Coexpression of Normally Incompatible Developmental Pathways in Retinoblastoma Genesis. *Cancer Cell,* 20**,** 260-275.

MCEVOY, J., NAGAHAWATTE, P., FINKELSTEIN, D., RICHARDS-YUTZ, J., VALENTINE, M., MA, J., MULLIGHAN, C., SONG, G., CHEN, X., WILSON, M., BRENNAN, R., POUNDS, S., BECKSFORT, J., HUETHER, R., LU, C., FULTON, R. S., FULTON, L. L., HONG, X., DOOLING, D. J., OCHOA, K., MARDIS, E. R., WILSON, R. K., EASTON, J., ZHANG, J., DOWNING, J. R., GANGULY, A. & DYER, M. A. 2014. RB1 gene inactivation by chromothripsis in human retinoblastoma. *Oncotarget,* 5**,** 438-450.

MCMURTREY, R. J. 2016. Analytic Models of Oxygen and Nutrient Diffusion, Metabolism Dynamics, and Architecture Optimization in Three-Dimensional Tissue Constructs with Applications and Insights in Cerebral Organoids.

MELLOUGH, C. B., BAUER, R., COLLIN, J., DORGAU, B., ZERTI, D., DOLAN, D. W. P., JONES, C. M., IZUOGU, O. G., YU, M., HALLAM, D., STEYN, J. S., WHITE, K., STEEL, D. H., SANTIBANEZ-KOREF, M., ELLIOTT, D. J., JACKSON, M. S., LINDSAY, S., GRELLSCHEID, S. & LAKO, M. 2019a. An integrated transcriptional analysis of the developing human retina. *Development,* 146**,** dev169474.

MELLOUGH, C. B., COLLIN, J., KHAZIM, M., WHITE, K., SERNAGOR, E., STEEL, D. H. W. & LAKO, M. 2015. IGF-1 Signaling Plays an Important Role in the Formation of Three-Dimensional Laminated Neural Retina and Other Ocular Structures From Human Embryonic Stem Cells. *Stem Cells,* 33**,** 2416-2430.

MELLOUGH, C. B., COLLIN, J., QUEEN, R., HILGEN, G., DORGAU, B., ZERTI, D., FELEMBAN, M., WHITE, K., SERNAGOR, E. & LAKO, M. 2019b. Systematic Comparison of Retinal Organoid Differentiation from Human Pluripotent Stem Cells Reveals Stage Specific, Cell Line, and Methodological Differences. *STEM CELLS Translational Medicine,* 8**,** 694-706.

MENDOZA, P. R. & GROSSNIKLAUS, H. E. 2015. Chapter Thirty - The Biology of Retinoblastoma. *In:* HEJTMANCIK, J. F. & NICKERSON, J. M. (eds.) *Progress in Molecular Biology and Translational Science.* Academic Press.

MEYER, J. S., SHEARER, R. L., CAPOWSKI, E. E., WRIGHT, L. S., WALLACE, K. A., MCMILLAN, E. L., ZHANG, S.-C. & GAMM, D. M. 2009. Modeling early retinal development with human embryonic and induced pluripotent stem cells. *Proceedings of the National Academy of Sciences,* 106**,** 16698.

MICALIZZI, D. S., FARABAUGH, S. M. & FORD, H. L. 2010. Epithelial-Mesenchymal Transition in Cancer: Parallels Between Normal Development and Tumor Progression. *Journal of Mammary Gland Biology and Neoplasia,* 15**,** 117-134.

MILYUSHINA, L. A., KUZNETSOVA, A. V., GRIGORYAN, E. N. & ALEKSANDROVA, M. A. 2011. Phenotypic Plasticity of Retinal Pigment Epithelial Cells from Adult Human Eye In Vitro. *Bulletin of Experimental Biology and Medicine,* 151**,** 506.

MO, Z., LI, S., YANG, X. & XIANG, M. 2004. Role of the Barhl2 homeobox gene in the specification of glycinergic amacrine cells. *Development,* 131**,** 1607-1618.

MOHAMMAD, R. M., GOUSTIN, A. S., ABOUKAMEEL, A., CHEN, B., BANERJEE, S., WANG, G., NIKOLOVSKA-COLESKA, Z., WANG, S. & AL-KATIB, A. 2007. Preclinical Studies of TW-37, a New Nonpeptidic Small-Molecule Inhibitor of Bcl-2, in Diffuse Large Cell Lymphoma Xenograft Model Reveal Drug Action on Both Bcl-2 and Mcl-1. *Clinical Cancer Research,* 13**,** 2226.

MOUGENOT, P., BRESSOLLE, F., CULINE, S., SOLASSOL, I., POUJOL, S. & PINGUET, F. 2006. In Vitro Cytotoxic Effect of Melphalan and Pilot Phase II Study in Hormone-refractory Prostate Cancer. *Anticancer Research,* 26**,** 2197.

MUEN, W. J., KINGSTON, J. E., ROBERTSON, F., BREW, S., SAGOO, M. S. & REDDY, M. A. 2012. Efficacy and Complications of Super-selective Intra-ophthalmic Artery Melphalan for the Treatment of Refractory Retinoblastoma. *Ophthalmology,* 119**,** 611-616.

MURDOCH, C., MUTHANA, M., COFFELT, S. B. & LEWIS, C. E. 2008. The role of myeloid cells in the promotion of tumour angiogenesis. *Nature Reviews Cancer,* 8**,** 618-631.

NAGY, J. A., CHANG, S.-H., SHIH, S.-C., DVORAK, A. M. & DVORAK, H. F. 2010. Heterogeneity of the Tumor Vasculature. *Semin Thromb Hemost,* 36**,** 321-331.

NAIK, A., JYOTHI, S. & SHAH, P. 2016. Retinoblastoma: A comprehensive review. *Kerala Journal of Ophthalmology,* 28**,** 164-170.
NAKANO, T., ANDO, S., TAKATA, N., KAWADA, M., MUGURUMA, K., SEKIGUCHI, K., SAITO, K., YONEMURA, S., EIRAKU, M. & SASAI, Y. 2012. Self-Formation of Optic Cups and Storable Stratified Neural Retina from Human ESCs. *Cell Stem Cell,* 10**,** 771-785.
NICHOLS, J. & SMITH, A. 2009. Naive and Primed Pluripotent States. *Cell Stem Cell,* 4**,** 487-492.
NORK, T. M., SCHWARTZ, T. L., DOSHI, H. M. & MILLECCHIA, L. L. 1995. Retinoblastoma: Cell of Origin. *Archives of Ophthalmology,* 113**,** 791-802.
NORRIE, J. L., NITYANANDAM, A., LAI, K., CHEN, X., WILSON, M., STEWART, E., GRIFFITHS, L., JIN, H., WU, G., ORR, B., TRAN, Q., ALLEN, S., REILLY, C., ZHOU, X., ZHANG, J., NEWMAN, K., JOHNSON, D., BRENNAN, R. & DYER, M. A. 2021. Retinoblastoma from human stem cell-derived retinal organoids. *Nature Communications,* 12**,** 4535.
O'HARA-WRIGHT, M. & GONZALEZ-CORDERO, A. 2020. Retinal organoids: a window into human retinal development. *Development (Cambridge, England),* 147**,** dev189746.
OLIVIER, M., HOLLSTEIN M FAU - HAINAUT, P. & HAINAUT, P. 2010. TP53 mutations in human cancers: origins, consequences, and clinical use.
ORLIC, M., SPENCER, C. E., WANG, L. & GALLIE, B. L. 2006. Expression analysis of 6p22 genomic gain in retinoblastoma. *Genes, Chromosomes and Cancer,* 45**,** 72-82.
OSAKADA, F., IKEDA, H., MANDAI, M., WATAYA, T., WATANABE, K., YOSHIMURA, N., AKAIKE, A., SASAI, Y. & TAKAHASHI, M. 2008. Toward the generation of rod and cone photoreceptors from mouse, monkey and human embryonic stem cells. *Nature Biotechnology,* 26**,** 215-224.
OSORIO, J. 2015. Repurposing MYC and E2F in the absence of RB. *Nature Reviews Molecular Cell Biology,* 16**,** 516-517.
PAEZ-ESCAMILLA, M., BAGHERI, N., TEIRA, L. E., CORRALES-MEDINA, F. F. & HARBOUR, J. W. 2017. Intracameral Topotecan Hydrochloride for Anterior Chamber Seeding of Retinoblastoma. *JAMA Ophthalmology,* 135**,** 1453-1454.
PAJOVIC, S., CORSON, T. W., SPENCER, C., DIMARAS, H., ORLIC-MILACIC, M., MARCHONG, M. N., TO, K.-H., THÉRIAULT, B., AUSPITZ, M. & GALLIE, B. L. 2011. The TAg-RB murine retinoblastoma cell of origin has immunohistochemical features of differentiated Muller glia with progenitor properties. *Investigative ophthalmology & visual science,* 52**,** 7618-7624.
PARTANEN, J. I., NIEMINEN, A. I. & KLEFSTROM, J. 2009. 3D view to tumor suppression: lkb1, polarity and the arrest of oncogenic c-myc. *Cell Cycle,* 8**,** 716-724.
PARULEKAR, M. V. 2010. Retinoblastoma — Current treatment and future direction. *Early Human Development,* 86**,** 619-625.
PEINADO, H., MARIN, F., CUBILLO, E., STARK, H.-J., FUSENIG, N., NIETO, M. A. & CANO, A. 2004. Snail and E47 repressors of E-cadherin induce distinct invasive and angiogenic properties in vivo. *Journal of Cell Science,* 117**,** 2827-2839.
PENG, Y.-R., SHEKHAR, K., YAN, W., HERRMANN, D., SAPPINGTON, A., BRYMAN, G. S., VAN ZYL, T., DO, M. T. H., REGEV, A. & SANES, J. R.

2019. Molecular Classification and Comparative Taxonomics of Foveal and Peripheral Cells in Primate Retina. *Cell,* 176**,** 1222-1237.e22.
PISTOLLATO, F., CHEN HL FAU - SCHWARTZ, P. H., SCHWARTZ PH FAU - BASSO, G., BASSO G FAU - PANCHISION, D. M. & PANCHISION, D. M. 2007. Oxygen tension controls the expansion of human CNS precursors and the generation of astrocytes and oligodendrocytes.
POBEZINSKAYA, E. L., WELLS, A. C., ANGELOU, C. C., FAGERBERG, E., ARAL, E., IVERSON, E., KIMURA, M. Y. & POBEZINSKY, L. A. 2019. Survival of Naïve T Cells Requires the Expression of Let-7 miRNAs. *Frontiers in Immunology,* 10.
POLYAK, K. & WEINBERG, R. A. 2009. Transitions between epithelial and mesenchymal states: acquisition of malignant and stem cell traits. *Nature Reviews Cancer,* 9**,** 265-273.
POTTER, V. R. 1958. The biochemical approach to the cancer problem. *Fed Proc,* 17**,** 691-7.
PRAHARAJ, P. P., BHUTIA, S. K., NAGRATH, S., BITTING, R. L. & DEEP, G. 2018. Circulating tumor cell-derived organoids: Current challenges and promises in medical research and precision medicine. *Biochimica et Biophysica Acta (BBA) - Reviews on Cancer,* 1869**,** 117-127.
QI, D. L. & COBRINIK, D. 2017. MDM2 but not MDM4 promotes retinoblastoma cell proliferation through p53-independent regulation of MYCN translation. *Oncogene,* 36**,** 1760-1769.
QIAN, B.-Z. & POLLARD, J. W. 2010. Macrophage Diversity Enhances Tumor Progression and Metastasis. *Cell,* 141**,** 39-51.
QUINN, P. M. J. & WIJNHOLDS, J. 2019. Retinogenesis of the Human Fetal Retina: An Apical Polarity Perspective. LID - 10.3390/genes10120987 [doi] LID - 987.
RAO, R. & HONAVAR, S. G. 2017. Retinoblastoma. *The Indian Journal of Pediatrics,* 84**,** 937-944.
RAO, R., HONAVAR, S. G., MULAY, K. & REDDY, V. A. P. 2018a. Eye salvage in diffuse anterior retinoblastoma using systemic chemotherapy with periocular and intravitreal topotecan. *Journal of American Association for Pediatric Ophthalmology and Strabismus,* 22**,** 235-237.e2.
RAO, R., HONAVAR, S. G., SHARMA, V. & REDDY, V. A. P. 2018b. Intravitreal topotecan in the management of refractory and recurrent vitreous seeds in retinoblastoma. *British Journal of Ophthalmology,* 102**,** 490.
RASHID, A., BHATIA, S. K., MAZZITELLO, K. I., CHRENEK, M. A., ZHANG, Q., BOATRIGHT, J. H., GROSSNIKLAUS, H. E., JIANG, Y. & NICKERSON, J. M. RPE Cell and Sheet Properties in Normal and Diseased Eyes. *In:* BOWES RICKMAN, C., LAVAIL, M. M., ANDERSON, R. E., GRIMM, C., HOLLYFIELD, J. & ASH, J., eds. Retinal Degenerative Diseases, 2016// 2016 Cham. Springer International Publishing, 757-763.
REGENT, F., CHEN, H. Y., KELLEY, R. A., QU, Z., SWAROOP, A. & LI, T. 2020. A simple and efficient method for generating human retinal organoids. *Mol, Vis,* 26**,** 97-105.
REGENT, F., MORIZUR, L., LESUEUR, L., HABELER, W., PLANCHERON, A., BEN M'BAREK, K. & MONVILLE, C. 2019. Automation of human pluripotent stem cell differentiation toward retinal pigment epithelial cells for large-scale productions. *Scientific Reports,* 9**,** 10646.

REIS, A., VARGAS, F. & LEMOS, B. 2012. More epigenetic hits than meets the eye: microRNAs and genes associated with the tumorigenesis of retinoblastoma. *Frontiers in Genetics,* 3.

RIVLIN, N., BROSH R FAU - OREN, M., OREN M FAU - ROTTER, V. & ROTTER, V. 2011. Mutations in the p53 Tumor Suppressor Gene: Important Milestones at the Various Steps of Tumorigenesis.

ROWINSKY, E. K. & KAUFMANN, S. H. 1997. Topotecan in combination chemotherapy. *Seminars in oncology,* 24**,** S20-11-S20-26.

ROZANSKA, A., CERNA-CHAVEZ, R., QUEEN, R., COLLIN, J., ZERTI, D., DORGAU, B., BEH, C. S., DAVEY, T., COXHEAD, J., HUSSAIN, R., AL-AAMA, J., STEEL, D. H., BENVENISTY, N., ARMSTRONG, L., PARULEKAR, M. & LAKO, M. 2022. pRB-Depleted Pluripotent Stem Cell Retinal Organoids Recapitulate Cell State Transitions of Retinoblastoma Development and Suggest an Important Role for pRB in Retinal Cell Differentiation. *Stem Cells Translational Medicine***,** szac008.

RUBIN, S. M., GALL, A.-L., ZHENG, N. & PAVLETICH, N. P. 2005. Structure of the Rb C-Terminal Domain Bound to E2F1-DP1: A Mechanism for Phosphorylation-Induced E2F Release. *Cell,* 123**,** 1093-1106.

RUSHLOW, D. E., MOL, B. M., KENNETT, J. Y., YEE, S., PAJOVIC, S., THÉRIAULT, B. L., PRIGODA-LEE, N. L., SPENCER, C., DIMARAS, H., CORSON, T. W., PANG, R., MASSEY, C., GODBOUT, R., JIANG, Z., ZACKSENHAUS, E., PATON, K., MOLL, A. C., HOUDAYER, C., RAIZIS, A., HALLIDAY, W., LAM, W. L., BOUTROS, P. C., LOHMANN, D., DORSMAN, J. C. & GALLIE, B. L. 2013. Characterisation of retinoblastomas without RB1 mutations: genomic, gene expression, and clinical studies. *The Lancet Oncology,* 14**,** 327-334.

RŮŽIČKOVÁ, Š. & STANĚK, D. 2017. Mutations in spliceosomal proteins and retina degeneration. *RNA Biology,* 14**,** 544-552.

SAAVEDRA, H. I., WU, L., DE BRUIN, A., TIMMERS, C., ROSOL, T. J., WEINSTEIN, M., ROBINSON, M. L. & LEONE, G. 2002. Specificity of E2F1, E2F2, and E2F3 in Mediating Phenotypes Induced by Loss of Rb. *Cell Growth Differentiation,* 13**,** 215-225.

SACHDEVA, U. M. & O'BRIEN, J. M. 2012. Understanding pRb: toward the necessary development of targeted treatments for retinoblastoma. *The Journal of Clinical Investigation,* 122**,** 425-434.

SAENGWIMOL, D., ROJANAPORN, D., CHAITANKAR, V., CHITTAVANICH, P., AROONROCH, R., BOONTAWON, T., THAMMACHOTE, W., JINAWATH, N., HONGENG, S. & KAEWKHAW, R. 2018. A three-dimensional organoid model recapitulates tumorigenic aspects and drug responses of advanced human retinoblastoma. *Scientific reports,* 8**,** 15664-15664.

SAHA, A., CAPOWSKI, E., FERNANDEZ ZEPEDA, M. A., NELSON, E. C., GAMM, D. M. & SINHA, R. 2022. Cone photoreceptors in human stem cell-derived retinal organoids demonstrate intrinsic light responses that mimic those of primate fovea. *Cell Stem Cell,* 29**,** 460-471.e3.

SALERO, E., BLENKINSOP, TIMOTHY A., CORNEO, B., HARRIS, A., RABIN, D., STERN, JEFFREY H. & TEMPLE, S. 2012. Adult Human RPE Can Be Activated into a Multipotent Stem Cell that Produces Mesenchymal Derivatives. *Cell Stem Cell,* 10**,** 88-95.

SAMIMI, K., PATTNAIK, B. R., CAPOWSKI, E. E., SAHA, K., GAMM, D. M. & SKALA, M. C. 2022. In situ autofluorescence lifetime assay of a

photoreceptor stimulus response in mouse retina and human retinal organoids. *Biomedical Optics Express,* 13**,** 3476-3492.
SAMPSON, V. B., RONG NH FAU - HAN, J., HAN J FAU - YANG, Q., YANG Q FAU - ARIS, V., ARIS V FAU - SOTEROPOULOS, P., SOTEROPOULOS P FAU - PETRELLI, N. J., PETRELLI NJ FAU - DUNN, S. P., DUNN SP FAU - KRUEGER, L. J. & KRUEGER, L. J. 2007. MicroRNA let-7a down-regulates MYC and reverts MYC-induced growth in Burkitt lymphoma cells.
SAROSY, G., LEYLAND-JONES, B., SOOCHAN, P. & CHESON, B. D. 1988. The systemic administration of intravenous melphalan. *Journal of Clinical Oncology,* 6**,** 1768-1782.
SASAI, Y. 2013. Next-Generation Regenerative Medicine: Organogenesis from Stem Cells in 3D Culture. *Cell Stem Cell,* 12**,** 520-530.
SCHAIQUEVICH, P., FRANCIS, J. H., CANCELA, M. B., CARCABOSO, A. M., CHANTADA, G. L. & ABRAMSON, D. H. 2022. Treatment of Retinoblastoma: What Is the Latest and What Is the Future. *Frontiers in Oncology,* 12.
SCHMALHOFER, O., BRABLETZ, S. & BRABLETZ, T. 2009. E-cadherin, β-catenin, and ZEB1 in malignant progression of cancer. *Cancer and Metastasis Reviews,* 28**,** 151-166.
SEARS, CYNTHIA L. & GARRETT, WENDY S. 2014. Microbes, Microbiota, and Colon Cancer. *Cell Host & Microbe,* 15**,** 317-328.
SEMENZA, G. L. 2008. Tumor metabolism: cancer cells give and take lactate. *The Journal of Clinical Investigation,* 118**,** 3835-3837.
SEMENZA, G. L. 2010. HIF-1: upstream and downstream of cancer metabolism. *Current Opinion in Genetics & Development,* 20**,** 51-56.
SHAHRIYARI, L. & KOMAROVA, N. L. 2013. Symmetric vs. asymmetric stem cell divisions: an adaptation against cancer? *PLOS ONE,* 8.
SHARMA, R., GEORGE, A., NIMMAGADDA, M., ORTOLAN, D., KARLA, B.-S., QURESHY, Z., BOSE, D., DEJENE, R., LIANG, G., WAN, Q., CHANG, J., JHA, B. S., MEMON, O., MIYAGISHIMA, K. J., RISING, A., LAL, M., HANSON, E., KING, R., CAMPOS, M. M., FERRER, M., AMARAL, J., MCGAUGHEY, D. & BHARTI, K. 2021. Epithelial phenotype restoring drugs suppress macular degeneration phenotypes in an iPSC model. *Nature Communications,* 12**,** 7293.
SHAW, R. J. 2009. Tumor Suppression by LKB1: SIK-ness Prevents Metastasis. *Science Signaling,* 2**,** pe55-pe55.
SHAY, J. W. & WRIGHT, W. E. 2000. Hayflick, his limit, and cellular ageing. *Nature Reviews Molecular Cell Biology,* 1**,** 72-76.
SHIELDS, C. L., BIANCIOTTO, C. G., JABBOUR, P., GRIFFIN, G. C., RAMASUBRAMANIAN, A., ROSENWASSER, R. & SHIELDS, J. A. 2011. Intra-arterial Chemotherapy for Retinoblastoma: Report No. 2, Treatment Complications. *Archives of Ophthalmology,* 129**,** 1407-1415.
SHIELDS, C. L., MANJANDAVIDA, F. P., AREPALLI, S., KALIKI, S., LALLY, S. E. & SHIELDS, J. A. 2014. Intravitreal Melphalan for Persistent or Recurrent Retinoblastoma Vitreous Seeds: Preliminary Results. *JAMA Ophthalmology,* 132**,** 319-325.
SIGAL, A. & ROTTER, V. 2000. Oncogenic Mutations of the p53 Tumor Suppressor: The Demons of the Guardian of the Genome. *Cancer Research,* 60**,** 6788-6793.

SIM, Y.-J., KIM, M.-S., NAYFEH, A., YUN, Y.-J., KIM, S.-J., PARK, K.-T., KIM, C.-H. & KIM, K.-S. 2017. 2i Maintains a Naive Ground State in ESCs through Two Distinct Epigenetic Mechanisms. *Stem Cell Reports,* 8**,** 1312-1328.

SINGH, H. A.-O., SHAYLER, D. W. H., FERNANDEZ, G. A.-O., THORNTON, M. A.-O., CRAFT, C. A.-O., GRUBBS, B. H. & COBRINIK, D. A.-O. 2022. An immature, dedifferentiated, and lineage-deconstrained cone precursor origin of N-Myc-initiated retinoblastoma.

SINGH, H. P., WANG, S., STACHELEK, K., LEE, S., REID, M. W., THORNTON, M. E., CRAFT, C. M., GRUBBS, B. H. & COBRINIK, D. 2018. Developmental stage-specific proliferation and retinoblastoma genesis in RB-deficient human but not mouse cone precursors. *Proceedings of the National Academy of Sciences,* 115**,** E9391-E9400.

SINGH, R., PHILLIPS, M. J., KUAI, D., MEYER, J., MARTIN, J. M., SMITH, M. A., PEREZ, E. T., SHEN, W., WALLACE, K. A., CAPOWSKI, E. E., WRIGHT, L. S. & GAMM, D. M. 2013. Functional Analysis of Serially Expanded Human iPS Cell-Derived RPE Cultures. *Investigative Ophthalmology & Visual Science,* 54**,** 6767-6778.

SINGH, R. K., MALLELA, R. K., CORNUET, P. K., REIFLER, A. N., CHERVENAK, A. P., WEST, M. D., WONG, K. Y. & NASONKIN, I. O. 2015. Characterization of Three-Dimensional Retinal Tissue Derived from Human Embryonic Stem Cells in Adherent Monolayer Cultures. *Stem Cells and Development,* 24**,** 2778-2795.

SMITH E FAU - COCHRANE, W. J. & COCHRANE, W. J. 1946. CYSTIC ORGANOID TERATOMA: (Report of a Case). *Can Med Assoc J.,* 55.

SPENCER, C., PAJOVIC, S., DEVLIN, H., DINH, Q.-D., CORSON, T. W. & GALLIE, B. L. 2005. Distinct patterns of expression of the RB gene family in mouse and human retina. *Gene Expression Patterns,* 5**,** 687-694.

SRIDHAR, A., HOSHINO, A., FINKBEINER, C. R., CHITSAZAN, A., DAI, L., HAUGAN, A. K., ESCHENBACHER, K. M., JACKSON, D. L., TRAPNELL, C., BERMINGHAM-MCDONOGH, O., GLASS, I. & REH, T. A. 2020. Single-Cell Transcriptomic Comparison of Human Fetal Retina, hPSC-Derived Retinal Organoids, and Long-Term Retinal Cultures. *Cell Reports,* 30**,** 1644-1659.e4.

STENFELT, S., BLIXT, M. K. E., ALL-ERICSSON, C., HALLBÖÖK, F. & BOIJE, H. 2017. Heterogeneity in retinoblastoma: a tale of molecules and models. *Clinical and Translational Medicine,* 6**,** 42.

STENGEL, K. R., THANGAVEL C FAU - SOLOMON, D. A., SOLOMON DA FAU - ANGUS, S. P., ANGUS SP FAU - ZHENG, Y., ZHENG Y FAU - KNUDSEN, E. S. & KNUDSEN, E. S. 2009. Retinoblastoma/p107/p130 pocket proteins: protein dynamics and interactions with target gene promoters.

STEWART, E., FEDERICO, S. M., CHEN, X., SHELAT, A. A., BRADLEY, C., GORDON, B., KARLSTROM, A., TWAROG, N. R., CLAY, M. R., BAHRAMI, A., FREEMAN, B. B., XU, B., ZHOU, X., WU, J., HONNELL, V., OCARZ, M., BLANKENSHIP, K., DAPPER, J., MARDIS, E. R., WILSON, R. K., DOWNING, J., ZHANG, J., EASTON, J., PAPPO, A. & DYER, M. A. 2017. Orthotopic patient-derived xenografts of paediatric solid tumours. *Nature,* 549**,** 96-100.

STRAUSS, O. 2005. The Retinal Pigment Epithelium in Visual Function. *Physiological Reviews,* 85**,** 845-881.

STRÖH, S., PULLER, C., SWIRSKI, S., HÖLZEL, M.-B., VAN DER LINDE, L. I. S., SEGELKEN, J., SCHULTZ, K., BLOCK, C., MONYER, H., WILLECKE, K., WEILER, R., GRESCHNER, M., JANSSEN-BIENHOLD, U. & DEDEK, K. 2018. Eliminating Glutamatergic Input onto Horizontal Cells Changes the Dynamic Range and Receptive Field Organization of Mouse Retinal Ganglion Cells. *The Journal of Neuroscience,* 38**,** 2015.

SU, P.-Y., CHUANG, J.-Z., LEE, W., ZERNANT, J., TSANG, S. H., NAGASAKI, T., SUNG, C.-H. & ALLIKMETS, R. 2021. Characterization of Stargardt disease patient-derived human retinal organoids harboring the p.Gly1961Glu mutation in the ABCA4 gene. *Investigative Ophthalmology & Visual Science,* 62**,** 2595-2595.

SUNG, C.-H. & CHUANG, J.-Z. 2010. The cell biology of vision. *The Journal of cell biology,* 190**,** 953-963.

SÜSSKIND, D., HAGEMANN, U., SCHRADER, M., JANUSCHOWSKI, K., SCHNICHELS, S. & AISENBREY, S. 2016. Toxic effects of melphalan, topotecan and carboplatin on retinal pigment epithelial cells. *Acta Ophthalmologica,* 94**,** 471-478.

SYLVESTER, K. G. & LONGAKER, M. T. 2004. Stem Cells: Review and Update. *Archives of Surgery,* 139**,** 93-99.

TAKAHASHI, K., TANABE K FAU - OHNUKI, M., OHNUKI M FAU - NARITA, M., NARITA M FAU - ICHISAKA, T., ICHISAKA T FAU - TOMODA, K., TOMODA K FAU - YAMANAKA, S. & YAMANAKA, S. 2007. Induction of pluripotent stem cells from adult human fibroblasts by defined factors.

TAKAHASHI, K. & YAMANAKA, S. 2006. Induction of Pluripotent Stem Cells from Mouse Embryonic and Adult Fibroblast Cultures by Defined Factors. *Cell,* 126**,** 663-676.

TAKIMOTO, C. H. & ARBUCK, S. G. 1997. Clinical status and optimal use of topotecan. *Oncology (Williston Park, N.Y.),* 11**,** 1635-46; discussion 1649-51, 1655-7.

TALMADGE, J. E. & FIDLER, I. J. 2010. AACR Centennial Series: The Biology of Cancer Metastasis: Historical Perspective. *Cancer Research,* 70**,** 5649-5669.

TAMIYA, S., LIU, L. & KAPLAN, H. J. 2010. Epithelial-Mesenchymal Transition and Proliferation of Retinal Pigment Epithelial Cells Initiated upon Loss of Cell-Cell Contact. *Investigative Ophthalmology & Visual Science,* 51**,** 2755-2763.

TANAKA, S., KUNATH, T., HADJANTONAKIS, A.-K., NAGY, A. & ROSSANT, J. 1998. Promotion of Trophoblast Stem Cell Proliferation by FGF4. *Science,* 282**,** 2072-2075.

TAUBE, J. H., HERSCHKOWITZ, J. I., KOMUROV, K., ZHOU, A. Y., GUPTA, S., YANG, J., HARTWELL, K., ONDER, T. T., GUPTA, P. B., EVANS, K. W., HOLLIER, B. G., RAM, P. T., LANDER, E. S., ROSEN, J. M., WEINBERG, R. A. & MANI, S. A. 2010. Core epithelial-to-mesenchymal transition interactome gene-expression signature is associated with claudin-low and metaplastic breast cancer subtypes. *Proceedings of the National Academy of Sciences,* 107**,** 15449-15454.

TEDESCO, D., LUKAS J FAU - REED, S. I. & REED, S. I. 2002. The pRb-related protein p130 is regulated by phosphorylation-dependent proteolysis via the protein-ubiquitin ligase SCF(Skp2).
TEOTIA, P., VAN HOOK, M. J., WICHMAN, C. S., ALLINGHAM, R. R., HAUSER, M. A. & AHMAD, I. 2017. Modeling Glaucoma: Retinal Ganglion Cells Generated from Induced Pluripotent Stem Cells of Patients with SIX6 Risk Allele Show Developmental Abnormalities. *Stem Cells,* 35**,** 2239-2252.
THAKURI, P. S., LIU, C., LUKER, G. D. & TAVANA, H. A.-O. 2017. Biomaterials-Based Approaches to Tumor Spheroid and Organoid Modeling.
THIERY, J. P., ACLOQUE, H., HUANG, R. Y. J. & NIETO, M. A. 2009. Epithelial-Mesenchymal Transitions in Development and Disease. *Cell,* 139**,** 871-890.
TOMAR, S., SETHI, R., SUNDAR, G., QUAH, T. C., QUAH, B. L. & LAI, P. S. 2017. Mutation spectrum of RB1 mutations in retinoblastoma cases from Singapore with implications for genetic management and counselling. *PLOS ONE,* 12**,** e0178776.
VALVERDE, J. R., ALONSO, J., PALACIOS, I. & PESTAÑA, Á. 2005. RB1 gene mutation up-date, a meta-analysis based on 932 reported mutations available in a searchable database. *BMC Genetics,* 6**,** 53.
VAN HARN, T., FOIJER, F., VAN VUGT, M., BANERJEE, R., YANG, F., OOSTRA, A., JOENJE, H. & TE RIELE, H. 2010. Loss of Rb proteins causes genomic instability in the absence of mitogenic signaling. *Genes & Development,* 24**,** 1377-1388.
VANDER HEIDEN, M. G., CANTLEY, L. C. & THOMPSON, C. B. 2009. Understanding the Warburg Effect: The Metabolic Requirements of Cell Proliferation. *Science,* 324**,** 1029-1033.
VASQUEZ, K. M. 2010. Targeting and processing of site-specific DNA interstrand crosslinks. *Environmental and Molecular Mutagenesis,* 51**,** 527-539.
VLASITS, A. L., EULER, T. & FRANKE, K. 2019. Function first: classifying cell types and circuits of the retina. *Current Opinion in Neurobiology,* 56**,** 8-15.
VON MEYENN, F., IURLARO, M., HABIBI, E., LIU, NING Q., SALEHZADEH-YAZDI, A., SANTOS, F., PETRINI, E., MILAGRE, I., YU, M., XIE, Z., KROEZE, LEONIE I., NESTEROVA, TATYANA B., JANSEN, JOOP H., XIE, H., HE, C., REIK, W. & STUNNENBERG, HENDRIK G. 2016. Impairment of DNA Methylation Maintenance Is the Main Cause of Global Demethylation in Naive Embryonic Stem Cells. *Molecular Cell,* 62**,** 848-861.
WAHLIN, K. J., MARUOTTI, J. A., SRIPATHI, S. R., BALL, J., ANGUEYRA, J. M., KIM, C., GREBE, R., LI, W., JONES, B. W. & ZACK, D. J. 2017. Photoreceptor Outer Segment-like Structures in Long-Term 3D Retinas from Human Pluripotent Stem Cells. *Scientific Reports,* 7**,** 766.
WAN, J. & GOLDMAN, D. 2016. Retina regeneration in zebrafish. *Current Opinion in Genetics & Development,* 40**,** 41-47.
WANG, B., KOHLI, J. & DEMARIA, M. 2020. Senescent Cells in Cancer Therapy: Friends or Foes? *Trends in Cancer,* 6**,** 838-857.
WARE, C. B., NELSON, A. M., MECHAM, B., HESSON, J., ZHOU, W., JONLIN, E. C., JIMENEZ-CALIANI, A. J., DENG, X., CAVANAUGH, C., COOK, S., TESAR, P. J., OKADA, J., MARGARETHA, L., SPERBER, H., CHOI, M., BLAU, C. A., TREUTING, P. M., HAWKINS, R. D., CIRULLI, V. &

RUOHOLA-BAKER, H. 2014. Derivation of naïve human embryonic stem cells. *Proceedings of the National Academy of Sciences,* 111**,** 4484.
WEST, E. L., MAJUMDER, P., NAEEM, A., FERNANDO, M., O'HARA-WRIGHT, M., LANNING, E., KLOC, M., RIBEIRO, J., OVANDO-ROCHE, P., SHUM, I. O., JUMBU, N., SAMPSON, R., HAYES, M., BAINBRIDGE, J. W. B., GEORGIADIS, A., SMITH, A. J., GONZALEZ-CORDERO, A. & ALI, R. R. 2022. Antioxidant and lipid supplementation improve the development of photoreceptor outer segments in pluripotent stem cell-derived retinal organoids. *Stem Cell Reports,* 17**,** 775-788.
WINTER, U., ASCHERO, R., FUENTES, F., BUONTEMPO, F., ZUGBI, S., SGROI, M., SAMPOR, C., ABRAMSON, H. D., CARCABOSO, M. A. & SCHAIQUEVICH, P. 2019. Tridimensional Retinoblastoma Cultures as Vitreous Seeds Models for Live-Cell Imaging of Chemotherapy Penetration. *International Journal of Molecular Sciences,* 20.
WINTER, U., MENA, H. A., NEGROTTO, S., ARANA, E., PASCUAL-PASTO, G., LAURENT, V., SUÑOL, M., CHANTADA, G. L., CARCABOSO, A. M. & SCHAIQUEVICH, P. 2016. Schedule-Dependent Antiangiogenic and Cytotoxic Effects of Chemotherapy on Vascular Endothelial and Retinoblastoma Cells. *PLOS ONE,* 11**,** e0160094.
WONG, E. S., CHOY, R. W., ZHANG, Y., CHU, W. K., CHEN, L. J., PANG, C. P. & YAM, J. C. 2022. Global retinoblastoma survival and globe preservation: a systematic review and meta-analysis of associations with socioeconomic and health-care factors. *The Lancet Global Health,* 10**,** e380-e389.
WU, C., YANG, J., XIAO, W., JIANG, Z., CHEN, S., GUO, D., ZHANG, P., LIU, C., YANG, H. & XIE, Z. 2022. Single-cell characterization of malignant phenotypes and microenvironment alteration in retinoblastoma. *Cell Death & Disease,* 13**,** 438.
XIAO, B., SPENCER, J., CLEMENTS, A., ALI-KHAN, N., MITTNACHT, S., BROCEÑO, C., BURGHAMMER, M., PERRAKIS, A., MARMORSTEIN, R. & GAMBLIN, S. J. 2003. Crystal structure of the retinoblastoma tumor suppressor protein bound to E2F and the molecular basis of its regulation. *Proceedings of the National Academy of Sciences,* 100**,** 2363-2368.
XIE, H., ZHANG, W., ZHANG, M., AKHTAR, T., LI, Y., YI, W., SUN, X., ZUO, Z., WEI, M., FANG, X., YAO, Z., DONG, K., ZHONG, S., LIU, Q., SHEN, Y., WU, Q., WANG, X., ZHAO, H., BAO, J., QU, K. & XUE, T. 2020. Chromatin accessibility analysis reveals regulatory dynamics of developing human retina and hiPSC-derived retinal organoids. *Science Advances,* 6**,** eaay5247.
XU, X. L., ABRAMSON, D., JHANWAR, S. & COBRINIK, D. 2011. Rb1 Knockdown Selectively Induces Cone Precursor Proliferation Dependent On Cone Specific Signaling In Fetal Retinal Cells. *Investigative Ophthalmology & Visual Science,* 52**,** 5362-5362.
XU, X. L., FANG, Y., LEE, T. C., FORREST, D., GREGORY-EVANS, C., ALMEIDA, D., LIU, A., JHANWAR, S. C., ABRAMSON, D. H. & COBRINIK, D. 2009. Retinoblastoma Has Properties of a Cone Precursor Tumor and Depends Upon Cone-Specific MDM2 Signaling. *Cell,* 137**,** 1018-1031.
XU, X. L., SINGH, H. P., WANG, L., QI, D.-L., POULOS, B. K., ABRAMSON, D. H., JHANWAR, S. C. & COBRINIK, D. 2014. Rb suppresses human cone-precursor-derived retinoblastoma tumours. *Nature,* 514**,** 385.

XUE, K., REN, H., MENG, F., ZHANG, R. & QIAN, J. 2019. Ocular toxicity of intravitreal melphalan for retinoblastoma in Chinese patients. *BMC ophthalmology,* 19**,** 61-61.
YAN, W., PENG, Y. R., VAN ZYL, T., REGEV, A., SHEKHAR, K., JURIC, D. & SANES, J. R. 2020. Cell Atlas of The Human Fovea and Peripheral Retina. *Scientific Reports,* 10.
YANG, C., GEORGIOU, M., ATKINSON, R., COLLIN, J., AL-AAMA, J., NAGARAJA-GRELLSCHEID, S., JOHNSON, C., ALI, R., ARMSTRONG, L., MOZAFFARI-JOVIN, S. & LAKO, M. 2021a. Pre-mRNA Processing Factors and Retinitis Pigmentosa: RNA Splicing and Beyond.
YANG, G., FU, Y., LU, X., WANG, M., DONG, H. & LI, Q. 2019. miR-34a regulates the chemosensitivity of retinoblastoma cells via modulation of MAGE-A/p53 signaling. *Int J Oncol,* 54**,** 177-187.
YANG, J., LI, Y., CHAN, L., TSAI, Y.-T., WU, W.-H., NGUYEN, H. V., HSU, C.-W., LI, X., BROWN, L. M., EGLI, D., SPARROW, J. R. & TSANG, S. H. 2014. Validation of genome-wide association study (GWAS)-identified disease risk alleles with patient-specific stem cell lines. *Human Molecular Genetics,* 23**,** 3445-3455.
YANG, J., LI, Y., HAN, Y., FENG, Y., ZHOU, M., ZONG, C., HE, X., JIA, R., XU, X. & FAN, J. 2021b. Single-cell transcriptome profiling reveals intratumoural heterogeneity and malignant progression in retinoblastoma. *Cell Death & Disease,* 12**,** 1100.
YANG, J. & WEINBERG, R. A. 2008. Epithelial-Mesenchymal Transition: At the Crossroads of Development and Tumor Metastasis. *Developmental Cell,* 14**,** 818-829.
YANG, S., ZHOU, J. & LI, D. 2021c. Functions and Diseases of the Retinal Pigment Epithelium. *Frontiers in Pharmacology,* 12.
YANG, X., YU, X.-W., ZHANG, D.-D. & FAN, Z.-G. 2020. Blood-retinal barrier as a converging pivot in understanding the initiation and development of retinal diseases. *Chinese Medical Journal,* 133.
YANıK, Ö., GÜNDÜZ, K., YAVUZ, K., TAÇYıLDıZ, N. & ÜNAL, E. 2015. Chemotherapy in Retinoblastoma: Current Approaches. *Turkish journal of ophthalmology,* 45**,** 259-267.
YAU, K.-W. & HARDIE, R. C. 2009. Phototransduction Motifs and Variations. *Cell,* 139**,** 246-264.
YILMAZ, M. & CHRISTOFORI, G. 2009. EMT, the cytoskeleton, and cancer cell invasion. *Cancer and Metastasis Reviews,* 28**,** 15-33.
YIN, X., MEAD, BENJAMIN E., SAFAEE, H., LANGER, R., KARP, JEFFREY M. & LEVY, O. 2016. Engineering Stem Cell Organoids. *Cell Stem Cell,* 18**,** 25-38.
YING, P., HUANG, C., WANG, Y., GUO, X., CAO, Y., ZHANG, Y., FU, S., CHEN, L., YI, G. & FU, M. 2021. Single-Cell RNA Sequencing of Retina:New Looks for Gene Marker and Old Diseases.
YU, J., VODYANIK, M. A., SMUGA-OTTO, K., ANTOSIEWICZ-BOURGET, J., FRANE, J. L., TIAN, S., NIE, J., JONSDOTTIR, G. A., RUOTTI, V., STEWART, R., SLUKVIN, I. I. & THOMSON, J. A. 2007. Induced Pluripotent Stem Cell Lines Derived from Human Somatic Cells. *Science,* 318**,** 1917.
ZARKOWSKA, T., U, S., HARLOW, E. & MITTNACHT, S. 1997. Monoclonal antibodies specific for underphosphorylated retinoblastoma protein identify

a cell cycle regulated phosphorylation site targeted by CDKs. *Oncogene,* 14**,** 249-254.

ZEITLIN, B. D., ZEITLIN, I. J. & NÖR, J. E. 2008. Expanding circle of inhibition: small-molecule inhibitors of Bcl-2 as anticancer cell and antiangiogenic agents. *Journal of clinical oncology : official journal of the American Society of Clinical Oncology,* 26**,** 4180-4188.

ZHANG, H., HU, L., QIU, W., DENG, T., ZHANG, Y., BERGHOLZ, J. & XIAO, Z. X. 2015. MDMX exerts its oncogenic activity via suppression of retinoblastoma protein. *Oncogene,* 34**,** 5560-5569.

ZHANG, J., BENAVENTE, C. A., MCEVOY, J., FLORES-OTERO, J., DING, L., CHEN, X., ULYANOV, A., WU, G., WILSON, M., WANG, J., BRENNAN, R., RUSCH, M., MANNING, A. L., MA, J., EASTON, J., SHURTLEFF, S., MULLIGHAN, C., POUNDS, S., MUKATIRA, S., GUPTA, P., NEALE, G., ZHAO, D., LU, C., FULTON, R. S., FULTON, L. L., HONG, X., DOOLING, D. J., OCHOA, K., NAEVE, C., DYSON, N. J., MARDIS, E. R., BAHRAMI, A., ELLISON, D., WILSON, R. K., DOWNING, J. R. & DYER, M. A. 2012. A novel retinoblastoma therapy from genomic and epigenetic analyses. *Nature,* 481**,** 329-334.

ZHANG, J., GRAY, J., WU, L., LEONE, G., ROWAN, S., CEPKO, C. L., ZHU, X., CRAFT, C. M. & DYER, M. A. 2004. Rb regulates proliferation and rod photoreceptor development in the mouse retina. *Nature Genetics,* 36**,** 351-360.

ZHENG, C., SCHNEIDER, J. W. & HSIEH, J. 2020. Role of RB1 in human embryonic stem cell-derived retinal organoids. *Developmental Biology*.

ZHONG, X., GUTIERREZ, C., XUE, T., HAMPTON, C., VERGARA, M. N., CAO, L.-H., PETERS, A., PARK, T. S., ZAMBIDIS, E. T., MEYER, J. S., GAMM, D. M., YAU, K.-W. & CANTO-SOLER, M. V. 2014. Generation of three-dimensional retinal tissue with functional photoreceptors from human iPSCs. *Nature Communications,* 5**,** 4047.

ZHOU, H., WU, S., JOO, J. Y., ZHU, S., HAN, D. W., LIN, T., TRAUGER, S., BIEN, G., YAO, S., ZHU, Y., SIUZDAK, G., SCHÖLER, H. R., DUAN, L. & DING, S. 2009. Generation of Induced Pluripotent Stem Cells Using Recombinant Proteins. *Cell Stem Cell,* 4**,** 381-384.

ZHOU, L., NG, D. S.-C., YAM, J. C., CHEN, L. J., THAM, C. C., PANG, C. P. & CHU, W. K. 2022. Post-translational modifications on the retinoblastoma protein. *Journal of Biomedical Science,* 29**,** 33.

ZHU, G., PAN, C., BEI, J. X., LI, B., LIANG, C., XU, Y. & FU, X. 2020. Mutant p53 in Cancer Progression and Targeted Therapies.

ZHU, Z., SHENDURE J FAU - CHURCH, G. M. & CHURCH, G. M. 2005. Discovering functional transcription-factor combinations in the human cell cycle.

ZOLFAGHARI, E., KIM, J. W., KRISHNAN, S., CHÉVEZ-BARRIOS, P. & BERRY, J. L. 2018. Atypical Retinal Pigment Epithelial Hyperplasia and Glial Proliferation Masquerading as Progressive Recurrent Retinoblastoma: A Case Report Review and Clinicopathologic Correlation. *Ocular Oncology and Pathology,* 4**,** 116-121.

ZUMSTEG, A. & CHRISTOFORI, G. 2009. Corrupt policemen: inflammatory cells promote tumor angiogenesis. *Current Opinion in Oncology,* 21.